PhD-FSTM-2024-044

The Faculty of Science, Technology and Medicine

DISSERTATION

Presented on 29/05/2024 in Esch-sur-Alzette

to obtain the degree of

DOCTEUR DE L'UNIVERSITÉ DU LUXEMBOURG

EN PHYSIQUE

by

Ricardo Jorge GONÇALINHO POEIRA

Born on 13th October 1994 in Lisbon (Portugal)

SYNTHESIS AND CHARACTERIZATION OF CU(IN,GA)SE_2 MICRO SOLAR CELLS FOR HIGH EFFICIENCY APPLICATIONS

Dissertation Defence Committee:

Dr. Phillip DALE, dissertation supervisor
Professor, Université du Luxembourg

Dr. Daniel ABOU-RAS
HZB, Helmholtz-Zentrum Berlin

Dr. Daniele BRIDA, Chairman
Professor, Université du Luxembourg

Dr. Theresa FRIEDLMEIER
ZSW, Zentrum für Sonnenenergie und Wasserstoff-Forschung Baden-Württemberg

Dr. Diego COLOMBARA, Vice Chairman
Professor, Università degli Studi di Genova

Declaration of Authorship

I, Ricardo Jorge GONÇALINHO POEIRA, declare that this thesis titled, "Synthesis and characterization of Cu(In,Ga)Se_2 micro solar cells for high efficiency applications" and the work presented in it are my own. I confirm that PhD thesis entitled "Synthesis and characterization of Cu(In,Ga)Se_2 micro solar cells for high efficiency applications" has been written independently and without any other sources than cited.

Luxembourg, _____ _____

Name

"Shoot for the moon, even if you miss, you'll land amongst the stars."

Norman Vincent Peale

"If I have seen further than others, it is by standing upon the shoulders of giants."

Isaac Newton

"The greatest thing about big ideas is being able to share them!"

Albert Einstein

"L'argent ne fait pas le bonheur, mais qu'est-ce qu'il y contribue. "

Patricia Ramoa

Abstract

The worrying progression of climate change is urging for scientists and engineers to rapidly deploy renewable energy technologies and to develop pedagogic methods to explain to the public the urgent need for changing our energy infrastructure and potentially even our way of life.

Photovoltaics are a cheap and reliable solution that can convert sunlight into electricity and greatly contribute to decarbonize the current world energy mix. Thin film $Cu(In,Ga)Se_2$ (CIGSe) solar cells are a mature technology that is well-known for using 100-fold less absorber material compared to silicon solar cells. Furthermore, CIGSe solar cells were demonstrated to be compatible with micro-concentrator photovoltaics (micro-CPV), which combines optical lenses, to concentrate more sunlight, with an array of miniaturized solar cells to generate more electricity, i.e. increase the solar cell's power conversion efficiency (PCE). This allows to simultaneously achieve higher PCEs from the same active area and considerable semiconductor material savings. As an example, a 100 X light concentration would lead to a 100-fold material savings. However, so far, only material wasteful methods have produced CIGSe micro solar cells with PCEs similar to the world record CIGSe solar cells (23.6 %). To minimize the use of materials, material efficient deposition methods have been proven to effectively produce arrays of CIGSe micro solar cells. However, a large gap in PCE still exists compared to material wasteful methods. To understand the reasons for this discrepancy, both material wasteful and material efficient synthesis methods are investigated in this work, with the aim of growing CIGSe on patterned substrates, containing the arrays of holes that define the micro solar cells.

Firstly, since each array contains a high number of individual future micro solar cells, a simple methodology was developed to characterize each individual cell and to statistically compare them. From optical and topographic images, acquired with confocal microscopy at each step of the synthesis, four conclusions were drawn: (i) that the morphology of the precursor layers play a major role in determining both the morphology and phase formation of the respective absorber. (ii) a new optical method to measure elemental composition in sequential processes, (iii) which combined with the phase diagram, allowed to spatially predict which phases would form at the end of the synthesis process. (iv) the ability to quickly differentiate phases in a material.

Secondly, a reference co-evaporation growth method was used to investigate whether the use of a SiO_2 patterned substrate itself influences the growth of CIGSe. It was found that the patterned SiO_2 layer, acts as a diffusion barrier layer for alkali dopants, from the substrate, which redirected and enhanced the diffusion of sodium through the holes meant for the micro solar cells. This led to the formation of a $Na(In,Ga)_3Se_5$ secondary

phase and to a poor adhesion between the CIGSe film and the molybdenum back contact. Three distinct methods were studied to control the sodium diffusion and the most effective was the implementation of a sodium barrier, grown directly on the sodalime glass substrate. Further comparison with the reference growth method unveiled that the selenium partial pressure, during CIGSe formation, regulates the sodium diffusion from the patterned substrate, and influences the morphology and composition homogeneity of the resulting CIGSe absorber.

Thirdly, a novel material efficient synthesis method was demonstrated to yield micro solar cells with PCEs up to 5 % at 1 Sun, which is the highest PCE reported for island-shaped micro solar cells. It was observed that a fine control of the selenium supply is crucial to optimize the morphology, phase purity and PCE of the CIGSe devices. Also, the design of the substrate pattern was proven to three dimensionally shape the CIGSe absorber and the diameter of the holes has an influence in the formation mechanism of CIGSe and adhesion to the back contact.

Finally, a new pedagogic tool was developed to explain the abstract concept of energy, involved in every citizen's lifestyle, without visible calculations. Here, a description of the design and involved calculations are detailed with the aim of demonstrating that complex topics can be conveyed in widely-known terms, such as dimensions, weight and area.

The optical method developed for the characterization of micro solar cells, can be applied to other systems, in particular for sequential processes, in order to study morphology, relative composition, diffusion processes, all with statistical weight. Furthermore, confocal microscopy was demonstrated to be a diagnosis tool to monitor the progression of a process or to highlight possible issues, allowing to intervene at an early stage. The examples shown in this work widen the range of applications for confocal microscopy and confirms its applicability for thin film characterization.

Regarding the material efficient synthesis of CIGSe micro solar cells, this work has highlighted issues, inherent to the method, and has laid out solutions to circumvent them. This allowed to highlight the relevant experimental parameters to reproduce CIGSe micro solar cells with higher PCE. Nevertheless, further optimization of the experimental parameters (temperature, precursor composition, selenium partial pressure, alkali post-deposition treatment) is expected to result in even higher PCEs, decreasing the gap to the material wasteful methods.

Last but not least, the developed pedagogic tool demonstrates a method to popularize a complex topic, which can be used to easily inform the regular citizen about current problematics or research, and in this case, hopefully trigger further interest and momentum in the fight against climate change.

Acknowledgements

Good things do come to an end, but their memories last. I am extremely proud of my professional and personal achievements during my PhD period. And even more so for having been able to share all those moments with the people that helped me or followed my journey. It was a blessing to interact with so many kind, interesting and supportive people. You all made this journey very enjoyable and unforgettable. For these reasons, I take this chance to materialize my gratitude towards them all.

To kick-off this session, I would like to thank my supervisor and mentor Prof. Phillip Dale for giving me the chance to do a PhD in a challenging and interesting topic, for guiding me throughout my scientific journey, for challenging my ideas but always encouraging me to pursue them, for sharing your passions and giving me the opportunity to explore the thrilling world of science outreach, which opened up new directions for my professional career. Thank you, Phil.

I thank Prof. Susanne Siebentritt and Prof. Alex Redinger for their feedback and ideas during our PV group meetings, which were always a trigger for further questioning and a source of new ideas to try out. A special thank you to Prof. Susanne Siebentritt for her guidance during my Bachelor, which ultimately lead me to do my PhD in Physics.

I also thank my CET members for following my journey and for the valuable suggestions. Also, I thank all jury members for being interested in my work and for participating at my defence.

A special thank to my collaborators that helped me with measurements or by providing substrates. More precisely, I thank Prof. Daniel Abou-Ras for the EBSD measurements that shed some light on the mysterious sodium phase that we formed. A special thank you to Dr. Ana Pérez-Rodriguez, to Marina Alves and to Dr. Sascha Sadewasser for the interesting discussions and for tirelessly providing substrates and adjusting to our requests.

A heart-warming thank you to everyone in FNR who was involved in the PACE doctoral training unit, for designing and funding such a thrilling programme. To all PACE supervisors and students, a special thank you for making this a very enjoyable and enriching experience.

To my colleagues in the LEM, LPV and SPM groups (current and former members), I really enjoyed the time with you in the lab and in the office. Thank you for the jokes and the nice moments. Thank you to Daniel Siopa for helping me exploring the intricacies of micro-dots. Thank you to Alice Debot for all the fun moments and to Hasan Yetkin for being a caring office neighbour. Thank you to Mohit Sood and Evandro Lanzoni for being such nice Senpai and very good friends. A pre-ordered thank you to Aubin Prot for taking the gargantuan task of measuring, or trying to, PL from micro-dots so many times. A similarly large thank you to Taowen Wang for growing the samples that shed some light on the mysteries of micro-dots.

To Thomas Schüler, ach... was soll ich sagen... Thank you for allowing me to use your tools and fix my own problems. Danke für alle deine Hinweise und Hilfe. I am very sorry for all the times I unintentionally scared the shit out of you. I hope it did not affect your lifespan. Oh and thank you for the good music! Rock on!

Michelissimo, what an incredible support you are. Thank you so much for all your help during my PhD, for your heroic attempts at making my micro-dots work, for being such an amazing office buddy and for being such a good friend. Also, grazie per tutti momenti, the jokes, the board games and for so many good memories. Grande Michele!!!!

A very sincere thank you to Patricia Ramoa, Elodie Duriez, Adamantia Galani, Astrid Tobias and Ida Ienna for their excellent work and for greatly simplifying my stay at the University in terms of administration. Thank you for all the fun discussions and moments, specially during the Christmas events. Merci beaucoup à Patricia d'avoir été une excellente collègue de bureau à temps plein. J'ai vraiment apprécié nos discussions. Merci à Elodie Duriez et Ida Ienna pour les visites agréables dans notre bureau.

A sweet thank you to everyone who shared with me their well-deserved slice of bread during lunch.

A special thank you to Alexander Medina and Louis Krieger for the good moments and very interesting conversations. Thank you Louis for that amazing ice cream on a random summer afternoon.

To my dearest friends, Aubin Prot and Taowen Wang, I cannot summarize how much we have experienced together during these years, it was simply amazing. Thank you for always being there unconditionally. The board games, the renovations, the sweet potato fries, the jokes, the awesome music, the encouragement during the thesis writing (and the breaks from it as well) and so much more, they are all priceless memories. You're like family! Thank you! Looking forward for more, but it will never be enough, for me!

À familia Machado, um grande obrigado por partilharem tantos bons momentos comigo, por todo o apoio e ajuda em todos os momentos e por me fazerem sempre sentir em familia. Gosto muito de vocês!

Não posso deixar de mencionar o apoio e carinho incondicional dos meus pais e irmãos desde sempre. Obrigado por estarem presentes em todos os momentos e por acreditarem em mim. Sinto-me muito agradecido por vos ter! Adoro-vos!

Joana, Joana... és um enorme pilar na minha vida. Já passámos por muitos momentos bons e menos bons e contigo tudo se torna mais fácil e divertido. Obrigado por seres quem és e por partilhares a tua joie-de-vivre comigo. Obrigado pelo teu apoio e confiança em todos os momentos. Contigo, todos os dias são especiais e tudo vale a pena ser vivido e relembrado. És muito especial! Adoro-te!

Finally, I thank everyone that was present during my defence.

Contents

Chapter 1

Introduction

1.1 Climate change - the greatest threat to human kind

Energy is the pillar of modern life. Since the industrial revolution, humankind has exploited multiple sources of energy to power and expand our society. This allowed to drastically improve the general quality of life by boosting production, and therefore economical growth, general comfort and development. For the last three centuries, fossil fuels have been the dominant share of energy sources [1], however their use emits greenhouse gases (GHGs), like carbon dioxide (CO_2) and methane (CH_4), into the atmosphere. Numerous studies have correlated the emission of GHGs with the global warming of the planet, that is the increase of the average temperature at the surface of the Earth [2–5], which is the driving force of climate change. Direct or indirect consequences of climate change include, but are not limited to, higher frequency for extreme weather, extinction of ecosystems, higher sea level, fauna and flora migration, deforestation, etc. "*Acknowledging that change in the Earth's climate and its adverse effects are a common concern of humankind*", a first international treaty on climate change was signed in 1992, with the aim "*to achieve [...] stabilization of greenhouse gas concentrations in the atmosphere at a level that would prevent dangerous anthropogenic interference with the climate system*" [6]. Given the worrying progression of CO_2 emissions and global average temperature [7, 8], the Paris agreement was put forward in 2015 urging "*to strengthen the global response to the threat of climate change*" with the aim of "*holding the increase in the global average temperature to well below 2 °C above pre-industrial levels*" [9]. The most recent assessment report from the Intergovernmental Panel on Climate Change (IPCC), highlights that the global average temperature continues to rise dramatically, having already reached in 2023 1.45 °C above pre-industrial levels [10], and considerable efforts, beyond current policies, will be required to hold the global average temperature below 2 °C during the 21st century.

In recent years, the consequences of climate change have become present in everyone's life, with every year establishing new temperature records, more frequent and devastating wildfires, heavy rains leading to flooding, longer and more extreme droughts, extinction of species, to name only a few. Furthermore, the emitted CO_2 will remain in the atmosphere for thousands of years, which means the current extreme weather events

are the new norm for the future. Continuing to underestimate climate change will be catastrophic for humankind.

1.2 Solutions to address climate change

The IPCC report has laid out a clear pathway to mitigate climate change and decarbonize the world economy, while meeting the human being's requirement for energy. To address climate crisis, it is essential to first and foremost minimize the emissions of GHGs related to anthropogenic activities. For this, renewable energies like solar, wind, geothermal and hydropower must become the dominant energy source, as these have minimal GHGs emission compared to fossil fuels [11]. On top of that, renewable energies have already become a cheaper energy source compared to fossil fuels [12]. Another approach to reduce GHGs emissions is to reduce and optimize energy consumption, both at the industrial level, as well as, for citizens' economical and societal behavior. In general, industries already tend to optimize their processes in order to reduce costs, which usually aligns with energy savings. In terms of citizens, it is not necessarily obvious which practices and products entail a low GHGs emission or energy requirement. To complement this gap, experts can impartially educate the general public in order to raise awareness, allowing each and every one to take educated decisions regarding their energy consumption habits and behaviors. After all, industry exists to satisfy the needs of citizens, therefore I believe every consumer is also responsible for the energy requirements and GHGs emissions of the respective services and products. Additionally, if the energy demand can be reduced, it also implies that less energy storage capacity is required, facilitating the decarbonization of countries. Finally, one can reduce the concentration of GHGs in the atmosphere, by capturing them at the source or directly from air and store it in long-term stable locations. One must be aware that no single technology can address the whole extent of the climate change and thus a combination of multiple solutions is required.

The most adapted renewable energy source depends on the location that is considered, however solar and wind power are anticipated to become the dominant share of energy sources in most regions, given their low cost, efficiency, robustness, rapid deployability and CO_2 contribution. On the one hand, wind power consists in the use of wind turbines that utilize the kinetic energy of the wind to operate turbines and convert it into electricity. On the other hand, solar power is based on the photovoltaic (PV) effect, that is the absorption of sunlight, by a semiconductor material, to generate electricity. In both cases, the source of energy, i.e. the Sun, is endless on human timescales. The world's current renewable energy consumption is estimated to roughly 27 000 TWh [1, 13]. Yearly, about 180 000 TWh energy is required to run today's world economy and the projected needs amount to 208 000 TWh by 2050, which directs to an urge for high efficiency renewable energy generators to limit the impact of climate change [1, 14].

1.2.1 Solar cells as renewable energy source

Decades of research on solar cells has resulted in a wide range of photovoltaic technologies with efficiencies up to 47.6 % power conversion efficiency (PCE) [15] and a large variety of materials which open up new opportunities in terms of energy generation. In the context of the climate crisis, the commercial solar cell modules that dominate the market are based on crystalline Si, as the light absorbing material, and their record PCE is currently at 26.81 % ($\sim$ 90 % of the respective theoretical limit of 29.4 % PCE) [16]. To complement the Si-based technology, thin-film technologies, like Cu(In,Ga)Se_2 (CIGSe) and CdTe, have achieved PCEs above 22 % and require 100$\times$ less material to operate, which also enables the production of flexible solar cell modules. These can easily find applications in building and vehicle integrated photovoltaics for instance and drastically expand the deployment possibilities for solar cells.

To go beyond the traditional PCE limit (Shockley–Queisser limit), two major strategies have been explored: (i) multi-junction solar cells and (ii) concentration photovoltaics (CPV). Both concepts and the respective theoretical PCEs are shown in Figure 1.1. The first case aims at optimizing the usage of the solar spectrum, as illustrated in Figure 1.1a. In fact, by stacking multiple solar cells with distinct energy bandgaps, it is possible to reduce the optical losses, present in the single-junction case, and therewith achieve PCEs above 45 %. Indeed, in the case of a stack of two cells, Figure 1.1b shows a map of theoretical PCE for a two terminal tandem device as a function of the bandgaps of the top and the bottom solar cells. In the second case, the solar cells are combined with optical lenses to concentrate the incoming light onto the solar cells, effectively increasing the sunlight's intensity, i.e. the number of incoming photons (see Figure 1.1c for schematic). This is equivalent to having multiple Suns illuminating the same solar cell, which leads to a more efficient use of the same land surface. In terms of PCE, the theoretical absolute gain by light concentration depends on the bandgap of the semiconductor material as shown in Figure 1.1d. Combining the two approaches, high efficiencies were demonstrated for III-V semiconductors with a record PCE of 47.6 % under 665$\times$ Suns [15], however this technology is too costly for terawatt deployment and currently not compatible with high throughput. Instead, Si and thin film technologies are mature candidates to meet the requirements for efficiency and high throughput. Combining these technologies with light concentration could effectively improve the efficiency of the modules, and thus potentially reduce their costs, however conventional solar cells show issues with the generated heat and resistive losses which lead to the deterioration of PCE [17].

1.2.2 Micro-concentrator photovoltaics

To overcome these issues, micro-scale concentrator photovoltaics (micro-CPV) was put forward. It consists of replacing the standard absorber layer, in the solar cell configuration, with an array of miniaturized absorbers with dimensions smaller than 1 mm^2. On the one hand, multiple benefits can ensue, such as material savings, costs reduction, thermal management, lower series resistance and enhanced PCE [17, 22]. On the other

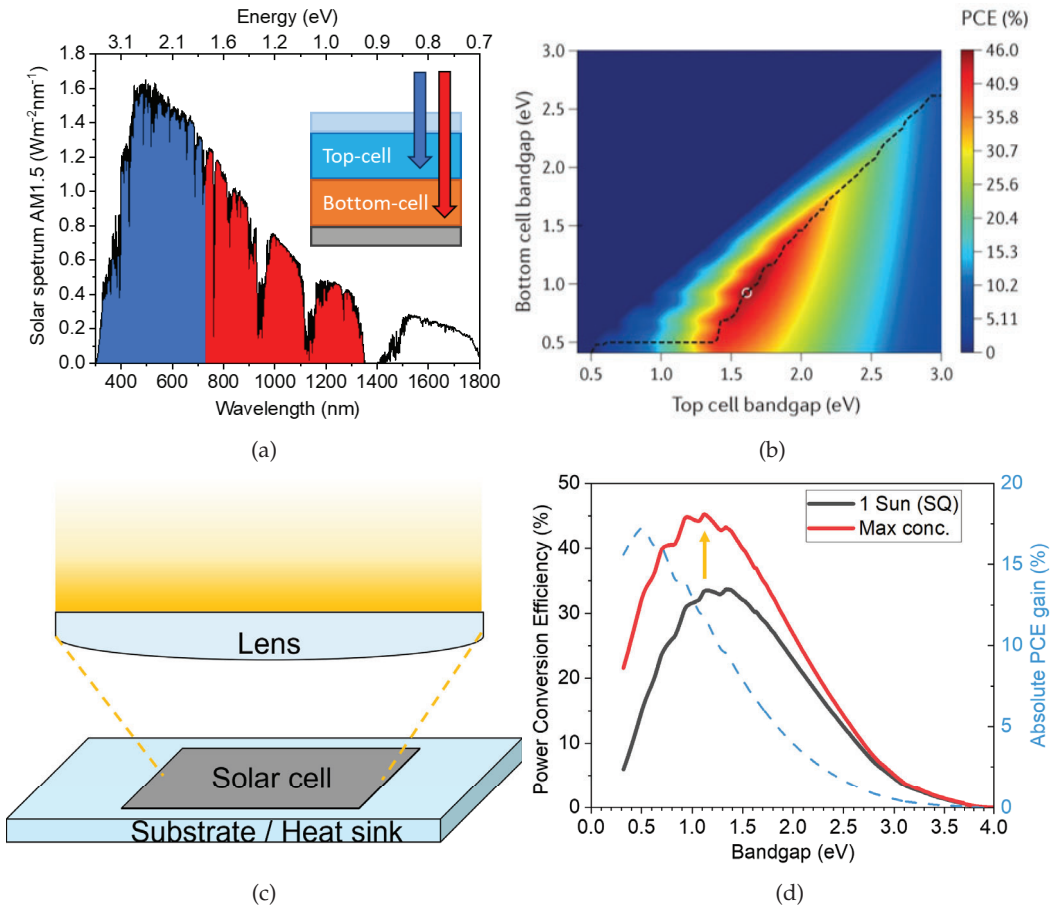

Figure 1.1: a) Solar spectrum AM1.5 with schematics of a tandem solar cell as inset, where higher-energy photons are absorbed by the top cell (in blue) and the lower-energy photons by the bottom cell (in red). b) Theoretical maximum PCE as a function of the top and bottom sub-cell bandgap for a two-terminal configuration. Dashed black line indicates the maxima PCE over the range of top cell bandgaps. The white circle indicates the overall maximum PCE. Figures a and b were adapted from [18]. c) Schematics of the typical components characteristic of CPV. d) Theoretical maximum PCE achievable at 1 Sun (Shockley–Queisser limit) and at maximum concentration (46 165× [19]) as a function of the solar cell's bandgap [20, 21]. Absolute PCE gain is also plotted to illustrate the increase in PCE for different bandgaps.

hand, reducing the absorber's dimensions implies increasing the surface area to bulk volume ratio, which results in detrimental surface effects, like edge recombination, to become more consequent. In this context, CIGSe is a technology of particular interest as it was demonstrated to overcome the above constraint when miniaturized. Indeed, Paire et al. have shown the resistive losses, which were the limiting factor for planar CIGSe concentrator cells [23], become negligible for smaller cell areas and allow to predict PCEs up to 30 % under concentrated sunlight for micro solar cells in the μm^2 range [22, 24]. In terms of thermal management, Sadewasser et al. simulated that island-shaped micro solar cells, with diameter smaller than 200 µm, have a temperature increase below 30 °C for a concentration of up to 1000 Suns [25]. In fact, this study served as the baseline for the design of the micro solar cells explored in this thesis. Experimentally, Paire et al. measured, through photoluminescence, that micro solar cells with a diameter of 50 µm

heat up by less than 20 °C even at a concentration of 1000 Suns [24]. Finally, the study of Paire et al. on the edge recombination of miniaturized CIGSe has evidenced that little to no losses in the open-circuit voltage V_{OC} were observed on micro solar cells down to 30 µm diameter ($\sim 10^{-5}$ cm^2) [26]. The result was attributed to the lower diffusion length of CIGSe (1 µm), which limits the detrimental effects of edges on V_{OC}. This is indeed an advantage compared to III-V crystalline solar cells, where roughly 10 % loss in V_{OC} was measured for a cell area of 10^{-3} cm^2 under 1 Sun, comparatively to a planar solar cell [27]. Under high concentration (1330 Suns), the V_{OC} loss dropped to 4 % compared to the planar configuration, which also highlights the benefits of micro-CPV. The same report presents a champion PCE of 33.8 % under 584 Suns for an active area of 0.25 mm^2. In this perspective, CIGSe is a fitting candidate for micro-CPV.

Over the last decade, two approaches were taken to fabricate CIGSe micro solar cells for micro-CPV. On the one hand, a top-down approach, or subtractive method, consists in removing or shadowing a fraction of a full area solar cell in order to reduce the active area down to the desired dimensions, while hopefully maintaining the same properties and performance as the complete absorber or device. Different fabrication methods have been demonstrated and were covered in the following review [17]. Through such methods, Paire et al. fabricated 50 µm wide CIGSe micro solar cells with an efficiency of 21.3 % under 475 Suns [28], which is comparable with the current record, 23.6 %, for the full area CIGSe device [29]. On the other hand, a bottom-up approach, or additive method, optimizes the usage of material by depositing only the required amount of material, directly assembling the micro structures. The major advantage of the method being the optimization of critical material usage. Distinct methods have been put forward, these include: (i) a pre-patterning of the Mo substrate, either by removing excessive Mo [30] or covering it with an insulating layer [31], followed by an electrodeposition and annealing process. (ii) the creation of nucleation sites by laser structuring the glass/Mo substrate, followed by a selective physical vapor evaporation of In islands and a full-covering layer of Cu, which subsequently react under Se evaporation to form $CuInSe_2$ micro absorbers [32, 33]. (iii) a laser-induced transfer of microscopic precursor material, from a planar precursor layer (donor) onto an acceptor substrate, followed by an annealing process in Se [34]. Despite the diverse bottom-up approaches, the achieved efficiencies are still distant compared to the top-down methods [35]. In fact, for island-shaped micro solar cells, the best PCE was obtained by a two-step process (electrodeposition followed by annealing), where a single micro solar cell was reported with 4.8 % PCE at 33 Suns [36]. In this perspective, both the PCE and the optimal concentration factor are one order of magnitude from the best top-down produced micro CIGSe solar cell. This highlights that further investigation is required to reduce the gap in performance between the two approaches and to provide statistical weight to the bottom up CIGSe micro solar cells.

1.2.3 Cu(In,Ga)Se_2 material and solar cells

CIGSe is a ternary semiconductor material with multiple properties that are important for photovoltaic applications, like tunable direct bandgap, high absorption coefficient, low production cost and phase stability [37–40]. It crystallizes in a tetragonal chalcopyrite structure (space group $I\bar{4}2d$) [41, 42], similarly to its base counter parts $CuInSe_2$ and $CuGaSe_2$, as shown in Figure 1.2a. In fact, it is the proportion of In to Ga atoms, in the compound, that determines the bandgap of the semiconductor layer and allows to cover the range from 1.0 eV ($CuInSe_2$) to 1.7 eV ($CuGaSe_2$) [39]. For this, the GGI=[Ga]/([Ga]+[In]) ratio is commonly used to characterize the distribution of the group III elements. Another revelant compositional ratio is the CGI=[Cu]/([Ga]+[In]) which plays a major role in the phase formation when synthesizing the CIGSe compound. For simplicity, the phase diagram of the binary system, Cu_2Se and In_2Se_3, is considered in Figure 1.2b, as it contains equivalent information regarding the $CuInSe_2$ phase [43]. For this work, the relevant synthesis temperatures are below 600 °C and as the phase diagram displays, the formation of a pure chalcopyrite phase (α-CISe) is restricted to a particular composition interval. Indeed, any excess of Cu, i.e. CGI > 1.0 or X=[In_2Se_3] < 50 mol. %, leads to the formation of a secondary phase Cu_2Se. This metallic phase is in fact detrimental for solar cell applications [44]. Conversely, a Cu deficiency, i.e. CGI < 1.0 or X > 50 mol. %, merely causes Cu-vacancies in the chalcopyrite structure at first and only for higher In contents, do these form an ordered vacancy compound (β-CISe: $CuIn_3Se_5$).

In terms of reaction mechanism, Hergert et al. highlights that the first reactions in the synthesis of CIGSe involve the formation of the binary compounds Cu_2Se, In_2Se_3 (or InSe depending on synthesis method) and Ga_2Se_3 [46]. Then, the formation of the $CuInSe_2$ chalcopyrite phase takes place, as follows:

$$\frac{1}{2}Cu_2Se + \frac{1}{2}In_2Se_3 \rightarrow CuInSe_2 \tag{1.1}$$

The reaction path involving Ga requires a higher thermal activation (> 425 °C or longer annealing time) to take place [46].

$$\frac{1}{2}Cu_2Se + \frac{1}{2}Ga_2Se_3 \rightarrow CuGaSe_2 \tag{1.2}$$

After the above reactions occur, the final CIGSe phase is formed by interdiffusion of the $CuInSe_2$ and $CuGaSe_2$ phases.

$$x\ CuInSe_2 + y\ CuGaSe_2 \rightarrow Cu(In_x,Ga_y)Se_2 \tag{1.3}$$

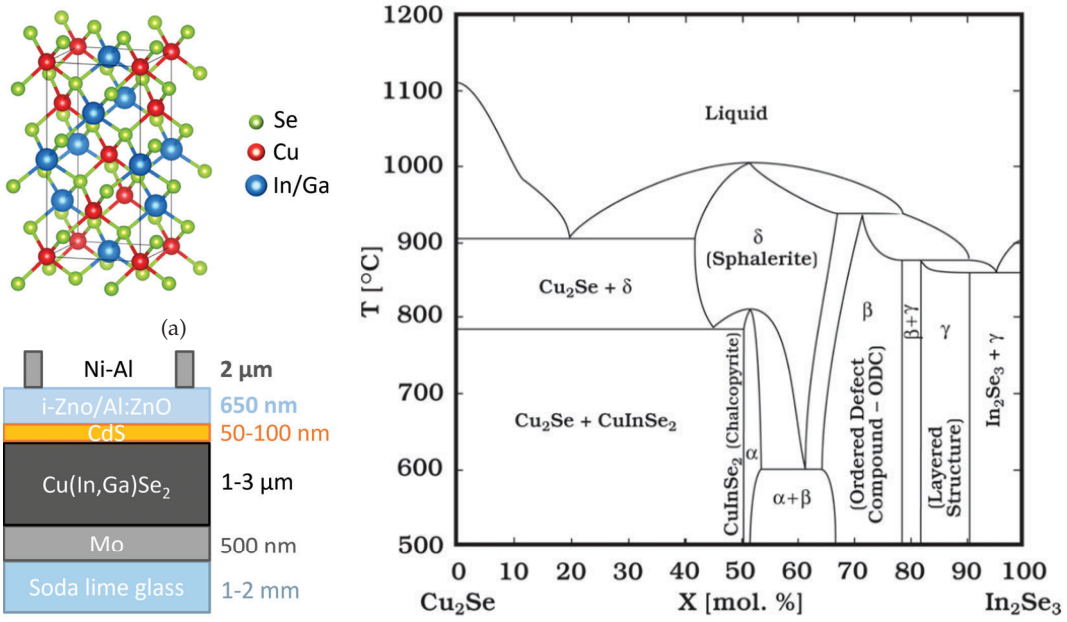

Figure 1.2: Schematic representation of the: a) crystalline lattice structure of CIGSe, produced with VESTA. Adapted from [42]. b) typical stack configuration of a CIGSe-based solar cell. i-ZnO indicates intrinsic ZnO and Al:ZnO is ZnO doped with Al. c) Phase diagram of the binary section of the copper - indium - selenium system. The diagram was taken from [45]. The Greek letters refer to the following phases: α-CISe: $CuInSe_2$ (chalcopyrite), β-CISe: $CuIn_3Se_5$, γ-CISe: $CuIn_5Se_8$, δ-CISe: $CuInSe_2$ (sphalerite). No further phase transitions are observed below 500 °C.

To obtain a solar cell from a semiconductor material, it is required to introduce an asymmetry (chemical potential, band structure, etc) across the structure of the solar cell. This provides a driving force which effectively separates the photo-generated electron-hole pairs and allows to ultimately collect them at the electrical contacts to extract work from the device. Focusing on an asymmetric band structure, two methods are commonly used: (i) to sandwich the semiconductor between selective transport layers, which are responsible to collect the generated electrons and holes separately, or (ii) to form a pn-junction, which generates a built-in potential, i.e. a band bending across the junction, enabling to separate the free carriers. The pn-junction structure has been the main method used for CIGSe-based solar cells. The typical layer stack for a CIGSe solar cell is depicted in Figure 1.2c and consists of a soda lime glass coated with a 500 nm Mo electric back contact, followed by the p-type CIGSe absorber layer a few microns thick, an n-type CdS buffer layer, an n-type window layer which comprise an intrinsic ZnO layer and an Al-doped ZnO layer and finally the Ni-Al front contact grids. Lastly, the power generated by the solar cell device can be applied onto an external load that is connected to the device's front and back contacts. Further details on the working principle of solar cells can be found in the following references [47, 48].

1.3 Challenges and objectives

In this context, the challenges tackled in this thesis are: (i) to develop a methodology to characterize the individual micro structures in the array, in order to monitor the quality of the synthesis methods and perform statistical analysis, ideally without modifying the individual structures. (ii) to understand the influence that using a patterned substrate, designed for micro solar cells, has on the growth of CIGSe. (iii) to investigate two additive synthesis methods in order to fabricate arrays of CIGSe micro solar cells, while maximizing reproducibility and PCE. (iv) to develop a pedagogical tool to interact with the general public and set the background for conveying the importance of energy consumption and renewable energy production.

To address these challenges, the outline of this thesis is structured in the following way:

Chapter 2 details the synthesis methods for the fabrication of the patterned substrates, as well as, the different growth routes and patterns that are explored in the following chapters. Additionally, an overview of the fundamental principles and technical details for the distinct characterization techniques is presented.

Chapter 3 puts forward the applicability of scanning laser confocal microscopy to statistically characterize arrays of thin film absorbers. Specifically, a new optical method is developed to characterize and monitor the morphology, composition and phase formation in sequential processes. The method is showcased with a common two-step electrodeposition and annealing synthesis process for CIGSe thin-films.

Having an appropriate characterization technique for arrays of absorbers, chapter 4 investigates the synthesis of CIGSe, using a high quality growth method, on the patterned substrate and explores methods to mitigate the observed detrimental effects of geometry-induced secondary phases. Furthermore, a comparison between different synthesis methods is made to understand how the growth of CIGSe is impacted by the synthesis routine. This allows to differentiate which of the observed phenomena are due to use of a patterned substrate from those due to the material's synthesis process.

In chapter 5, the methodology developed in chapter 3 and the substrate-related findings from chapter 4 are applied to two material-efficient synthesis methods in order to synthesize and characterize CIGSe micro solar cells.

The research on solar cells being covered, chapter 6 shifts the topic to the education of general population. Here, a methodology is presented to expose simply the concept of energy consumption and renewable energy provision, by illustrating the energetic impact of every day choices.

Finally, chapter 7 summarizes the main findings of this thesis and outlines the next steps for future research work.

Chapter 2

Synthesis and characterization techniques

This chapter contains an introduction and experimental details to the synthesis and characterization techniques used to support the findings discussed in this thesis. First, the synthesis processes are presented, starting with the distinct substrates used, followed by the sequence of techniques that make up the different synthesis routes explored. Second, the characterization techniques are put forward, with a brief discussion of their respective working principle, main experimental parameters and setup.

2.1 Synthesis

This section details the synthesis process of the micro solar cells that are discussed in this thesis. Starting from the production of the substrate layers and the different patterns used, followed by the two material-efficient routes that were investigated and finally the reference synthesis process, physical vapor deposition, for growth of high-quality material is presented.

2.1.1 Substrate synthesis and structure

The substrates start with a cleaned 1 mm thick soda lime glass onto which a 500 nm layer of Mo is sputtered. The metallic Mo plays the role of the back contact layer in the solar cell stack. For the patterning of the substrates, a 2 µm SiO_2 layer is first deposited by plasma enhanced chemical vapor deposition. Then, to define the pattern, a resist is spin-coated onto the SiO_2 and exposed to UV light (405 nm) in a direct write laser lithography system. The resist is then developed, resulting in a patterned resist. To pattern the SiO_2 layer itself, an oxide reactive ion etching tool is used to etch the SiO_2 layer and recreate the pattern. The leftover resist is removed with a plasma asher. Finally, a thorough cleaning process is done to ensure the removal of organics and oxides from the patterning process. This includes ultrasound baths in acetone and deionized water. An example of the resulting substrate is shown Figure 2.1, where the light grey circular structures correspond to the exposed Mo, where the micro solar cell will be grown, and the

darker regions are where the SiO_2 is located. Additionally, the Mo layer is exposed at the corners of the substrate to allow access to the back contact layer during the solar cells' synthesis and characterization. The patterning of the substrates was done by Dr. Ana Pérez-Rodríguez and Marina Alves at the International Iberian Nanotechnology Laboratory. The full details on the synthesis of the patterned substrates can be found in [31].

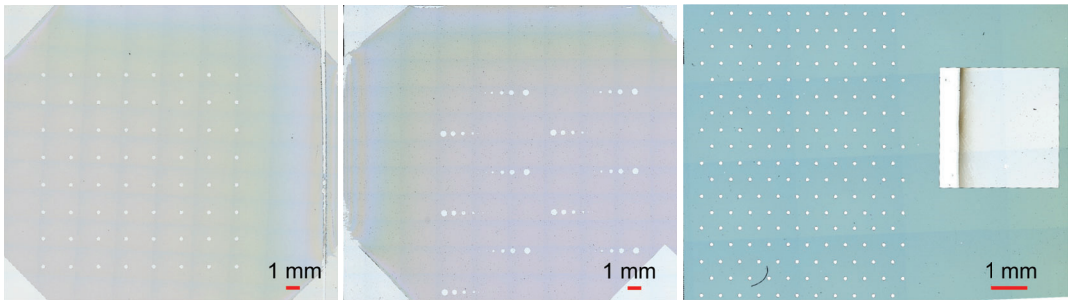

(a) (b) (c)

Figure 2.1: Top-view optical images of the three substrate patterns used in this work. a) Square pattern of 64 micro-dots with identical diameter. b) Pattern containing 11 arrays of 13 micro-dots with diameters ranging from 500 µm down to 10 µm. c) Hexagonal pattern containing 198 micro-dots with the same diameter. The vertical and horizontal lines are an artifact from the CLSM due to the acquisition of multiple images to form a stitched image.

Depending on the synthesis route or the properties investigated, three different patterns were used for the substrates. The first pattern is made up of 64 holes, or micro-dots, with the same diameter are arranged in a square pattern, as shown by the top-view image in Figure 2.1a. The diameters used were 300 µm, 100 µm and 50 µm. This pattern was used for the results discussed in chapter 3 and for the micro solar cells synthesized with electrodeposition in chapter 5. The second pattern is composed of 11 lines of 13 micro-dots each. In each line, the diameter of the micro-dots ranges from 500 µm down to 10 µm, as shown in Figure 2.1b. This pattern was used for the micro solar cells synthesized by sputtering in chapter 4 and 5, as well as, with physical vapor deposition in chapter 4. The third pattern is made up of 198 micro-dots arranged in an hexagonal lattice, with a diameter of either 100 µm, as illustrated in Figure 2.1c, or 50 µm. Additionally, a 3x3 mm^2 square hole in the SiO_2 is present to access the Mo back contact. For this substrate, the SiO_2 thickness was 1 µm instead of 2 µm. The pattern was used for the Cu-rich micro solar cells synthesized by sputtering in chapter 5.

2.1.2 Precursor

The micro solar cells produced by electrodeposition or sputtering involve a two-step process to synthesize the CIGSe absorber layer. The first step being the deposition of the metal precursor layer(s), either by electrodeposition or magnetron sputtering and the second step is an annealing routine in a selenium containing atmosphere, which converts the precursor into the absorber layer. In the following, a description of the metal precursors' synthesis techniques is given.

Electrodeposition

Electrodeposition is a deposition method in which metal ions in solution are electrochemically reduced, by means of an applied electrical field, onto a conductive electrode. Experimentally, electrodeposition uses a three-electrode setup, as depicted in Figure 2.2a. Applying a particular voltage between the working electrode (WE) and the counter electrode (CE) leads to the reduction of the metal ions in the vicinity of the WE. The reference electrode (RE) defines the voltage scale. The result is the deposition of a metallic layer onto the WE, in our case the Mo back contact.

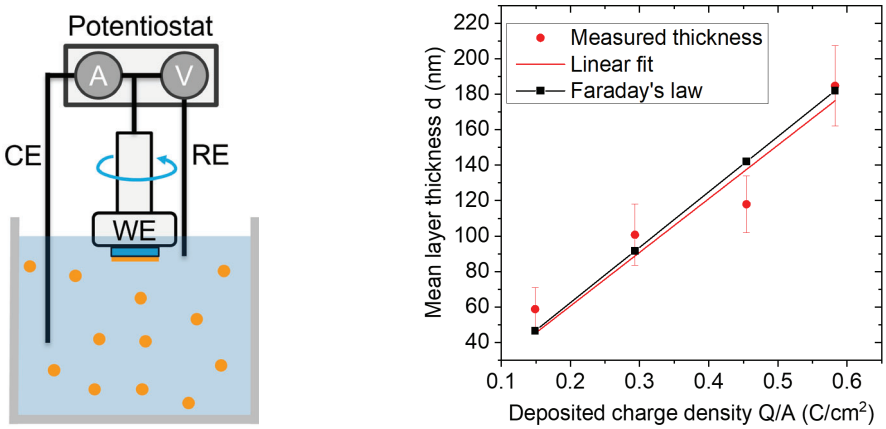

(a) (b)

Figure 2.2: a) Schematic representation of a three-electrode electrodepositon setup. The substrate, or working electrode (WE), is attached to a rotating disk electrode, which connected to the potentiostat in parallel with the reference electrode (RE) and in series with the counter electrode (CE). All three electrode are placed inside the electrolyte, where the metal ions are dissolved. b) Graphical representation of the average Cu layer thickness as a function of the deposited charge density. Red circles are the measured data values, with the error bars representing the standard deviation of each dataset. Red line is a linear fit to the experimental data. Black points, and line, show the calculated values based on Faraday's law.

The reduction process involves a charge transfer Q, which according to Faraday's laws of electrolysis (equation 2.1) is proportional to the mass of deposited material m:

$$m = \frac{M \cdot \eta}{F \cdot z} \cdot Q \tag{2.1}$$

Where F is Faraday's constant, z is the number of electrons needed to reduce the deposited species, M is the molar mass and η: is the faradaic efficiency. Using the material's density ρ, Faraday's law can be rearranged to relate the deposited film's thickness d to the transferred charge density Q/A:

$$d = \frac{M \cdot \eta}{F \cdot z \cdot \rho} \cdot \frac{Q}{A} \tag{2.2}$$

With A being the electroactive area and M the material's molar mass. Thus, by measuring the charge transferred through the system, it is possible to control the thickness of

the precursor layers. This is demonstrated in Figure 2.2b, where the measured thickness of four different Cu layers agrees with the predicted thickness given the deposited charge density. In this case, the assumed faradaic efficiency is 85 % [49]. Further details on the working principle of electrodeposition can be found in the following references [50, 51].

The synthesis of the metal precursor's layer consists of a two-step electrodeposition process. First, the electrodeposition of thickness-controlled Cu layers is performed, followed by the co-electrodeposition of In and Ga. Given that SiO_2 is an insulating layer, the deposition only occurs within the micro-dots, where the Mo, or Cu, layer is exposed. This makes the method material-efficient, as all the deposited material is effectively used. The thickness control of the precursor layers is crucial as it determines the compositional ratio CGI. Indeed, the CGI is determined by calculating the ratio of the number of deposited Cu atoms N_{Cu} and the number of In and Ga atoms, N_{Ga} and N_{In} respectively, in the second precursor layer (see equation 2.3).

$$CGI = \frac{N_{Cu}}{N_{Ga} + N_{In}} \tag{2.3}$$

The number of atoms N_X is related to the layer's thickness d as follows:

$$N_X = \frac{N_A \cdot \rho \cdot A}{M} \cdot d \tag{2.4}$$

With N_A: Avogadro's constant. To account for the proportion of Ga and In atoms, in the co-electrodeposited layer, the $GGI = \frac{[Ga]}{[Ga]+[In]}$ ratio is used in the calculation of N_{Ga} and N_{In}. Thus, with the electrodeposited charge, one can control the thickness of each layer and therefore obtain the expected compositional ratio. The full experimental details on the electrodeposition procedure for Cu and In, Ga are available in reference [36].

Sputtering

The second material-efficient method consists of depositing the precursor layer by magnetron sputtering. Magnetron sputtering is a vacuum-based physical vapor deposition technique, which relies on the bombardement of a target material to deposit the ejected atoms onto a substrate. A schematic representation of the working principle of magnetron sputtering is shown in Figure 2.3. In short, a plasma is generated by confining Ar gas within an electric field. The resulting ions are then accelerated towards the target by means of a magnetic field, stripping material from the target due to the collision. The constant stream of extracted material is then deposited onto the substrate. The amount of deposited material is dictated by the deposition rate, which is regulated by the input power, as presented in the following article [52]. Further details on the working principle of magnetron sputtering can be found in the following references [53, 54].

In the scope of this thesis, two methods were explored. In the first case, the patterned substrate was introduced, in the sputtering system, after the cleaning process, that is, the

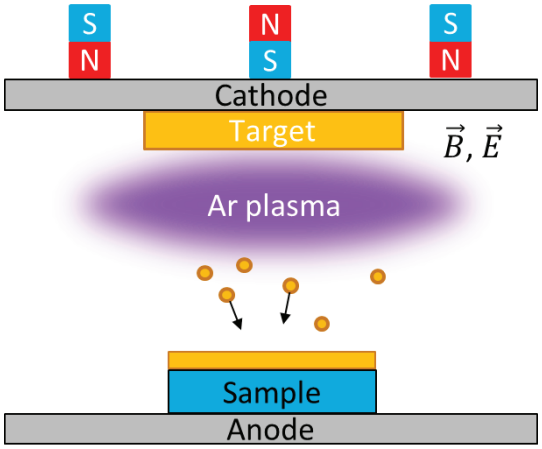

Figure 2.3: Schematic representation of the working principle of magnetron sputtering.

resist layer is no longer present on the SiO_2. This results in the deposition of the precursor layer both inside the micro-dots (on the Mo back contact), but also on the SiO_2 layer. This method is not material-efficient and was used for comparison purposes in the results discussed in chapter 4. In the second case, the patterned substrate was introduced before the cleaning process, that implies that the Cu(In,Ga) precursor layer is deposited inside the micro-dots and on the remaining resist layer. Here, the cleaning process removes the resist layer along with the precursor on top of it, leaving only the micro-dots filled with precursor material. The resist and the excess precursor material can potentially be separated, making this method material-efficient. This route is investigated to produce material-efficient micro solar cells in chapter 5. The full experimental details on the sputtering process of Cu, In and Ga are available in reference [52].

2.1.3 Absorber

Having covered the synthesis of the precursor layers, the following section describes the annealing process that converts the precursor layers into semiconductor absorbers. Additionally, the direct synthesis of CIGSe absorber by physical vapor deposition is covered.

Annealing

To convert the Cu(In,Ga) precursor into CIGSe absorber, an annealing in a Se-containing atmosphere is required. This is performed in a tube oven, inside which a SiC coated graphite box is used as the reaction chamber, as illustrated in Figure 2.4.

In practice, the precursor sample is placed inside the graphite box with a lid along with a specific mass of Se powder m_{Se}. The graphite box is then introduced in the quartz tube, which contains a N_2 inert atmosphere. The tube is connected to a dry pump and a N_2 source. To minimize the O contamination, three cycles of purging and N_2 filling

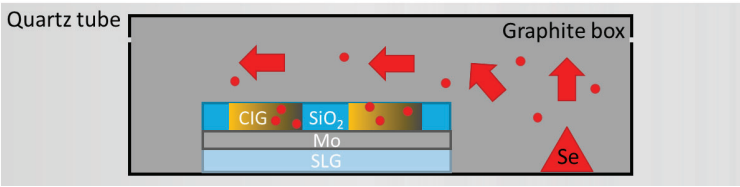

Figure 2.4: Schematic representation of the annealing process.

are performed. Finally, the pressure inside the tube is regulated to the desired N_2 background pressure $P_{N,RT}$, after which the annealing routine can be initiated. During the annealing procedure, the equilibrium Se partial pressure $P_{Se,eqm}$ can be modeled by the ideal gas law, as demonstrated by Han et al. [55]. In short, the model shows that the Se partial pressure depends in particular on the mass of Se powder and on the N_2 background pressure. Furthermore, the authors show that the equilibrium Se partial pressure impacts the annealing process and consequently influences the device performance of the resulting CIGSe absorbers. A more detailed discussion is presented in section 5.1.2 of chapter 5.

Physical vapor deposition

The last synthesis route to be discussed is the physical vapor deposition (PVD) of the individual elements, by thermal evaporation, onto the substrate to directly form the CIGSe absorber layer. The background pressure inside the deposition chamber is around $\sim 10^{-9}$ mbar. A schematic representation of the annealing chamber is shown in Figure 2.5a. To grow the CIGSe absorbers, a three-stage evaporation process was followed, as illustrated in Figure 2.5b, in order to form a Ga gradient and improve the absorber's optoelectronic properties [56, 57].

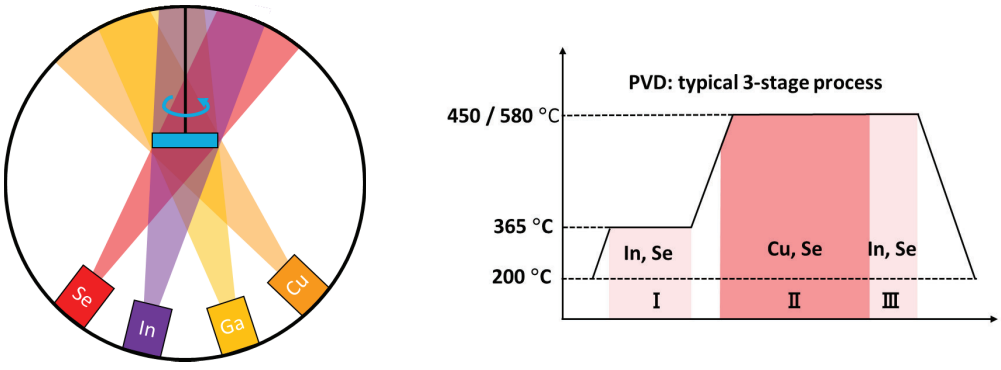

(a) (b)

Figure 2.5: a) Schematic representation of the physical vapor deposition process. b) Graphical representation of the growth procedure of the three-stage co-evaporation process. Adapted from [56].

During the deposition, the substrate is kept at the annealing temperature and constantly under rotation to maximize spatial homogeneity. In this case, the CIGSe is grown both inside the micro-dots and on the SiO_2 layer. The advantage of this method is that it

is known to produce high quality CIGSe absorbers, which is used in this thesis to discriminate the effects due to the patterned substrate from those associated with the absorber, as elaborated in chapter 4. All PVD synthesis processes, involved in this work, were performed by Dr. Taowen Wang and Sevan Gharabeiki.

2.1.4 Synthesis summary

Since different substrates are used with distinct synthesis routes, Figure 2.6 summarizes which substrates and synthesis methods are combined throughout the results chapter. Additionally, the cross-section of the stacks are depicted to highlight when the Na barrier is used.

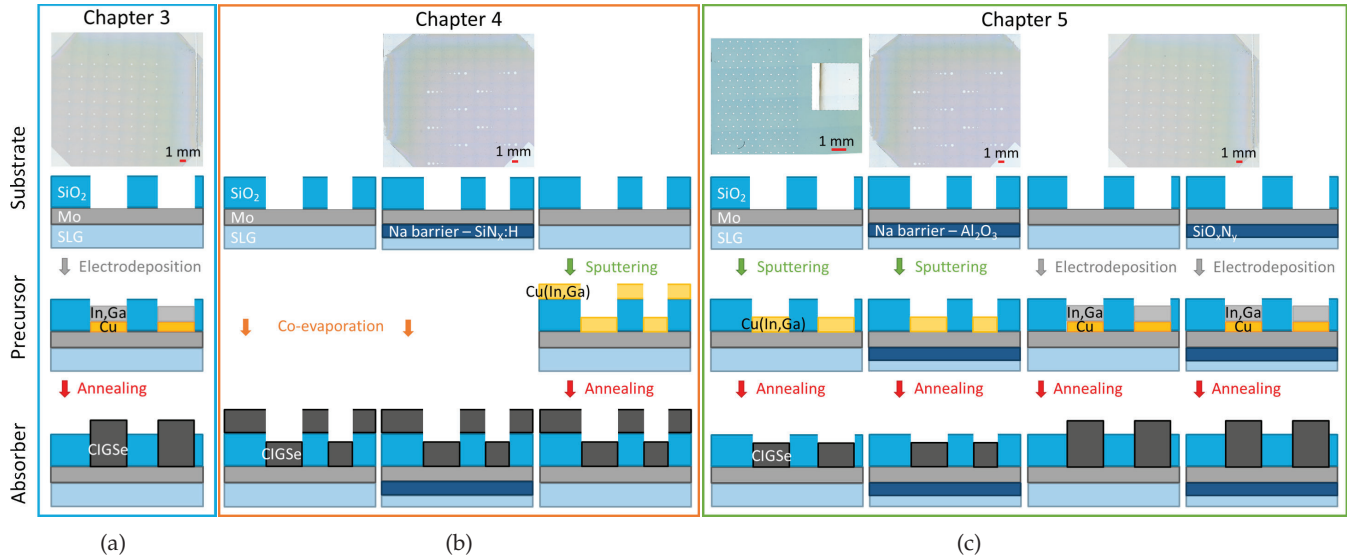

Figure 2.6: Summary of substrates, stacks and synthesis methods used in: a) chapter 3 b) chapter 4 and c) chapter 5. For each case, the top row contains the top-view optical images of the pertinent empty substrate and the subsequent rows show cross-sectional representations of the stacks at the different steps of the synthesis methods.

2.1.5 Solar cells

After the absorber layer is grown on the patterned substrate, the next step in the synthesis process is to perform a potassium cyanide (KCN) bath to remove eventual oxides and copper selenide phases from the absorber, to improve the final solar cell's performance. Specifically, if the absorber's composition is Cu-poor (CGI < 1.0), the sample is put in a 5 wt% KCN solution for 30 s, whereas for Cu-rich (CGI > 1.0) absorbers, a 10 wt% KCN solution is used during 60 s. The process is followed by the chemical bath deposition of the CdS buffer layer [58]. To characterize each individual micro-dot in the sample, it is required to electrically isolate it. This is achieved by making scribing lines around each micro-dot, which separates the conductive window layers into individual regions containing each a single micro-dot. However, it was not possible to make well-defined and debris-free scribing lines from the window layers that were deposited

on the SiO_2/CdS. Instead, it was found that using a (tape) mask template (which only exposes the target regions around the individual micro-dots, i.e. where the window layers are effectively needed), before the window layers' deposition, leads to an improved shunt resistance and thus better device performance. The window layers are made up of a 50 nm intrinsic ZnO layer and a 400 nm Al-doped ZnO layer, which were deposited by radio-frequency magnetron sputtering. Removing the tape at this stage results in the window layers being only deposited on the individual micro-dots and not in-between micro-dots. In general, for the characterization of the micro solar cells, no front contacts were used. Instead, the front contact probes were placed directly on the Al-doped ZnO layer, as close as possible to the micro-dot, paying attention not to shadow the micro solar cell itself with the probes.

2.2 Characterization techniques

In this section, a brief introduction to the characterization techniques, used in this work, is presented. The basic working principle for each technique is addressed, while focusing on its application to this thesis. The relevant technical details for each technique are also provided, where appropriate.

2.2.1 Confocal laser scanning microscopy

Confocal laser scanning microscopy (CLSM) is a non-invasive optical characterization technique which measures a material's surface topography and outputs a three-dimensional height map and, in our case, an optical image of the same region. To illustrate the working principle of CLSM, in reflectance mode, Figure 2.7 shows a schematics of the different components involved in the process. A laser light source is focused onto the material's surface at a height position z_0. The reflected light is guided towards a pinhole which screens the out-of-plane light, while allowing the light from the focal plane to reach the detector. A set of scanning mirrors rasters the focal plane leading to an xy intensity image, where all the surface's features that are located at this height z_0 will show a maximum reflection intensity. The objective lens is then vertically moved, which shifts the focal plane to height position z_1, and an xy intensity map of the new focal plane is acquired. This causes the surface features that were in focus in position z_0, to be out-of-focus in position z_1. This means the reflection intensity of these same features is now lower. By tracking the movement of the objective lens along the z-axis, one can correlate it with the intensity maps for all x,y positions and extract reflectance maxima for each position. The maximum in reflectance intensity is judged to be the surface of the material under investigation. This way, the height data at every x,y position can be used to generate a topography map. Further details may be found in the following references [59, 60].

In practice, CLSM is a fast optical technique with a depth resolution of tens of nanometer and sub-micrometer spatial resolution, allowing to investigate morphological changes

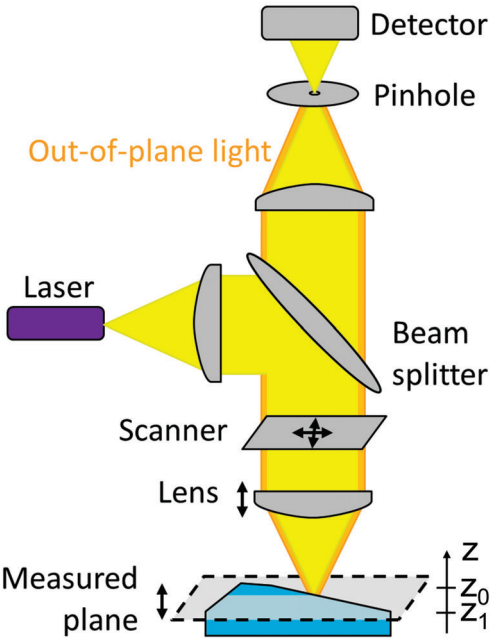

Figure 2.7: Schematic representation of the CLSM components and working principle.

like surface roughness, particle size, shape and distribution, growth modes and layer thickness. No sample preparation, nor particular environment is required for the measurement. Furthermore, the low power (1 mW) laser probe does not damage nor contaminates the investigated surface.

The CLSM used for this work is a Keyence VK-X1000 with an UV-laser (wavelength of 404 nm) and Nikon IC EPI PLAN lenses with the following magnification and respective numerical aperture (N.A.): 5X/0.13, 20X/0.46, 50X/0.95 (APO) and 150X/0.95 (APO). This system can acquire one image, and the respective height map, in about 30 seconds. The CLSM was also able to obtain an inch by inch navigation image, which is crucial to perform same location analysis and have an overview of the material. Furthermore, the ability to measure the exact same region before and after any process, allows to perform correlative studies, to follow the evolution of the sample and to quantify morphological changes. The assumed measurement error, based on the manufacturer, corresponds to the measurement repeatability of 12 nm for the 50X/0.95 and 150X/0.95 lenses and 40 nm for the 20X/0.46 lens.

2.2.2 Stylus profilometer

Stylus profilometry is a contact measurement where a diamond stylus mechanically traces the morphology of the target's surface. More precisely, the microscopic stylus is put in direct contact with the surface and moved along the horizontal surface. The changes in the surface height are followed by the stylus causing a vertical displacement of the latter in the perpendicular z-direction. The displacement of the stylus is recorded and combined with the horizontal displacement to produce a height profile that replicates

the scanned surface. Typically, stylus profilometry is used for roughness and step height measurements. Figure 2.8 shows a schematics of the technique's measurement principle. For further details on the technique, the reader is kindly invited to refer to [61].

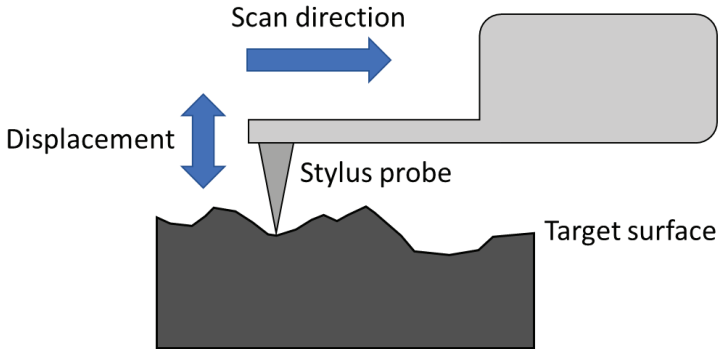

Figure 2.8: Schematic representation of the working principle of stylus profilometer.

The stylus profilometer used for this work is a KLA Tencor P-17 equipped with a diamond stylus with a radius of curvature of 2 µm, making it appropriate to measure height differences from 100 µm down to tens of nanometers. The estimated measurement error for this technique was 10 nm. To minimize damage on the surface of the samples while maintaining a high height resolution, a force of 2 mg was used. The scan speed used for the measurements was 20 µm/s. The technique requires little to no sample preparation, in particular for hard materials.

2.2.3 Atomic force microscopy

Atomic force microscopy (AFM) is technique that also uses a physical probe to measure the morphology of a surface. The typical dimensions, where AFM is used, extend from the sub-nanometer scale up to a few tens of micrometers. The simplified measurement principle of AFM is summarized in Figure 2.9.

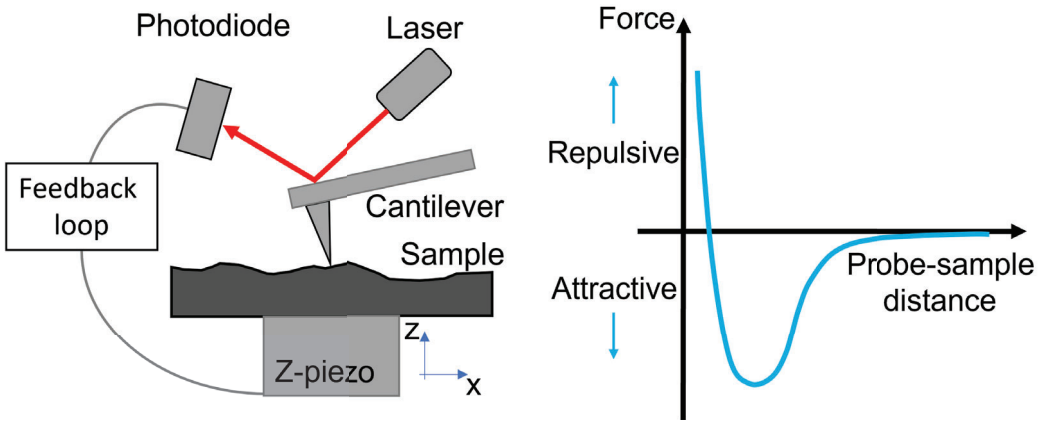

(a) (b)

Figure 2.9: Schematic representation of the: a) AFM components and working principle. b) Morse potential.

The probe used in AFM is a cantilever with a sharp tip (radius of curvature around 10 nm) which interacts with the sample's surface. The interaction between sample and tip follows a Morse potential, leading to attractive or repulsive forces depending on the separation between the two. These forces deflect the cantilever, whose motion is monitored through a laser and a photodiode. A feedback loop and a piezo-electric stage compensate for the change caused by the tip-sample interaction, generating an electrical signal from which a topography map, of the sample's surface, can be extracted. For further details on AFM measurements, the reader is kindly invited to refer to [62]. The AFM measurements discussed in this thesis were performed by Joana Ferreira with a MultiMode AFM and a Nanoscope V controller.

2.2.4 Scanning electron microscopy

Scanning electron microscopy (SEM) is an imaging technique that uses an electron beam to periodically sweep the material's surface and is able to resolve features down to sub-nanometer scale. Figure 2.10a highlights the main components of the scanning electron microscope. The electron beam is generated in the electron gun, by heating up a filament, which emits electrons through thermionic emission. The electrons are accelerated towards an anode by means of an electric field. The corresponding acceleration voltage is typically up to 30 kV. The divergent electron beam is then focused onto the sample's surface through a set of condenser lenses. The size of the focused electron beam is typically in the 100 nm range. A set of coils is used to deflect the electron beam and therewith raster the sample's surface. Upon reaching the sample, the electrons from the beam interact with the atoms within the material, generating a multitude of electronic and electromagnetic signals, such as secondary electrons, backscattered electrons, X-rays, among others. Each type of signal has a characteristic energy range, which defines an interaction volume from which the produced electrons and X-rays may originate and still reach the detector, as illustrated in Figure 2.10b. Note that the volume of interaction depends on the electron beam acceleration voltage, with a higher voltage leading to a larger volume of interaction. The type of information that can be drawn from the different signals include morphology and composition.

In the context of SEM measurements done in this work, the focus is put on the secondary electrons, which are generated near the surface (roughly 10-100 nm) and thus carry information about the surface morphology. As indicated in Figure 2.10c, the secondary electrons are ejected from the atoms through inelastic scattering with the electron beam. The ejected electrons may have an energy in the range 0-50 eV, but are mostly below 5 eV. By rastering the sample in the xy-direction and collecting the respective secondary electrons, an image of the morphology can be reconstructed. The whole system is operated under vacuum to minimize electron collisions with the atmosphere, and consequently maximize image resolution. Since the beam is charged, the investigated sample needs to be conductive to redistribute the incoming charges and avoid surface charging, which would cause image drift and lower image quality. To minimize this effect, a

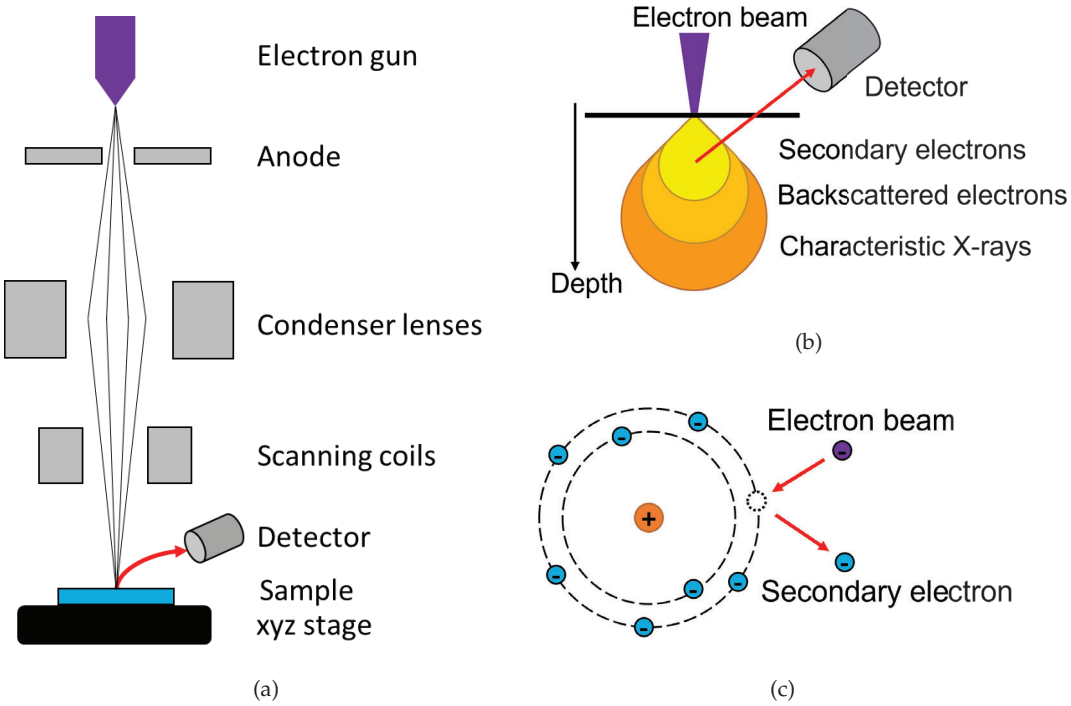

Figure 2.10: Schematic representation of the: a) SEM components and working principle. b) cross-section of the interaction volume and generated signals. c) Bohr atom to illustrate the generation of secondary electrons.

conductive C-tape is used to evacuate the excess of charges from the sample's surface to the conductive sample holder. The measurements discussed in this work were acquired with a Zeiss Evo10 scanning electron microscope, equipped with a standard Everhart-Thornley secondary electron detector. For further details, please refer to the following document [63].

2.2.5 Energy dispersive X-ray spectroscopy

Energy dispersive X-ray spectroscopy (EDX) is an elemental analysis technique that allows to measure the composition of a material. This is achieved by exciting the atoms in the target material, with an electron beam, and measuring the corresponding characteristic X-ray emission. The measurement principle of EDX is the same as SEM, except that the detector is designed to spectrally resolve electromagnetic emission, in particular X-rays. In fact, given the high compatibility and complementarity of the two techinques, they are commonly combined into the same system. The detector used for EDX measurements is an Ultim Max 40 model. The system is able to acquire spectra from point or area measurement and to have spatial resolution through mapping analysis.

Similarly to SEM, an electron beam excites the material by ejecting electrons from the atoms' core energy levels, leaving an empty energy level behind. To minimize the energy of the system, an electron from a higher energy level relaxes to the unoccupied level and releases a photon with an energy matching the difference between the energy

levels. This process is depicted in Figure 2.11a. Depending from which shell the electron is ejected, different energy transition, or spectral lines, can be observed. This work refers to the Siegbahn notation to identify the different spectral lines [63]. This notation takes the general form of $K\alpha_1$, where the first character indicates from which shell (K, L and M) the electron is ejected. The second refers to the number of shells the second electron skips to reach the unoccupied energy level ($\alpha = 1$, $\beta = 2$ and $\gamma = 3$). The third indicates from which subshell the electron is relaxing. In the case two spectral lines cannot be resolved, multiple numerical subscripts may be used, for instance $K\alpha_{1,2}$. Note that, in order to observe a spectral line, the electron beam's acceleration voltage should be at least twice the energy of the electronic transition.

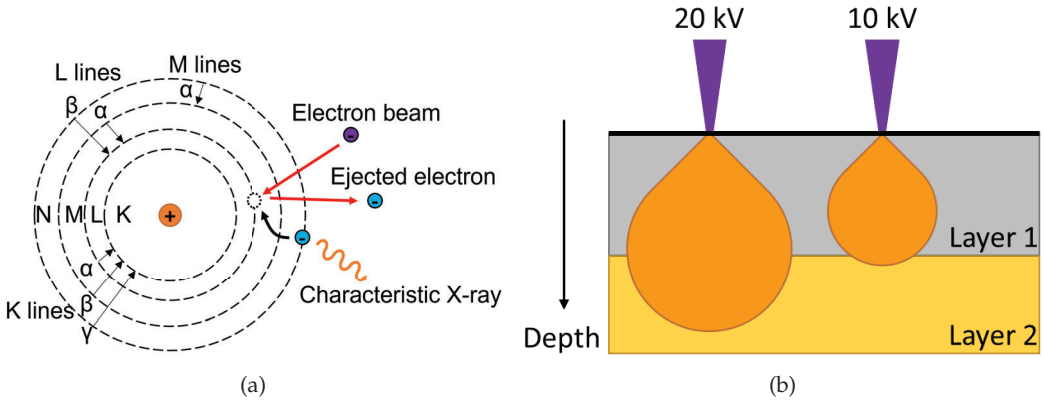

(a) (b)

Figure 2.11: Schematic representation of the: a) Bohr atom to illustrate the generation of characteristic X-rays and the possible spectral lines. b) cross-section of the interaction volume for a stacked layer material. Effect of acceleration voltage on the interaction volume is also depicted.

Each element in the periodic table has its characteristic arrangement of electronic levels with discrete energies. The spectral resolution of EDX allows to discriminate which transitions are observed in the material and by referencing to literature [64], one can identify which elements make up the material. Table 2.1 regroups the spectral lines for the elements that are discussed in this thesis.

Table 2.1: List of characteristic spectral lines for the elements encountered in this thesis [64].

Element	Spectral lines energy (keV)							
	$K\alpha_1$	$K\alpha_2$	$K\beta_1$	$L\alpha_1$	$L\alpha_2$	$L\beta_1$	$L\beta_2$	$L\gamma_1$
C	0.277							
O	0.525							
Na	1.041	1.041	1.071					
Si	1.740	1.739	1.836					
Cl	2.622	2.621	2.816					
Cu	8.048	8.028	8.905	0.930	0.930	0.950		
Ga	9.252	9.225	10.264	1.098	1.098	1.125		
Se	11.222	11.181	12.496	1.379	1.379	1.419		
Mo	17.479	17.374	19.608	2.293	2.290	2.395	2.518	2.624
In	24.210	24.002	27.276	3.287	3.279	3.487	3.714	3.921

Quantitative EDX analysis can be calculated from the spectral line intensity of the respective element. This allows to determine the absolute composition of each element in the material. Since the detection of elements depends on many factors, calibration standards are required to calibrate the detection of each element. The standards used are usually pure elements or compounds of known composition. As stated previously, the interaction volume of the electron beam and the material depends on the acceleration voltage. This is particularly relevant for the elemental analysis of stacked layers, as depicted in Figure 2.11b. In fact, given the asymmetric shape of the volume of interaction, X-rays from the top layer have a higher probability to escape the material and reach the detector compared to those from the bottom layer. This leads to a weighted average of the composition based on the shape of the interaction volume. This effect is further emphasized with lower voltages and thicker layers, which complexifies the quantitative composition analysis of layered materials. For further details about the technique, the reader is kindly referred to the following book [63].

2.2.6 Electron backscattered electron diffraction

Electron backscattered electron diffraction (EBSD) is a surface sensitive technique based on electron scattering by the crystal structures. In fact, the incident electrons can be diffracted by the crystallographic planes of the probed material. The diffraction events that fulfill Bragg's law (equation 2.5) lead to constructive interference, resulting in a diffraction pattern that is characteristic of the phase present in the material.

$$n\lambda = 2d \sin\theta \tag{2.5}$$

Where n is the diffraction order, d the distance between consecutive crystallographic planes, θ the scattering angle and λ the electron's wavelength. Typically, the setup is similar to SEM, except that the sample is tilted ($\sim 70\,^{\circ}$) and the detector is a phosphorescent screen which detects the Kikuchi lines, that make up the diffraction pattern. The electron beam size is in the range of 1 nm and the excitation volume is in the range of hundreds of nanometers. However, within this volume, most of the emitted electrons are absorbed, resulting in a depth resolution of a few tens of nanometers. Analysis of the Kikuchi lines allows to identify crystallographic structures, their orientation, strain, etc. For further details about the technique, the reader is kindly referred to the following book [63]. The EBDS measurement and analysis discussed in this thesis were performed by Prof. Dr. Daniel Abou-Ras.

2.2.7 Raman spectroscopy

Raman spectroscopy is a non-destructive, optical characterization technique typically used to investigate the vibrational transitions in a material. The working principle relies on the scattering of a monochromatic light-source, usually a laser, by the electron distribution in a molecule or crystalline structure. Considering a excitation source with

a frequency ω, two types of scattering are possible: elastic (or Rayleigh) scattering and inelastic (or Raman) scattering. In the first case, the lattice is excited to a virtual energy state and upon relaxing, a photon is emitted with the same frequency ω as the excitation. Rayleigh scattering has several orders of magnitude higher probability of happening compared to Raman scattering. In the second case, the scattered light has a shifted frequency Ω, which can be associated with the annihilation (anti-Stokes Raman scattering) or the creation (Stokes Raman scattering) of a phonon, i.e. a lattice vibration, with the same frequency Ω. Stokes transitions are more recurrent events, by one to two orders of magnitude, compared to Anti-Stokes. The different electronic transitions are schematically represented in Figure 2.12a. In a Raman measurement, one measures the Raman shift, or change in frequency, between the scattered and the excitation light, in order to identify the energy of the characteristic phonons. This is usually measured in wavenumbers (cm^{-1}) and relates to the scattered λ_{scatt} and excitation λ_{exc} lights' wavelength as follows:

$$\Omega = \frac{1}{\lambda_{scatt}} - \frac{1}{\lambda_{exc}} \tag{2.6}$$

Given the low probability of Stokes transitions, the sample's Rayleigh scattering radiation is filtered to allow the detection of Stokes Raman scattering, which is the transition of interest with highest probability. The frequency of the phonon Ω depends on the force constant k of the bond between the vibrating atoms and on their reduced mass μ, as shown by equation 2.7:

$$\Omega = \sqrt{k/\mu} \tag{2.7}$$

The relation implies that the Raman spectrum of a material depends on its elemental composition and how the constituents interact with each other, making the Raman spectrum a structural fingerprint for the material. This allows to extract information about the material's structure, phases, composition, etc. Being a surface sensitive technique, the collected information relates to the material within hundreds of nanometers from the surface. A schematic representation of the experimetal setup is shown in Figure 2.12b.

The measurement were performed using a Renishaw inVia micro-Raman spectrometer. which includes an optical microscope to navigate across the sample, focus the light beam and collect the backscattered light from the sample. The excitation laser used was a 532 nm and the beam size was on the order of 1 µ. After filtering out the Rayleigh scattering contribution, a 2400 lines/mm grating is used to spectrally disperse the sample's radiation and project it onto a charge-coupled device (CCD) detector. Technical settings, like acquisition time, laser power and measurement accumulations, were adjusted to maximize signal-to-noise ratio. For further details about the technique, the reader is kindly referred to [65–67].

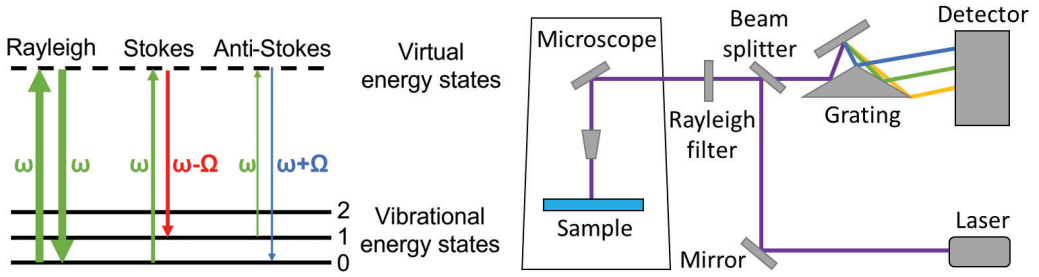

(a) (b)

Figure 2.12: Schematic representation of: a) Three types of scattering observed after excitation by a photon with frequency ω. The arrows' line thickness correlates with the probability of the transitions to happen. b) Typical Raman scattering measurement setup. Dimensions not to scale.

2.2.8 Photoluminescence

Luminescence is the emission of light, from a material, resulting from the relaxation of the charge carriers after being excited into a higher energy state. Depending on the excitation mechanism, different types of luminescence are distinguished. Photoluminescence (PL) is a particular example of luminescence where the charge carriers in the material, are promoted into unoccupied higher energy levels through the absorption of photons. Focusing on semiconductors, the energy of the absorbed photons must be higher than the material's bandgap E_{gap}, so that electrons can reach the conduction band (CB). After absorption, the electrons typically thermalize to the CB minimum, by emission of phonons, and eventually relax back to the valence band (VB) by emitting a photon with an energy similar to the bandgap E_{gap}. A schematic representation of these steps is depicted in Figure 2.13, in the case of a direct semiconductor.

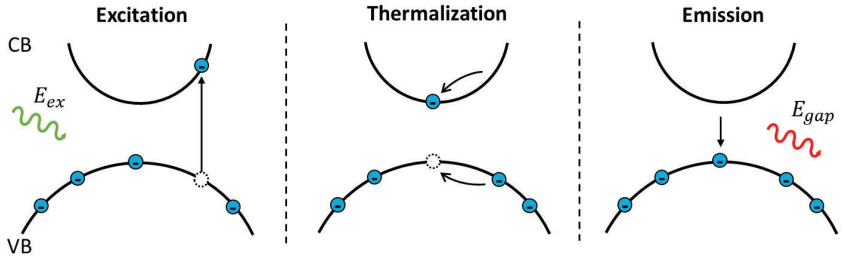

Figure 2.13: Schematic representation of the steps involved in a photoluminescence experiment. From left to right: a photon with energy E_{ex}, higher than the bandgap E_{gap}, is absorbed and an electron is promoted to the CB. Electron thermalizes to CB minimum. The electron relaxes to the VB by emitting a photon with energy corresponding to the bandgap E_{gap}.

Under illumination, electron-hole pairs are generated in the semiconductor, which modifies the carriers concentration. To describe the equilibrium between absorption and emission, the introduction of a second Fermi level is required to account for the concentration of electrons and holes. This leads to the definition of the quasi-Fermi level splitting ΔE_F, which is the energy difference between the electron and hole Fermi levels. ΔE_F

is a key parameter for solar cell characterization as it determines the radiative emission and is thus related to the maximum voltage that the device can develop, the open-circuit voltage V_{OC}. In fact, only radiative emission in the semiconductor will contribute to the solar cell's V_{OC}. The radiative photon flux $\phi(E)$ from a semiconductor under illumination can be described by Planck's generalized law:

$$\phi(E) = \frac{2\pi}{h^3c^2} \cdot \frac{a(E) \cdot E}{exp(\frac{E-\Delta E_F}{k_B T}) - 1} \tag{2.8}$$

With h: Planck's constant, c: the speed of light, $a(E)$: the absorptivity, k_B: Boltzmann constant.

In real materials, the absorptivity is not a step function, but is smeared out at the edges, due to the presence of band tails, that is energy states of the CB and VB that extend into the bandgap. This leads to the definition of the Shockley–Queisser (SQ) open-circuit voltage V_{OC}^{SQ}, which is the limit voltage for a semiconductor whose carriers can only recombine radiatively. This value depends on the material's bandgap and is tabulated in the following reference [68]. In more realistic semiconductors, the relaxation of the carriers can happen either radiatively, that is the process results in the emission of a photon, or non-radiatively, in which case phonons are generated. Typically, radiative emission can originate from band-to-band or defect-assisted transitions, whereas non-radiative relaxation (Shockley-Read-Hall recombination) happens through deep defects or surface defects. Since Shockley-Read-Hall recombination does not result in a photon emission, the radiative photon flux of a semiconductor, containing such defects, decreases and therewith the ΔE_F also decreases. These losses in radiative flux are accounted by the voltage drop due to non-radiative recombination ΔV_{OC}^{nrad} and can be quantified by the photoluminescence quantum yield (PLQY):

$$\Delta V_{OC}^{nrad} = \frac{k_B T}{q} \ln(PLQY) \tag{2.9}$$

With q: the elementary charge. The PLQY is defined as the ratio between the integrated emitted photon flux and the absorbed photon flux. Equation 2.10 breaks the theoretical limiting voltage V_{OC}^{SQ} for a semiconductor into the radiative ΔE_F and non-radiative ΔV_{OC}^{nrad} contributions.

$$qV_{OC}^{SQ} = \Delta E_F + k_B T \ln(PLQY) \tag{2.10}$$

Both contributions can be measured using PL and allow to gauge the quality of the synthesized semiconductor comparatively to its theoretical limit. In this thesis, depending on the aim of the experiment, one of two methods were used to measure ΔE_F and $PLQY$. These are spectrally-resolved PL and spatially-resolved PL. In both cases, an

intensity calibration was necessary to measure absolute PL. The respective setups are presented in Figure 2.14.

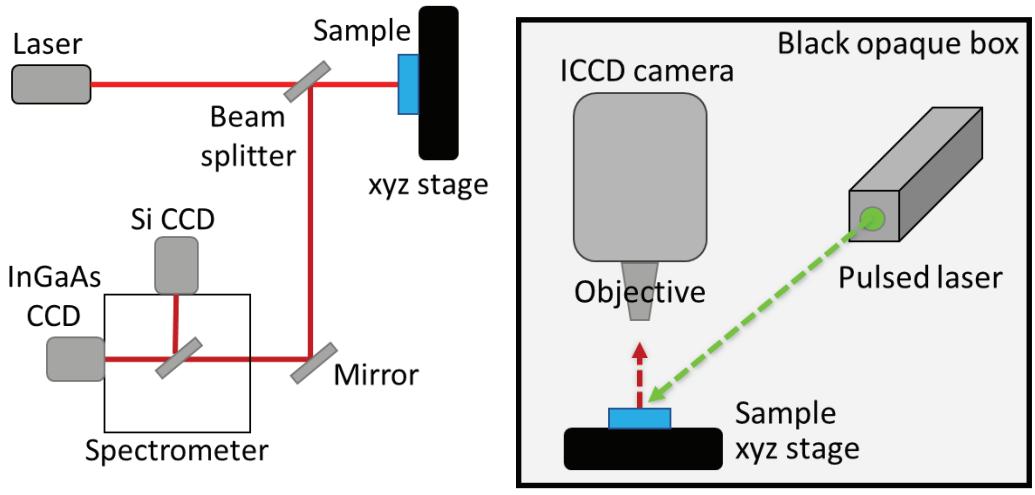

(a) (b)

Figure 2.14: Schematic representation of setup used to measure: a) Spectrally-resolved PL. b) Spatially-resolved PL. Dimensions not to scale.

Both setups are house built and the general aim is to excite the sample with a laser source and focus the sample's radiation onto the detectors. For the spectrally-resolved setup, in Figure 2.14a, a 633 nm laser is used and the detector is a spectrometer combined with a Si and an InGaAs CCD detectors to cover a wide wavelength interval (200-1600 nm). The output of the measurement is a PL spectrum, from which both ΔE_F and $PLQY$ can be extracted. On the one hand, the spectrum is fitted with generalized Planck's law, with particular assumptions, the ΔE_F can be determined. On the other hand, the integral of the spectrum, i.e. the radiative emission, is measured and with the laser flux, $PLQY$ can be calculated. The spectrally-resolved PL measurements and respective analysis were performed by Aubin Prot and Dr. Taowen Wang. As for the spatially-resolved setup, a 532 nm excitation laser is used and the detector is a Xenics Cheetah InGaAs camera. The output is a panchromatic map of the investigated region, whose intensity is related to the radiative emission. Again, measuring the laser flux allows to calculate the $PLQY$. For further details about the technique and the measurement analysis, the reader is kindly referred to [47, 69–71].

2.2.9 External quantum efficiency

The quantum efficiency measurement is an electrical characterization technique to understand how a solar cell interacts with the light spectrum. In theory, every photon with an energy E larger than the material's bandgap E_g could be converted into an electron, by photovoltaic effect, and contribute to the solar cell's current. However, multiple mechanisms can lead to the loss of a fraction of the incoming photons depending on the photon's wavelength and on the solar cell's properties. The quantum efficiency is a

spectrally-resolved measurement that allows to identify the different loss mechanisms in the solar cell, as illustrated in Figure 2.15a, and also calculate the short-circuit current. Given the multi-layer configuration of solar cells, the external quantum efficiency is typically preferred to internal quantum efficiency. In this case, the ratio of the generated electrons to the incoming number of photons is measured within a spectral region of interest, leading to an EQE spectrum as plotted in Figure 2.15a.

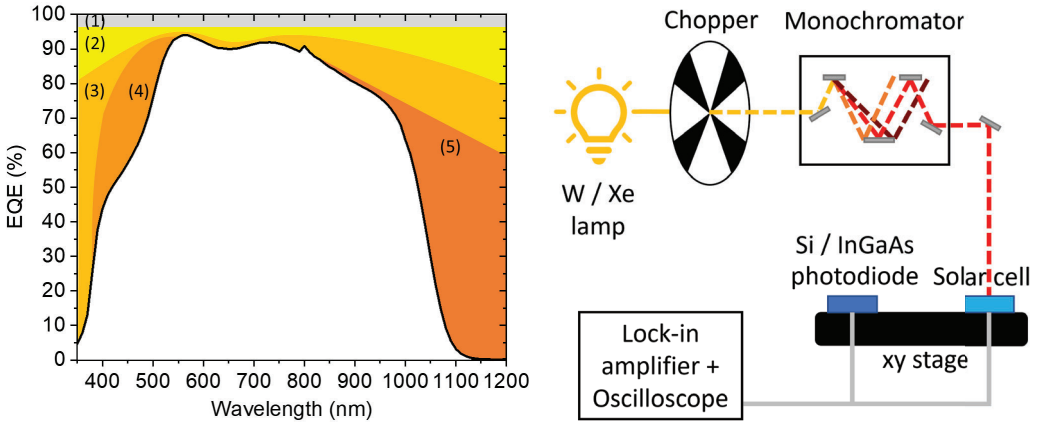

(a) (b)

Figure 2.15: a) EQE spectrum of a typical CIGSe solar cell with the breakdown of losses involved: (1) grid shading, (2) reflections, (3) ZnO window layer parasitic absorption, (4) CdS buffer layer parasitic absorption, (5) insufficient photon absorption and carrier recombination. Jump in EQE around 800 nm is due to the change of lamp and grating during measurement. b) Schematic representation of the EQE measurement setup. Dimensions not to scale.

As indicated previously, the ideal EQE spectrum is a step-function around the semiconductor's bandgap energy E_g. In a real solar cell, multiple losses lead to the deviation from the ideal case [72]. First, the metal contacts, needed to collect the carriers, are mostly reflective and thus shade part of the CIGSe absorber. Second, the layers above the CIGSe absorber, i.e. window and buffer layers, are not totally transparent and consequently reflect a fraction of the incoming light. Third, the window layer, typically ZnO, absorbs light with energy above its bandgap (∼3.4 eV) and in the infrared region. Fourth, the CdS buffer layer also has a relatively low bandgap (∼2.4 eV) [73], leading to parasitic absorption in this region. All the aforementioned losses reduce the number of photons that reach the CIGSe absorber. Fifth, the losses in this regions can be related to an incomplete absorption of the incoming photons and/or poor transport properties. Additionally, photons with lower energy than the CIGSe absorber's bandgap are not absorbed.

The EQE measurement setup, illustrated in Figure 2.15b, is a home built setup which consists of a Xe and a W halogen lamps as illumination source in the wavelength range of interest, a chopper to generate a periodic signal, a monochromator to select the wavelength and a lock-in amplifier and an oscilloscope to measure the current from either the solar cell of interest or the reference photodiodes for calibration. Si and InGaAs photodiodes were used for calibration. For solar cells smaller than 0.15 mm^2, i.e. with diameter

smaller than 500 µm, a different system, with a smaller beam size, is used to measure EQE. However, in this case, only a Si photodiode is used, meaning that the wavelength range covered only goes up to 1100 nm. In the scope of this thesis, the measurements were performed at short-circuit conditions (voltage = 0 V). This implies that the short-circuit current J_{SC} can be calculated by taking the area under the EQE spectrum multiplied by the AM 1.5 standard spectrum, as given by equation 2.11. This is indeed true if the beam size is smaller than the active area of the solar cell. For more details on the technique, the reader is kindly referred to [47, 70, 72].

$$J_{SC}^{EQE} = -\frac{q}{hc} \int EQE(\lambda)\phi^{AM1.5}(\lambda)\lambda d\lambda \tag{2.11}$$

2.2.10 Current-voltage measurement

Current-voltage (JV) measurement is a characterization technique aimed at assessing the electrical performance of a solar cell. The electrical behavior of a solar cell in the dark can be represented by a single diode model, where the current density J_{dark} through a solar cell is described by the diode equation 2.12. Here, the saturation current density J_0 accounts for the recombination current in the device and should be minimized for better PCE. Additionally, A is the ideality diode factor and accounts for deviations from the ideal case. Upon illumination, a photocurrent density J_{SC} is generated in the solar cell which shifts the diode equation by the short-circuit current. Thus, the current density in an illuminated solar cell J_{ill} is given by equation 2.13.

$$J_{dark} = J_0 \left[\exp\left(\frac{qV}{Ak_BT}\right) - 1 \right] \tag{2.12}$$

$$J_{ill} = J_0 \left[\exp\left(\frac{qV}{Ak_BT}\right) - 1 \right] - J_{ph} \tag{2.13}$$

Experimentally, the JV characteristics of a solar cell is typically measured under dark and under illumination. The first case is of interest to extract the shunt and series resistance from the curve's slope around the short-circuit current J_{SC} and beyond the open-circuit voltage V_{OC}, respectively. A detailed description for the determination of both shunt and series resistance is given in the following reference [74]. The shunt resistance is a measure of how easily the light-generated current leaks through an alternate current path, whereas the series resistance relates to how easily it is to extract the carriers. In the ideal case, the shunt resistance is infinite and the series resistance is zero. In the case of the JV measurement under illumination, the key parameters for the solar cell's performance can be extracted such as, the maximum power point P_{max}, the fill-factor FF, the J_{SC} and the V_{OC}, as highlighted in Figure 2.16a.

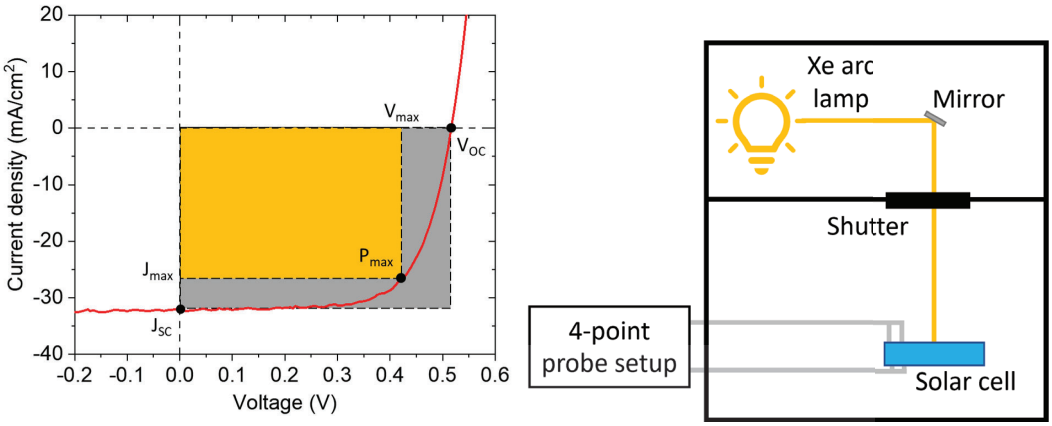

(a) (b)

Figure 2.16: a) JV curve of a typical CIGSe solar cell under illumination with the main parameters highlighted. b) Schematic representation of the current-voltage measurement setup.

The P_{max}, determined by the maximum of the power curve $P = I \cdot V$, indicates at which conditions the solar cell has to be operated for optimal performance. FF is a measure of the squareness of the JV curve and is defined, in equation 2.14, as the ratio of the two rectangles shown in Figure 2.16a. The FF is mainly impacted by the shunt and series resistances of the solar cell.

$$FF = \frac{J_{max} \cdot V_{max}}{J_{SC} \cdot V_{OC}} \tag{2.14}$$

V_{OC} and J_{SC} are the voltage and current produced by solar cell at open-circuit and short-circuit conditions, respectively. In the best case, the V_{OC} equals the ΔE_F, measured in PL, however interface losses can lead to a decrease in V_{OC}. Typically, J_{SC} differs from J_{SC}^{EQE} because of the shadowing caused by the metal grids, during the JV measurement. Finally, the PCE of the solar cell η can be calculated with equation 2.15, where P_{ill} is the illumination power.

$$\eta = \frac{P_{max}}{P_{ill}} = \frac{J_{max} \cdot V_{max}}{P_{ill}} = \frac{J_{SC} \cdot V_{OC} \cdot FF}{P_{ill}} \tag{2.15}$$

The JV characteristics were measured on a home built setup using a Xe arc lamp (100 mW/cm^2, i.e. 1 Sun), as illumination source, and a Keithley four probe setup, as depicted in Figure 2.16b. To calibrate the power of illumination, a certified silicon solar cell was used. As detailed in section 2.1.5, since no front contacts were used for the micro solar cells, the front probes were placed directly on the Al-doped ZnO layer. For more details, the reader is kindly referred to the following documents [47, 70, 75].

JV measurements under light concentration

Concentration photovoltaics relies on the increase of the photon flux, incident on a solar cell, by concentrating the incoming light in order to improve the device's PCE. Traditionally, solar cells are measured under a photon flux of 1 Sun, which leads to a photocurrent density J_{ph}^{1Sun}. Under light concentration, the incident photon flux is multiplied by a concentration factor C, which results in a proportional increase of the photogenerated current density J_{ph}^{Conc}:

$$J_{ph}^{Conc} = C \cdot J_{ph}^{1Sun} \tag{2.16}$$

According to the single diode model under illumination, i.e. equation 2.13, at open-circuit conditions ($V = V_{OC}$) no current flows, that is $J_{ill} = 0$. Assuming a high enough shunt resistance, V_{OC} can be expressed as follows:

$$V_{OC} = \frac{Ak_BT}{q} \cdot \ln\left(\frac{J_{ph}}{J_0} + 1\right) \tag{2.17}$$

To obtain the open-circuit voltage under concentration V_{OC}^{Conc}, J_{ph} is substituted by J_{ph}^{Conc}, which is given by equation 2.16. Furthermore, assuming that A and J_0 remain unchanged under concentrated light and that $J_{ph}^{1Sun}/J_0 \gg 1$, one can express V_{OC}^{Conc} as a function of the open-circuit voltage measured at 1 Sun V_{OC}^{1Sun} and C:

$$V_{OC}^{Conc} = \frac{Ak_BT}{q} \cdot \ln\left(\frac{CJ_{ph}^{1Sun}}{J_0} + 1\right) \approx V_{OC}^{1Sun} + \frac{Ak_BT}{q} \cdot \ln C \tag{2.18}$$

In terms of solar cell's performance, the PCE under concentration $\eta(C)$ is given by the ratio of the new P_{max} and the concentrated incident power $P_{ill}^{Conc} = C \cdot P_{ill}^{1Sun}$ and can be expressed in terms of the non-concentrated parameters (measured at 1 Sun) and C:

$$\eta(C) = \frac{J_{SC}^{Conc} \cdot V_{OC}^{Conc} \cdot FF(C)}{P_{ill}^{Conc}} = \frac{J_{SC}^{1Sun} \cdot V_{OC}^{1Sun} \cdot FF(C)}{P_{ill}^{1Sun}} \cdot \left[1 + \frac{Ak_BT}{qV_{OC}^{1Sun}} \ln C\right] \tag{2.19}$$

This analysis neglects the changes in series and shunt resistances due to light concentration. A major advantage of micro solar cells is the lower series resistance under high light concentration [24, 76, 77], which allows to achieve a higher C [22], and, by the same token, improving the FF. Both factors result in an increase of the absolute gain in PCE through light concentration. For more details, the reader is referred to the following documents [17, 22, 78].

The setup to measure JV under concentrated light is similar to the standard setup discussed above, however, the illumination source can either be a red (660 nm) or blue (405 nm) laser diode with varying power.

Chapter 3

Confocal laser microscopy applied to thin films

The first challenge that is addressed is to develop a methodology to characterize an array of micro-dots, allowing to assess both the evolution of the morphology of individual micro-dots, at every step of a synthesis process, as well as, to monitor the relative composition of thin films synthesized by sequential processes. This methodology will allow to characterize the morphology, composition, phase formation and quality of processes in the two following chapters.

Surface metrology is the measurement of surface features and has become increasingly important as technology tends to miniaturize products and devices while maintaining or improving their performance. This implies that surface properties play a primary role and thus require precise manufacturing and control. In fact, physical and mechanical properties, such as, adhesion, friction, reflectance, electrical conductivity are largely dictated by how the material's surface is engineered [79–82]. The standard surface metrology techniques can be categorized by the surface features' dimensions, as illustrated in Figure 3.1. For macroscopic features down to the micrometer scale, stylus profilometer is the preferred technique, whereas for sub-nanometer resolution scanning probe microscopy (SPM) is necessary. Both techniques rely on a physical probe to scan the area of interest and form the associated profile or topographical map based on the interaction between the probe and the surface. In contrast, optical profilometry uses light to probe the surface and measure its topography. The use of light as probe, in these measurements, inherently limits their lateral resolution to the light source's wavelength. Two commonly used techniques are optical interferometry and confocal microscopy [83]. On the one hand, optical interferometry is the basis of Michelson's interferometer, which measures the phase difference between the probe beam and the reference beam to image the surface's morphology. Given its sub-nanometer vertical resolution, optical interferometers are more suitable to characterize flat, i.e. nanometer-range roughness, surfaces. On the other hand, confocal microscopes rely on the light reflected from a diffraction-limited spot, at an interface, to measure height differences (see chapter 2 for more details) and are able to measure features from tens of nanometers up to micrometers, which are the

dimensions of interest in this work. Adding that the time scale of a measurement is about 1 min, for the lens' respective field of view, makes confocal microscopy an appropriate technique to characterize the morphology of thin films, specially in arrays.

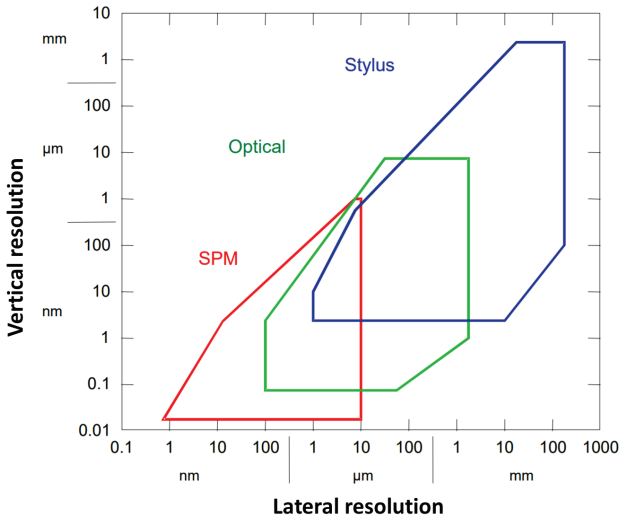

Figure 3.1: Steadman diagram showing vertical and lateral resolution range for three classes of surface metrology techniques (mechanical stylus, optical microscopes, and SPM). Figure adapted from [84, 85].

For the sequential processes studied in this thesis, it is essential to monitor more than the morphology of the thin film layers, like composition and phase formation. Traditional thin film characterization techniques can individually measure morphology or composition with nanoscale resolution, however they often imply altering the sample prior or during the measurement, exposing the sample to vacuum or lengthy measurements for restrictively small areas, which either makes them inconvenient to characterize arrays of thin films or modifies the sample in-between the synthesis process. Also, the sample's dimensions may be an issue as some require a higher volume to generate meaningful signal, while others only allow small fractions of the sample to be analyzed. In fact, in this work, a single array may contain tens to hundreds of individual micro-dots, millimeters away from each other. In this context, a method that does not require alteration of the sample, uses a low-energy probe, can measure large areas with micrometer resolution within few minutes, allows to easily perform analysis in an identical location after each process step and leaves no contamination would be ideal. To fill the gap, this chapter explores the abilities and limitations of applying confocal laser scanning microscopy (CLSM) to thin films in order to extend the technique's current range of applications beyond topography and therewith, demonstrate a novel methodology for characterizing arrays of samples and studying sequential processes.

In the first section of this chapter, a comparison of CLSM height profiles with standard techniques like stylus profilometry and atomic force microscopy (AFM) is made to validate the technique's resolution when applied to the materials used in this work. In the second section, the methodology to measure the thickness of a thin film layer grown

inside a micro-dot is presented. Furthermore, a correlation between morphology, composition and phases formed during synthesis is established in order to deduce and anticipate information from later synthesis stages. In the third section, a few examples, related to thin films, are illustrated where a simple optical analysis of the materials can be associated with different physical properties. This chapter demonstrates that CLSM is an effective thin film characterization and general diagnostic technique to quickly assess samples, to find problems and pinpoint the next pertinent specialized technique to address the issue.

3.1 CLSM measurements testing

To test the reliability of CLSM height measurements, a comparison with a stylus profilometer attempting to measure the exact same location on three distinct stack configurations, comprising materials that are used in this thesis. First, in Figure 3.2a, a height step between a Cu thin film deposited on a Mo layer is measured, showing that both techniques yield very similar height profiles both in nanometer and micrometer scale. Second, Figure 3.2b shows a similar agreement between the two techniques when measuring a step profile this time on a continuous CIGSe film. Third, a cross-section profile of an empty 60 µm diameter micro-dot is plotted in Figure 3.2c, where the CLSM and the stylus profilometer show the same overall profile shape, however for both the depth of the micro-dot and at the interfaces with SiO_2, the CLSM shows an erroneous profile. In fact, given the transparency of SiO_2, it is speculated that the laser probe of CLSM (404 nm) has a low reflectance at the interface between air and SiO_2 [86] and thus underestimates the depth of the micro-dot. Note that this error is systematic as the measured profiles, on sister samples, yield very similar micro-dot depths. Similar issues were faced, when measuring interfaces involving other materials like CdS, Zn(O,S). Since the profile of the empty micro-dots will be important for the determination of the deposits' thickness, further comparison with stylus profilometer is discussed later in section 3.2, where the methodology to measure a layer's thickness is presented. Regarding the diameter of the micro-dot, CLSM measures 60 µm, whereas the stylus profilometer gives a slightly lower value ($\sim$56 µm) likely due to the stylus artifact associated with the dimensions of the probing tip itself [62].

Finally, to compare the accuracy of the CLSM measurements with a higher resolution technique like AFM, a Br etching study performed on CIGSe films is used. With the aim of reducing the roughness of the CIGSe morphology, four different etching durations are compared to the film's initial roughness. Figure 3.2d shows the arithmetical roughness *Ra* and the root-mean square roughness *RMS*, measured from a $\sim 10 \times 10\,\mu m^2$ CIGSe film area using CLSM and AFM, as a function of the films' etching duration. For both roughness parameters *Ra* and *RMS*, CLSM and AFM show the same trend, with the respective measured values found to be within a 10 % interval of each other, which validates the z-resolution of the CLSM.

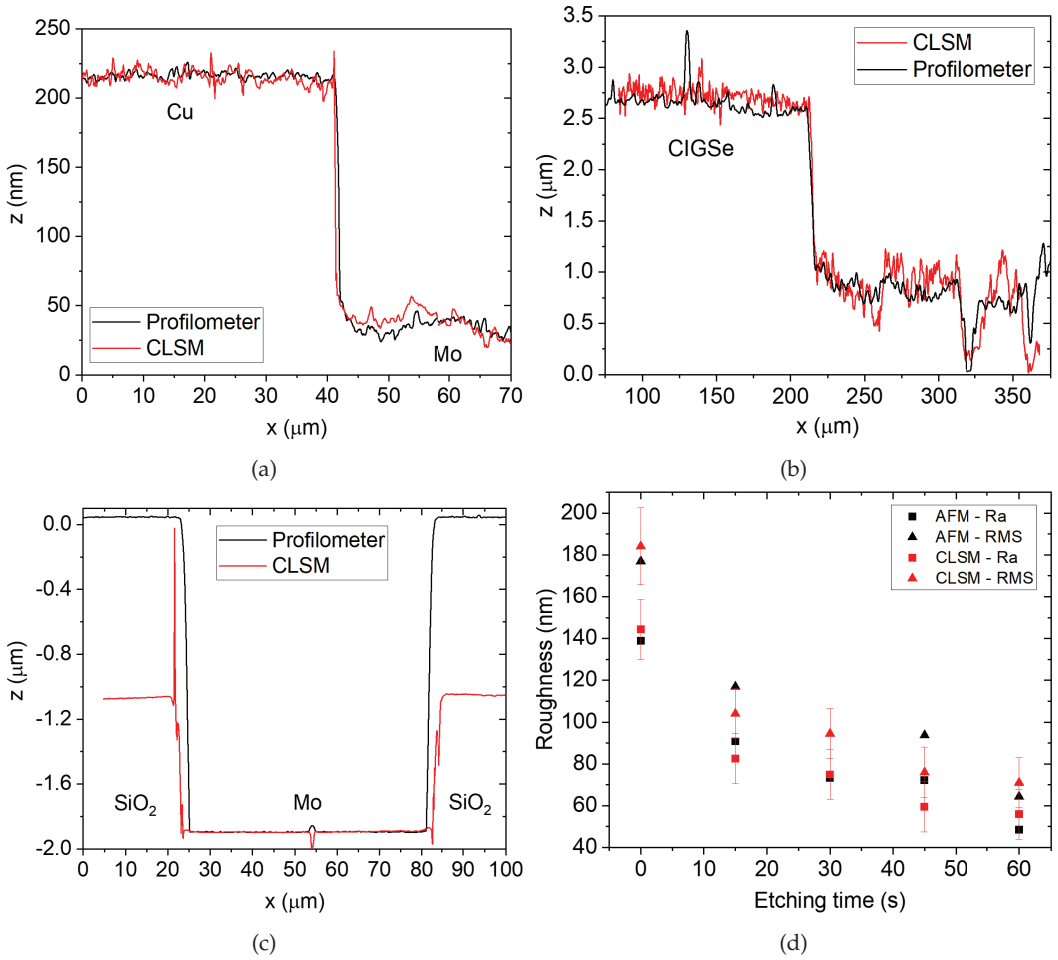

Figure 3.2: Comparison of line height profiles measured with CLSM and stylus profilometer: a) on a step interface between different materials (Cu and Mo films) and b) across the same material (CIGSe film) with a step height due to the templated SiO_2 layer (edge of a micro-dot). c) Line height profile across a 60μm diameter empty micro-dot. d) Comparison of arithmetical *Ra* (squares) and root-mean square *RMS* (triangles) roughness, measured on a polycrystalline CIGSe film, with CLSM (red symbols) and AFM (black symbols), as a function of the Br etching time. Measured area, in both techniques, is about $10 \times 10\,\mu m^2$

.

Thus, CLSM shows a similar height resolution to stylus profilometry and AFM, which is necessary for thin film analysis. However, it seems that height steps involving materials with low reflectance around the CLSM laser's wavelength (404 nm) are problematic. It is speculated that the low reflectance leads to a detected intensity profile, along the measurement axis (z-direction), for which it is not obvious where the maximum of intensity is located, leading to an errouneous height profile. In the following, the methodology to characterize micro-dots in terms of morphology, composition and phase formation, is showcased with the material-efficient synthesis route featuring electrodeposition and annealing, which is a sequential process.

3.2 CLSM correlative analysis

The work presented in this section is based on the publication [87] and demonstrates how to apply CLSM to thin film sequential deposition processes in order to obtain elemental composition and use that information to predict spatially the phase formation. More precisely, it illustrates how to measure stacked films' thickness and composition, perform statistics on an array, correlate morphology changes in-between process steps, and correlate measured precursor composition with formed phases. To demonstrate these concepts, the sequential electrodeposition synthesis route, described in section 2.1.2, is chosen and CLSM optical images and height maps, of all the micro-dots in the array, are measured before and after each electrodeposition and annealing step.

3.2.1 Morphology analysis

Individual deposits

In sequential synthesis processes, being able to control and monitor the thickness and roughness of each deposit is critical as they influence both the subsequent synthesis steps and the final device's performance. On the one hand, since CLSM measurements of an area yield the corresponding height map, the roughness of the region of interest can be directly assessed. On the other hand, given that the deposits are inside the holes of the SiO_2 matrix, it is not possible to directly extract the thickness of the film. Figure 3.3 exemplifies how to determine the xy-resolved thickness map of a Cu film micro-dot, from the corresponding empty and electrodeposited Cu height maps. First, the surrounding SiO_2 matrix is set as the height reference (height = 0 µm) for all the involved height maps, as it is flat and does not change throughout the process. Then, to obtain the Cu thickness map (Figure 3.3c) the empty micro-dot height map (Figure 3.3a) is subtracted from the Cu film height map (Figure 3.3b).

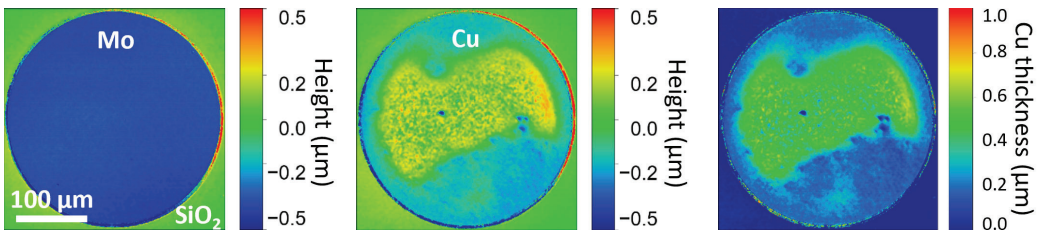

(a) (b) (c)

Figure 3.3: CLSM height maps for a) empty micro-dot and b) electrodeposited Cu film. c) Cu layer thickness calculated from height maps: $c = b - a$. The region surrounding the micro-dot is a SiO_2 layer used as a zero-reference height. Note the change in scale for c).

The attentive reader will notice the empty micro-dot depth, shown in Figure 3.3a, is measured to be 0.5 µm instead of the 2 µm mentioned in the methods section 2.1.1. This is due to the SiO_2 being mostly transparent to the CLSM light source's wavelength (404 nm) [86], leading to a systematic underestimation of the measured depth. However, since the SiO_2 layer is only used as reference height, and is not modified throughout the process,

the subtraction of the two height maps yields a reliable measurement of the thickness. To demonstrate that the method is accurate, four homogeneous Cu deposits with distinct thicknesses were grown in an empty micro-dot substrate. CLSM and stylus profilometer techniques were used to measured the four micro-dots before and after the electrodeposition. The layer thickness was obtained by subtracting the profile of the empty micro-dot from that of its corresponding Cu deposit. The individual layer thicknesses are plotted in Figure 3.4. Note that the line profiles (from stylus profilometer and CLSM) were taken from approximately the same position within the micro-dot. Figure 3.4 shows that both techniques are in agreement, within the experimental error.

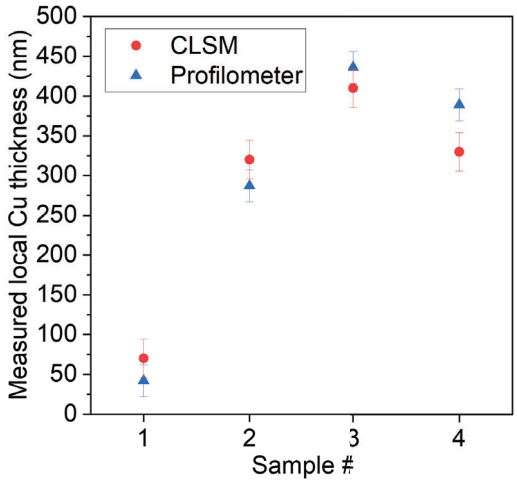

Figure 3.4: Measurement of the local layer thickness of Cu deposits with different thicknesses measured with stylus profilometer (blue triangle) and CLSM (red circle). The measurement error attributed to stylus profilometer is 20 nm and for CLSM is 24 nm.

The xy-resolved thickness map allows to quickly assess the deposits' thickness distribution as well as its homogeneity, which relate to the film's roughness and porosity. To maximize the quality of the resulting CIGSe absorber, synthetized from stacked precursor layers, it is crucial to produce compact, smooth and thickness-controlled metal precursor layers [36, 88]. A deposit showing the opposite case is presented in Figure 3.3c, where a non-uniform thickness distribution is seen. More precisely, the Cu film shows a preferential growth at the centre of the micro-dot, resulting in a thinner Cu layer at the periphery. A possible explanation is an inhomogeneously oxidized or contaminated Mo substrate in this particular micro-dot, which is known to impact the nucleation process at the early stages of the electrodeposition [88, 89].

To further demonstrate the utility of this method, Figures 3.5a and 3.5b display the height map of the precursor metal stack Cu/(In,Ga) and the calculated thickness map of the (In,Ga) layer, respectively. In the first case, the typical formation of In islands embedded in a (In,Ga) alloy layer is visible, as also observed in literature [90]. Merely from the height map (i.e. surface information) of the Cu/(In,Ga) stack, it is not possible to assess the (In,Ga) deposit's homogeneity, as its morphology is highly impacted by the underlying inhomogeneous Cu layer. However, when isolating the (In,Ga) layer thickness map

from the metal stack (see Figure 3.5b), it is clear that the In islands grew preferentially in the lower edge of the micro-dot and that only a thin (In,Ga) alloy layer was formed. Note that, for simplicity, the interdiffusion between the Cu and (In,Ga) metal layers was neglected [91].

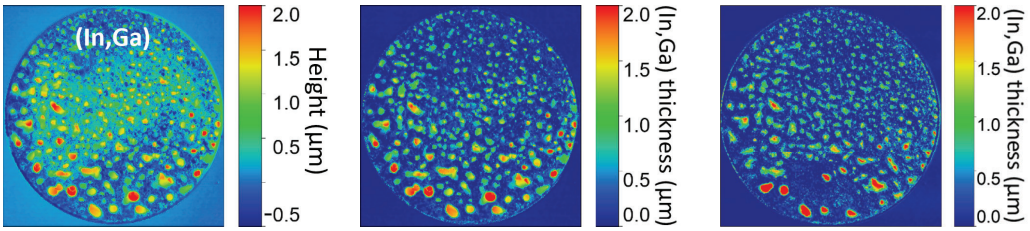

(a) (b) (c)

Figure 3.5: CLSM height map for a) Cu/(In,Ga) stack. b) Calculated (In,Ga) film thickness from stack's height and Cu thickness maps. c) Calculated thickness of (In,Ga) film after annealing routine in N_2. Note each image has a different scale.

Another example of application is to monitor the diffusion study of the deposits upon an annealing routine. As mentioned previously, smooth precursor metal layers contribute to improving the quality of the final absorber phase and given the peculiar morphology formed during the (In,Ga) co-electrodeposition (see Figure 3.5b), it is of interest to reduce the overall roughness of the deposits. This can be achieved by supplying thermal energy to the deposits in an inert environment. For this reason, an annealing routine in N_2 atmosphere was applied to the array of micro-dots for 10 min at 300 °C, in a closed pot chamber. The resulting morphology of the annealed (In,Ga) layer is represented in Figure 3.5c. By comparing the morphologies of the micro-dot before and after the annealing procedure, the major difference appears at the level of the In islands, with their projected area being modified but more strikingly their thickness changes. On the one hand, the phenomenon of Ostwald ripening is observed, as the previously large islands grew bigger at the expense of neighboring smaller In islands, some of which are no longer visible in the map in Figure 3.5c. This is particularly visible when comparing the lower half of the deposits. On the other hand, after annealing, some In islands have their size reduced and their delimitations become blurry, for instance on the left part of the deposits, which suggests the diffusion of the In into the underlying (In,Ga) layer. However, this effect cannot be resolved with CLSM as its impact on the layer's thickness is below the microscope resolution. Note that this micro-dot is representative for the whole array in that both effects are always observed, however the extent of each phenomenon seems to vary. For instance, in this particular micro-dot, the Ostwald ripening is especially pronounced. All in all, the annealing routine reduced the roughness of the precursor layers on average by about 6 %, which aligns with the aim of the experiment.

Statistical analysis

This analysis at the individual micro-dot level can be extended to the complete array, which allows to perform statistics and put forward wafer-scale effects, that could

otherwise be overlooked. For this, the average layer thickness and respective root mean square (RMS) roughness of each individual micro-dot are plotted in a heatmap configuration, thus retaining the positional information of each micro-dot with respect to the array. In addition, the frequency distribution of each heatmap is also shown in Figure 3.6.

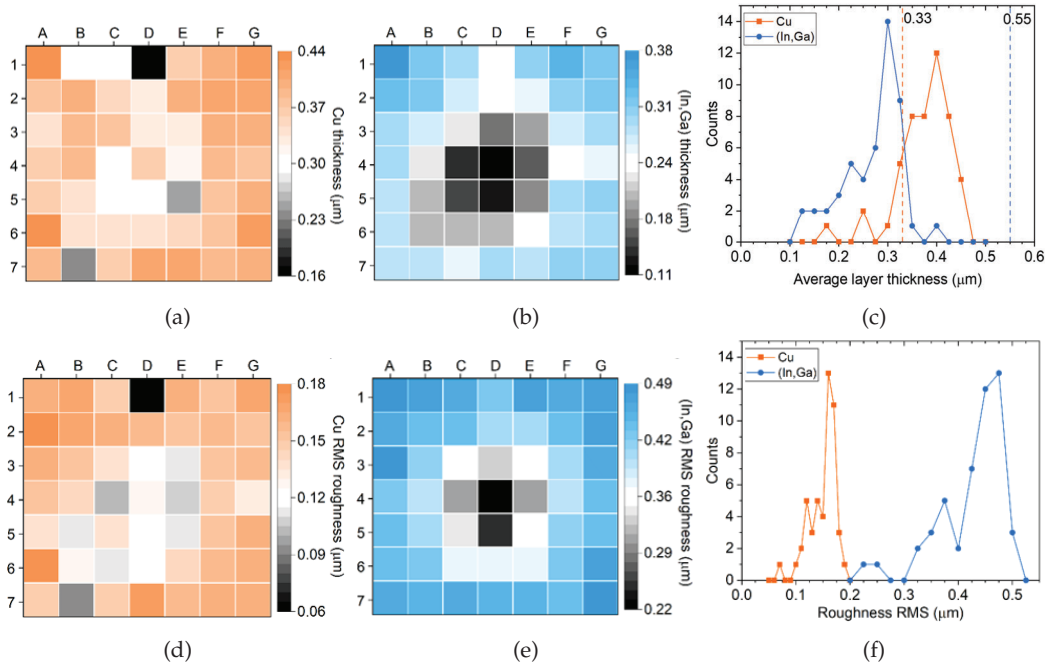

Figure 3.6: Statistics at the array level of Cu and (In,Ga) average layer thickness (a-c) and roughness (d-f). Heatmap representation of the array of Cu layers' a) thickness and d) *RMS* roughness. Heatmap of (In,Ga) layers' b) thickness and e) *RMS* roughness. Frequency distribution of the 49 micro-dots of Cu and (In,Ga) c) layer thickness and f) *RMS* roughness. The vertical dashed lines indicate the targeted average layer thickness for the Cu (orange) and (In,Ga) (blue) deposits.

Addressing the average layer thickness map of Cu, in Figure 3.6a, in general the average thickness of Cu deposited in each micro-dot was similar, with a few outliers. This suggests the Mo surface in these micro-dots, prior to the deposition, was contaminated or particularly oxidized, causing an unfavourable local growth. A different scenario is put forward for the (In,Ga) deposits' spatial distribution in Figure 3.6b. In fact, a thickness gradient is clearly visible from the periphery to the centre of the array. Uniformly thick In and Ga deposits have been demonstrated over larger areas than in our case, which required a sufficiently negative potential, above a threshold, to be applied to the substrate [90]. If the potential in the micro-dot is below this threshold, the rate of electrodeposition would proceed slower. Since the electrical contacts to the array are made on the corners of the sample, it is possible that the deposition potential was insufficiently negative at the center of the array, due to a higher than expected Mo resistance, causing a more positive potential towards the array's centre. This would lead to less (In,Ga) deposition in this region. Proceeding to the layers' thickness distribution, in Figure 3.6c, the target was to electrodeposit 330 nm of Cu and 550 nm of (In,Ga) in each micro-dot. An average thickness of 360 nm with a deviation of 50 nm was measured for Cu, which is in agreement

with the targeted value. Conversely, in the case of (In,Ga), a lower than expected average thickness of 260 ± 60 nm was observed, which could be due to the low faradaic efficiency of the co-electrodeposition, enhanced by the potential gradient discussed previously.

An analogous analysis for the spatial distribution of Cu and (In,Ga) layers' roughness is shown in Figures 3.6d and e. In fact, a close correlation with the respective thickness maps is recognized, as in general, the roughness increases with the layer's thickness. More specifically to the (In,Ga) layers, the deposits at the centre were relatively thin, resulting in a low roughness whereas, the peripheral micro-dots grew thicker, with larger In islands, causing a high roughness. Regarding the layers' roughness frequency distribution (Figure 3.6f), the Cu layers are much smoother compared to the (In,Ga) layers, which is due to the island growth mode of In during the co-electrodeposition [90]. Furthermore, the roughness distribution of (In,Ga) is broader than that of Cu, due to the potential edge to centre gradient discussed previously.

To sum up, a methodology based on CLSM was demonstrated: (i) to reliably measure the thickness of a thin film layer grown inside a matrix, as well as, the thickness of a stack of layers, (ii) to characterize the morphology of individual layers over a relatively large area and therewith correlate morphology changes in-between process steps, (iii) to perform statistics over a complete array of micro-dots to compare processes easily. In the next section, the methodology is extended to deduce elemental composition of stacked layers.

3.2.2 Calculating elemental composition of stacked layers

The morphological analysis provided information on the shape, thickness and roughness of the different layers involved in our synthesis process. This information can be used to gain insights on their elemental composition. As a matter of fact, from the average thickness d of the layer and its volume density ρ_x, the number of atoms N_x that make up the deposit can be calculated using equation (3.1). The surface area A, molar mass M_x and Avogadro's number N_A being constants. Transforming the height data in this way allows us to perform elemental analysis on each individual layer using CLSM.

$$N_x = \frac{\rho_x \cdot A \cdot N_A}{M_x} \cdot d \tag{3.1}$$

In our case, the interest of measuring the composition of the precursor stacked layers is the ability to measure the elemental ratio CGI, which contains information about the potential phases that form during the synthesis process, as discussed in chapter 1. Monitoring both its value and homogeneity across the absorber is key to achieve high quality CIGSe material. From the thickness maps of Cu and (In,Ga) layers, the respective number of constituent atoms is determined. In both cases, a constant volume density is assumed, which were considered to be the bulk values. More precisely, a density of 8.96 g/cm^3 for Cu, whereas for the (In,Ga) layer a weighted average of the respective

densities is calculated, 7.31 g/cm^3 for In and 5.90 g/cm^3 for Ga [92]. Therewith CGI is calculated for each individual precursor micro-dot and plotted in Table 3.1a retaining the spatial arrangement of the micro-dots within the array. To validate the values obtained from CLSM, a standard elemental composition technique, namely EDX, is used to characterize the precursors' CGI, which are regrouped in Table 3.1b. For ease of comparison, a common color scale was applied to both sets of results.

	A	B	C	D	E	F	G
1	2.4	1.9	2.1	1.4	2.4	2.4	2.8
2	2.4	2.6	2.8	2.9	3.2	2.8	2.7
3	2.5	2.9	3.5	4.0	3.6	3.1	2.9
4	2.6	3.7	4.6	6.9	4.1	3.4	3.0
5	2.7	3.6	4.5	5.0	2.8	2.7	2.8
6	3.2	3.4	3.5	3.5	3.1	2.8	3.0
7	2.8	1.8	2.8	2.9	3.0	2.6	2.7

(a)

	A	B	C	D	E	F	G
1	0.9	0.9	0.9	0.6	1.0	0.9	0.9
2	1.0	1.0	1.0	1.2	1.0	0.9	0.9
3	0.8	1.1	1.3	1.4	1.2	1.0	0.9
4	1.1	1.3	1.0	2.0	1.4	1.1	1.0
5	1.1	1.3	1.5	1.8	1.3	1.1	0.9
6	1.0	1.3	1.2	1.4	1.3	1.0	0.9
7	1.1	0.8	1.1	1.0	1.0	1.3	0.9

(b)

Table 3.1: Average CGI ratio of the precursor micro-dots array measured with: a) CLSM b) EDX. EDX measurements were acquired with an acceleration voltage of 20 kV.

Although the two datasets do not match in absolute values, both show similar trends in CGI across the array. In fact, the correlation coefficient of the two sets yields 0.85, which translates the positive correlation that is equally visible between the two tables' color patterns. Alternatively, in Figure 3.7a the precursors' CGI values are plotted to demonstrate the linear trend between the two techniques, CLSM and EDX. It is worth noting that EDX elemental analysis on stacked layers is not straightforward, due to the interaction volume of electrons (see discussion in section 2.2.5 of chapter 2) [93, 94]. This could explain the deviation from the ideal case $y = x$, shown as a reference in Figure 3.7a. In any case, the high correlation value implies that CLSM can in principle reliably measure the relative elemental composition of stacked layers.

Nevertheless, for solar cell applications, the relevant parameter is the final absorbers' CGI ratio, where the precursor bi-layer has reacted to form the CIGSe phase. Therefore, a set of precursors which span a CGI interval of interest for device fabrication is measured. This allows to compare the CGI ratio of the precursors, measured with CLSM, and the CGI of the CIGSe absorber, obtained from EDX analysis after selenization, as plotted in Figure 3.7b.

The relation between the CGI ratios measured with both techniques suggests a direct linear trend, putting forward that the average composition of the CIGSe absorber can be accurately measured with CLSM from the precursor stack, that is, before the reactive annealing step takes place. In fact, the ability of anticipating the absorber's composition is relevant as it allows to anticipate the quality of the CIGSe absorber at an early synthesis stage. Assuming that EDX perfectly describes the CGI ratio of the absorber, the linear fit deviation from the ideal case ($y = x$), may be due to an overestimate of the (In,Ga) alloy

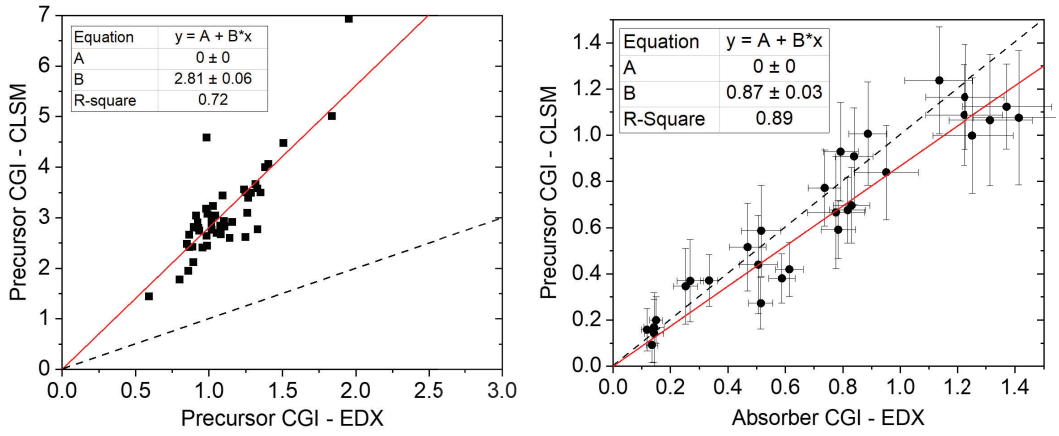

(a) (b)

Figure 3.7: Compositional CGI ratio of precursor stack measured with CLSM compared to: a) the precursor layer CGI ratio measured with EDX. b) the transformed absorber layer CGI ratio measured with EDX. Linear fitting parameters are shown as inset. Red solid line is a linear fit whereas dashed line corresponds to the ideal case $y = x$. The error bars for the CLSM CGI were calculated assuming a thickness error of 24 nm for each the Cu and (In,Ga) layers, whereas the EDX CGI was calculated assuming an error of 1 at% for each element. All EDX measurement were acquired with an acceleration voltage of 20 kV.

layer's density. In fact, the simplified weighted average may not give an appropriate estimation given the layer's peculiar island morphology. Another possible factor influencing the layer's density is the interdiffusion of the precursors, which can take place already during the co-electrodeposition [91].

To summarize, this section demonstrated how to calculate an average elemental composition of stacked layers and validated the method by comparing with a standard composition technique, EDX. In fact, the CLSM methodology could correlate CGI composition values, measured from the precursor stack, i.e. before the annealing in Se, with the absorber's CGI measured with EDX after the annealing. This is useful to anticipate the composition the absorber would have and adjust the synthesis process if necessary. Similarly to the previous section, the composition analysis can be done for the individual micro-dot, as well as for the whole array, without the need for further measurements than those already acquired for morphology analysis. In the following, instead of averaging the layers' thickness maps, to measure an average elemental composition, the micrometer spatial resolution of the CLSM thickness maps is used to assess local composition and deduce which phases could be formed.

3.2.3 Measure composition map and predict phases

Composition map

To demonstrate the ability of measuring elemental composition with CLSM, the average layer thickness of the individual micro-dot was considered. However, one can

directly exploit the micrometer spatial resolution of the CLSM thickness maps and compute a qualitative CGI ratio map for each micro-dot. This is achieved by calculating the ratio between the Cu and (In,Ga) thickness maps. In the particular case of the (In,Ga) morphology, in some regions, the thin-film's thickness is in the resolution limit of CLSM. This may lead to values close to zero or even negative, which would distort the CGI scalebar. To circumvent this issue, these regions are set to 10 nm, which is below the CLSM resolution.

Looking inside a single micro-dot helps to distinguish between high CGI (Cu-richer) and low CGI ratio (Cu-poorer) regions, which has been shown to be critical for the formation of secondary phases, impacting the performance of the CIGSe absorber [95, 96]. Conversely to device-oriented precursor layers, this study requires inhomogeneously thick Cu and (In,Ga) layers in order to have a spatially dependent CGI distribution including both low (« 1) and high (» 1) CGI regions within the same micro-dot. An example is shown in Figure 3.8a. For a direct comparison of the CGI distribution, EDX elemental maps of Cu, In and Ga were measured before and after the selenization of the precursor, so that one may calculate CGI maps of the precursor and the absorber. The calculated maps are shown in Figures 3.8b and c, respectively.

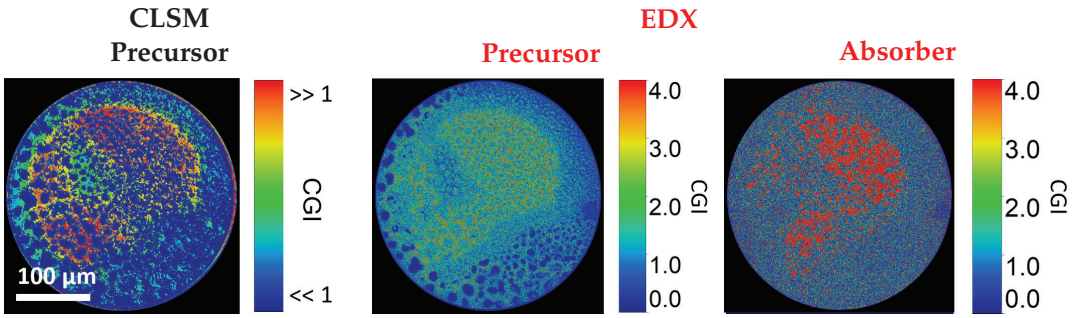

Figure 3.8: Spatially resolved CGI mapping of: a) precursor stack measured with CLSM with non-calibrated scaling due to the divide by zero error discussed in the text. b) precursor stack measured with EDX. c) absorber stack measured with EDX. EDX maps were acquired with an acceleration voltage of 20 kV.

Focusing on the precursor CGI maps, both techniques yield a similar CGI spatial distribution within the micro-dot. In both cases, the maps are characterized by a high CGI central region, which covers almost half of the micro-dot's area, and a low CGI region that is located along the periphery. The latter is characterized by dark blue patches that are due to the morphology of the In islands that are known to form during the co-electrodeposition of In and Ga [90]. Indeed, the localized high concentration of In leads to a low CGI ratio. Conversely, the central region of the micro-dot, i.e. with a high CGI ratio, comes about due to the preferential deposition of Cu in this particular area.

The selenization step provides both the elemental selenium to form the CIGSe absorber, as well as, thermal energy that drives the intermixing of the elements, through diffusion. On the one hand, the chemical potential drives the system to form the phase,

or phases depending on the relative composition, that is stable at the operated temperature and pressure. On the other hand, it also induces diffusion of the reacting species within the micro-dot, given the concentration gradient, created by the inhomogeneously thick precursor layers. Nevertheless, given the short selenization period (10 min at target temperature), the relatively low target temperature (450 °C) and the amplitude of the concentration gradient, it is expected that the CGI map of the absorber is more spatially homogeneous, however it should retain the main features that characterize the precursor's CGI map. Indeed, the resulting CGI spatial distribution of the absorber, shown in Figure 3.8c, agrees with the description of the CLSM precursor CGI map in that the central region of the absorber has a high CGI ratio, whereas the periphery shows a low CGI. Nevertheless, when comparing both CGI maps, the effect of diffusion of elements during the selenization process is clearly visible. In fact, the precursor's In islands are completely smeared out after the formation of CIGSe, whereas the Cu-rich central region can still be identified. This suggests that the lateral diffusion length of Cu is not high enough to compensate the CGI inhomogeneous distribution of the precursor, at the operated conditions. Therefore, in such sequential processes, it is important that the morphology of the Cu layer is smooth and uniformly thick to obtain a homogeneous CGI distribution at the absorber level and ultimately obtain a higher absorber quality.

Phase prediction

With the CLSM information, the absorber's CGI lateral profile can be anticipated from the precursor layers' morphology. Additionally, with the composition's spatial distribution and based on the material's phase diagram, one can anticipate which phases are most likely to form in the different regions of interest. In this case, assuming the supply of Se during selenization is sufficient, a CGI > 1.0 gives rise to the formation of a secondary phase, more precisely $Cu_{2-x}Se$, in addition to the main CIGSe phase. Referring back to the CGI maps, in Figure 3.8, the regions most likely to form a $Cu_{2-x}Se$ phase are the regions shown in red, that is, with a high CGI. To test this hypothesis, micrometer resolved Raman spectroscopy is performed, which provides information on the vibrational modes of the crystalline structures and allows the identification of the phases that are present at the surface of the material. According to literature, the main vibrational modes of CIGSe and $Cu_{2-x}Se$ in Raman spectroscopy are characterized by peaks at 174 cm^{-1} and 260 cm^{-1}, respectively [97–99]. To obtain spatial information, a map of spectra was measured from the same absorber discussed in Figure 3.8 (repeated in Figure 3.9a for easier comparison), and the intensities measured at 174 cm^{-1} and 260 cm^{-1} are mapped in Figure 3.9b and c, respectively. As a guideline, a higher intensity suggests the respective phase is present, whereas a lower intensity means it is absent.

As anticipated, the Raman maps show a similar pattern to the one seen in the CGI ratio maps discussed previously, putting forward the relation between composition and phase formation. In fact, the low CGI regions match the spatial distribution of the CIGSe phase on the Raman map, whereas the high CGI regions are where the formation of the

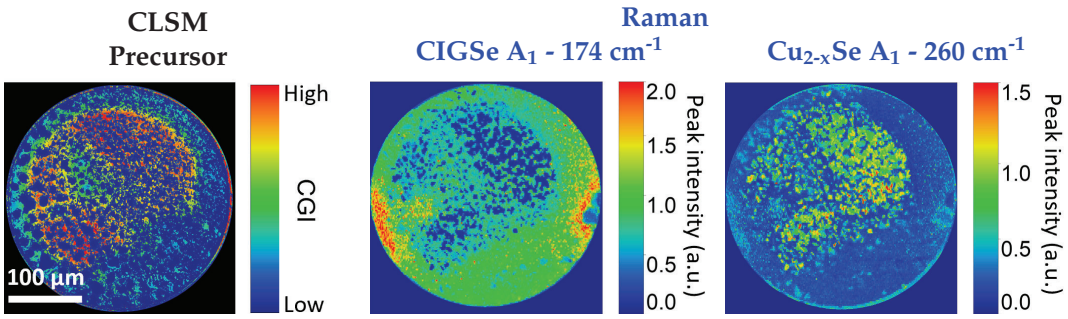

(a) (b) (c)

Figure 3.9: a) Spatially resolved CGI ratio mapping of precursor stack measured with CLSM. Raman intensity mapping of final absorber: b) CIGSe A_1 mode at 174 cm^{-1}. c) $Cu_{2-x}Se$ A_1 mode at 260 cm^{-1}. A 532 nm laser was used as excitation source.

$Cu_{2-x}Se$ phase was expected, which agrees with the material's phase diagram. As Raman is essentially a surface sensitive technique, it is not possible to obtain information from the phases in the bulk, which also explains why the Raman maps are complementary.

Thus, the methodology based on CLSM, is extended to measure qualitative CGI composition maps, with micrometer spatial resolution, for a layer stack and therewith anticipate which phases will form after the annealing process, and their respective location.

To summarize, the methodology presented in this section demonstrates how to apply CLSM to thin films to characterize a sample beyond the conventional morphology parameters (height differences and surface roughness). In fact, based solely on the height maps, measured in-between each synthesis step, it was possible to measure each layer's thickness and roughness, follow the evolution of the stack's and individual layer's morphology, thickness and assess their growth process. For sequential deposition processes, the methodology allows to obtain relative elemental composition and use that information to predict spatially the phase formation. Here, it was showcased for an array of micro-dots, however the methodology can be adapted to other stacked elemental layer systems. Furthermore, given the technique's quick measurement time, statistics over the complete array of micro-dots could be studied and allowed to emphasize effects visible only at the array-level. It is also worth emphasizing that all the above information is obtained without modifying the sample, and without influencing the synthesis process, and is based only on the measurements acquired from the precursor layers. This implies that the sample is not affected by the characterization method in-between synthesis steps and any potential issue can be identified early in the synthesis process. Two limitations for the general use of this method are that (i) the layers' surface of interest should be sufficiently reflective to avoid erroneous measurements and (ii) the knowledge of the density of the deposited layers is required to determine the elemental ratios. To complement the methodology showcased in this section, an optical analysis is presented in the following to illustrate how to use high optical resolution and contrast of CLSM to quickly identify phases and assess the quality of processes.

3.3 Optical analysis

Solar cells are multi-layered structures that require a meticulous control during the synthesis in order to maximize the device's performance. Nevertheless, each layer has distinct optical properties, like bandgap or reflectance, which results in a different appearance, or color, depending on the illumination. The characteristic light interaction of materials can be exploited to identify and distinguish the different phases or layers present in our structures, avoiding the need for advanced and complex characterization techniques. The next two sections present examples of situations where just an optical analysis can help identifying phases and their delimitations, as well as, to check and assess the quality of intermediate processes, like mechanical scribing for solar cell isolation.

3.3.1 Phase identification

Let us consider semi-transparent solar cells synthesized by etching a CIGSe absorber into stripes, with sub-milimeter width, and alternating them with transparent glass to achieve the semi-transparency [100]. Figure 3.10a is an optical top-view image showing a fraction of one solar cell stripe across its width and Figure 3.10b is a schematic representation of the cross-section of the stripe, color coded to distinguish the different layers. The optical image shows five distinct regions, starting from the edge towards the center: the glass is shown in black, Mo layer has a white color, the CIGSe absorber layer displays a grey appearance, the buffer and window layers are green and finally the metal grid is also white/grey. To maximize efficiency and transparency, only the interface between glass and the window layer would be visible from a top-view perspective, however the uncontrolled etching resulted in different widths for each layer, as illustrated by the height profile in Figure 3.10c. In addition to performance deterioration, the distinct widths also complicate the determination of the active area, necessary for accurate devices' characterization.

To confirm the spatial delimitations of each layer, EDX mapping of elements, characteristic of each layer, was acquired from the same solar cell stripe segment. The acceleration voltage used for the EDX mapping was 10 kV, in order to be mostly surface sensitive while still being able to detect the relevant elements. Figures 3.10d-f show the spatial elemental distribution of Se, Zn and O respectively and the color scale shows higher content with brighter colors and lower with darker colors. Starting with the Se map (Figure 3.10d), the Se signal originates from the uncovered $MoSe_2$ bottom layer, as well as from the exposed side walls of the CIGSe absorber layer. The distinction between $MoSe_2$ and CIGSe is clear thanks to the Se signal constrast, which arises due to the thickness difference between the nanometer thick $MoSe_2$ and the 2 µm CIGSe absorber. Note that the dark regions correspond to glass and the buffer/window layers which do not contain any elemental Se. Comparing this spatial distribution with the color code in the optical image (Figure 3.10a), it overlaps with the white colored Mo/$MoSe_2$ layer, along with the uncovered grey CIGSe absorber. A similar analysis and conclusion can be

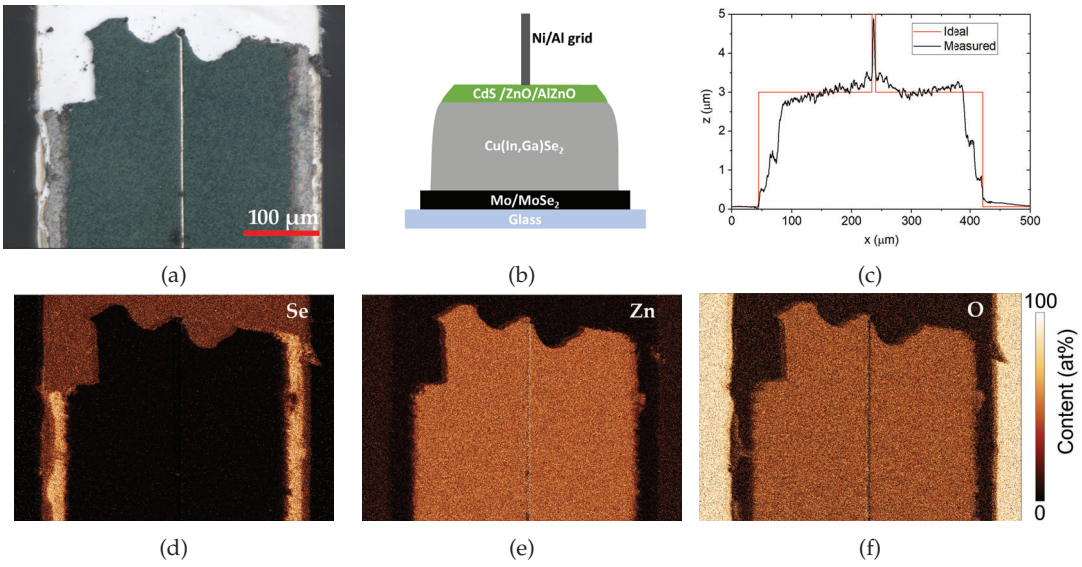

Figure 3.10: a) CLSM optical image of a top-view solar cell stripe. b) Schematics of the cross-section stack making up the stripe solar cell. c) Ideal (red) and measured (black) line height profile across the solar cell stripe. EDX elemental distribution, measured in the same region as shown in a), for: d) Se, e) Zn and f) O. The acceleration voltage used was 10 kV. All three maps share the same scalebar.

drawn from the Zn spatial distribution map, in Figure 3.10f, in the sense that the window layers delimitations coincide with the green region shown in Figure 3.10a. Finally, the O map highlights the delimitations of the glass substrate and again those of the window layers. This shows the possibility of identifying the phases' spatial delimitations, at a macroscopic scale, by simple optical analysis.

Since the wavelength of visible light is in the range of hundreds of nanometers, a similar optical analysis can be applied at the microscopic scale in order to, for instance, identify secondary phases with distinct optical properties from the main phase. Just like in our previous example, this method is solely for identification of materials that interact differently with light and requires prior knowledge on which phases may be present. Nevertheless, the ability to identify foreign phases remains of wide interest, for instance to study a compound's phase purity, as in the case of the multinary CIGSe. The following example concerns secondary phases formed during the synthesis of Cu-rich (CGI > 1.0) CIGSe in the array of micro-dots, produced by the two-step electrodeposition and annealing synthesis method, discussed in the previous section. Figures 3.11a and b show optical images of two sister CIGSe micro-dots near the interface with the SiO_2 matrix. Raman spectra were acquired from the distinct phases, at the locations indicated in the images, and plotted in Figure 3.11c.

In both cases, different color contrasts are visible both inside the micro-dots and on the SiO_2 matrix. Focusing inside the micro-dots, three distinct phases can be identified. In Figure 3.11a, black and grey granular phases are visible, whereas Figure 3.11b shows a similarly grey phase and black polygon shaped structures. The Raman spectra of the grey

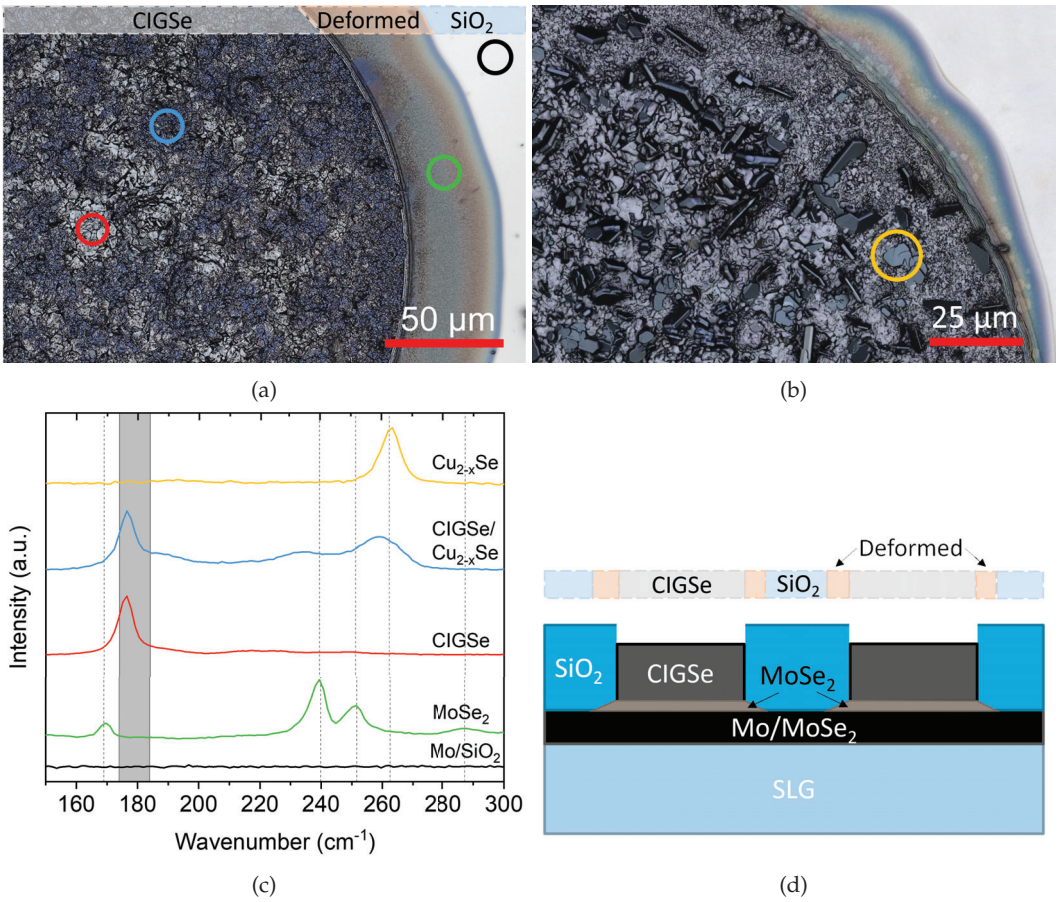

Figure 3.11: a) and b) CLSM optical images of the morphology and distinct phases resulting from the synthesis of two Cu-rich CIGSe absorbers in a patterned substrate. Circles highlight the locations where Raman spectra were acquired. c) Raman spectra measured on the regions indicated in a) and b). Spectra line colors match the measurement location indicator's color. d) Schematics representation of a cross-section view of a) and b) to illustrate the $MoSe_2$ layer extending underneath the SiO_2. Dimensions are not to scale.

phase shows the characteristic A_1 vibration mode of CIGSe, typically in the range 174-184 cm^{-1} depending on the Ga content [99, 101], whereas the black granular phase additionally displays a vibration peak, at 262 cm^{-1}, associated with $Cu_{2-x}Se$ [98]. This suggests the CIGSe micro-dot contains regions with pure CIGSe intercalated with CIGSe/$Cu_{2-x}Se$ regions. Here, the mixed B_2/E mode of CIGSe is also detected around 230 cm^{-1} [99]. As for the polygon structures in Figure 3.11b, they are associated with the $Cu_{2-x}Se$ Raman peak and also appear similar in literature with SEM [102]. Outside the micro-dot, the aura formed around the periphery corresponds to the $MoSe_2$ layer that forms in-between the Mo back contact and the CIGSe absorber, and in this case extended underneath the SiO_2 layer, as illustrated in the stack's cross-section schematics in Figure 3.11d. Here, the main observed Raman modes are the E_{1g} at 169 cm^{-1}, A_{1g} at 240 cm^{-1} and E_{2g} at 288 cm^{-1} [99, 103]. Conversely, the fourth peak measured at 251 cm^{-1} does not seem to come from a $MoSe_2$, but could possibly show the presence of elemental Se, in particular Se_8 rings [103, 104]. Finally, the pristine Mo underneath SiO_2 does not have any particular Raman

signature in this range.

These examples show that the optical analysis of thin films can be an effective and simple method to identify phases present and their spatial delimitations. In the following section, CLSM is applied as a troubleshooting tool to rapidly inspect the quality and integrity of the layers.

3.3.2 CLSM as quality control technique

The synthesis of solar cells being done layer by layer, it is important to monitor the quality of the underlying layer before proceeding with the next step of the synthesis. In the following, examples are addressed where CLSM can help to qualitatively assess the substrate and deposit before and after the synthesis, respectively. Additionally, two examples where CLSM optical analysis can help assess the electrical isolation of solar cells are also discussed.

The conditions of the substrates are crucial to ensure a controlled synthesis and optimize resulting properties. In fact, impurities modify the substrate surface's properties and may lead, among others, to poor adhesion of the film to the substrate [105] or to the formation of pinholes during synthesis of thin films [106]. Traditionally, samples are stored in a desiccator to maintain their properties, however the repeated access to the desiccator can lead to the contamination and oxidation of the substrate's surface, as shown in Figure 3.12a. Here, a zoom-in on an empty micro-dot shows an oxidized Mo surface, visible by its yellowish appearance, and the accumulation of contaminants. Naturally, these impact the synthesis process and deteriorate the quality of the resulting device. Through optical analysis, CLSM can quickly assess the condition of the substrate, for instance, after a cleaning procedure, as shown in Figure 3.12b or even the quality of the Cu deposit, in the case of Figure 3.12c, here showing a mostly smooth and uniform Cu layer.

A different application of CLSM can be found later in the synthesis of solar cells, specifically when isolating solar cells from any unwanted shunt path. This is generally achieved by scribing, either mechanically or using a laser. Figure 3.12d shows the scribed region around a complete micro solar cell, where the CIGSe absorber was deposited inside the micro-dot as well as on the SiO_2 layer, implying that the buffer and window layers are not in contact with the SiO_2. Here, the scribing lines are generally sharp, isolating the region of interest from its surrounding. In this particular cell, the measured shunt resistance, which translates to what extent the cell is electrically isolated, was fairly low ($25\,\Omega cm^2$ compared to typically $10^4\,\Omega cm^2$ for an isolated solar cell). Possibly, this is due to the two holes, highlighted by the red dashed boxes inside the micro-dot and likely down to Mo layer, which cause a shunt path between front and back contact layers. In contrast, Figure 3.12e shows a group of three sister micro solar cells where the surrounding CIGSe on the SiO_2 was removed, which led to the deposition of the buffer and window layers directly on SiO_2. In this configuration, the scribing of the buffer and window layers, directly on SiO_2, is ineffective and leaves some debris, as highlighted with red

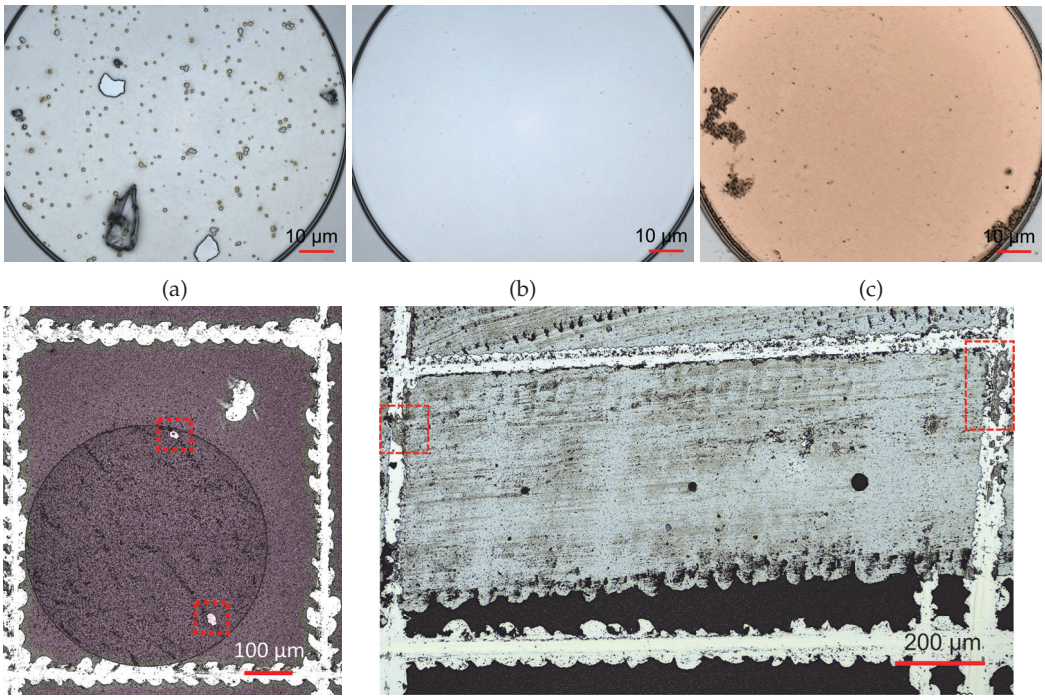

Figure 3.12: CLSM optical images of a micro-dot structure: a) before cleaning, b) after cleaning and c) after electrodeposition of a Cu layer. Region inside the circular micro-dot is the exposed Mo and the Cu layer respectively, whereas region outside is the SiO_2 layer. d) CLSM optical image of a finished CIGSe micro solar cell after scribing (white lines). Red dashed boxes highlight two holes in the CIGSe layer, which may cause the low shunt resistance. The images' brightness and contrast was adjusted to better highlight the micro-dot's delimitations. e) CLSM optical image of three finished CIGSe micro solar cells, connected in parallel, after scribing for electrical isolation. The red dashed squares indicate the regions, within the scribed lines, where potential shunt paths are located.

dashed squares in Figure 3.12e, which creates shunt paths and deteriorates the performance of the devices.

To conclude, the ability of CLSM to quickly capture high quality images of large areas is useful to easily identify and pinpoint regions of interest to investigate surface properties, to distinguish phases, assess quality of film's morphology, etc. Even if the required information cannot be directly measured with CLSM, it can potentially identify issues and thus guide the user to the appropriate method or characterization technique.

3.4 Summary

This chapter presents CLSM as a non-invasive, simple and reliable technique for morphology measurements with a wide range of applications, with particular emphasis on the synthesis of thin films. CLSM was demonstrated to effectively characterize an array of micro-dots, allowing to measure the thickness of each layer, their roughness and assess the evolution of the layers' morphology, at every step of a synthesis process. This enables

both a detailed study at the individual micro-dot level, as well as, a statistical approach to study their behavior at the array level. A new methodology to measure relative composition in sequential processes, from the CLSM morphology maps, has been detailed and verified with EDX. Combining with the phase diagram of the material, it was possible to spatially predict which phases would form at the end of the synthesis process. Therewith, it was demonstrated the impact the precursor's morphology has on the final absorber's spatial composition, and consequently on the formed phases. Furthermore, examples of how optical microscopy can be used to quickly differentiate phases in a material and to assess the quality of substrates and thin films were discussed. In this context, CLSM was shown to also be a diagnostic tool to monitor the process or to rapidly pinpoint possible issues, allowing to intervene at an early stage.

Chapter 4

Discovery of Na-based phase by growing CIGSe on patterned substrates

Having highlighted CLSM as an appropriate characterization technique to investigate arrays of micro-dots, in the previous chapter, the next step is to study the impact of using the patterned substrates for the growth of CIGSe material, as compared to the standard planar configuration. The aim is to discriminate the effects that are due to the choice of using a patterned substrate from those due to the growth process. This knowledge will be essential when investigating the material-efficient synthesis methods, in chapter 5, as these are typically more challenging to control and thus harder to achieve high quality material.

In this context, the PVD co-evaporation synthesis method aligns with the aim of this chapter, as it is reproducible and has synthesized multiple world record level CIGSe absorbers [29, 107, 108]. This comes about due to the well controlled environment in which the material is grown, as well as the particular order of evaporation of the different constituents of CIGSe [57]. In short, this chapter explores the fundamental limitations of growing absorber material onto patterned substrates by decoupling the intricacies of growing high-quality CIGSe, i.e. with a pure phase and state of the art optoelectronic properties, from the contributions due to the substrate. Indeed, a critical aspect for CIGSe grown on Mo, the back contact substrate of choice, is the back surface recombination that can cause a severe drop in V_{OC} and thus limit the PCE [109]. To reduce back surface recombination, either a Ga gradient across the CIGSe absorber or the addition of a passivation layer have been put forward [57]. An example of the latter is the development of a passivation layer with small openings to form point-like contacts, which minimize the area of back contact with the absorber, leading to lower voltage losses [109]. Typically, dielectric layers like aluminum oxide (Al_2O_3), silicon oxide (SiO_2) or hydrogenated silicon nitride (SiN_x:H) are used as passivation layers [109, 110], as they are considered ideal substrates, i.e. lead to less interface defects. The patterned substrates investigated in this work, presented in section 2.1.1 of chapter 2, share a similar configuration as the above

described point-like contacts, although with different dimensions. Thus, comparable passivation effects are expected when growing CIGSe on the patterned substrates, in terms of voltage losses. Furthermore, CIGSe growth studies have shown that the diffusion of dopants, like Na, is beneficial for the solar cell's performance [111, 112]. These dopants originate from the underlying substrate, typically from the soda lime glass underneath the Mo layer. However, these studies do not consider the impact that the patterned dielectric layers have on the diffusion of dopants, given that they also act as diffusion blocking layers [113, 114]. Thus, it is of interest to investigate how the patterned substrates, used in this work, impact the diffusion of dopants during the synthesis of high-quality CIGSe. For comparison purposes, the same growth process and analysis are also performed on absorbers grown on conventional, unpatterned, substrates. In this case, the resulting solar cells have achieved PCEs of 13 % consistently and without particular post-deposition optimization [56].

In the present chapter, the questions that will be addressed are in section 4.1, whether the SiO_2 patterned substrates interfere with the growth of the CIGSe absorber and what is their impact on the CIGSe's morphology and optoelectronic performance. In section 4.2, three methods to circumvent the found impacts are explored. Lastly, in section 4.3, a comparison between the co-evaporation method and the sputtering synthesis route is made to investigate the impact of the synthesis method. To have an overview of the synthesis routes discussed in this chapter, the reader can refer to the summary schematics (Figure 2.6) shown in chapter 2.

4.1 Diffusion in co-evaporated absorbers

4.1.1 Formation of secondary phase due to patterned substrate

The high-quality CIGSe absorbers were grown with a three-stage co-evaporation process in a PVD chamber at 580 °C [56]. The target thickness of the CIGSe absorber was 1 µm, to facilitate the distinction between the material grown inside the 2 µm deep SiO_2 holes and that grown directly on SiO_2, while retaining a thick enough absorber to absorb most (95%) of the incident solar spectrum [115]. A cross-sectional schematic of the resulting configuration is shown in Figure 4.2a.

Morphology analysis

Before addressing the morphology of the CIGSe grown on the patterned substrate, it is of interest to observe the morphology of the reference sample, that is, CIGSe grown on the unpatterned Mo substrate. Given the novelty of using CLSM to characterize the morphology of CIGSe, Figure 4.1 shows an SEM image and a CLSM optical image, respectively, of the surface morphology of the same CIGSe absorber layer.

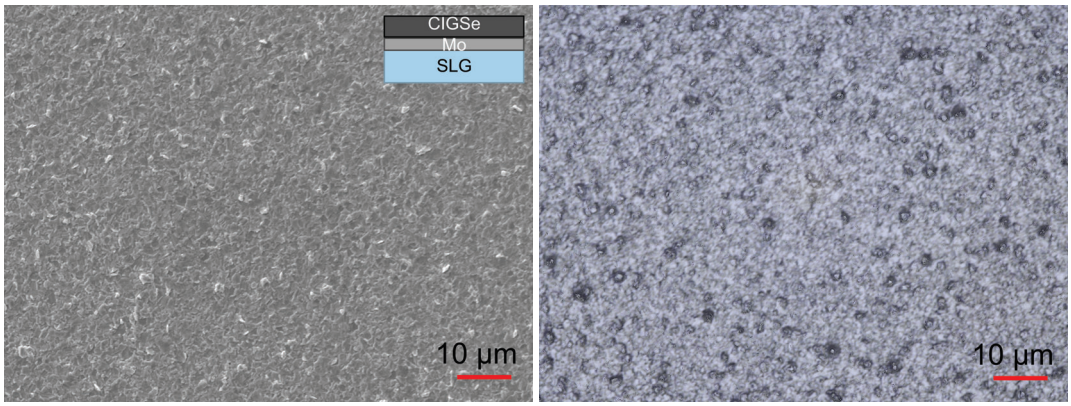

(a) (b)

Figure 4.1: a) SEM image of the surface morphology of the reference CIGSe absorber. Image acquired with an acceleration voltage of 20 kV. A schematics of the cross-section of the sample is shown as inset. b) CLSM optical image of the same reference absorber but in a different location than a).

The techniques show a similar morphology, that is, a homogeneous granular surface. The optical image shows, in addition, the color of the granular phase to be grey, which was already associated with CIGSe in chapter 3 and is also confirmed here.

The patterned substrates used for this analysis contain three regions of interest, on which CIGSe was grown, that are highlighted in Figure 4.2b: (I) arrays of micro-dots with diameters ranging from 500 µm to 10 µm. Note that the micro-dots with diameters below 100 µm are not distinguishable at this scale. (II) SiO_2 matrix, which accounts for most of the area of the substrate. (III) Large area of exposed Mo located at the corner of the substrate. The different regions can also be distinguished by the CIGSe layer's color. To investigate whether the morphology, at the microscopic level, also differs from one region to the other, CLSM optical images of the respective locations are shown in Figures 4.2c-f.

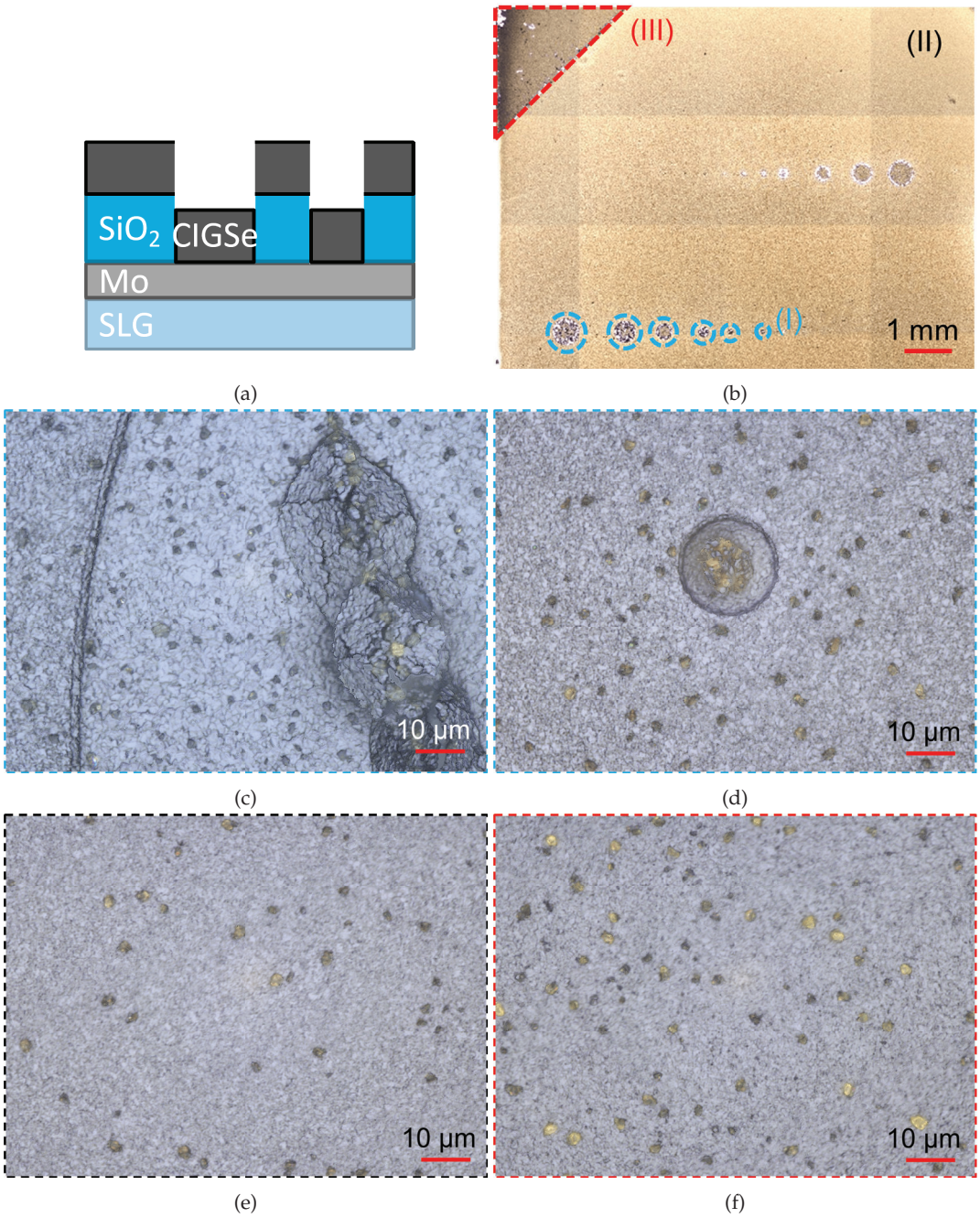

Figure 4.2: a) Cross-sectional schematic representation of the CIGSe absorber (along region I) deposited on the patterned substrate. b) Optical image of the three regions of interest of the patterned substrate after CIGSe deposition. Region I (in blue) corresponds to the micro-dots, region II (in black) to the CIGSe grown on SiO_2 and region III (in red) to the CIGSe grown on Mo at the corner of the substrate. CLSM optical images of the film's morphology at the microscopic level in: c) and d) region I, e) region II and f) region III.

Looking at the film's morphology, the typical grey polycrystalline morphology of CIGSe is observed in all three regions. Surprisingly, a secondary phase, with an appearance of yellow crystals, co-exists with the main phase in the different regions. Focusing on the material grown inside the micro-dots, in region (I), in addition to the CIGSe phase

and the yellow phase, the film also shows cracks and blisters. As an example, in Figure 4.2c, a blister is visible on the right side of the image, near the edge of the micro-dot (curved line along the left side of the image). This implies a poor film adhesion to the Mo layer underneath. Interestingly, a particularly high density of yellow phases is located along the blister and the cracks. Alternatively to the blisters, larger yellow structures have also been observed inside the micro-dots, as shown in Figure 4.2d. This was observed consistently inside the micro-dots independently of their diameter. For comparison purposes, Figures 4.2e and f show the morphology of the film grown on the SiO_2 matrix and on the corner large area Mo, respectively. In both regions (II and III), the CIGSe phase and the yellow phases are observed, with the film grown on Mo, showing a higher density of yellow phases. Nevertheless, the largest yellow phases were found inside the micro-dots, suggesting that the source of formation of these secondary phases could originate from the micro-dots. Also, neither blisters nor peeling of the CIGSe from the SiO_2 were observed, contrarily to the CIGSe grown on Mo at the corner of the sample (not shown). Furthermore, the formation of yellow phases is particular to the patterned substrate, as the morphology of the film grown on the unpatterned substrate, in Figure 4.1, shows only the grey polycrystalline CIGSe phase.

In literature, the formation of a secondary phase, with similar dimensions and geometries as the yellow phase, was reported on unpatterned substrates for different CIGSe evaporation processes, all of which used a NaF precursor layer [116–119]. In fact, Lee et al. report an optical image where yellow microstructures are visible alongside CIGSe after a three-stage process with a NaF precursor layer [117]. Nevertheless, the above mentioned studies do not agree on a particular phase, but rather discuss the formation of a (Cu,Na)–(In,Ga)–Se compound.

Composition analysis

A first approach to identify our yellow phase is to measure its composition. For this, EDX analysis is performed at an acceleration voltage of 10 kV in order to be more surface sensitive and avoid signal from a possible phase underneath the yellow phase. To easily identify the location of the yellow phase on the SEM image (see Figure 4.3b), an optical image from CLSM was used as reference (Figure 4.3a). Four EDX point spectra were measured to distinguish between: (1) CIGSe phase grown on the SiO_2 matrix, (2) CIGSe grown inside the micro-dot, directly on Mo, (3) large yellow phase inside the micro-dot and (4) small yellow phase located outside the micro-dot. The locations where the spectra were acquired are indicated by numbered dots shown on the SEM and CLSM images. The corresponding energy spectra are plotted in Figure 4.3c, where the two spectra, pertinent to the yellow phases, were shifted upwards for ease of comparison. The identified peaks have been assigned according to their respective elements' electronic transitions [64].

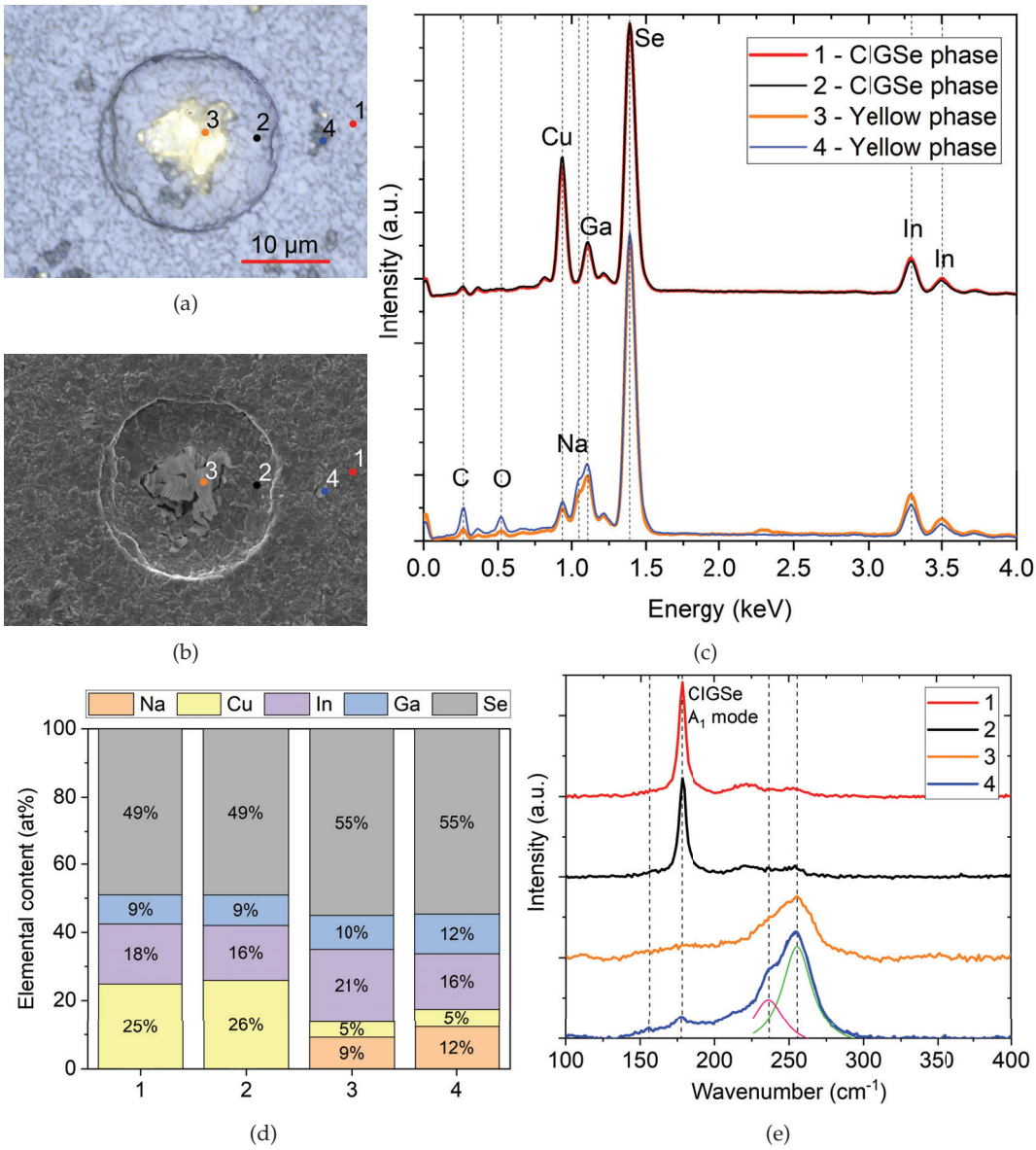

Figure 4.3: a) CLSM optical image and b) SEM image of the region from which the EDX spectra in c) were acquired. The precise locations are indicated with numbered circles and color-coded to match the corresponding EDX spectra and label. c) EDX spectra measured from the corresponding locations at 10 kV. The two spectra from the CIGSe phase (1 and 2) were shifted upwards and are overlapped to show their similarity. The bottom two spectra (3 and 4) are related to the secondary phase. The relevant peaks were labelled with the corresponding elements. d) Elemental composition distribution, extracted from the EDX spectra, for the four different regions. The error expected for elemental content is in the range of 1-2 at%. e) Raman spectra measured from the same four regions.

The spectra taken from the CIGSe phases inside (2) and outside (1) the micro-dot are indistinguishable and show the characteristic x-ray peaks of Cu, In, Ga and Se. This suggests that the grown phase is identical in both regions. In the case of the yellow phases, the spectra are also similar inside (3) and outside (4) the micro-dots with only slight variations in the peaks' intensity. Here, the main identified peaks are those of O, Na, Cu, In,

Ga and Se. The differences with the CIGSe spectra are the appearance of the Na $K\alpha_{1,2}$ and the O $K\alpha_1$ lines in addition to the pronounced decrease in intensity of the Cu $L\alpha_1$ peak. Note that the increase from the C signal could be associated with the extended exposure to the electron beam, given that the measurements were performed in the same chronological order as their labeling [120]. Given the controlled environment in the deposition chamber, the origin of O is likely from the exposure of the sample to ambient air, whereas the surprisingly high Na content ($\sim$10 at%), within the yellow phases, is hypothesized to come from the soda lime glass by diffusion during the evaporation process at 580 °C. The analysis of this abnormal diffusion of Na will be carried out in the next section, after further characterization of the Na-based secondary phase.

To illustrate the changes in elemental composition between the two phases, Figure 4.3d shows the relative atomic content of the constituents of the two phases in the four discussed regions. As mentioned before, within the same phase, little to no changes are observed. However, when comparing the two phases, the relative composition differs considerably. In fact, the Cu(In,Ga)Se_2 phase (regions 1 and 2) shows indeed the 1:1:2 ratio (Cu:III:Se measured 25:27:49 for region 1), whereas the yellow phases (regions 3 and 4) clearly show a different composition ratio. One hypothesis to justify the composition measured from regions 3 and 4, is to assume that the measured Cu originates from an underlying CIGSe 1:1:2 phase (measured 5:5:10 for region 3) and that the yellow phases contain no Cu, i.e., Cu is completely substituted by Na in the chalcopyrite structure. In this case, the yellow phases have a composition ratio close to 1:3:5 (measured 9:26:45 for region 3). The results that support the assumption of Na substituting Cu are discussed in the following paragraphs. Thus, the yellow phases would correspond to the OVC phase Na(In,Ga)$_3Se_5$. To further investigate the possible phases that make up these yellow phases, Raman spectroscopy is measured on the same four regions described above and the resulting spectra are plotted in Figure 4.3e. The CIGSe phase, inside (2) and outside (1) the micro-dot, displays the typical CIGSe A_1 mode at 177.7 cm^{-1} [101]. In both regions (3) and (4), the yellow phases show a broad peak which was fitted by two Gaussian functions centered at 236.3 cm^{-1} and 255.6 cm^{-1}. These two peaks are also characteristic of the E modes of $CuIn_3Se_5$ and $CuGa_3Se_5$, respectively [121] or more generally associated to In-Se and Ga-Se phases [122]. This common point between these phases could suggest that the E modes are unaffected by the group I cation, in the OVC phase. However, the main A_1 modes of the OVC phases ($CuIn_3Se_5$ and $CuGa_3Se_5$) are expected at 154 cm^{-1} and 166 cm^{-1}, respectively [121], which were not present in our case. Indeed, since the A_1 mode is associated with the Se atoms' vibration [123], which are bonded to the group I cations (Cu or Na), its frequency is expected to change depending on which cation is present. EDX analysis does suggest a major substitution of Cu by Na in the yellow phases, which could explain the absence of the A_1 mode. This further suggests the yellow phases to correspond to the OVC phase Na(In,Ga)$_3Se_5$. Note that in region (4), the small signal from the A_1 mode of CIGSe is visible, however it is likely arising from the underlying CIGSe phase.

The enhanced diffusion of Na in the patterned substrates was observed to cause a very poor adhesion of CIGSe to Mo, leading to blisters and peeling inside the micro-dots. This has unveiled Na-based phases located directly on the Mo/$MoSe_2$ layer, which suggests that they are also present in the bulk of the film. Additionally, it allows to characterize these Na-rich phases without the signal from the CIGSe phase, as shown in Figure 4.4. Note that the color of the Na-based phases has changed to orange with time, i.e., with air exposure.

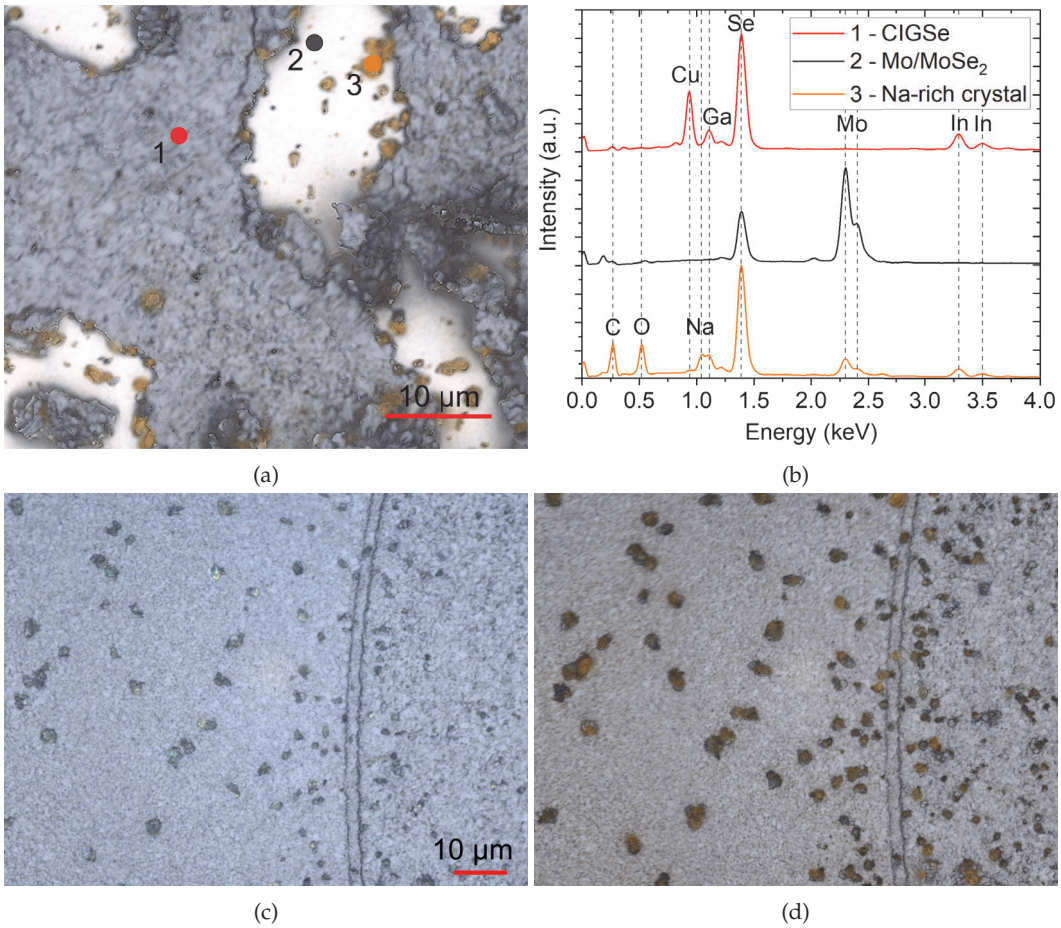

Figure 4.4: a) CLSM optical image of the region, inside a 500 µm micro-dot, from which the EDX spectra in b) were acquired. The precise locations are indicated with numbered circles and color-coded to match the corresponding EDX spectra and label. b) EDX spectra measured from the corresponding locations at 10 kV. The relevant peaks were labelled with the corresponding elements. CLSM optical image of the periphery of a micro-dot measured c) directly after and d) six months after the CIGSe deposition. The change in color of the Na-based phases and the CIGSe phase are attributed to oxidation.

Figure 4.4a is a CLSM optical image of a region, inside a 500 µm micro-dot, where partial delamination of the CIGSe film took place and exposed both the Mo/$MoSe_2$ underlying layer (2) and some isolated Na-based phases (3). The spectrum acquired from the Na-rich phase (3) highlights the presence of C, O, Na, In, Ga and Se, however the Cu peak is absent. Indeed, when measuring an isolated Na-rich crystal, no Cu signal is measured, suggesting that Na completely substitutes Cu in the CIGSe structure [124]. The C

and O peaks are clearly more pronounced comparatively to the other two investigated regions, which suggests a higher contamination due to air exposure. This could also explain the observed change in color of the phase and renders the composition analysis more complicated. The Mo/$MoSe_2$ layer shows only the peaks associated with Mo and Se, whereas the spectrum measured on the CIGSe film (1), puts forward the presence of Cu, In, Ga and Se, as expected.

The effect of oxidation can clearly be seen by comparing the same region of the sample at different times. Figure 4.4c shows the periphery of a micro-dot freshly measured after deposition, whereas 4.4d presents the same region after six months. An attentive comparison of the two images infers that the density of Na-based phases remained the same, however the grains grew in diameter by 20 ± 10 % on average, possibly due to the incorporation of C and O in the grains with time. Studies on the influence of Na during the growth of CIGSe have shown that large concentrations of Na lead to the formation of sodium-polyselenide Na_2Se_x precipitates, which oxidize in contact with humid air to form Na_2SeO_3 and Na_2CO_3 [125, 126]. However, neither the measured EDX ratios nor the Raman literature database [127–129] match the above mentioned phases and are thus discarded here.

Structural analysis

Finally, to attempt to determine the crystallographic structure of the yellow phases, x-ray and electron diffraction techniques were employed. Given the relatively small size of the Na-based phases comparatively to the CIGSe phase, the x-ray diffractograms only detected the latter phase. Thus, the focus is put on the Kikuchi lines, from the CIGSe and the Na-based phases, obtained by EBSD and shown in Figure 4.5. Additionally, an indexing overlay for the theoretical tetragonal crystal structure of $CuInSe_2$ is also presented to identify the matching planes.

For the CIGSe phase, in Figures 4.5a and b, the Kikuchi lines are sharp and the indexing to the chalcopyrite structure shows a good agreement with the measured planes. Regarding the EBSD pattern from the Na-based phase, in Figures 4.5c and d, the Kikuchi lines are fainter, possibly relating to a lower crystallinity. Nevertheless, the indexing to the chalcopyrite structure seems to also agree, albeit to a relatively lower extent than for the CIGSe phase. The poorer agreement could be due to the lattice distortion caused by the different atomic size of Na comparatively to Cu. This suggests that the Na-based secondary phase could in fact have a chalcopyrite structure and thus be identified as $Na(In,Ga)_3Se_5$.

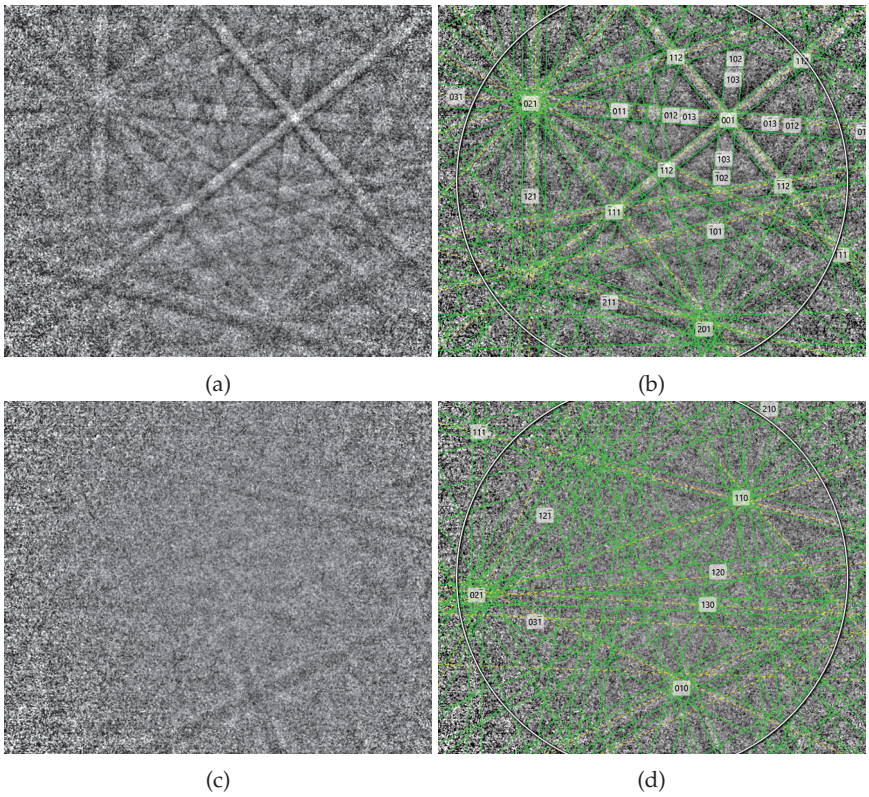

Figure 4.5: a) Raw and b) indexed EBSD Kikuchi pattern recorded from the CIGSe phase. c) Raw and d) indexed EBSD Kikuchi pattern recorded from the Na-rich phases on Mo/$MoSe_2$. In both cases, indexation was done based on the chalcopyrite tetragonal structure. Green lines correspond to the simulated Kikuchi bands expected from the chalcopyrite tetragonal structure and the yellow dashed lines are the Kikuchi lines identified experimentally.

To sum up, the formation of a Na-enriched secondary phase was put forward when growing CIGSe specifically on the patterned substrates. Chemical and structural analysis suggest the secondary phase corresponds to $Na(In,Ga)_3Se_5$.

4.1.2 Enhanced Na diffusion due to patterned substrates

Having identified the yellow phases, the origin of the high Na content is explored in the current section. As hypothesized previously, the relatively high Na content is coming from the soda lime glass by diffusion during the evaporation process at 580 °C, driven by the concentration gradient. Traditionally, for unpatterned CIGSe films, it is known that the Na contained in the soda lime glass diffuses through the columnar structured Mo layer [130] and is incorporated within the CIGSe phase [131]. In these cases, the concentration of Na is spatially homogeneous and below 1 at%, which is below the EDX detection limit. Thus, the low Na density within CIGSe, in the standard substrate case, does not form the yellow crystals secondary phase, as observed previously by CLSM and reminded in Figure 4.6a. A schematic representation of the Na diffusion in a standard substrate is depicted in Figure 4.6c.

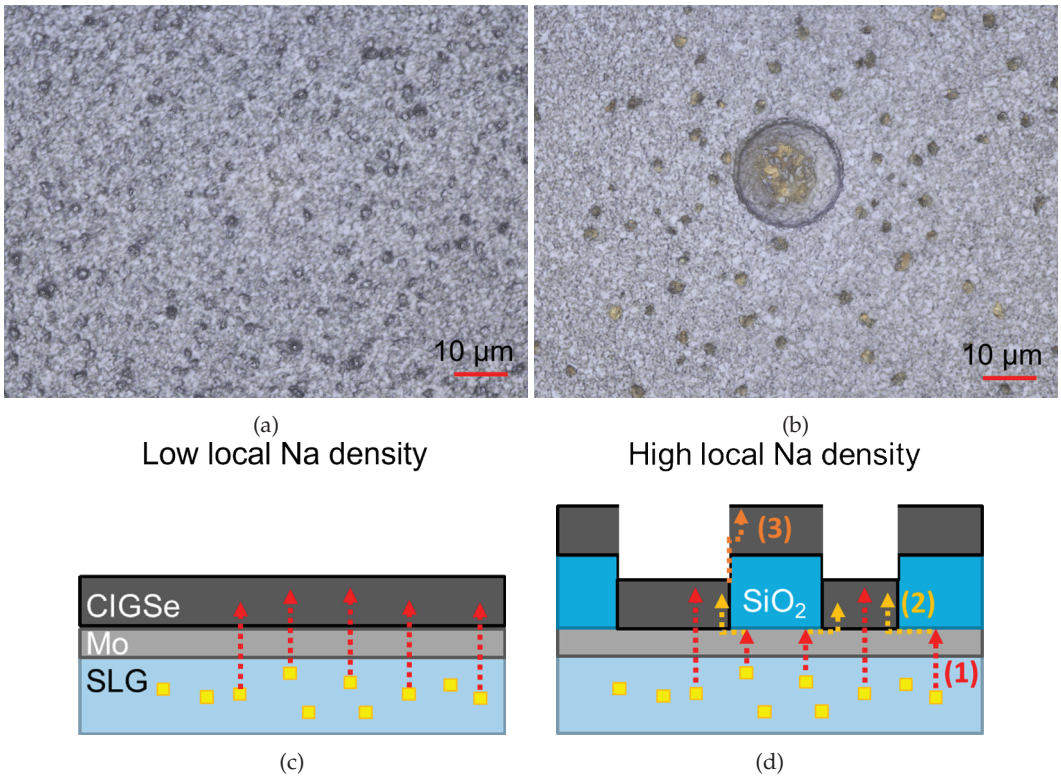

Figure 4.6: CLSM optical image of the CIGSe surface morphology grown on a) an unpatterned substrate (repeated from Figure 4.1b) and b) a patterned substrate (repeated from Figure 4.2d). Simplified schematic representation of a cross-sectional view of the diffusion of Na, during a high-temperature synthesis process, on c) a conventional unpatterned substrate and d) an SiO_2 patterned substrate. Red dashed arrow (1) represents the typical diffusion of Na driven by the concentration gradient, orange dashed arrow (2) depicts the redirection of Na diffusion induced by the diffusion barrier layer and dark orange dashed arrow (3) illustrates the access path of Na to the CIGSe grown on SiO_2. Dimensions are not to scale.

With the patterned substrates, a locally high concentration of Na ([Na]/[Cu]≈2) was observed, where the yellow crystals formed. Furthermore, the region with the largest yellow crystals was inside the micro-dots, as reminded in Figure 4.6b, which suggests this region to be the access path for Na diffusion, from the soda lime glass. However, assuming a similar diffusion path as for the standard substrate does not explain the observed excess of Na content. Instead, taking into account that the SiO_2 matrix is a diffusion barrier, an important Na content is hypothesized to accumulate at the Mo/SiO_2 interface, which builds up a Na concentration gradient between the Mo/SiO_2 interface and the Mo/CIGSe interface. This results in a second diffusion path which drives the Na content at the Mo/SiO_2 interface towards the CIGSe grown inside the holes of the SiO_2 matrix, i.e. the micro-dots. Thus, as illustrated in Figure 4.6d, a high enough local Na density would be supplied, to the CIGSe phase, to form a Na-based secondary phase.

As for the Na present in the smaller yellow crystals, located above the SiO_2 layer, it is hypothesized to have diffused through the CIGSe phase itself to migrate outside of the micro-dots region. In fact, the adsorption profile of the elements in the PVD chamber is

spherically symmetric, thus the film grows not only perpendicular to the Mo layer but also along the side walls of the micro-dots. This creates a diffusion path for Na to access the fraction of film grown directly on the SiO_2, that is, outside of the micro-dots. To be more precise, Na is known to preferentially diffuse in CIGSe through grain boundaries and Cu-vacancies [131], which should be present in the film given its polycrystalline aspect and Cu-poor composition, i.e. CGI = 0.92 ± 0.05.

Conceding that Na diffuses through the micro-dots, it would be expected to measure a Na concentration with a typical point-source diffusion distribution, i.e. a radially symmetric 2D Gaussian, around the micro-dots. To investigate this hypothesis, EDX elemental mapping was performed around a micro-dot. Figure 4.7 presents a secondary electron image of the investigated region and the elemental maps of Na and Cu, which are the main signatures of the two relevant phases. To compare with the unpatterned substrate case, a similar EDX analysis is performed on the corresponding CIGSe absorber.

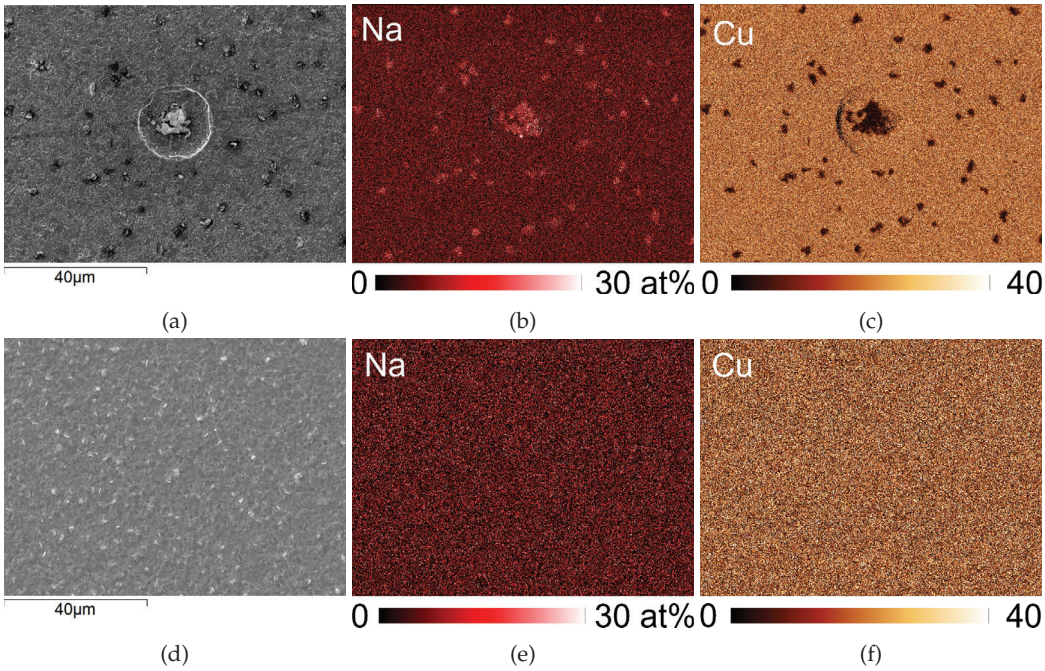

Figure 4.7: a) Zoom-out SEM image, of the same micro-dot region as in Figure 4.3a, from which EDX elemental maps were acquired. Corresponding EDX elemental distribution maps for b) Na and c) Cu acquired at 10 kV. d) SEM image of the CIGSe surface morphology grown on the unpatterned substrate. Corresponding EDX elemental distribution maps for e) Na and f) Cu.

Using the electron image as location reference, the distribution of Na does not follow the anticipated Gaussian behavior around the micro-dot, but rather shows a seemingly random distribution of microscopic sized regions with higher Na content. These correspond to the locally formed yellow crystals. Note that the non-zero homogeneous background signal is artificially created by the analysis software, as inspection of the respective spectra shows no Na peak is measured, just like in Figure 4.3. This means that Na only aggregates in particular nucleation sites to form the yellow crystals, otherwise it

is below EDX detection limit. When discussing the Na-enriched phases in unpatterned substrates, Hariskos and Powalla suggest that the formation of the Na phases is explained by the limited solubility of Na in CIGSe and can be interpreted as a "phase separation" from the chalcopyrite phase [132]. This result could be a reason for having a random distribution of Na yellow crystals, instead of a Gaussian distribution. For the unpatterned substrate, both elemental maps are spatially homogeneous as expected and no Na is detected. This confirms that the peculiar distribution of Na is particular to the patterned substrates.

Comparing the elemental maps of Na and Cu, in Figures 4.7b and c, highlights the two elements to be complementary over a range of 100 µm, which implies that Na diffused at least this distance during synthesis. In fact, although the Na-based yellow crystals are mainly present inside the micro-dots, they were also found throughout the sample, as pointed out previously in Figure 4.2. Supposing the process is solely driven by diffusion through the CIGSe phase, the average square radius of spreading $< r^2 >$ is given by a two-dimensional random walk and thus can be calculated with equation 4.1 [133]. Therewith, one can estimate the distance $< r >$, from the source, at which no more Na-based crystals should be found. The diffusion time t is given by the growth time 30 min, whereas the bulk diffusion coefficient D of Na in CIGSe at 580 °C was estimated to $7.4 \cdot 10^{-10}$ $cm^2 s^{-1}$ from an exponential fit to similar data found in the following references [131, 134].

$$< r^2 >= 4D(T)t \tag{4.1}$$

Thus, the estimated distance $< r >$ travelled by Na, during the synthesis process, is 23 µm. However, yellow crystals were found at much higher distances from the possible sources of Na (micro-dots, large area exposed Mo at sample's corner and sample's edge). Figure 4.8 shows CLSM optical images of the film's morphology taken at different distances from the possible Na sources, as indicated in Figure 4.8a.

Figure 4.8b is measured 0.5 mm away from the closest micro-dot and the density of yellow crystals found is comparable to that observed outside of a micro-dot. This already discards diffusion through the bulk CIGSe phase as an argument, as it could only justify 23 µm of spreading. Moving further away, Figure 4.8c is acquired 3 mm from the closest micro-dot and despite the density of yellow crystals not changing much, their size seems to reduce. Finally, in Figure 4.8d, 5 mm away from the micro-dot, and roughly 2 mm from the edge of the sample, little to no yellow crystals are present. This gives an order of magnitude for the spreading distance of Na and indicates that the edge of the sample is not a major source of Na. Possible explanations would be either: (i) diffusion of Na along the surface of CIGSe film or (ii) the formation of a Na, elemental or compound, gas phase that could diffuse in vacuum and then nucleate and form the yellow crystals away from the micro-dots. This could be possible due to the synthesis high temperature and low pressure ($\sim 10^{-9}$ mbar) inside the PVD chamber. Although it is not possible to

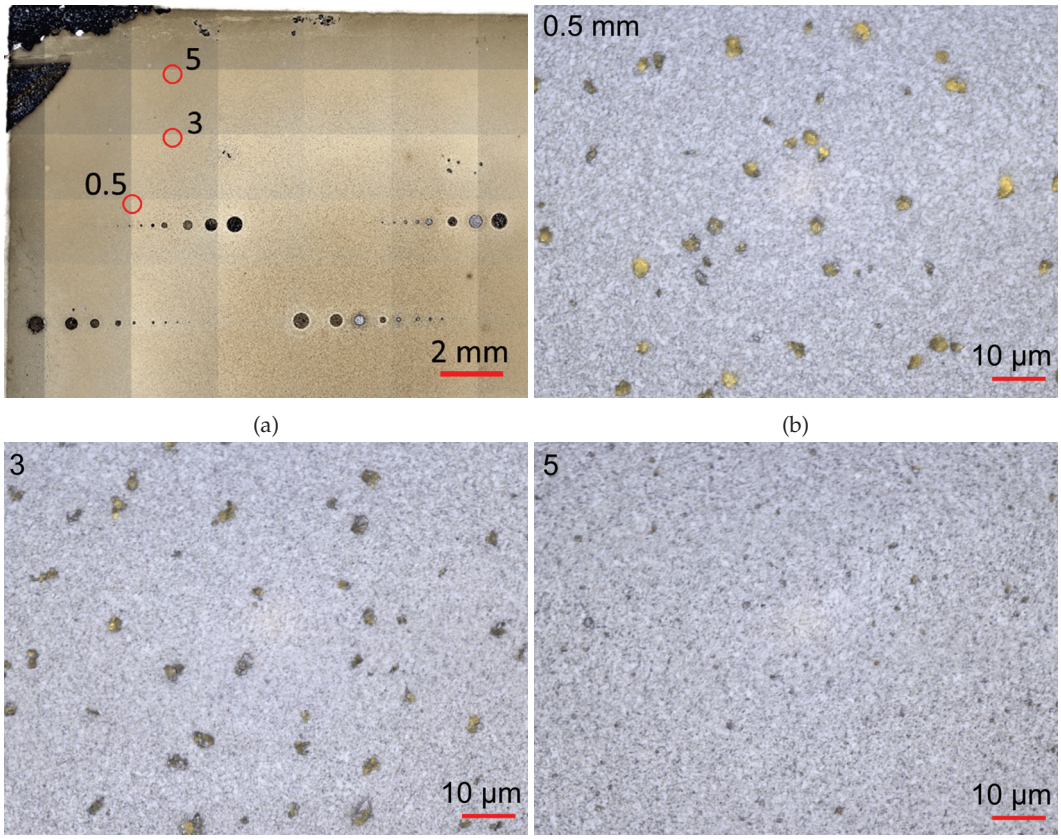

Figure 4.8: a) Optical image showing a macroscopic overview of the CIGSe absorber grown on the patterned substrate and the approximate locations of the measured images shown in b), c) and d). The red circles indicate the measurement location and their labels correspond to the distance, in mm, from the micro-dot array, i.e. the source of Na. CLSM optical images of the absorber's morphology at the microscopic level: b) 0.5 mm, c) 3 mm and d) 5 mm away from the micro-dot array.

distinguish between the two cases, both align with our observations. In both situations, the diffusion coefficient is orders of magnitude higher than bulk diffusion. In fact, studies have estimated the surface diffusion coefficient on many distinct systems, like Na diffusing on a defective phosphorus monolayer [135] or the diffusion of elements on substrates with different crystallographic orientations [136]. The reported surface diffusion coefficients were typically around 10^{-4} cm^2s^{-1}. Extrapolating to our system, such a surface diffusion coefficient would indeed justify the formation of Na-based yellow crystals millimeters away from the micro-dots. In fact, the higher diffusion coefficients would also give enough time for Na to diffuse and nucleate only at preferential nucleation sites, which in turn would result in a random distribution of yellow crystals at the surface of the film, as was in fact observed.

To summarize, the use of patterned substrates, which are also diffusion barriers, leads to locally enhanced diffusion of dopants from the substrate, which can reach distances in the mm-range away from its source.

4.1.3 Impact of Na diffusion

The enhanced diffusion of Na on the patterned substrates has several implications for the synthesis of CIGSe. As discussed in the previous sections, the formation of secondary phases appears to be associated with the delamination of the CIGSe layer, rendering it unusable. On the same note, the enhanced diffusion of Na seems to reduce the adhesion between the Mo and the CIGSe layer, causing fissures and blisters, as was seen in Figures 4.2 and 4.4. These likely originate from the extra strain due to the diffusion of Na and lead to delamination of the film or additional interface defects which deteriorate the CIGSe absorber optoelectronic quality. In fact, even if some of the micro-dots did not show fissures nor blisters after growth, their weak adhesion to Mo is manifested after the CdS buffer layer deposition, where the CIGSe film is partly or totally delaminated into the solution, as shown in Figure 4.9 with the respective optical images and height maps.

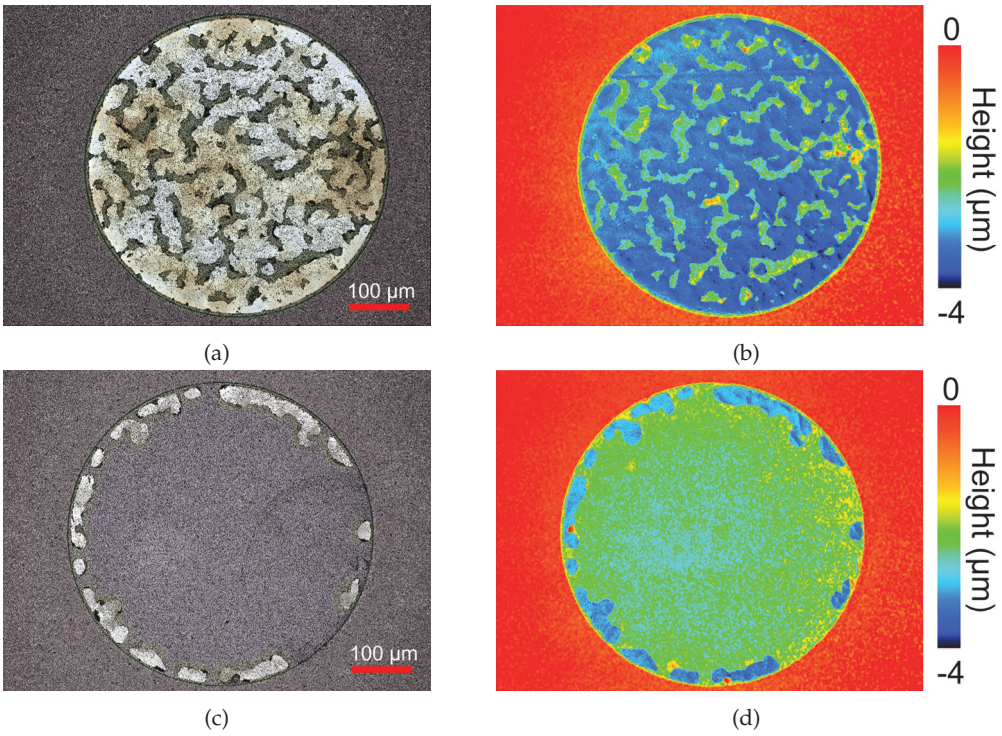

Figure 4.9: a) CLSM optical image of a micro-dot from which the CIGSe absorber layer mostly delaminated after the deposition of the CdS buffer layer. b) CLSM height map corresponding to the optical image in a). c) CLSM optical image of a sister micro-dot from which the CIGSe layer partly delaminated after the CdS deposition. d) CLSM height map corresponding to the optical image in c).

The incorporation of Na in the CIGSe phase during synthesis has been associated with a controversial change in grain size, depending on the synthesis process [126, 137]. In fact, an increase was observed for co-evaporation [138, 139] and sequential process [140, 141], whereas a decrease was reported for three-stage co-evaporated films [142–144]. Figures 4.10a and b show the polycrystalline morphology of CIGSe near the periphery of two micro-dots (right side of the images), with different diameters, from the same array.

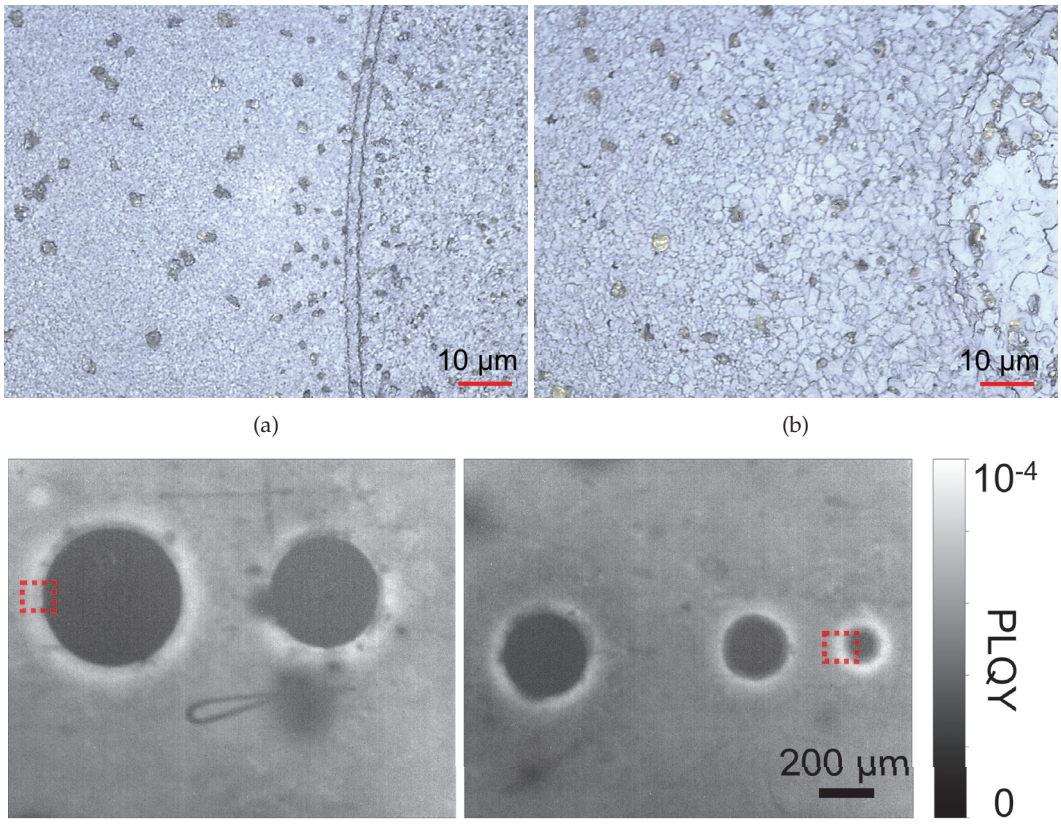

Figure 4.10: a) and b) are CLSM optical images showing the morphology of the CIGSe absorber at the periphery of two micro-dots from the same array. A fraction of the micro-dots can be identified on the right side of the images, with their periphery visible through two vertically curved lines. The contrast, brightness and sharpness of the images were adjusted to highlight the delimitations of the grains. c) Panchromatic PLQY maps of two regions containing five micro-dots in total. The red dashed squares indicate the approximate location of the CLSM optical images in a) - left square and b) - right square.

On the one hand, in Figure 4.10a, the grain size (1.4 ± 0.2 µm) does not seem to change with radial distance from the micro-dot. On the other hand, in Figure 4.10b, the grain size does show a radial dependence, as the grains located close to the micro-dot, i.e. the source of Na, have an average diameter of 2.3 ± 0.4 µm whereas further away grains are smaller (1.6 ± 0.4 µm). Also, no particular trend between grain size and micro-dot diameter was observed. This suggests that either the distribution of Na in the soda lime glass is inhomogeneous or the Mo in each micro-dot is different enough to cause a different flux of Na. Regarding the latter hypothesis, it is worth mentioning that, in this case, no particular cleaning procedure was applied to the substrate prior to the CIGSe deposition. This led to a few micro-dots having an outlier grain structure (like in Figure 4.10b). Introducing a cleaning procedure targeted for removing organics and oxides (for instance MoO_3, which is known to influence Na diffusion [131]) resulted in grain structures similar to Figure 4.10a in all micro-dots. This could imply that the controversial change in grain morphology is also determined by the surface properties of the Mo layer. Nevertheless,

in both hypothesis, it is different fluxes of Na, through different micro-dots, that affect the grain structure of the resulting CIGSe during synthesis.

Another effect of Na incorporation in CIGSe is the increase in radiative photoluminescence due to the passivation of defects and larger hole concentration induced by Na doping [126, 145]. This would be visible in a mapping of photoluminescence quantum yield (PLQY), as shown in Figure 4.10c. The approximate location of measurement of the optical images, in Figures 4.10a and b, is indicated in the PLQY map by red dashed squares. For all measured micro-dots, the PLQY maps show an aura, surrounding each micro-dot, with a higher PLQY which decreases with radial distance from the micro-dot. The width of the aura is roughly 50 µm, which matches the width of the region with large grains in Figure 4.10b and is on the same order as the bulk diffusion distance of Na (23 µm). Note that the relatively low PLQY inside the micro-dots could be due to an excessively high Na content that led to non-radiative defects [131, 146, 147].

Both the grain size and the photoluminescence radial dependence are examples of effects directly caused by the diffusion of Na and also corroborate with the model describing its diffusion from the soda lime glass through the micro-dots. Despite that, the radial dependence was not observed in the EDX Na map (in Figure 4.7), possibly because the Na content in the CIGSe phase is below EDX's detection resolution, whereas the yellow crystals contain a substantial amount of Na.

In short, the enhanced diffusion of Na, due to the patterned substrate, has both beneficial (assisted grain growth, less non-radiative defects) and detrimental (weak layer adhesion to substrate, inhomogeneous properties) effects on the synthesized CIGSe layer.

To conclude, this section has demonstrated that the SiO_2 patterned substrates interfere with the growth of the CIGSe absorber in that it induces a locally enhanced diffusion of Na through the micro-dots, which causes a poor adhesion of the CIGSe layer to the Mo back contact, leading to the delamination of the latter. Thus, the patterned substrate cannot be used as is to synthesize micro solar cells. Therefore, in the following, methods to circumvent the enhanced diffusion of Na are explored.

4.2 Reduce Na diffusion

In this section, three different approaches are discussed to counter the excessive diffusion of Na in the patterned substrates. First, since diffusion is thermally driven, one possibility is to reduce the temperature of growth during synthesis, therewith reducing the flux of Na from the substrate. Second, given that one diffusion channel for Na is the presence of Cu-vacancies, the growth of CIGSe absorber with a slight excess of Cu is expected to also decrease the flux of Na during growth. Third, a diffusion barrier for Na is introduced between the soda lime glass and the Mo layer. Whenever possible, electronic characterization of the absorbers is performed to assess the quality of the produced films.

4.2.1 Lower synthesis temperature

Morphology analysis

The temperature dependence of the diffusion coefficient follows an Arrhenius equation [148], meaning that the diffusion coefficient decreases exponentially when the temperature is reduced. The synthesis temperature was reduced to 450 °C inspired on the multistage co-evaporation process, demonstrated by Hertwig and co-workers [149], which yielded high quality CIGSe absorbers. Figure 4.11 shows CLSM optical images of the resulting CIGSe absorber's morphology, grown at 450 °C, measured in the three regions of interest within the sample (see Figure 4.2b for details, in blue (I) array of micro-dots, in black (II) SiO_2 matrix and in red (III) large area exposed Mo located at the corner of the substrate).

Starting with the array of micro-dots, in Figures 4.11a and b, the morphology of the film shows the main grey CIGSe phase and, around some micro-dots, a radial distribution of small ($\sim$ 1 µm) $Na(In,Ga)_3Se_5$ yellow crystals can also be distinguished within a distance of $\sim$ 20 µm from the micro-dot (see Figure 4.11b). No blisters were observed, suggesting that the CIGSe has now a better adhesion to the Mo back layer and, by the same token, it corroborates that the peeling of the CIGSe, seen in the high temperature absorber (see Figure 4.4), was caused by the excessive flux of Na through the micro-dots during synthesis. Regarding the film grown on SiO_2 (in Figure 4.11c) and on Mo at the sample's corner (in Figure 4.11d), only the CIGSe phase seems to be present. Note that the distinct texturing of the CIGSe morphology, on these two regions, may be due to the growth happening on distinct underlying layers. In fact, the texture of the CIGSe phases grown on Mo, that is, inside the micro-dots (Figure 4.11a) and at the edge of the sample (Figure 4.11d), are very similar. In all cases, the density of $Na(In,Ga)_3Se_5$ yellow crystals was reduced, although not completely suppressed, implying that the flux of Na from the substrate was lower. As a reference, Figure 4.11e presents the morphology of the CIGSe absorber grown on an unpatterned substrate at 450 °C, during the same process batch as the patterned substrate. Just like for the reference absorber grown at 580 °C, shown in Figure 4.1 and repeated here in Figure 4.11f, no secondary phase is present and the texture of the CIGSe phase is rather similar to those grown on Mo on the patterned substrate.

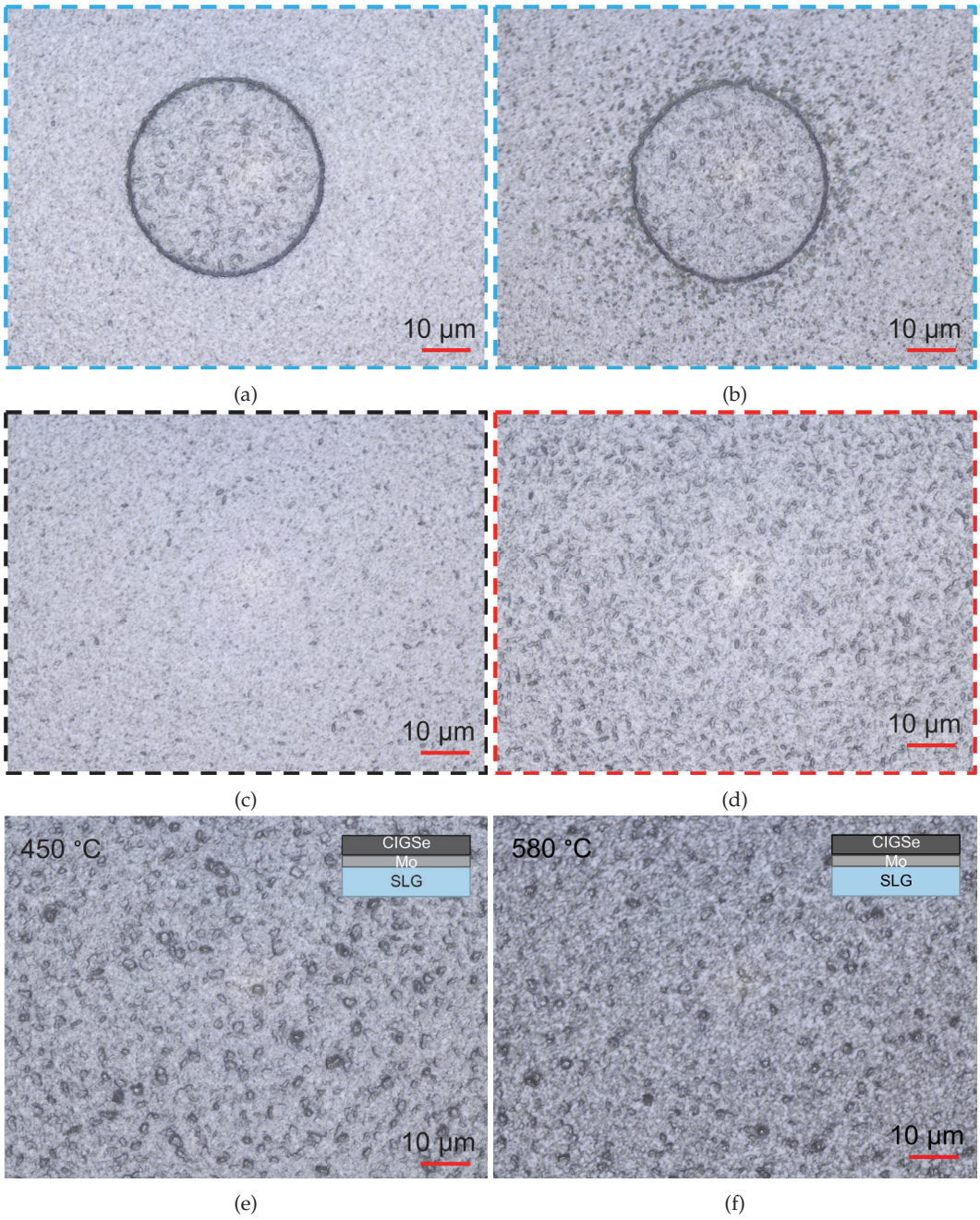

Figure 4.11: CLSM optical images of the CIGSe morphology grown on a) and b) two sister micro-dots, c) the SiO_2 matrix, d) the Mo at the corner of the sample, e) the unpatterned Mo substrate at 450 °C and f) the unpatterned Mo substrate at 580 °C (repeated from Figure 4.1).

Since the morphology of the absorbers, inside the micro-dots, is adhering to the Mo back layer, a CdS buffer layer was deposited to mimic the process of synthesizing solar cells. Here, a 5 wt% KCN treatment for 30 s was performed prior to the buffer deposition. The deposition of the window layers (intrinsic ZnO and Al-doped ZnO) was performed by radio-frequency magnetron sputtering. In principle, this is a baseline process and is

not expected to impact the underlying layers. However, in the case of the patterned substrate, the sputtering process has caused the partial detachment of the CIGSe layer from the Mo back contact, in particular in the micro-dots with larger diameters. To visualize this effect, Figure 4.12 shows optical images of the same array of micro-dots at each stage.

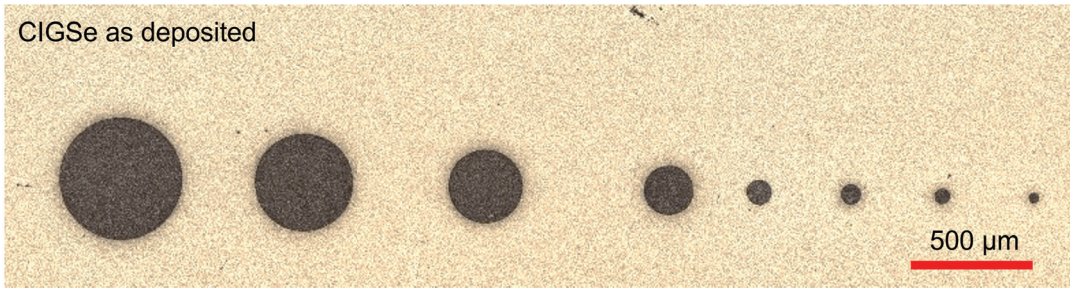

(a)

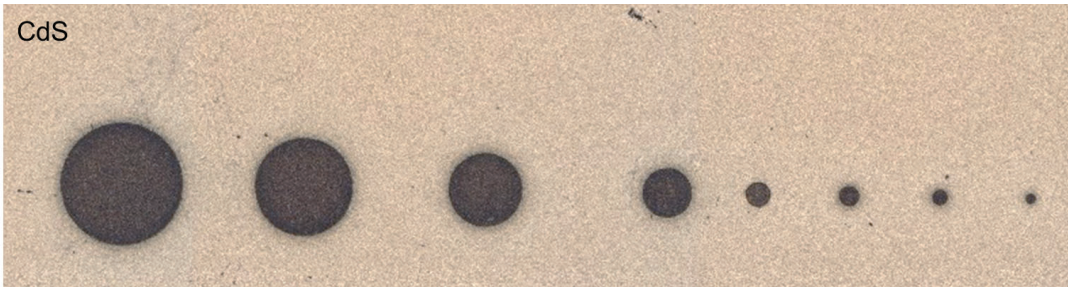

(b)

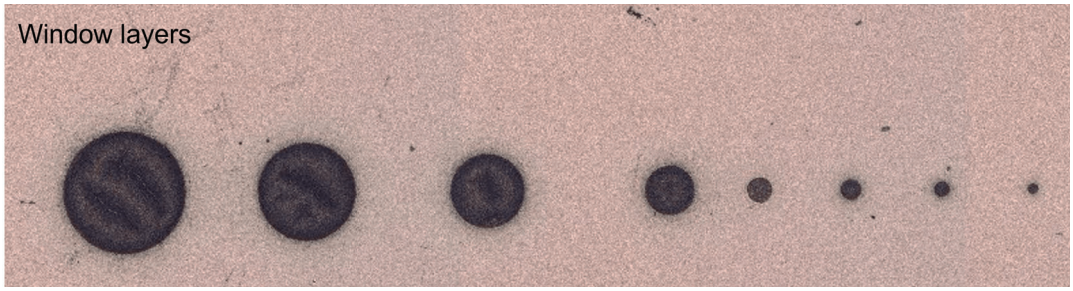

(c)

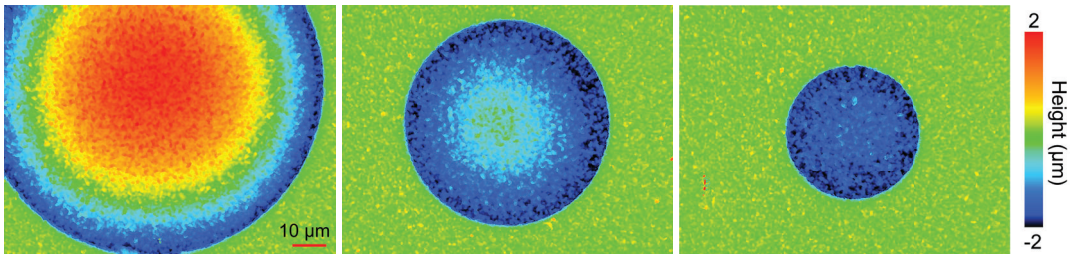

(d) (e) (f)

Figure 4.12: Overview optical images of an array of micro-dots: a) after deposition of CIGSe absorber, b) after deposition of the CdS buffer layer and c) after deposition of the window layers. The brightness and contrast of these three images was adjusted in the same way to highlight the changes in morphology, in particular inside the micro-dots, at each step of the process. CLSM height maps measured after the deposition of the window layers of three micro-dots with diameters of: d) 100 µm, e) 60 µm and f) 40 µm. All height maps share the same scalebar. The CIGSe grown on SiO_2 is used as reference plane (height = 0 µm).

Figures 4.12a and b show the array after the growth of the CIGSe absorber and after the deposition of the CdS buffer layer, respectively. At this point, no major morphological difference is observed between the two images. However, after the sputtering of the window layers (in Figure 4.12c), it is visible that the morphology of the micro-dots, specially with larger diameters, was deformed. This is confirmed by the height maps taken from a selection of micro-dots, shown in Figures 4.12d-f. The surface of the CIGSe grown on SiO_2 is used as height reference (height = 0 µm). Figures 4.12d and e highlight that the films, inside the micro-dots, inflated considerably, which led to delamination in some cases. Conversely, the micro-dots with smaller diameters (< 60 µm) show no damage after the sputtering (see Figure 4.12f).

The excessive flux of Na from the soda lime glass, observed in the sample grown at 580 °C, caused a severe delamination of the CIGSe film directly after growth. With that in mind, it is hypothesized that despite lowering the synthesis' temperature to 450 °C, and thus reducing the Na flux, the persisting flux of Na does not allow for a good enough adhesion of the CIGSe absorber to the Mo layer to withstand the sputtering process. This suggests that lowering temperature is not enough to control the Na content from the substrate effectively, for solar cell applications. Nevertheless, it was still possible to make solar cells with the micro-dots that did not inflate after sputtering.

Device characterization

To characterize an individual micro solar cell, it is required to electrically isolate it from the others in the array. For this, mechanical scribing was used to scribe a region enclosing only the micro-dot of interest, while allowing some space to place the JV electrical probes. Figure 4.13a shows the JV characteristics of the three best micro solar cells for three different diameters, whereas Figure 4.13b shows the EQE of the 100 µm micro solar cell. Note that the determination of the active area was based on the respective micro-dot's diameter, despite the surrounding CIGSe absorber, on SiO_2, also being illuminated. This simplification is based on the argument that the typical diffusion length of carriers in CIGSe is around 1-2 µm [150], which is small compared to the micro-dots' diameter. Thus, the real active area is expected to be similar to the micro-dot's area.

The 100 µm micro solar cell's JV curve, in the dark, shows the typical diode behavior with a relatively low shunt resistance of $\sim$110 Ωcm^2, identified from the inverse slope around 0 V. Under illumination, it is characterized by a high V_{OC} of 584 mV, reflecting the good quality of the CIGSe absorber. In fact, for all three measured diameters, the V_{OC} of the micro solar cells is similar. However, the illumination has induced a drastically low shunt resistance of $\sim$7 Ωcm^2, which resulted in low PCEs. This effect was observed in all measured micro solar cells, despite trying different electrical isolation methods. Furthermore, it was noticed that simply switching on and off the JV's lamp shutter would increase the front contacts' resistance, which was not observed for the large area solar cells, discussed in the next paragraph. Also, the measured current densities in all cases are excessively high compared to the expected values for CIGSe solar cells

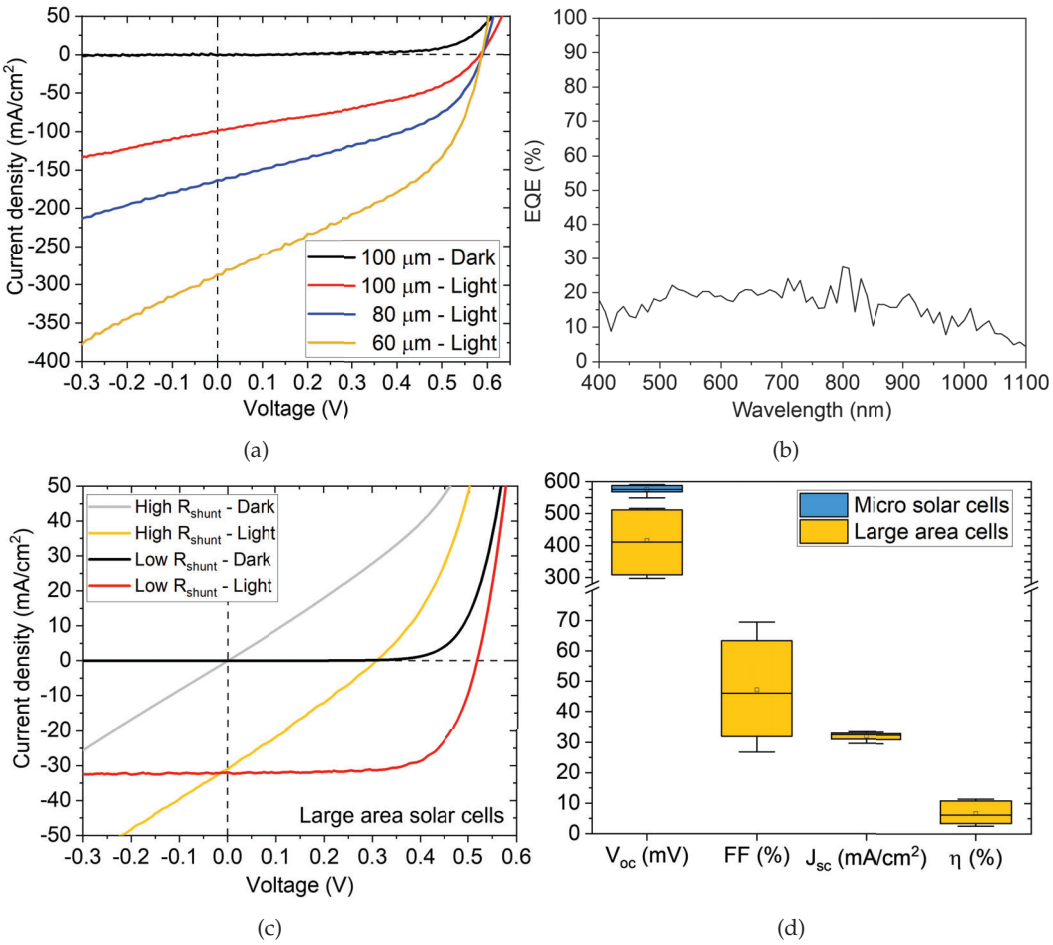

Figure 4.13: a) JV characteristics of the three best micro solar cells, grown at 450 °C, with diameters of 100 µm, 80 µm and 60 µm. The JV curve of the 100 µm micro solar cell, measured under dark, is representative for the other cases. b) EQE spectrum measured from the 100 µm micro solar cell. Note that the wavelength range, covered by the EQE setup for smaller areas, is restricted to 400-1100 nm. c) JV characteristics of the solar cells with highest and lowest PCE, obtained from the large area reference sample grown at 450 °C. d) Box plot of the main JV parameters covering the seven large area solar cells. For comparison, the V_{OC} extracted from all measured micro solar cells is also shown. In the box plot, the box represents the interquartile range (25th to 75th percentile), the middle black line is the median value, the square is the mean value and the whisker is based on the 1.5 interquartile range value.

(30-40 mA/cm^2), suggesting contributions other than the targeted CIGSe micro solar cell. The EQE spectrum shows an overall low quantum efficiency, which is likely also related to the light-induced shunt resistance observed in the JV curve. Nevertheless, it can be drawn that the induced resistance is not wavelength dependent. Mo et al. have shown that Na, segregated at the absorber's surface, can induce shunt paths [151], however this was observed both under dark and illumination, which is not the case here. Thus, the source of the light-induced resistance could not be clearly identified here.

For comparison purposes, the unpatterned sample, grown under the same conditions, was also finished into solar cell devices and scribed in seven $\sim 0.5\,cm^2$ solar cells. Two extreme JV characteristics of sister solar cells are plotted in Figure 4.13c. On the one

hand, a healthy solar cell shows an efficiency of 11.5 % and no evident issues both in the dark and under illumination. On the other hand, from the same sample, a different solar cell shows a heavily shunted solar cell, both in the dark and under illumination, with only a 2.6 % PCE. This variability in the sample is further illustrated in Figure 4.13d, where boxplots of the main JV parameters are shown. It is clear the both the V_{OC} and the *FF* are the most varying parameters, which is caused by the variation in shunt resistance, as exemplified above. It is worth noting that in this case, the shunt resistance is observed both in the dark and under illumination, which was not the case for the micro solar cells. Nevertheless, when comparing the V_{OC}, the micro solar cells show consistently higher values, which could be related to a higher Na content inside the CIGSe micro-dots [111], induced by the patterned substrate.

In brief, lowering the synthesis temperature to 450 °C did reduce the diffusion of Na, in the patterned substrates, however some $Na(In,Ga)_3Se_5$ yellow crystals were still observed. Nevertheless, it was possible to finish the corresponding CIGSe absorbers into micro solar cells. Regarding their electronic performance, a light-induced shunt resistance was observed in all micro devices, compromising their performance. Thus, in the following, the second method to reduce the excessive diffusion of Na is addressed.

4.2.2 Cu-rich CIGSe absorber

Morphology analysis

As discussed previously, Na is known to diffuse through grain boundaries and Cu-vacancies [131] present in the CIGSe phase. A naive approach to reduce Na diffusion is then to block either channel, by growing a single crystal or grow Cu-rich CIGSe absorbers, respectively. Given the available equipment, only the second method is explored. Indeed, adjusting the evaporation profile of elements in the PVD, the CGI of the resulting absorber can be adjusted. A small excess of Cu (CGI > 1.0) allows to suppress the Cu-vacancies without inducing too many $Cu_{2-x}Se$ secondary phases. In this case, the grown absorber had a CGI of 1.1 ± 0.1, both inside and outside the micro-dots. Figures 4.14b-f show CLSM optical images of the resulting CIGSe morphology grown on the three distinct regions of the sample, reminded in Figure 4.14a: (I) array of micro-dots, (II) on the SiO_2 layer and (III) on Mo, at the corner of the substrate.

Interestingly, there is no sign of yellow crystals in any of the regions and this despite the synthesis temperature of 580 °C. Furthermore, EDX analysis also did not detect any Na (see Figure 4.14g). This confirms that without Cu-vacancies, the diffusion of Na is considerably reduced. In fact, given the polycrystalline aspect of the CIGSe absorber, one can speculate that the diffusion through the Cu-vacancies is more consequent than through the grain boundaries. Additionally, part of the Cu-rich CIGSe film on SiO_2 delaminated from the substrate, possibly due to the lack of Na [141], however no delamination was observed inside the micro-dots.

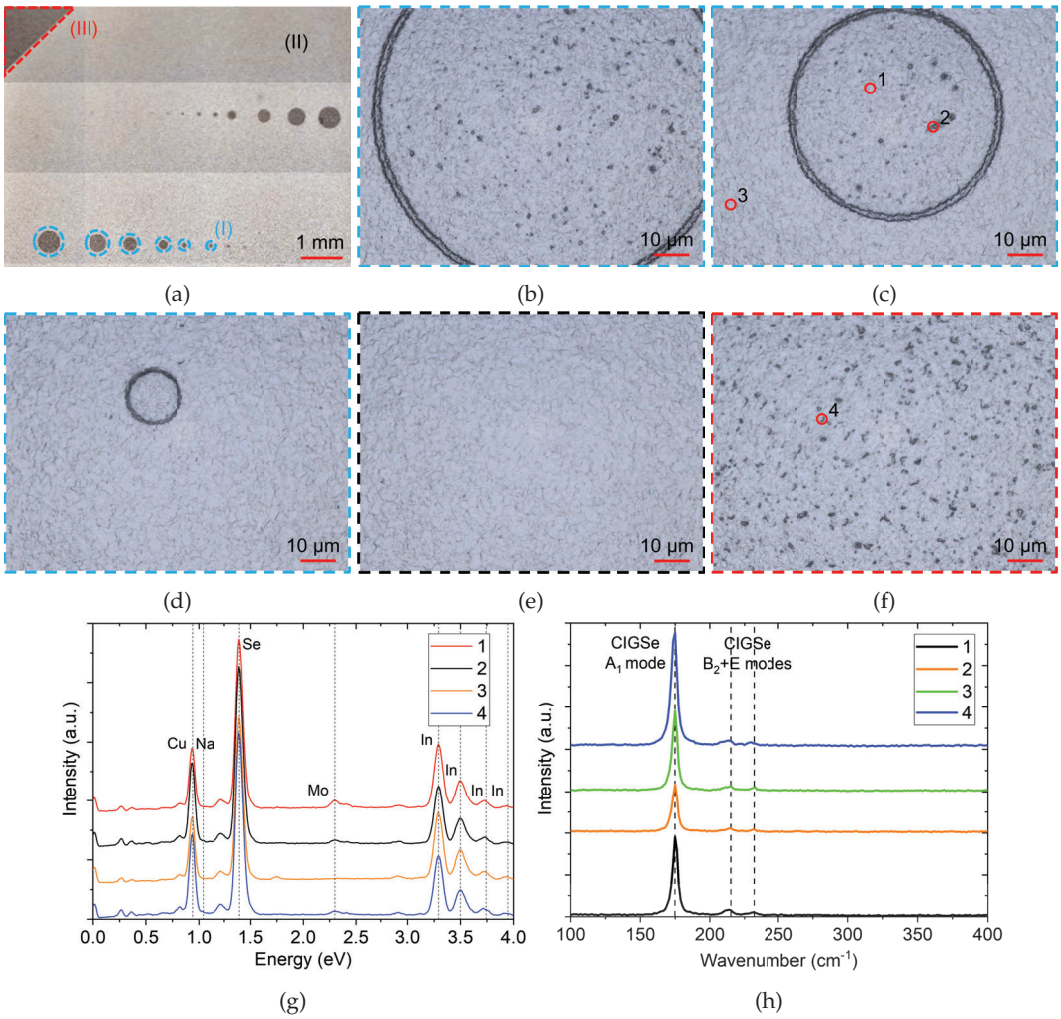

Figure 4.14: a) Optical image of the three regions of interest of the patterned substrate after CIGSe deposition. Region I (in blue) corresponds to the micro-dots, region II (in black) to the CIGSe grown on SiO_2 and region III (in red) to the CIGSe grown on Mo at the corner of the substrate. CLSM optical images of the film's morphology at the microscopic level in: b), c) and d) region I, e) region II and f) region III. g) EDX spectra measured, at 20 kV, from the locations indicated by red circle in the optical images. The relevant peaks were labelled with the corresponding elements. h) Raman spectra measured from the same four regions.

Addressing each region separately, Figures 4.14b-4.14d focus on the morphology of CIGSe inside three micro-dots with distinct diameters (300 µm, 60 µm, and 15 µm respectively). Here, the grey polycrystalline CIGSe phase is present, along with some darker grains, whose density increases with the diameter of the micro-dot. However, outside of the micro-dots, hardly any darker grains are visible. This is also verified for the CIGSe film grown on SiO_2, away from any micro-dot, as depicted in Figure 4.14e. Conversely, the CIGSe grown on Mo, at the corner of the substrate, contains a very high density of the dark grains, as visible in Figure 4.14f. EDX analysis, performed at the locations indicated in Figures 4.14c and f, shows the same composition everywhere (see Figure 4.14g). This suggests that the black grains are also CIGSe but with a different texturing, which is

hypothesized to be induced by the underlying substrate. Thus, the correlation between the density of dark grains and the diameter of the micro-dots, can also be justified by the change in the surface ratio of Mo to SiO_2 walls. In fact, the larger the diameter, the higher the influence of Mo and conversely, the smaller the diameter the higher the influence of the SiO_2 walls on the CIGSe morphology. As for the grain size, it does not seem to vary spatially and is estimated to $3.0 \pm 0.7\,\mu m$, which is larger than in the Cu-poor (CGI < 1.0) case, in line with literature [44]. Finally, Raman analysis on the different regions yields four identical spectra, where only the CIGSe A_1 and mixed B_2+E modes are detected, at 175 cm^{-1}, 215 cm^{-1} and 232 cm^{-1} respectively [97] (see Figure 4.14h). These arguments highlight the similarity of the CIGSe grown on Mo and on SiO_2 and more importantly the suppression of the excessive Na diffusion.

As a side note, the keen reader will have noticed the absence of Ga in the CIGSe phase, in both EDX and Raman spectra. This was due to a technical issue during the synthesis process, resulting in the formation of $CuInSe_2$ instead, which does not affect the results of this section.

To convert the CIGSe absorbers into solar cells, a 10 wt% KCN treatment for 60 s was performed prior to the buffer deposition, given their Cu-rich composition. The CdS layer is deposited by CBD and prior to the window layers deposition, the samples' edge is taped to minimize the risk of shunt paths. Unlike in the previous section, no deformation of the absorber's morphology was noticed following the sputtering of the window layers. This is proved by the flat morphology of the CIGSe inside the micro-dots illustrated by the CLSM height maps in Figure 4.15. This suggests that the adhesion of the CIGSe to the Mo layer is stronger and corroborates with the hypothesis that the excessive Na diffusion was the culprit for the previously observed CIGSe deformation.

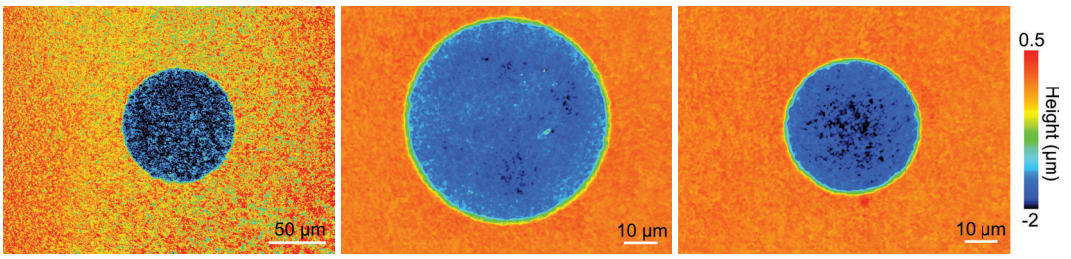

(a) (b) (c)

Figure 4.15: CLSM height maps of the Cu-rich CIGSe absorbers after deposition of the window layers. Diameter of micro-dots: a) 100 µm, b) 60 µm and c) 40 µm. The height of the CIGSe grown on SiO_2 is used a reference plane (height = 0 µm). All height maps share the same color scale, however a) has a different spatial scale than b) and c).

Device characterization

The electrical isolation of the individual micro solar cells was done by mechanical scribing. Figure 4.16a shows the EQE spectrum measured from the 500 µm micro solar cell. The expected parasitic absorption by the CdS buffer layer can be identified in the

blue wavelength region, whereas the lower EQE, at longer wavelengths, can be attributed to multiple factors like the ZnO window layer absorption, an incomplete absorption of long-wavelength photons and/or the carrier recombination at the unpassivated back interface. The J_{SC} is calculated by integrating the product of the EQE and the solar spectrum, as detailed in section 2.2.9 of chapter 2, and equates to 31.5 mA/cm^2.

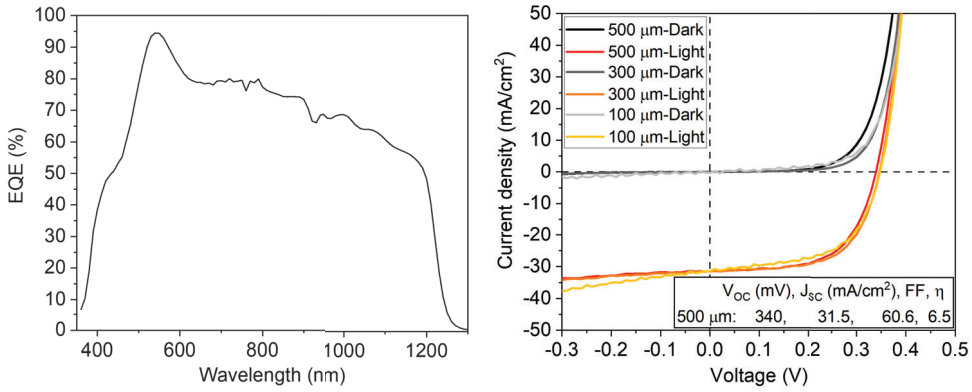

(a) (b)

Figure 4.16: a) EQE spectrum measured from the 500 µm micro solar cell. This spectrum was measured with two EQE setups to first obtain the shape up to 1300 nm (setup for larger areas) and second to correct the intensity (setup for small areas). b) JV characteristics, in the dark and under illumination, of three micro solar cells with 500 µm, 300 µm and 100 µm diameter. Current was corrected based on J_{SC}^{EQE} value measured from EQE. Main JV parameters are shown in a table as inset.

The dark and illuminated JV curves of three individual micro solar cells, with distinct diameters, are measured and plotted in Figure 4.16b. Since all three JV curves had originally a similar J_{SC}, the same current correction factor, calculated from the J_{SC}^{EQE} measurement of the 500 µm micro solar cell, was applied. In all cases, a typical diode behavior is observed and no particular diameter dependence is discerned in the covered range. Regarding the shunt resistance, both in the dark and under illumination, a relatively low value of 170 Ωcm^2 is measured (typically 10^4 Ωcm^2 for a well isolated solar cell). More importantly, no light-induced shunt resistance behavior is observed, as was the case for the Cu-poor micro solar cells, in the previous section. The series resistance was estimated to 0.1 Ωcm^2, which is similar to high PCE CIGSe devices [74]. The champion device showed a V_{OC} of 340 mV, a *FF* of 60.6%, leading to a PCE of 6.5%.

To summarize, getting rid of the Cu-vacancies, by growing a Cu-rich CIGSe, is an effective method to block the Na diffusion, from the patterned substrate. Also, it allowed to obtain working micro solar cells with decent PCE. However, Cu-rich absorbers are known to be limited by interface recombination, which explains the lower V_{OC} compared to the Cu-poor case [44]. The third and last method, to hinder Na diffusion from the patterned substrate, is to implement a Na barrier underneath the Mo back contact, which does not impose any constraint on the CGI compositional ratio.

4.2.3 Na diffusion barrier

Morphology analysis

A commonly used method to stop the diffusion of Na is the introduction of a diffusion barrier in between the soda lime glass and the Mo layer. For our purpose, a 100 nm thick layer of SiO_xN_y was grown by radio-frequency magnetron sputtering directly on the 1 mm thick soda lime glass, followed by the usual 500 nm thick Mo layer. With the Na flux blocked, the synthesis of the CIGSe absorber layer is performed again at 580 °C by the three-stage co-evaporation process. Figure 4.17 shows CLSM optical images of the resulting absorber both at macroscopic and microscopic levels.

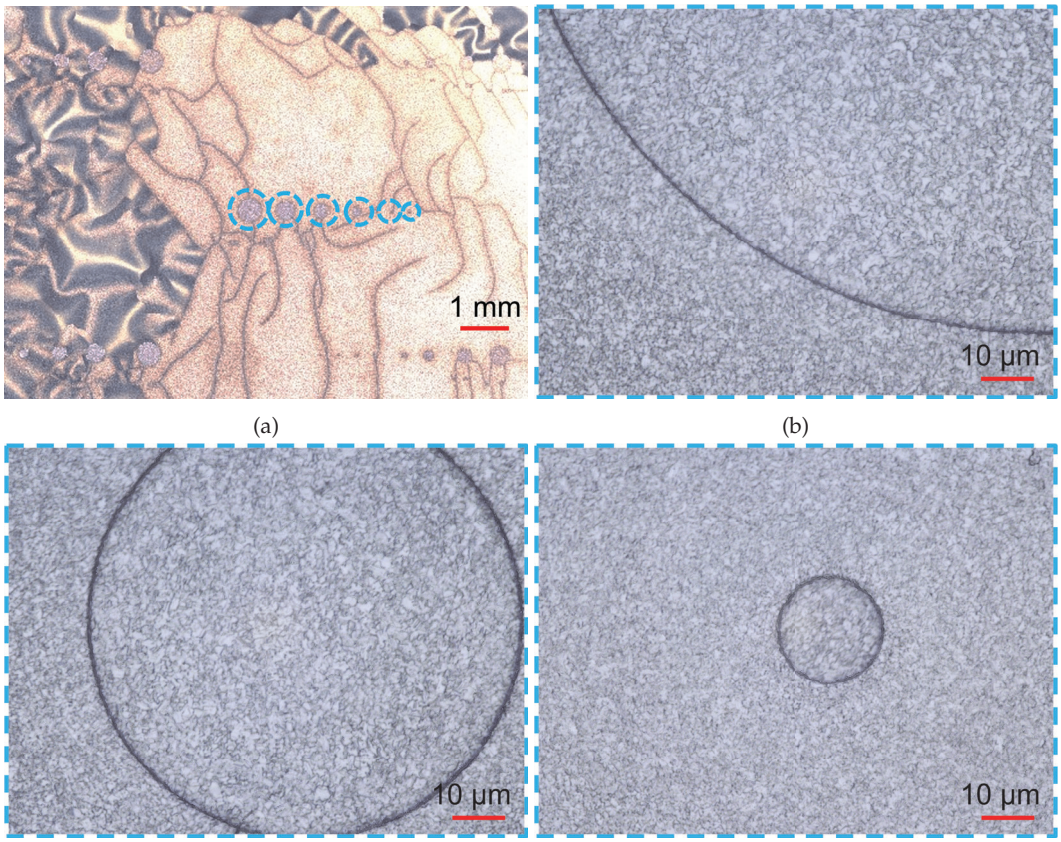

Figure 4.17: a) Overview optical image of the CIGSe absorber grown on the patterned substrate with a Na barrier. CLSM optical images of the film's morphology, at the microscopic level, in micro-dots with a diameter of: b) 200 µm, c) 80 µm and d) 20 µm.

Starting at the macroscopic level, the sample shows cracks running across the whole surface and a large portion of the CIGSe film has delaminated from the substrate, as visible on the left side of Figure 4.17a. Further inspection revealed that not just the CIGSe film, but the whole stack (SiO_2 and Mo layers) detached from the glass substrate. Although the cracks seen here are from the SiO_2 layer, they most likely originate from the higher mismatch between the thermal expansion coefficients of soda lime glass ($9 \cdot 10^{-6}\,K^{-1}$) and SiO_xN_y ($3.3 \cdot 10^{-6}\,K^{-1}$) compared to Mo ($5.9 \cdot 10^{-6}\,K^{-1}$) and soda lime glass

[152–154]. This indicates that in order to include the Na barrier (SiO_xN_y) in the stack configuration, either or both the synthesis temperature and cooling down rate must be reduced to avoid cracks. Regarding the delamination of the CIGSe film from the substrate, reports have observed that the thermal mismatch, between absorber and substrate during cool-down, is responsible for a higher defect density in the CIGSe layer, which could lead to a poor adhesion to the underlying layer [141, 155]. The same reports suggest that the presence of Na plays an important role in improving the film's adhesion, possibly by reducing the thermally induced stress. In the first report, Colombara et al. show that the growth of CIGSe on quartz (i.e. Na-free), results in the peeling of the absorber, whereas in the second reference, Hultqvist et al. add a NaF layer on top of the Na-free substrate and report that no peeling was observed. As seen in Figure 4.17a, a portion of the CIGSe film remained attached to the substrate. Figures 4.17b-d show CLSM optical images of three micro-dots with different diameters (200 µm, 80 µm and 20 µm respectively) from the same array. Independently of the diameter, the morphology of the CIGSe phase, grown inside the micro-dots and on the SiO_2, is similar. This differs from the observations in the two previous sections, where a texture difference was highlighted between the CIGSe grown on Mo and the CIGSe grown on SiO_2. These observations suggest the Na diffusion also plays a role in the growth mechanism of CIGSe, influencing its texture, i.e. grain orientation, as also reported in literature [156, 157].

The delamination of the stack makes it impossible to access the back contact of the micro dots and thus it is not possible to fabricate micro solar cells from this sample. However, it is also an argument that demonstrates the Na barrier completely blocked the Na diffusion, which was the aim. Nevertheless, to effectively use this method, to fabricate micro solar cells, an external source of Na and careful control of the synthesis temperature are required.

To conclude the study of methods to reduce the enhanced Na diffusion from the patterned substrates, it was proven that the most effective method is to implement a Na barrier, however it still requires some adjustment to produce micro solar cells. Growing Cu-rich CIGSe absorber was also effective at blocking a consequent diffusion channel of Na, i.e. Cu-vacancies, and made possible the fabrication of micro solar cells, with different diameters, reaching PCEs around 6.5 %. However, the V_{OC}, being limited by interface recombination, would need further investigation to achieve similar values as the Cu-poor counter part, which is not the aim of this work. Continuing with the Cu-poor CIGSe absorbers, reducing the synthesis temperature did slow down the diffusion of Na to the extent that it was possible to fabricate some micro solar cells with very high V_{OC}, however some issues persisted, like the poor adhesion of CIGSe to Mo, presence of some $Na(In,Ga)_3Se_5$ secondary phases or the light-induced resistance seen in the JV characteristics. Furthermore, it was confirmed that Na plays an important role in the adhesion to the substrate, during the growth and the resulting optoelectronic properties of CIGSe. Knowing now the impact of growing CIGSe on patterned substrates and how to mitigate the resulting constraints, the next section pivots to the sputtering synthesis method to

compare it with the co-evaporation method, and thus investigate if the diffusion of Na differs when the synthesis method is changed.

4.3 Diffusion in sputtered absorbers

Co-evaporation is a material wasteful synthesis process for micro solar cells, nevertheless it provided useful information for the bottom-up approaches discussed in chapter 5. To investigate if the choice of synthesis process has an impact on the Na diffusion from the substrate, this section focuses on growing CIGSe, on the same patterned substrates (arrays of micro-dots with varying diameter), by combining sputtering of the metal precursors followed by annealing in Se atmosphere. Since in the co-evaporation method, the Na diffusion was not restrained to the micro-dots, but also millimeters away from them, the precursor material is sputtered on the SiO_2 layer as well. For the annealing in Se atmosphere, two methods are compared, those are: (i) annealing in the PVD chamber while exposed to the same Se flux, used for the co-evaporated samples in the previous sections and (ii) annealing in a tube oven, analogue to what is reported in chapter 5.

4.3.1 Precursor characterization

As described in chapter 2, the sputtering of the Cu(In,Ga) precursor is done by DC magetron sputtering, nominally at room temperature, and thus no Na diffusion is expected to take place during this step. The morphology of the precursor layer, in the three distinct regions of the sample (array of micro-dots, on the SiO_2 layer and on Mo, at the corner of the substrate), is presented in Figure 4.18.

The morphology of the precursor layer inside the micro-dots (shown representatively in Figure 4.18a) shows two co-existing phases, consisting of a compact underlying layer and a rough top layer composed of irregularly shaped agglomerates. A similar morphology is observed on the precursor layer grown on SiO_2 (Figure 4.18b) and, at the corner of the sample, on Mo (4.18c). Based on similar studies and EDX analysis, the underlying layer has a characteristic CGI of 1.7 ± 0.1, suggesting that it is composed of Cu-rich $Cu_{16}(In_{1-x},Ga_x)_9$ and/or Cu_3Ga phases [158, 159]. The top layer is consistent with the co-existence of elemental In and intermetallic phases like Cu_2In, CuIn, Cu_3Ga. An area scan over $100\,\mu m^2$ shows an average composition of 0.99 ± 0.06 for the CGI ratio and a GGI=[Ga]/([Ga]+[In]) of 0.28 ± 0.03. Note that the EDX spectra only put forward the presence of C, Cu, In and Ga within the sample, as highlighted in Figure 4.18d. The presence of C may be due to an incomplete removal of the resist, used to pattern the SiO_2 matrix, before the sputtering of the precursor layer.

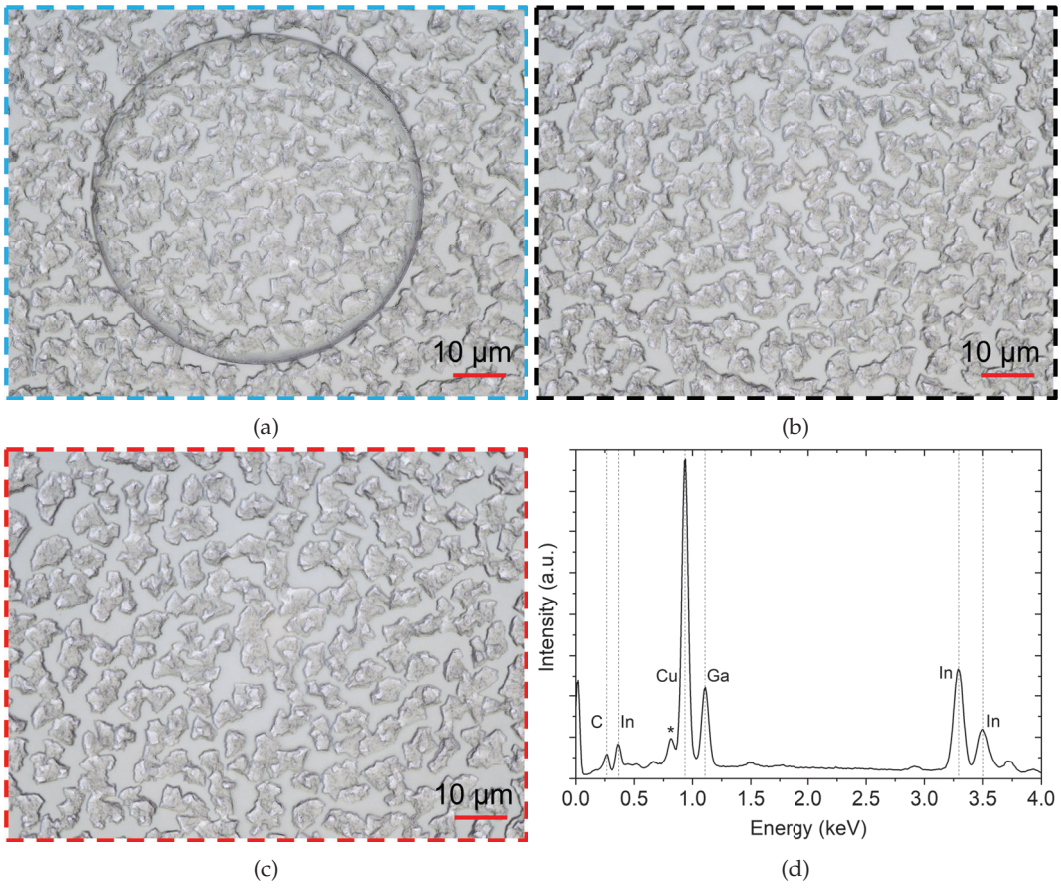

Figure 4.18: CLSM optical images of the sputtered precursor film's morphology, at the microscopic level, deposited: a) in a micro-dot with a 60 µm diameter, b) on the SiO_2 layer and c) on Mo, at the corner of the substrate. d) EDX area spectrum acquired at 10 kV. The small peak located at 0.82 eV, indicated with an asterisk, could not be attributed to any element. The same border color scheme is used, as in the previous section, to denominate the region that is being studied (in blue - micro-dots, in black - on SiO_2 and in red - on Mo at corner of the sample).

Given the precursor's morphology, an attempt at reducing the roughness of the precursor layer was performed by annealing it in an N_2 inert atmosphere at 250 °C for 10, 100 and 1000 min. The N_2 background pressure was about 400 mbar. Figure 4.19 shows the morphology and height map of the same micro-dot before (Figures 4.19a and b) and after (Figures 4.19c and d) the 10 min annealing process. The initial measured *RMS* was of 240 nm. Conversely to the annealing of the electrodeposited metal precursors, in section 3.2.1 of chapter 3, no smoothing effect was observed (< 1 % change in roughness) independently of the annealing time. Also, no noticeable optical nor morphological changes were observed in the precursors after the annealings (10, 100 or 1000 min). This is possibly because, in the sputtering case, the equilibrium phases are already formed, whereas in the electrodeposited layers, the alloys are forming during the annealing procedure. However, this hypothesis was not further investigated.

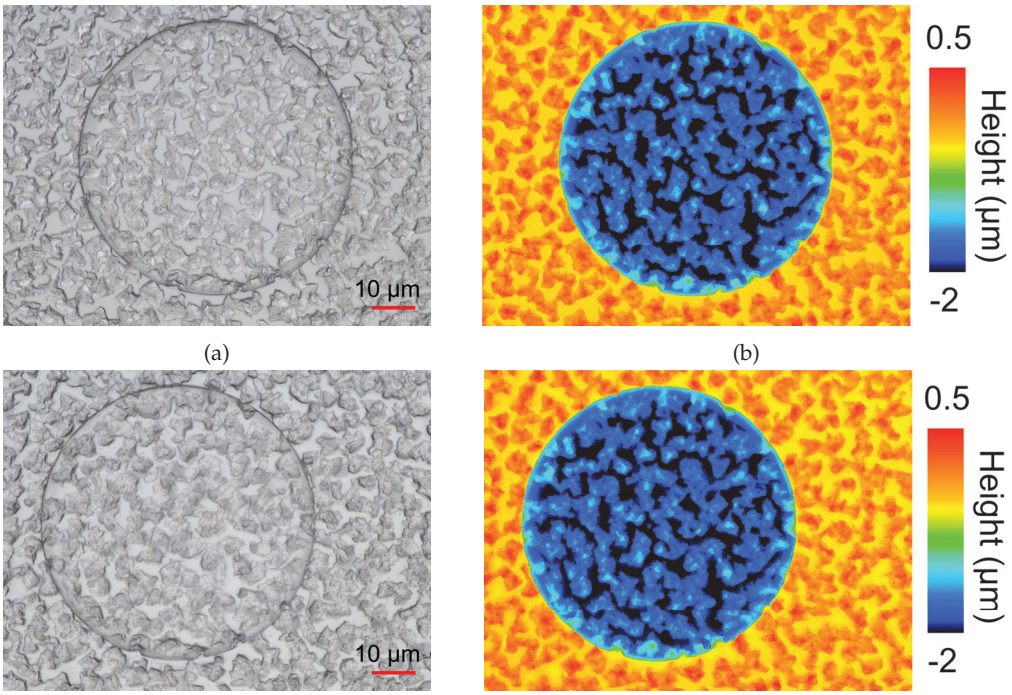

Figure 4.19: CLSM optical image of the sputtered metal precursor, around a 60 µm micro-dot: a) before and c) after the 10 min annealing treatment. The brightness of image c) was increased by 10 % for easier comparison. CLSM height map, of the same region as the optical images in a) and c) respectively, b) before and d) after the annealing.

4.3.2 Characterization of absorbers' morphology

To convert the sputtered precursors into the CIGSe absorbers, two annealing routines in Se atmosphere were investigated: (i) annealing in the PVD chamber and (ii) annealing in a tube oven. In both cases, the target annealing temperature was 450 °C for 10 min, to avoid excessive Na diffusion. In this sense, the first routine has the same conditions as in section 4.2.1, except that instead of co-evaporating all elements simultaneously, the precursor Cu(In,Ga) layer was already sputtered. Thus, the sample is exposed only to Se vapor. The Se partial pressure in this case is around 10^{-6} mbar. In contrast, the second routine uses a tube oven to anneal the precursor, which is inside a graphite box along with the Se powder, and convert it into the CIGSe absorber layer. The Se partial pressure here is about 120 mbar (calculated from equation 5.1 discussed in chapter 5) and the inert gas used is N_2. This is in essence one of two material-efficient routines that will be studied, in chapter 5. The aim of this study is to investigate whether the choice of synthesis process has an impact on the Na diffusion from the substrate. Additionally, it allows to study the impact of the Se partial pressure on the formation of CIGSe, since this is a major difference between the two investigated routines.

Annealing sputtered precursor in PVD chamber

For comparison purposes, the morphology of the co-evaporated absorber, at 450 °C in section 4.2.1, is repeated in Figure 4.20a. Figures 4.20b and 4.20c show a representative CLSM optical image, and respective height map, of the morphology of the resulting CIGSe inside the micro-dots and on the SiO_2.

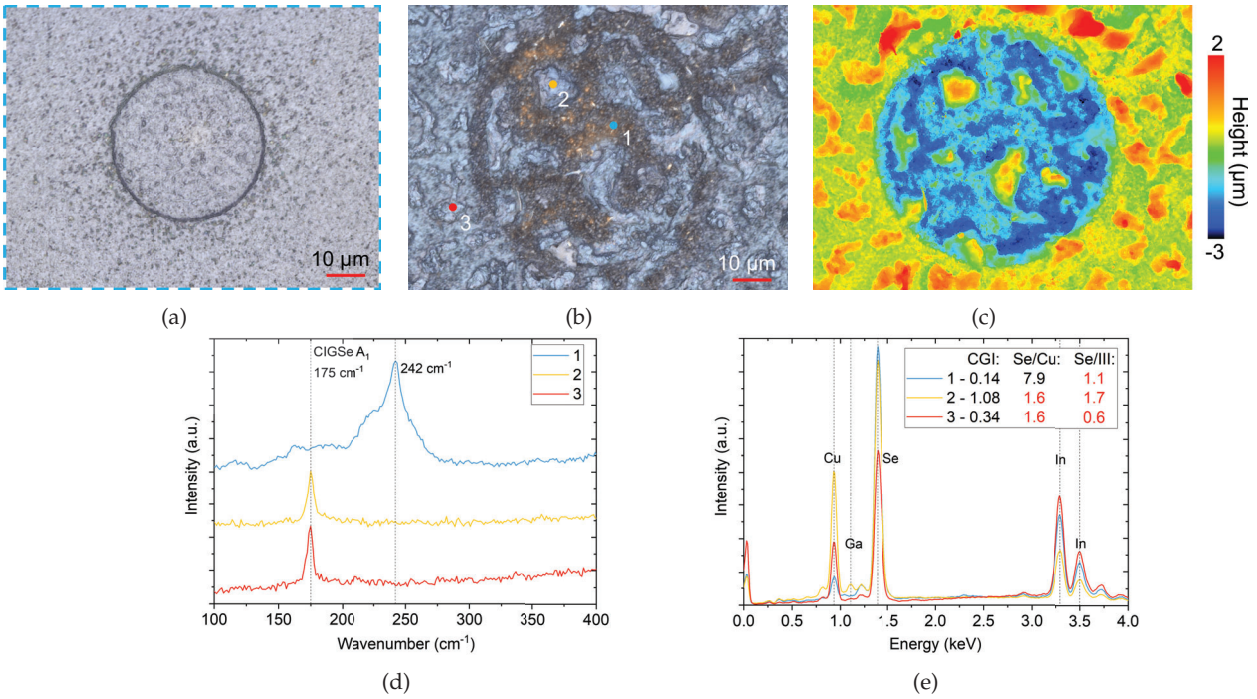

Figure 4.20: CLSM optical image of: a) the co-evaporated absorber at 450 °C, discussed in section 4.2.1. b) the absorber annealed in the PVD chamber, under Se flux (10^{-6} mbar), at 450 °C. c) CLSM height map corresponding to the CLSM image in b). d) Raman spectra measured, using a 532 nm laser, from the numbered locations in b). e) EDX spectra measured, at 10 kV, from the numbered locations in b). The calculated CGI, Se/Cu and Se/III (or Se/[In+Ga]) ratios are also shown in the legend for the respective locations.

A first comparison of the optical images highlights that the two routines yielded distinct CIGSe morphologies on SiO_2 and especially inside the micro-dots. In contrast to the co-evaporated layer, the sputtered and annealed CIGSe layer has a blue appearance and a considerably higher *RMS* roughness (490 nm compared to 180 nm in the co-evaporated case). Inside the micro-dots, secondary phases are additionally visible. Although, the higher roughness could be justified by the initially high roughness of the precursor layer, it is nevertheless clear that the co-evaporation and the sputtering plus annealing routines yield rather different layers, in particular inside the micro-dots. This already demonstrates that the synthesis method has a critical impact on the absorber's morphology. Raman analysis confirms that the phase with a blue appearance shows the CIGSe A_1 mode, characteristic of the chalcopyrite phase. However, based on Raman and composition information, the orange phase could not be identified. Elemental characterization of the CIGSe phase shows that the CGI ratio varies widely, as shown in the legend of Figure 4.20e. Furthermore, a lack of Se was measured in all locations, comparatively to the

expected CIGSe ratios, i.e. Se/Cu=2 and Se/III=2. The lower Se ratios are highlighted in red, in the legend of the EDX spectra. Additionally, EDX surprisingly unveils that no Na is detected. These results suggest the Se flux was too low to form a homogeneous CIGSe phase and allow us to hypothesize that the Na diffusion is also influenced either by the Se partial pressure or the synthesis process. This hypothesis is tested in the following, as the partial pressure of Se, used in the tube oven annealing, is orders of magnitude higher.

Annealing sputtered precursor in tube oven

The annealing in the tube oven involves placing the precursors, along with the Se powder (40 mg), inside a graphite box and anneal it in a Se atmosphere, where the Se partial pressure (120 mbar) is orders of magnitude larger than in the PVD chamber (10^{-6} mbar). Figure 4.21 shows CLSM and SEM images of the morphology of the resulting absorber.

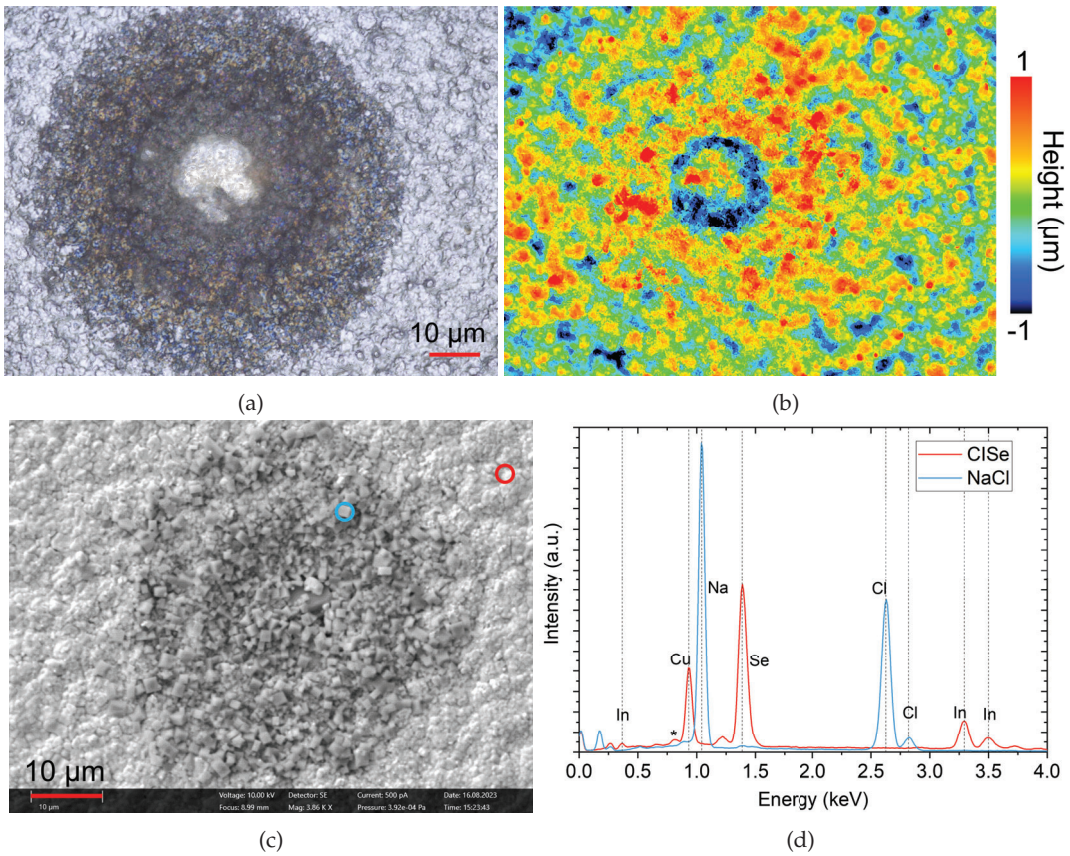

Figure 4.21: a) CLSM optical image and b) respective height map of the absorber's morphology, at the microscopic level, in a micro-dot with a diameter of 20 µm. c) SEM image of the same region as b). d) EDX spectra acquired, at 10 kV, from the two locations indicated in c). The red spectrum corresponds to the grey CISe phase (red circle) and the blue spectrum to the NaCl phase in and around the micro-dot (blue circle).

Focusing on the CLSM optical image and respective height map, in Figures 4.21a-b, a 20 µm micro-dot shows a representative morphology. On the one hand, the interior of the micro-dot shows a mix of black, yellow and blue phases, surrounded by an aura with

mostly blue and yellow phases. Some micro-dots additionally show yellow crystals with around 10 µm in size. On the other hand, further away from the micro-dots, the CIGSe grey granular phase is visible, similar to the co-evaporated absorber. In fact, away from the micro-dots the CIGSe phase shows a homogeneous morphology and its *RMS* roughness is around 300 nm, which is much closer to that of the precursor, suggesting a more compact morphology. To have a higher lateral resolution on the micro-dot, shown in Figure 4.21a, an SEM image is acquired with similar magnification in Figure 4.21c. Here, it is possible to resolve that the micro-dot and its aura are populated with cubic crystals, which are surrounded by the CIGSe polycrystalline phase. Surface sensitive (10 kV acceleration voltage) EDX analysis, in these two distinct regions, unveils that the cubic crystals are composed of Na and Cl, whereas the polycrystalline phase is $CuInSe_2$ (CISe) and this time with the Se ratios closer to the expected values (Se/Cu=1.7 and Se/III=2.1). Thus, one can already conclude that depending on the synthesis routine that is taken, a different Se partial pressure is required to obtain a similarly compact and homogeneous CIGSe phase.

Regarding the NaCl crystals, given that no Na was intentionally added and the crystals are only observed around the micro-dots, it is safe to assume that the Na is diffusing from the soda lime glass substrate. Since the synthesis routine here is the same as previously, i.e. precursor sputtering followed by annealing in Se, it stands out that the Se partial pressure drives the Na diffusion from the substrate. Referring back to the co-evaporation case (in section 4.1), possibly, the Se has an easier access to the substrate since the Mo layer is directly exposed and thus a lower Se partial pressure is required to drive enough Na to form a secondary phase. Conversely, with the sputtered precursor, a lower Se partial pressure implies the Se atoms are less likely to reach the substrate interface, which means that a Na-enriched secondary phase is formed only at high enough Se partial pressures.

The origin of Cl could not be clearly pinpointed. Nevertheless, no Cl peak was measured during the EDX analysis on the precursor layer, in Figure 4.18d. Thus, the Cl contamination may have arisen from previous annealings of electrodeposited metal precursors in the same graphite box. In fact, the In and Ga electrodeposition solution does contain a substantial amount of Cl, which could have been incorporated in the deposited layer and subsequently evaporated into the graphite box's walls. At the annealing temperature, the chlorine gas phase desorbs from the graphite box's wall and only reacts where Na is available, that is within micro-dots. Nevertheless, the Cl is not expected to influence the diffusion of Na from the substrate, as it was never observed to incorporate within the absorber layer, and consequently never sees the substrate interface.

To confirm the spatial distribution of the elements, EDX mapping was performed on a micro-dot close to a cleaved edge, in Figure 4.22. The interest here is to confirm whether Na can only diffuse through the micro-dots or also through a cleaved edge.

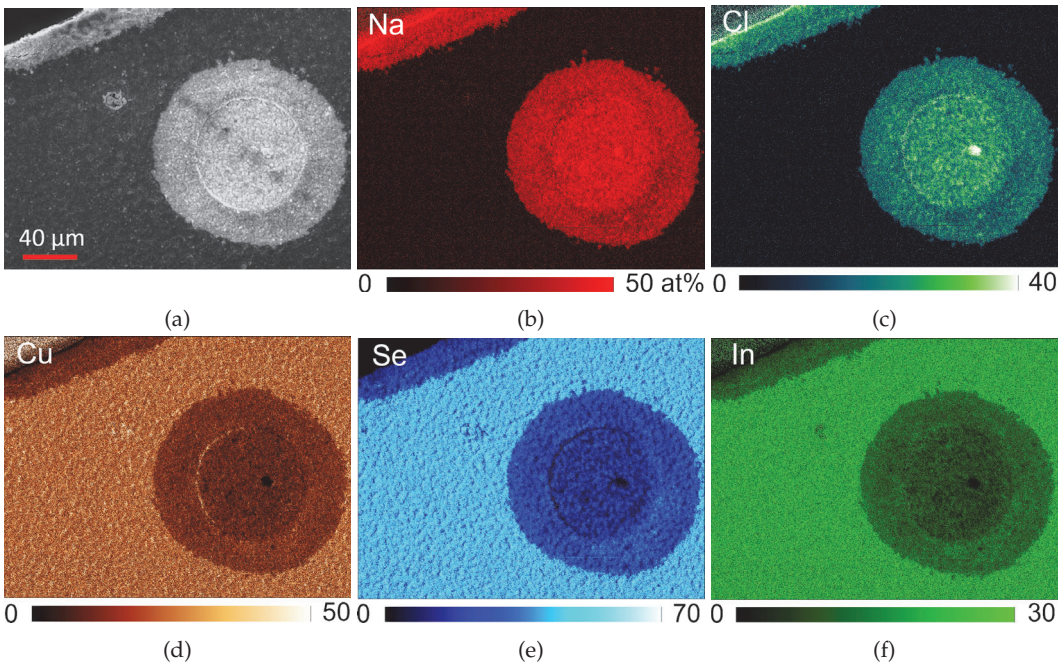

Figure 4.22: a) SEM image of an 80 µm micro-dot near the sample's edge, from which EDX elemental maps were acquired at 10 kV. Corresponding EDX elemental distribution maps for b) Na, c) Cl, d) Cu, e) In and f) Se. All maps' color scales indicate the respective elemental content in atomic ratio.

Figure 4.22a shows the SEM image of the investigated region. On the right side, an 80 µm wide micro-dot is visible and, on the top left side, a fraction of the cleaved edge can be identified. Referring to the Na and Cl elemental distribution maps, in Figures 4.22b-c respectively, both maps show the exact same trend. In fact, the two elements are only present inside the micro-dot and roughly 30 µm away from the edge of the micro-dot as well as from the edge of the sample. In these regions both elements are the main constituents of the film. No Na nor Cl is detected in the intermediate region. Conversely, the elements making up the CISe phase are measured in all regions, as presented in Figures 4.22d-e. The particular spatial distribution of Na observed, demonstrates that the diffusion of Na, from the underlying substrate, can take place through the micro-dots and through cleaved edges. In quantitative terms, a substantial amount of Na (∼50 at%) is found within the micro-dot, despite the relative low annealing temperature (450 °C). This disrupts the formation of CI(G)Se, making it impossible to synthesize the absorber layer in this way. Thus, the use of a barrier is required to control the diffusion of Na from the substrate. Regarding the Na diffusion itself, the radial distribution around the micro-dots is similar to the co-evaporated samples at 450 °C, however the amount of diffused Na is higher, presumably due to the higher Se partial pressure.

To conclude, this section has demonstrated that the synthesis routine has indeed an impact on the diffusion of Na from the substrate, however it is the Se partial pressure that plays a major role in regulating the Na diffusion. Indeed, the diffusion of Na is driven by Se partial pressure and the required pressure to drive the same amount of

Na, from the substrate, differs depending on the synthesis routine. Furthermore, the Se partial pressure was demonstrated to have a major influence on the morphology and composition homogeneity of the resulting absorber. Additionally, it was observed that an annealing routine in an inert atmosphere is not effective to reduce the precursor's roughness in the case of a sputtered mixed metal precursor.

4.4 Summary

In this chapter, the impact of using patterned substrates to grow CIGSe absorber layers was investigated and it was put forward that, for the two explored synthesis routines, a locally enhanced diffusion of Na takes place, from the soda lime glass and through the holes in the patterned matrix, due to the diffusion blocking effect of the matrix material (SiO_2 in our case). This enhanced diffusion interferes with the growth of the CIGSe absorber, causing a poor adhesion of the CIGSe layer to the Mo back contact, ultimately compromising the absorber's performance. To circumvent this issue, three methods were tested to reduce Na diffusion and it was proven that the most effective one is to implement a Na barrier. Nevertheless, with this method, providing some Na externally is essential to ensure CIGSe adhesion. It is worth mentioning that growing CIGSe in Cu-rich conditions also allowed to fabricate working micro solar cells with PCEs around 6.5 %, whereas Cu-poor CIGSe did yield a higher V_{OC} but suffered from light-induced resistance issues.

Knowing the impact of growing CIGSe on patterned substrates, a comparison between the reference co-evaporation method and the sputtering plus annealing routine is made to understand if changing the synthesis method impacts the diffusion of Na. The aim being to anticipate which parameters are important to account for when synthesizing the absorbers with the material-efficient synthesis methods, as discussed in chapter 5. In this context, the Cu(In,Ga) sputtered precursors were converted into CIGSe absorbers through two annealing routines: (i) annealing in similar conditions as the co-evaporated absorbers, i.e. with very low Se partial pressure. (ii) annealing in a tube oven with the same annealing parameters, but with high Se partial pressure. This comparison has demonstrated that the Se partial pressure has an important role in regulating the Na diffusion, from the patterned substrate, and it also influences the morphology and composition homogeneity of the resulting absorber.

Thus, for the synthesis of micro solar cells through material-efficient routines, the enhanced Na diffusion can be countered either by growing Cu-rich CIGSe absorbers or by implementing a Na barrier, underneath the Mo back contact, and grow Cu-poor CIGSe absorber while providing some Na. Furthermore, it is expected that controlling the Se partial pressure will be crucial to optimize the absorber's properties and performance.

Chapter 5

Material efficient growth of CIGSe on patterned substrates

In chapter 3, an effective method to characterize and monitor the morphology of thin films was developed for sequential processes. With this, it was possible to measure the composition and monitor the phases formed in the individual micro-dots that make up the arrays of the substrate. In chapter 4, a co-evaporation process was used to grow the absorber on the patterned substrate, as it should yield CIGSe solar cells with high PCEs. It was found that the patterned substrates enhance the diffusion of alkali dopants through the micro-dots. Based on these results, chapter 5 investigates the synthesis of CIGSe absorbers, in patterned substrates, using material efficient methods. The latter are typically more challenging to control and thus harder to achieve high quality material compared to the co-evaporation case. Two synthesis routes are explored. In the first case, the Cu(In,Ga) metal precursor is deposited, inside the micro-dots, by magnetron sputtering, followed by an annealing in a Se-containing atmosphere to form the CIGSe absorber. In the second case, a two-step electrodeposition process is chosen to grow first the Cu layer and second the In and Ga layer inside the micro-dots. Similarly to the first case, the CIGSe absorber are formed by an annealing in a Se-containing atmosphere. For the two cases, Cu-rich (CGI > 1.0) and Cu-poor (CGI < 1.0) precursors are investigated. The aim is to investigate the layer's morphology at each step of the two aforementioned material efficient methods and determine the relevant parameters to obtain working micro solar cells consistently. Also, the impact of using different patterned substrates is discussed. To have an overview of the synthesis routes and substrates discussed in this chapter, the reader may refer to the summary schematics (Figure 2.6) shown in chapter 2.

5.1 Sputtered solar cells

In this section, the first material efficient method, i.e. sputtering and annealing routine, is addressed, starting with the Cu-rich based solar cells. Given that the aim of the present chapter is to focus on material-efficient methods to produce micro solar cells, the Cu(In,Ga) precursor was sputtered only into the micro-dots, as detailed in section 2.1.2.

Note that the difference in the synthesis process, between the material-wasteful sputtering, discussed in section 4.3 and the material-efficient sputtering presented here, is the moment when the resist layer is removed. In the former case, the resist is removed before the sputtering of the Cu(In,Ga) metal precursor, leading to its deposition inside the micro-dots and on the SiO_2 layer. In the latter case, the resist is kept during the sputtering step and only dissolved afterwards, which results in the deposition of Cu(In,Ga) only inside of the micro-dots. The removed resist and excess precursor material can potentially be separated easily and reused, making this method material-efficient. Full details about synthesis process may be found in reference [160].

5.1.1 Cu-rich solar cells

This section is based on the publication [160], which demonstrates a proof-of-principle of working micro solar cells synthesized by sputtering, as a material efficient method.

Given that the lack of Cu-vacancies, i.e. a CGI > 1.0, was demonstrated to hinder the Na diffusion from the substrate, Cu-rich metal precursors were chosen as a starting point. In the following, the morphology and composition of the precursors is investigated and afterwards, the annealed absorbers are characterized.

Precursor characterization

Morphology and composition

The substrates used in this section differ slightly from the other substrates, in previous chapters, in the sense that the SiO_2 thickness is 1 µm. Additionally, the micro-dots are arranged in an hexagonal lattice and are accompanied by a $3\times3\,mm^2$ square hole in the SiO_2 to access the Mo back contact for electrical characterization, as shown in Figure 5.1a.

Looking at the morphology of the precursors, two extremes are observed. On the one hand, the precursor shows a flat and smooth surface with a white appearance, visible in Figure 5.1b. Figure 5.1c presents the corresponding height map, from which the following conclusions can be drawn: First, the smooth surface is confirmed as hardly any height fluctuation is perceived. Conversely, along the perimeter of the precursor, a narrow rim (1-2 µm width) is protruding higher (0.4-1 µm) than the inner region of the precursor. Finally, it stands out that, in this case, the metal precursor is slightly higher ($\sim$100 nm) than the SiO_2 layer, suggesting a precursor thickness of roughly 1 µm. On the other hand, in Figure 5.1d, the precursor has an uneven appearance instead and is populated by black structures, present both inside and outside of the micro-dot region. According to the height map, in Figure 5.1e, these structures can have heights larger than 2 µm. As previously, the underlying precursor itself has a flat morphology, except for the protruding rim along the perimeter.

Focusing first on the origin of the rim, cross-section SEM images were acquired before removing the resist. Figure 5.2a shows an SEM cross-section close-up at the periphery of a micro-dot directly after the sputtering of the Cu(In,Ga) metal precursor.

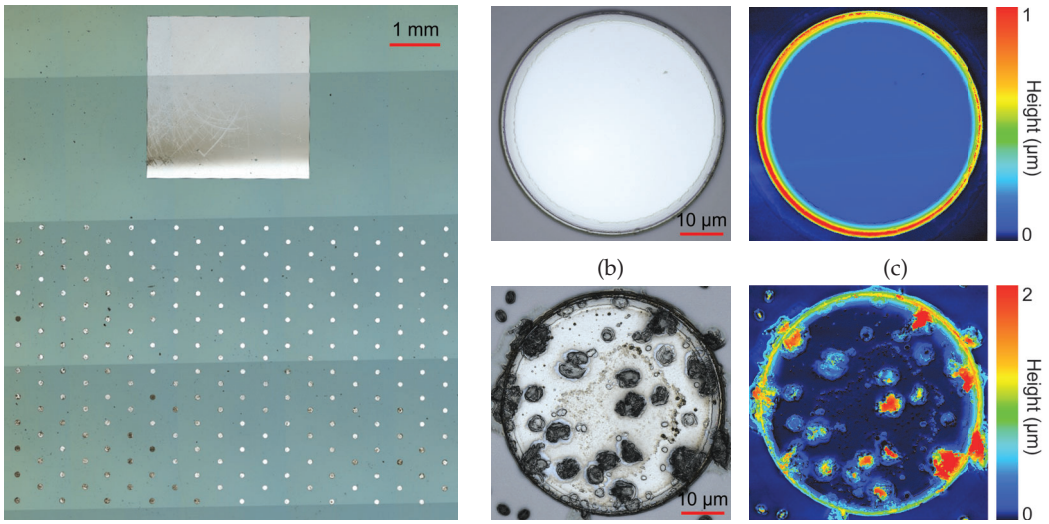

Figure 5.1: a) Top-view optical image of the array of micro-dots containing the Cu(In,Ga) precursor layer. The square at the top of the image is a hole in the SiO_2 matrix to access the Mo back contact. CLSM b) optical image and c) respective height map of a micro-dot containing the metal precursor without apparent contaminants. CLSM d) optical image and e) respective height map of a contaminated micro-dot precursor.

As expected, the topmost layer is the sputtered Cu(In,Ga), which covers the whole substrate. However, focusing at the periphery of the micro-dot (indicated by a double ended arrow in Figure 5.2a), a small fraction ($\sim$1.5 µm) of the SiO_2 layer is neither covered by the resist nor by the Cu(In,Ga). This suggests that the Cu(In,Ga) sputtering damaged and removed the resist. Since the width of the protruding rim is also roughly 1.5 µm, as observed with CLSM, its origin could be related to the abrasion of the resist during the sputtering step, leading to an accumulation of Cu(In,Ga) deposit at the periphery between the resist and the micro-dot. This hypothesis implies that the protruding rim is a blend of organic resist and Cu(In,Ga). Assuming this resist damage happens early on during the sputtering process, the incorporation of resist within the Cu(In,Ga) precursor is not limited to the surface, but might affect the whole micro-dot volume. In fact, damages to photolithography resists by magnetron sputtering processes have already been reported [161]. To verify the contamination hypothesis, EDX mapping of a filled micro-dot, after the removal of resist and similar to that in Figure 5.1b, was measured to have the spatial distribution of C content (signature element of the resist), in Figure 5.2b.

The C EDX mapping shows three regions that can be differentiated by their C content and correspond to the inner region of the micro-dot, the protruding rim and the surrounding SiO_2 layer. The latter acts as a reference for the eventual C deposition during the EDX measurement. According to the map, the rim indeed contains a higher content of C than the inner region of the micro-dot and both are clearly higher than the reference SiO_2 region. This is also demonstrated in Figure 5.2c, where the frequency distributions of C content in the three regions is plotted. The vertical dashed lines indicate the respective average C content in the respective regions and the error bar is the distribution's

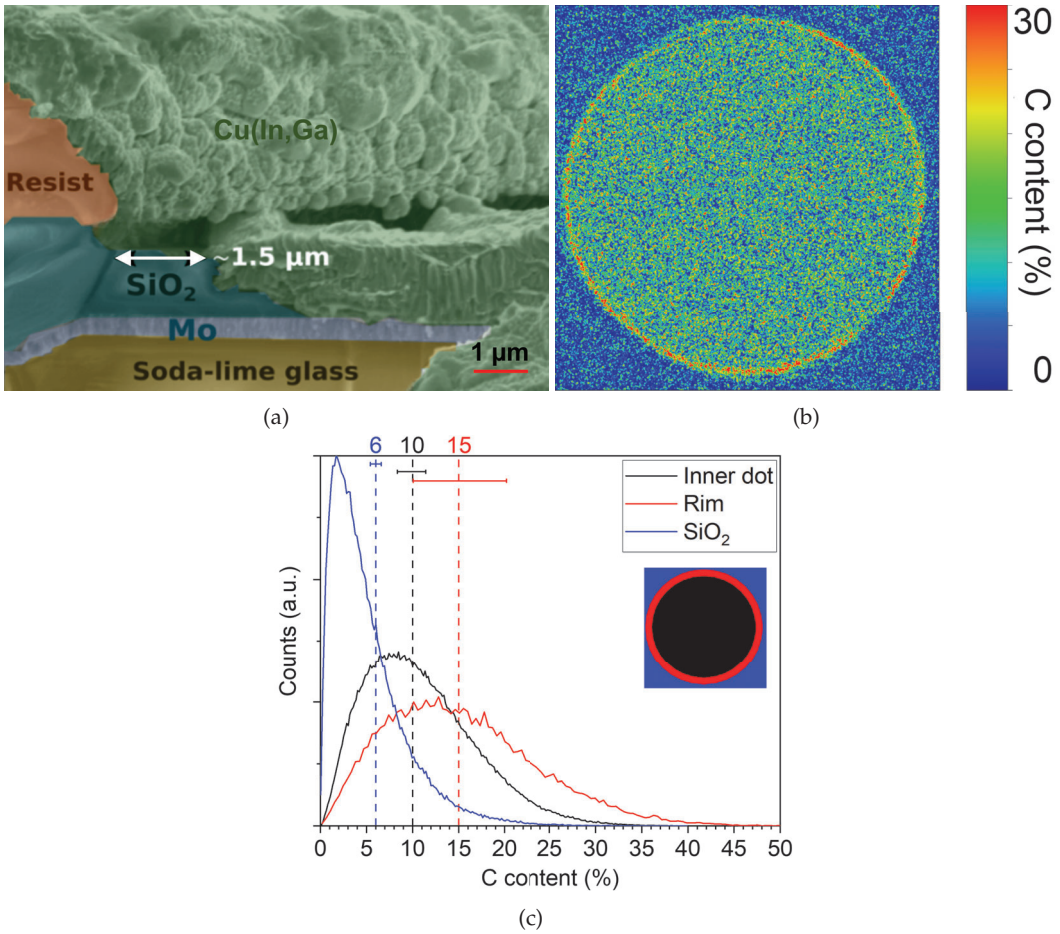

Figure 5.2: a) SEM cross-section image of a micro-dot before removing the organic resist (colors were added for easier distinction). White double arrow indicates region without resist nor Cu(In,Ga). The cross-section image was provided by Dr. Ana Pérez-Rodríguez and adapted here from [160]. b) Spatially resolved EDX map, measured at 10 kV, of a 50 µm diameter micro-precursor with distribution of C content. c) Frequency distributions of C content, extracted from Figure 5.2b, within the three regions schematized as an inset. Blue curve is related to the C content measured outside the micro-dot, black curve to the inner region of the micro-dot, i.e. the precursor, and the red curve related to the rim around the micro-dot.

standard deviation. Here again, the protruding rim shows the highest C content, as well as the broadest distribution, followed by the inner region of the micro-dot, with a lower C content and finally the SiO_2 region which has the lowest C content and sharpest distribution as expected. This observation corroborates with the hypothesis of resist contamination in the rim and within the precursor layer, despite its smooth morphology, suggesting an inherent contamination issue in the sputtering process. It is also speculated that the high density of micro-dots in this pattern, i.e. the reduced spacing between neighbour micro-dots, could also promote the abrasion of resist during the precursor's sputtering.

In terms of composition, the smooth metal precursors show a homogeneous composition within the array with a CGI ratio of 1.5 ± 0.1 and a GGI ratio of 0.46 ± 0.06. This is also verified for the micro-dots containing the observed black structures (see Figure 5.1d).

However, the C content is roughly three times higher in the flat regions, whereas the black structures themselves are made up of C, O and Na, as highlighted by the SEM images and EDX spectra in Figures 5.3a-c. Since the resist itself is organic, this also supports the hypothesis that the sputtering process causes an abrasion of the resist and creates a blend between the metal precursor and the resist within the whole volume of the micro-dot. However, the origin of the Na peak, visible in Figure 5.3c, could not be identified. It is worth mentioning that the dedicated cleaning procedure (ultrasound baths in acetone and deionized water) could not remove these black structures.

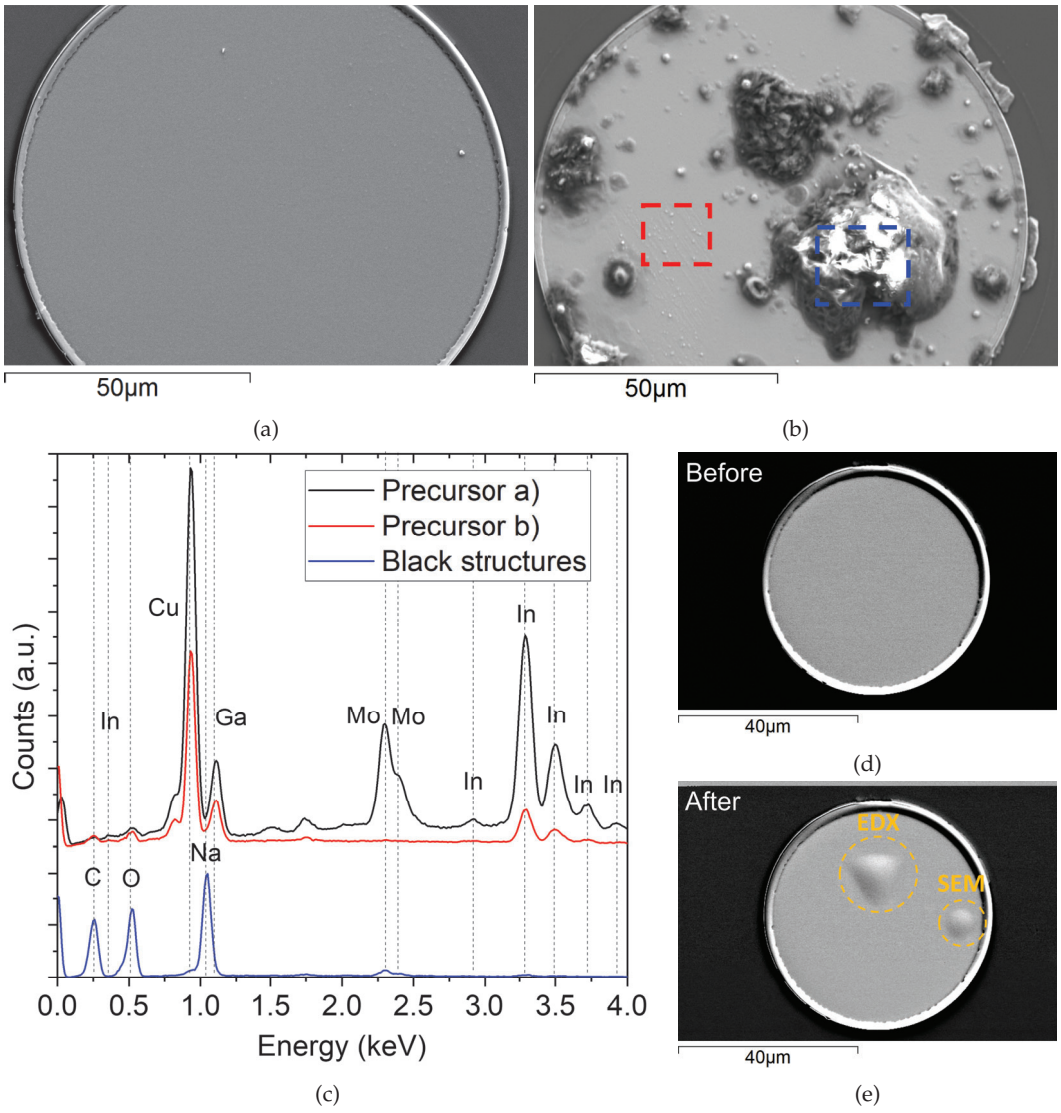

Figure 5.3: SEM image of a micro-dot precursor a) without visible contaminants and b) with contaminants. Dashed squares indicate the regions where EDX spectra, shown in c), were measured. c) EDX spectra measured at 10 kV from the corresponding locations in a) and b). The two spectra from the precursors (black and red) were shifted upwards. The bottom spectrum (blue) is related to the black structures. The relevant peaks were labelled with the corresponding elements. SEM images of a micro-dot precursor d) before and e) after EDX measurement and high focus with SEM electron beam. The respective locations are indicated with dashed circles.

As a side note, it was observed that the morphology of the precursor was irreversibly modified by the SEM/EDX electron beam after a spectrum measurement or when using very high magnification (> 40 kX). Figures 5.3d-e are SEM images of the same precursor micro-dot before and after an EDX measurement and a zoom-in to high magnification at the indicated locations, respectively. In both cases, the morphology of the precursor inflates locally and results in a bump with a height of a few hundreds of nanometers. This effect was not particularly studied, however it is hypothesized that the electron beam heats up the blend of metal precursor and organic resist, causing the latter to expand.

Attempt to remove contamination

In all cases, it is detrimental to have resist leftovers remaining within the metal precursor. A strategy to extract the contaminants from the precursor is to perform an annealing process to potentially vaporize the organics. In the synthesis process, an annealing routine in Se-containing atmosphere is anyway foreseen. Thus, two methods were tested, those are, (i) annealing the metal precursors directly in Se or (ii) perform an additional annealing step in an N_2 inert atmosphere before the annealing in Se. Both results, pertinent to the annealings in Se, are discussed in the following section.

The annealing in N_2 consists of heating the sample inside a sealed, and slightly under-pressure, vacuum chamber filled with N_2, to avoid oxidation of the precursors. The temperature of the annealing was 440 °C for 20 min. Figure 5.4 presents the morphology of two precursor micro-dots before (Figures 5.4a-d) and after (Figures 5.4e-h) the annealing routine to remove the contaminants. For the first micro-dot (Figure 5.4a), the morphology of the precursor looks flat, whereas in the second case (Figure 5.4c), some resist leftovers are already present both within the precursor and on the SiO_2 layer. The respective height maps are found next to the corresponding morphology image.

Addressing the first micro-dot, which looked unaffected by the resist abrasion, after the annealing routine its surface became rougher, marked by an apparently porous and granular morphology. This can be visible both in the SEM image and CLSM height map in Figures 5.4e and 5.4f. Note that the dome on the left side of the precursor was caused by an EDX measurement in between the first SEM image and the annealing routine. In fact, a fraction of the rim, at the periphery of the micro-dot, disappears after the annealing. This agrees with the EDX mapping discussed previously, which confirms the protruding rim to be a blend of Cu(In,Ga) and organic resist. Referring to the phase diagrams of CuGa and CuIn [162, 163], both have a liquid phase above 300 °C. Therefore, the annealing is partially melting the precursor. At 440 °C, the organic resist is expected to vaporize and degas out of the partially liquid Cu(In,Ga) phase, leading to the formation of the porous morphology upon cooling down to room temperature. A similar conclusion can be drawn from the second precursor as pinholes are clearly formed after the annealing. Furthermore, the resist leftovers that were on the SiO_2 layer, before the annealing (see Figure 5.4c), have been vaporized and are barely visible in Figure 5.4g. Regarding the resist on the precursor itself, the height maps before (Figure 5.4d) and after (Figure 5.4h)

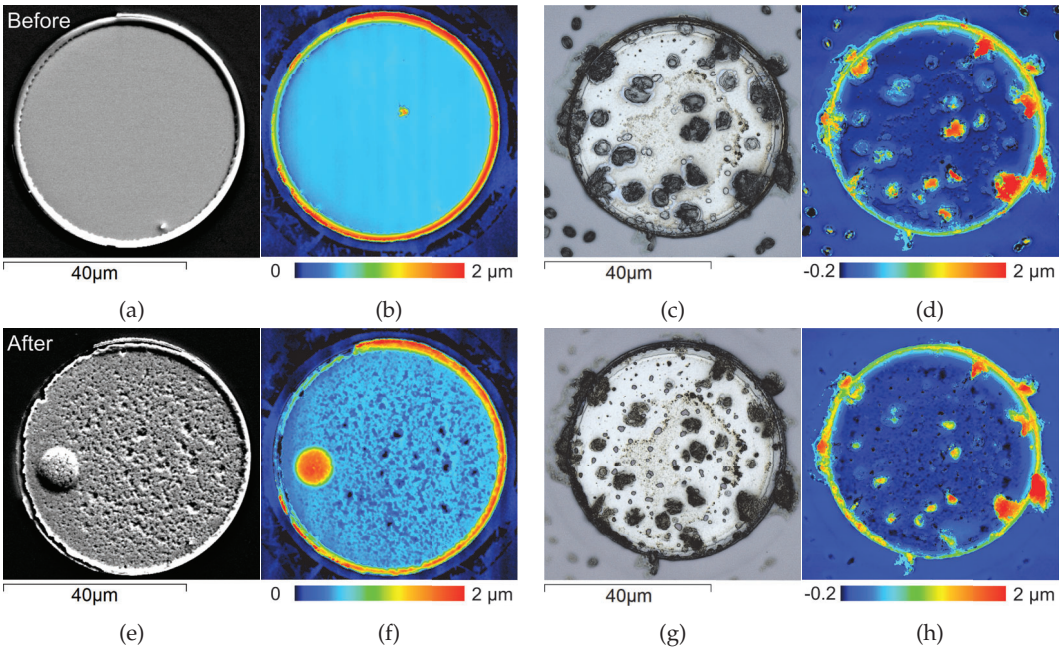

Figure 5.4: SEM and CLSM images of the morphology of two micro-dot precursors (a-d, top row) before and (e-h, bottom row) after the N_2 annealing routine at 440 °C. The CLSM height maps of the respective images are also presented.

the annealing demonstrate that their volume was reduced, meaning that at the very least they were partially vaporized. Thus, the annealing routine in N_2 is indeed effective in at least partly removing the resist leftovers that withstood the cleaning procedure.

Absorber formation

Having investigated how the contaminated metal precursors change after an annealing in inert N_2 atmosphere, the focus goes now to the annealing in Se-containing atmosphere, i.e. selenization, which converts the precursors into CIGSe absorbers. First, the selenization of the pristine precursors is discussed followed by the precursors already annealed in N_2.

The selenization process was performed in a tube oven, as described in chapter 2. The N_2 background pressure was 350 mbar, the amount of Se powder in the graphite box was 150 mg and the annealing time was 20 min for the selenization of pristine precursors, whereas for the already annealed precursors the annealing time was 10 min. For comparison, one N_2-annealed precursor was selenized also for 20 min and the only noticed impact, due to the longer annealing, was the extended damage on the SiO_2 layer. Different annealing temperatures were tested, ranging from 350 °C to 470 °C.

Selenization of pristine precursors

Building up on the results of the previous section, the selenization of the pristine precursors implies that both the vaporization of the contaminants and the formation of the CIGSe absorber happen in parallel. In fact, it was observed previously that the inert

annealing at 440 °C was not enough to completely remove the organics, implying that both processes do happen simultaneously. This is as problematic as it sounds, given that just to prevent the SiO_2 layer from deforming and cracking, the annealing temperature had to be reduced to below 450 °C. This is clearly visible macroscopically, but also at the microscopic level with the CLSM optical image and height map, in Figures 5.5a and b, where the morphology of an absorber annealed at 470 °C is depicted. Regarding the absorber itself, it puts forward a granular morphology that resembles that of CIGSe, as well as some $Cu_{2-x}Se$ platelets, which is expected given the precursor's Cu-rich composition. However, the absorber also seems to be cracked locally and heavily deformed, given its excessive height compared to the SiO_2 layer. The expected thickness of the CIGSe absorber is roughly double that of its precursor, due to the expansion of incorporating Se. In this case, the anticipated thickness of the CIGSe absorber is about 2 µm, that is almost ten-fold less compared to the measured heights.

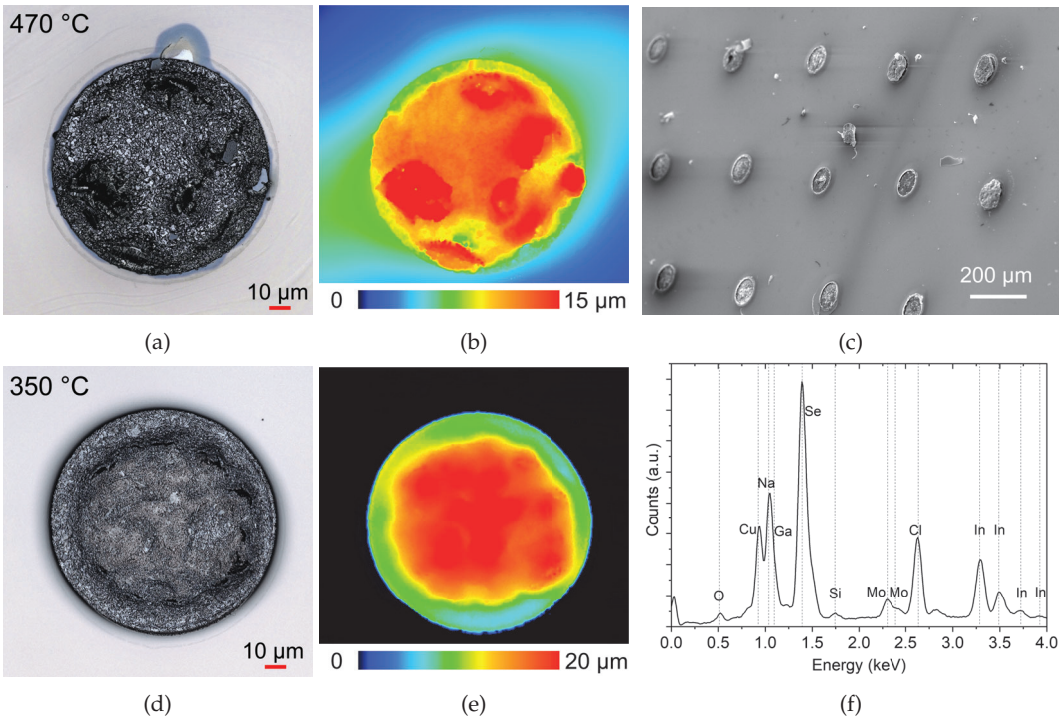

Figure 5.5: CLSM a) optical image and corresponding b) height map of a deformed CIGSe absorber (annealed at 470 °C) and SiO_2 matrix. c) SEM image of a fraction of the micro-dots array, measured with the sample at a 45°angle, to show that the absorbers are barely attached to the substrate. CLSM d) optical image and corresponding e) height map of a deformed CIGSe absorber (annealed at 350 °C). f) EDX spectrum acquired from a deformed CIGSe absorber, measured at 20 kV.

To have a different perspective on the absorber's morphology, an SEM image was captured with the sample inclined at about 45°, as shown in Figure 5.5c. The SEM image shows a fraction of the array of micro-dots, where some have the CIGSe layer barely attached to the underlying substrate, while others only have fractions of the layer and are mostly empty. This demonstrates that most of the absorber's measured volume is hollow,

which drastically compromises the contact between the CIGSe absorber and the Mo back contact layer. In fact, the low adhesion between the two layers also explains why some of the micro-dots were found mostly empty after the annealing. Lowering the annealing temperature to 350 °C did ensure the integrity of the SiO_2 layer, however the CIGSe absorber still shows an excessive deformation, as shown in Figures 5.5d and 5.5e. Obviously, these absorbers cannot be used for solar cells, given the poor adhesion of the CIGSe and the Mo layers. An EDX sprectrum was acquired from a deformed absorber layer and is plotted in Figure 5.5f. Interestingly, a considerable amount of Na (Na/Cu=1.3), and Cl, is observed in the absorber, in addition to the expected elements. Note that this ratio is excessively high compared to standard CIGSe synthesis (Na/Cu < 0.04) [141]. This could either be justified by the presence of Na in the resist contaminants or that the Cu-rich composition alone is not enough to mitigate the Na diffusion from the soda lime glass, at such Se partial pressures. In fact, extrapolating from the observations on the Cu-poor sputtered samples discussed in section 4.3, if the Se partial pressure is too high, the Na diffusion is still consequent, despite the partial blocking due to the suppression of Cu-vacancies. All in all, these results demonstrate that forming the CIGSe phase, having an excess of Na and removing the contaminants simultaneously is not appropriate to obtain a compact CIGSe morphology.

Selenization of N_2-annealed precursors

Given that direct selenization is not viable, in the following the selenization of the precursors, already annealed in N_2, is presented. The introduction of the additional annealing in N_2 improved the selenization process, in the sense that previously problematic annealing temperatures (450 °C), now hardly resulted in cracking of the SiO_2 layer and more importantly the morphology of most (∼60 %) of the arrays of absorbers were compact and within expected thicknesses, as shown in Figures 5.6a and b. Since these absorbers also show quite some Na (Na/Cu=0.4), possible reasons for not reaching 100 % success, may be different Na contents in the soda lime glasses or different amounts of resist contaminants incorporated with the metal precursors, which was also proved to contain Na.

The morphology of the compact absorbers is characterized by a high number of $Cu_{2-x}Se$ platelets on a CIGSe granular layer. To understand if the $Cu_{2-x}Se$ platelets were also present in the bulk of the absorber, a cross-section SEM image was acquired, as shown in Figure 5.6c. Clearly, the metallic-like $Cu_{2-x}Se$ platelets are also present within the absorber's bulk and some are even longer than the layer's thickness, which would make a detrimental shunt path between the top and bottom contact layers, in the case of a solar cell architecture.

An interesting question is how does the CIGSe expand due to the selenization. In fact, it was observed that some absorbers had a larger diameter than their respective precursor, while other absorbers retained a similar diameter. This is visible in Figures 5.7a

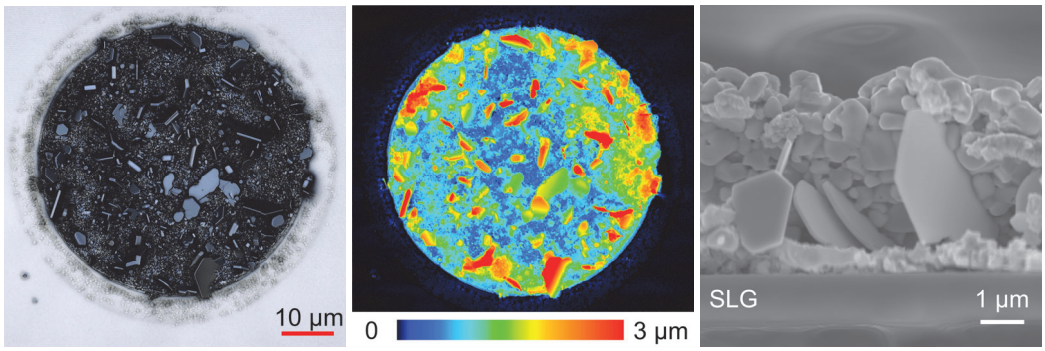

Figure 5.6: CLSM a) optical image and b) respective height map of a compact CIGSe absorber. c) Cross-section SEM of a Cu-rich CIGSe absorber. The $Cu_{2-x}Se$ platelets are visible across the whole absorber's thickness.

and b, where both situations are shown. Additionally, Figures 5.7c and d depict the representative morphology of the precursors to the aforementioned absorbers. In all cases, the measured diameter is highlighted and a schematic cross-section of the hypothesized layer configuration is shown next to the respective height map.

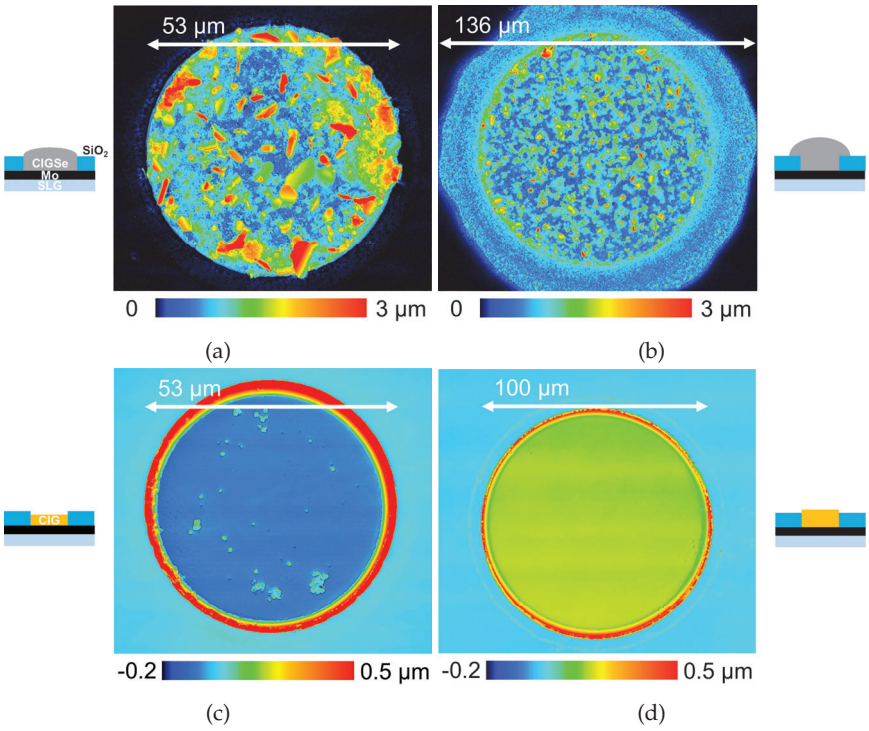

Figure 5.7: CLSM height map of: a) a compact CIGSe absorber. In this case, no expansion beyond the micro-dot's original region is observed. b) a CIGSe absorber that expanded onto the SiO_2 matrix during the annealing in Se. c) a sister micro-dot precursor to the absorber shown in a). Note that the precursor is recessed comparatively to the SiO_2 matrix. d) a sister micro-dot precursor to the absorber shown in b). Note that the precursor is protruding comparatively to the 1 µm thick SiO_2 matrix. A schematic cross-section of the hypothesized layer configuration is depicted next to the respective height map.

The fact that some absorbers have a larger diameter compared to their respective precursor suggests a three-dimensional expansion of the material's morphology during selenization. Although an expansion perpendicular to the substrate (z-direction) was expected, the reason for a growth in the xy-plane, in some cases, is not clear. Raman analysis (spectra not shown), highlight the presence of the chalcopyrite A_1 mode also beyond the micro-dot's original diameter, which confirms the CIGSe absorber is expanding in both directions. The extent of the absorber's lateral expansion seems to be correlated with the height of the respective precursor compared to the SiO_2 layer. More precisely, a precursor with a height lower than the SiO_2 layer, as in Figure 5.7c, resulted in a minimal lateral expansion after selenization, as Figure 5.7a shows. Conversely, a protruding precursor, as in Figure 5.7d, led to a consequent lateral expansion after selenization, as depicted in Figure 5.7b. Assuming that the SiO_2 matrix is not deformed, the observed expansion is likely related to the liquid phase, that the precursor forms at higher temperature, which flows beyond the original micro-dot's diameter.

To discard a deformation of the SiO_2 matrix, EDX was measured from the SiO_2 layer towards the center of the absorber, spatially resolving the Si signal, as shown in Figure 5.8a.

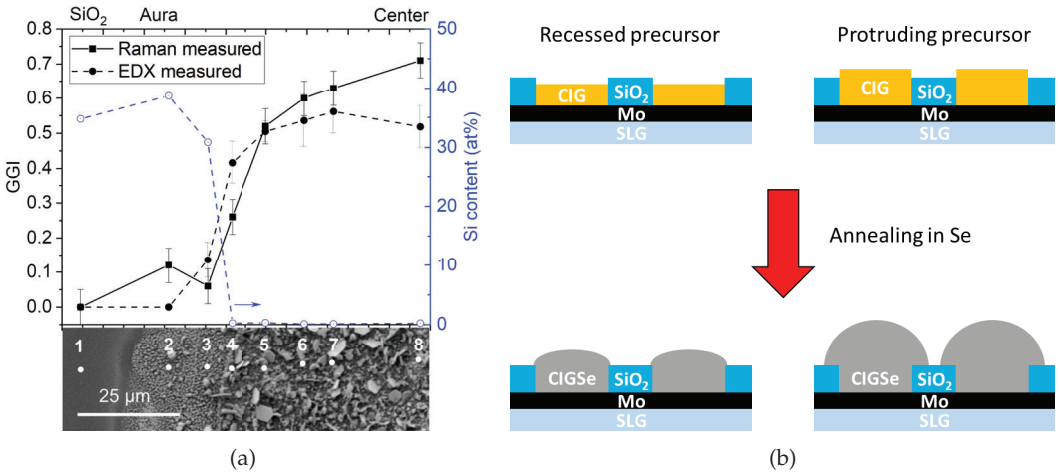

Figure 5.8: a) GGI ratio and Si content measured from the SiO_2 layer towards the center of the CIGSe micro-absorber. b) Schematic cross-section of the sample geometry before and after annealing in Se, illustrating the influence of the precursor's height, relative to the SiO_2 matrix, on the final absorber's morphology.

The Si content stays constant outside the original diameter of the micro-dot, i.e. micro-dot's aura, and quickly decreases to zero inside it. This confirms the CIGSe absorber grows in a muffin-top fashion, as illustrated in Figure 5.8b, and discards the deformation of the SiO_2 layer by the lateral expansion of the CIGSe.

Interestingly, the distribution of Ga in the absorber is different inside the micro-dot and within the aura, as demonstrated in Figure 5.8a through the GGI. The spatially resolved EDX and Raman analysis (GGI deduced from A_1 mode position) both corroborate that no or very low Ga is found in the aura region, whereas a high Ga content is found

inside the micro-dot's original diameter. This suggests that the chalcopyrite phase that lead to the formation of the aura, outside of the micro-dot, is $CuInSe_2$. Mainz et al. have shown that during selenization, In tends to migrate to the surface, causing Ga to segregate at the back of the absorber [164]. Here, it is speculated that the lateral diffusion of In hinders the diffusion of Ga towards the aura. Thus, one function of the SiO_2 layer is to retain the CIGSe film's shape and consequently, composition homogeneity. Since the targeted absorber thickness is in the 2 µm range, a similar SiO_2 thickness is preferable to guide the CIGSe absorber.

Despite clearly improving the outcome of the selenization, with a 60 % success rate, the addition of the inert annealing by itself does not guarantee a controlled absorber morphology and adhesion to the Mo layer. As also suggested in section 4.3 of chapter 4, the high Se partial pressure, during the selenization step, may increase the Na diffusion from the soda lime glass, which compromises the adhesion between the CIGSe and the Mo layer. This shows that controlling the Se partial pressure during the annealing is crucial to obtain compact CIGSe absorbers.

Device characterization

This section covers the characterization of absorbers that were converted into micro solar cells. Given the consequent Cu-rich composition of the absorbers, a KCN (10 wt% for 5 min) treatment [165], followed by the chemical bath deposition of a 50 nm CdS buffer layer are applied to the array. The former has the aim of removing the $Cu_{2-x}Se$ platelets from the absorbers and the CdS buffer layer to improve the CIGSe interface and form the pn-junction. To convert the absorbers into solar cells, the transparent conductive oxide layers (i-ZnO/ZnO:Al) are deposited by sputtering.

To assess the quality of the solar cells in the array, EQE and JV measurements were performed in Figure 5.9. From semi-quantitative EQE spectra on individual micro solar cells, as exemplified in Figure 5.9a, the average bandgap is estimated to $E_{gap}^{EQE} = 1.3 \pm 0.1$ eV. This value agrees well with the bandgap $E_{\text{gap}} = 1.3 \pm 0.2$ eV calculated empirically from the GGI of the metal precursors (GGI=0.46) [166]. The general shape of the EQE suggests a poor carrier collection in the infrared range above the bandgap. Additionally, the drop in the UV-region is associated to parasitic absorption by the CdS buffer layer.

The number of electrically active solar cells was estimated by probing each one with the EQE beam (at 532 nm) and by measuring the resulting current. Out of 198 solar cells, 182 were electrically active. Finally, JV measurements on groups of micro solar cells was performed. The preference of groups over individual solar cells was to facilitate the mechanical scribing of the window layers, meant to electrically isolate each group of solar cells, and to minimize the risk of shunt paths. It is noted that when connected in parallel, the current of each solar cell, in the group, contributes to the total measured current, while the open-circuit voltage of the group is given by the lowest individual open-circuit voltage. Figure 5.9b shows the JV characteristics of a pair of isolated micro solar

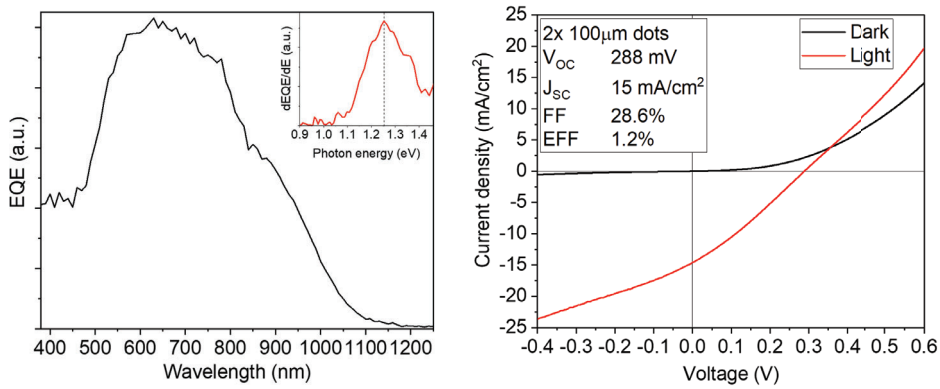

(a) (b)

Figure 5.9: a) Semi-quantitative EQE from one micro solar cell. The energy derivative of the EQE is shown as inset to determine the bandgap. The EQE is semi-quantitative because the laser beam size was larger than the micro solar cell's active area. b) JV characteristics in the dark and under illumination of a group of two micro solar cells connected in parallel. Key parameters are summarized as inset.

cells, connected in parallel. The devices show a diode-like behavior with an efficiency of $(1.2 \pm 0.3)\,\%$ under 1 Sun. A low shunt resistance ($60\,\Omega\text{cm}^2$) and a relatively high series resistance ($3.4\,\Omega\text{cm}^2$) were measured, as well as a voltage-dependent current collection. These are possibly related to shunt paths resulting from the large $Cu_{2-x}Se$ platelets within the absorbers and potential pinholes and defects caused by the platelets during the synthesis process and the KCN treatment. The short-circuit current density Jsc is found to be 15 ± 2 mA/cm^2 which is in line with the EQE showing very poor collection in the near-infrared region. Larger groups of micro solar cells also showed a diode behavior, however the shunt resistance was even lower in these cases. The active area used for the JV measurements was calculated by taking the number of individual micro solar cells in a group and multiplying by the area of a single disc of 100 µm diameter.

To conclude the synthesis of Cu-rich micro solar cells, it was demonstrated that this material-efficient sputtering and annealing route can lead to working micro solar cells, however multiple issues were encountered which limited the achieved PCEs. First, the sputtering process introduces resist contaminants in the precursors, which imposed the introduction of an extra synthesis step to extract the resist and obtain compact CIGSe absorbers. It is speculated that the high density of micro-dots in this pattern, i.e. the reduced spacing between neighbour micro-dots, could promote the abrasion of resist during the precursor's sputtering. Thus, in the following, patterns with a lower density of micro-dots are used. Increasing the space between micro-dots also simplifies the process of electrically isolating individual micro solar cells. Secondly, a significant amount of Na was found in all selenized absorbers, which could originate either from the contaminants or by diffusion from the soda lime glass. Since no Na was detected in the precursors without visible contaminants, the diffusion from the soda lime glass, also observed in chapter 4, seems more likely. In any case, this could explain why not all synthesized absorbers were compact. Finally, it was observed that the thickness of the SiO_2 is important,

as it helps holding the precursor's shape during the annealing step. Indeed, a SiO_2 thickness lower than that of the Cu(In,Ga) precursor will lead to a muffin-top morphology after annealing in Se. This was observed to cause a lateral composition inhomogeneity, which is detrimental for the solar cell's performance. For this reason, a thickness of 2 µm is used in the following. Despite these issues, multiple groups of working micro solar cells were achieved, with the highest PCE being 1.2 % for a group of two devices.

5.1.2 Cu-poor solar cells

Despite having achieved working micro solar cells with Cu-rich CIGSe absorbers, it is of particular interest to investigate Cu-poor CIGSe absorbers. This is the case as the Cu-rich absorbers are known to be limited by interface recombination and by tunnelling enhanced recombination, due to their high doping level, which reduces the resulting solar cell's V_{OC} and J_{SC}, respectively [44].

In chapter 4, an important finding about Cu-poor CIGSe absorbers is that the patterned SiO_2 layer causes a detrimental enhanced diffusion of Na, from the soda lime glass, through the micro-dots. This issue was mitigated by the introduction of a Na blocking layer, like Al_2O_3 or SiO_xN_y. However, completely depriving the CIGSe absorber of Na during synthesis led to the peeling of the material from the substrate. Therefore, the use of substrates with a Na blocking layer is complemented by performing the annealing step in a Na-containing graphite box. In this way, the peeling of the film is expected to be avoided [141].

For this section, a 100 nm Al_2O_3 layer was used as Na barrier and the SiO_2 pattern containing arrays of micro-dots with varying diameter is chosen. This allows to also investigate if the size of the micro-dots is relevant during the synthesis process.

Precursor characterization

In the following, the morphology of the Cu-poor sputtered precursors is investigated. Figures 5.10a and b show the morphology and respective height map of a filled micro-dot. As can be noticed, the morphology of the precursor is identical to that in section 4.3, where the metal precursor had been deposited both inside the micro-dots and on the SiO_2 layer. In short, the morphology consists of a relatively thin Cu-rich compact underlying layer and an In-rich rough top layer made up of irregularly shaped agglomerates. Further EDX analysis show an average compositional ratio CGI of 0.72 and a GGI of 0.21. Although the CGI ratio is rather low compared to stoichiometry, reports have demonstrated relatively high PCEs (∼10 %) can be obtained for CIGSe solar cells from precursors with a similar composition as here [167, 168]. Thus, these precursors are in line with the objectives of this study.

Given the resist contamination issues observed in the case of sputtered Cu-rich, an annealing in N_2 inert atmosphere at 250 °C for 20 min is also performed to cross-check the Cu-poor case. The resulting morphology and height map are depicted in Figure 5.10c and d.

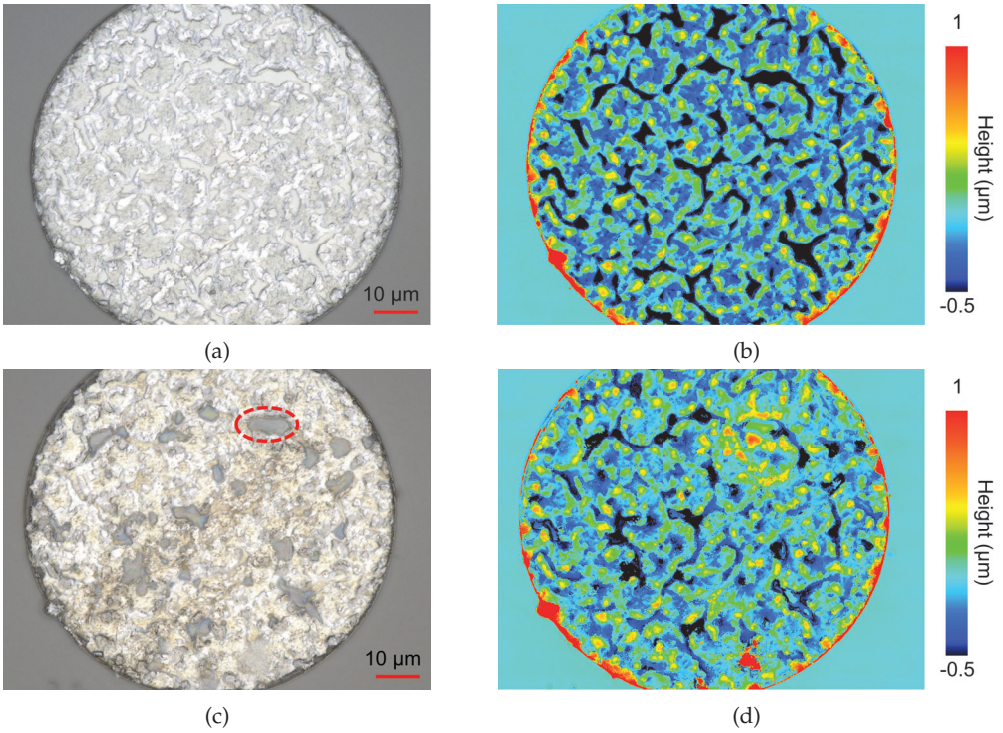

Figure 5.10: CLSM optical image and respective height map of the same micro-dot precursor (a and b) before and (c and d) after an inert annealing in N_2. Red dashed ellipse highlights one of the regions where the Mo layer was exposed after the N_2-annealing.

After annealing, both the appearance and the morphology of the metal precursors are rather different. In fact, the film seems to coalesce and form some holes in between the In-rich agglomerates, where the layer was already thinner. In these regions, the underlying Mo layer is even exposed after the N_2-annealing, as corroborated by EDX analysis (spectrum not shown). Anticipating the consequences for the annealing in Se atmosphere, the formation of these holes reveals an easy access for Se to form the conductive $MoSe_2$ layer, which is detrimental when excessively thick [169]. Additionally to the holes, the precursor layer changed to a yellowish appearance, which suggests that some resist contaminants were still present. Although, no large remnants of resist were found as was the case for the Cu-rich sputtered sample, implying decreasing the density of micro-dots was beneficial. However, the Cu-poor sample (discussed in section 4.3) sputtered without resist, did not show any modification after being annealed in the same way as the present precursors. These observations corroborate with the hypothesis of resist damage during sputtering and demonstrate that increasing the spacing separating micro-dots was not enough to avoid the contamination of the precursors by the resist.

Absorber formation

Impact of precursor's N_2-annealing

To assess the impact of the annealing in N_2, the pristine and N_2-annealed precursors are selenized in identical conditions. In this case, the annealing temperature was 450 °C for 10 min with 100 mbar of N_2 background pressure and 40 mg of Se powder. The morphology of the resulting CIGSe absorbers are discussed in the following, starting with the pristine precursor. Figure 5.11 regroups CLSM optical and height images of the same micro-dot before and after the annealing in Se.

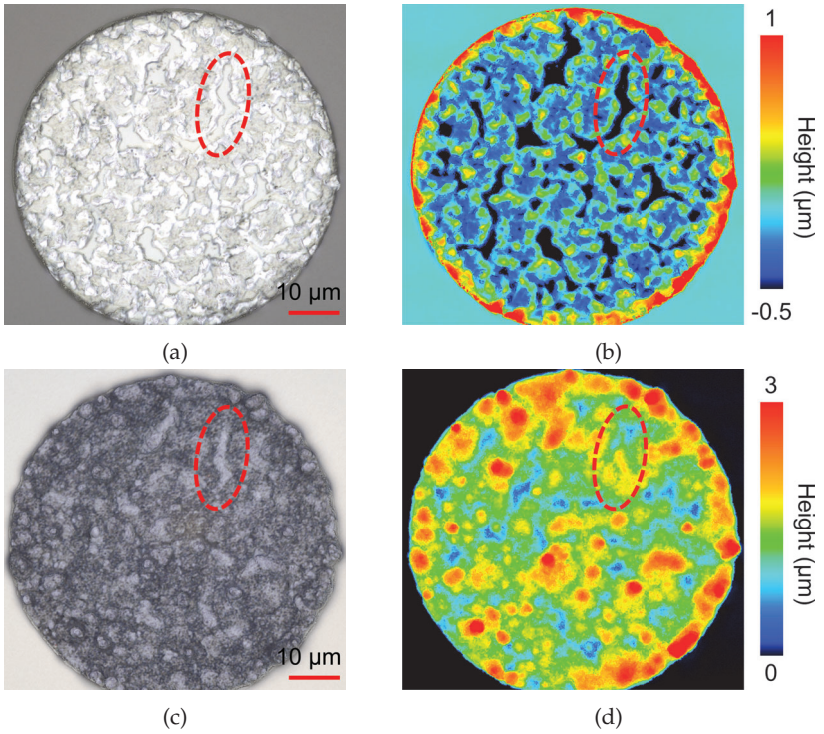

Figure 5.11: CLSM optical image and respective height map of: a) and b) micro-dot Cu(In,Ga) precursor. c) and d) CIGSe absorber after annealing in Se. Red dashed ellipses highlight the same region, in the precursor and in the absorber, where the precursor shows a valley in-between In agglomerates and, after annealing, the same region is identifiable in the absorber, however its morphology is substantially different.

Interestingly, when comparing the optical images of the precursor (Figure 5.11a) and absorber (Figure 5.11c), it appears that some regions, in particular the valleys in between In agglomerates, formed grains with a similar shape after the annealing in Se. However, this correlation between shapes is not visible when comparing the height maps (in Figures 5.11b and d). Nevertheless, the height maps do show a thinner absorber in some of the regions where the precursor was also thin, which suggests that the lateral diffusion of elements during the annealing in Se is rather consequent (estimated to a few micrometers) in the xy plane. Zooming in on a sister absorber, SEM imaging in Figure 5.12a unveils that the absorber layer has some micrometer-sized holes that, according to EDX spectra in Figure 5.12b and Raman in Figure 5.12c, expose the Mo/$MoSe_2$ back contact.

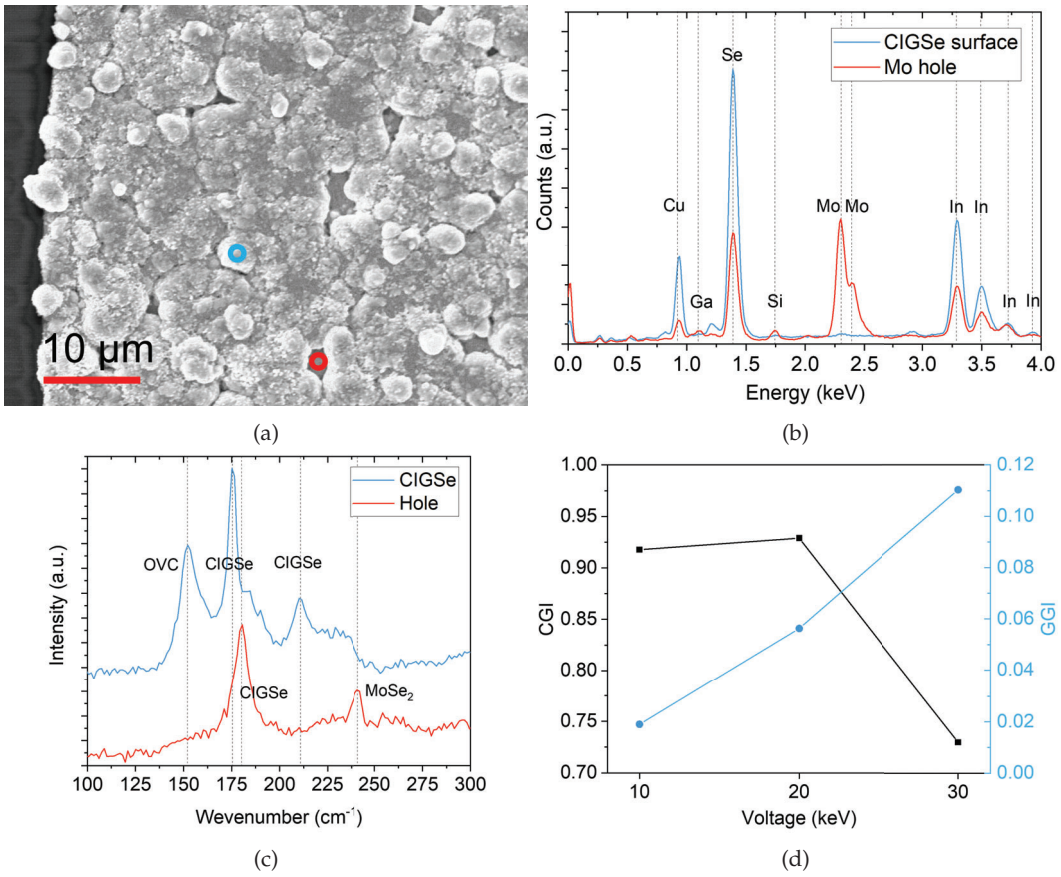

Figure 5.12: a) SEM close-up image on the edge of a micro-dot containing a CIGSe absorber. At this magnification, it is possible to identify microscopic holes in the absorber layer. Red and blue circles indicate the locations where EDX spectra in b) were acquired. b) EDX spectra measured at 20 kV from the locations drawn in a). c) Raman spectra measured from the locations indicated in a). A 532 nm excitation laser was used for surface-sensitivity, as it probes a depth of less than 100 nm [170]. d) Compositional ratios CGI and GGI, calculated from EDX spectra, as a function of the acceleration voltage.

Additionally, the Raman spectrum from the hole, also detects a Ga-rich CIGSe phase at 180 cm^{-1}, which would suggest a GGI of roughly 0.60. At the surface of the CIGSe micro-absorber, Raman detects a Ga-poor (GGI=0.1) CIGSe phase through the A_1 mode wavenumber position at 175 cm^{-1}. The second peak associated with the CIGSe, at 212 cm^{-1}, corresponds to the E/B modes [171]. Furthermore, an ordered-vacancy compound (OVC) phase is also detected, at 152 cm^{-1}, at the surface [172], which was to be expected given the low CGI of the metal precursors (CGI=0.72). To confirm the elemental depth distribution of the CIGSe phase, Figure 5.12d presents the elemental ratios CGI and GGI extracted from EDX spectra acquired at three acceleration voltages (10 kV, 20 kV and 30 kV). Starting with the lowest voltage, i.e., the most surface sensitive measurement, the average measured CGI was 0.92, however locally CGI values as low as 0.67 were measured, which suggests that only a few regions contain the OVC phase, as suggested by Raman. The lowest GGI value was indeed measured at the surface, however its absolute value (0.02) is lower than suggested by Raman. Nevertheless, at 20 kV, the GGI increases whereas the

CGI remains the same. Finally, at the back, or at 30 kV, EDX confirms the highest value for GGI (0.11). Note that despite the absolute GGI values being different, between Raman and EDX, the relative ratio between GGI at the surface and at the back is very similar. Studies on sequential selenization processes show that In diffuses to the front surface, due to the lower surface free energy of formation of $CuInSe_2$ compared to CIGSe [173, 174]. This pushes the Ga-containing phase towards the Mo interface, which corroborates with the above observations. The accumulation of Ga at the back is in fact beneficial, as it induces a Ga-rich phase, i.e. with a higher bandgap, which in turn reduces carrier recombination at the back contact, improving V_{OC} [175]. Interestingly, the micro-absorber shows a depletion of Cu at the back, as the CGI drops to 0.73. Together with Raman, these results suggest that the OVC phase is found either at the front and at the back or throughout the depth of the absorber. It is also worth noting that no Na peak is measured with EDX, which confirms the good behavior of the implemented Na barrier.

Moving to the CIGSe absorber that corresponds to the precursor annealed in N_2, Figure 5.13 presents CLSM optical and height images before and after the annealing in Se.

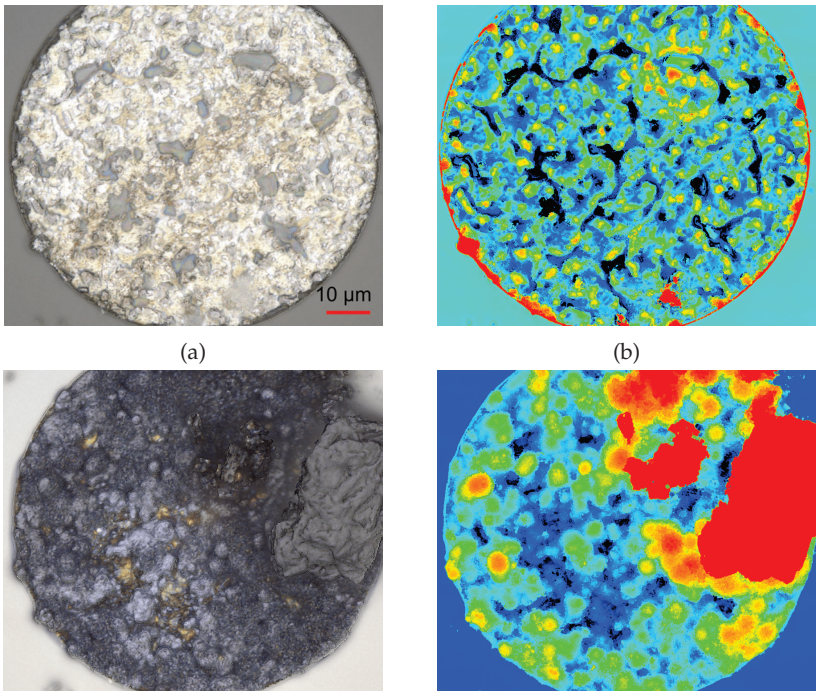

Figure 5.13: CLSM optical image and respective height map of: a) and b) micro-dot Cu(In,Ga) precursor annealed in N_2. c) and d) CIGSe absorber after annealing in Se.

The respective optical images, in Figures 5.13a and c, show that in the regions where the precursor had the Mo exposed, an orange phase seems to form, contrasting with the dark grey CIGSe phase. The orange phases will be discussed later in this section. Note that on the right side of the layer, a lump of Se solidified on the CIGSe layer covering part of the absorber morphology. Nevertheless, comparing the height maps, in Figures 5.13b and d, the holes in the precursor resulted in a thinner absorber in these particular regions,

which makes it prone to be more affected by interface recombination and ultimately result in a worse device performance [56]. Thus, the annealing in N_2 is not beneficial in this case and will therefore not be further investigated.

Influence of Se partial pressure on phase formation

In the following, different annealing conditions are investigated to optimize the morphology and the optoelectronic of the resulting CIGSe micro-absorbers. Literature has shown that a controlled supply of Se is required to optimize the morphological and optoelectronic properties of the resulting CIGSe absorber [55, 176]. On the one hand, an insufficient supply of Se compromises the chalcopyrite phase purity [177]. On the other hand, an excessive supply of Se implies that more Se will reach the Mo interface and form an overly thick $MoSe_2$ resistive layer [178]. Thus, it is of great interest to regulate the influx of Se that reaches the precursors. This is achieved by controlling the Se partial pressure in the system. The graphite box in a tube oven configuration being a common setup [179, 180], for the annealing in Se step, J. J. Scragg originally modelled the partial pressure of Se based on gas pressure equilibrium principle [181]. In short, the model starts with the graphite box and the respective lid inside a closed system. The background pressure, at room temperature, $P_{N,RT}$ is determined by the amount of N_2 introduced in the system before the annealing. At the annealing temperature T_{Anneal}, the Se powder, inside the graphite box, has partially evaporated leading to a Se partial pressure $P_{Se,box}$. This Se partial pressure lifts the lid and a fraction F of the Se gas phase escapes the graphite box until an equilibrium pressure, inside the graphite box and outside, is reached. Han et al. improved the model by additionally considering the pressure from the weight of the lid P_{lid} and the fraction of Se vapor C that condensates at the chamber's cold outer walls [55]. Note that C ranges from 0 to 1 and depends on the specific system configuration. Therewith, the equilibrium partial pressure of Se $P_{Se,eqm}$ inside the graphite box is given by:

$$\frac{P_{Se,eqm}}{P_{Se,box}} = 1 - F = 1 - \frac{P_{Se,box} + C \cdot P_{N,T_{anneal}} - P_{lid}}{(P_{N,T_{anneal}} + P_{Se,box}) \cdot (1 + \frac{V_{box}}{V_{chamber}}(1 - C))} \tag{5.1}$$

With $P_{N,T_{anneal}}$ being the N_2 partial pressure at T_{anneal} and is given by $P_{N,T_{anneal}} = P_{N,RT} \cdot \frac{T_{Anneal}}{T_{RT}}$. As specified above, P_{lid} is the pressure exerted by the lid's weight m with a surface A: $P_{lid} = \frac{mg}{A}$, with g being the gravitational acceleration constant. V_{box} and $V_{chamber}$ are the volumes inside of the graphite box and the chamber respectively. Finally, the partial pressure of Se inside the graphite box $P_{Se,box}$ is calculated with the ideal gas law assuming the Se vapor phase is composed of Se_2 molecules only.

Traditionally, CIGSe is known to demonstrate better device properties when annealed at higher temperatures, usually around 550 °C [182]. However, due to the introduction of the Al_2O_3 diffusion barrier to the stack, it was required to test for the thermal stability of the new stack. Indeed, it was found that the SiO_2 layer is severely cracked at 550 °C, however at 525 °C the cracking seems to be minimal. At these temperatures,

the effect of $P_{Se,eqm}$ on the morphology of micro-absorbers, with different diameters, is clearly visible. In fact, for both temperatures, a $P_{Se,eqm}$ around 120 mbar resulted in heavily damaged CIGSe layers for smaller diameters, whereas reducing $P_{Se,eqm}$ to 11 mbar led to compact CIGSe micro-absorbers independently of their diameter. To illustrate this effect, Figure 5.14a is a plot of the relevant annealing parameters, T_{Anneal} and $P_{Se,eqm}$, as a function of the damage of the CIGSe micro-absorber for the different diameters that were investigated. To assess the damage of the micro-absorber, the average height of the CIGSe, compared to the SiO_2 layer, is used as criteria to color-map the corresponding circle in the plot. To distinguish between the different diameters, the diameter of each circle is proportional to the corresponding micro-absorber's diameter. In other words, for each set of annealing parameters, 13 concentric circles, representing the 13 different diameters, are color-coded according to the respective absorber's extruded height. To exemplify the criteria that define the scale of the color map, the height map of a compact micro-absorber is shown in Figure 5.14b, giving a green ring in Figure 5.14a, and that of a deformed micro-absorber is presented in Figure 5.14c, giving a red ring.

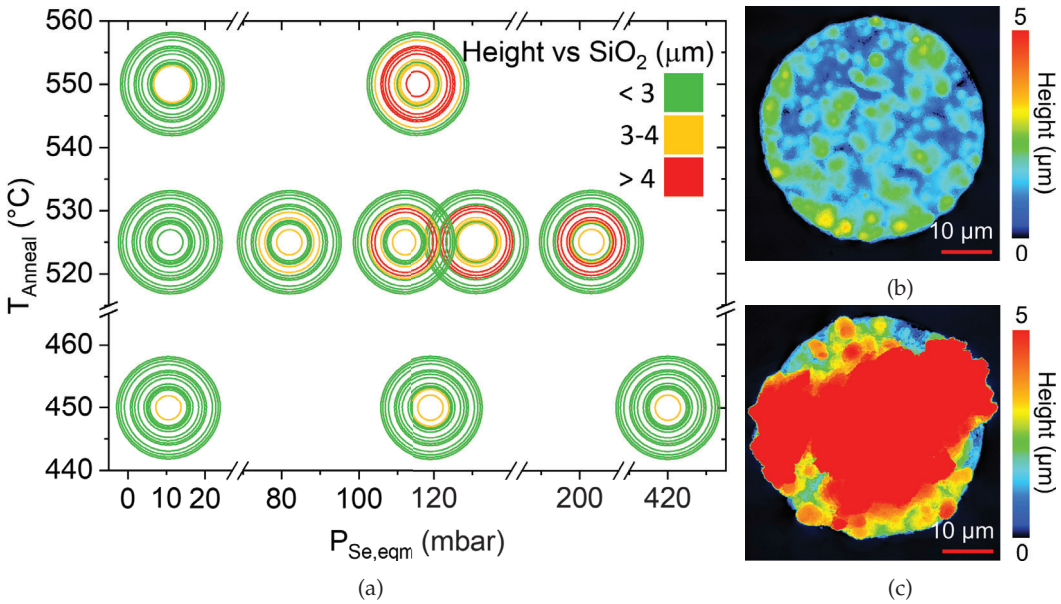

Figure 5.14: a) Colormap representation of the CIGSe absorber's average height, compared to the surrounding SiO_2 matrix, as a function of the annealing parameters (annealing temperature and Se partial pressure). Each group of concentric circles contains 13 data points pertinent to the micro-dots in the same array, i.e. annealed in the same conditions. The diameter of each micro-dot is represented by the diameter of the respective circle, which was calculated with the logarithm of the real micro-dot diameter in order to facilitate visualization. The real diameters are: 500, 400, 300, 200, 100, 80, 60, 40, 20, 15, 12.5, 10 and 5 µm. CLSM height map of a b) compact CIGSe absorber (shown as green in a) - 60 µm diameter, 525 °C and 11 mbar) and a c) deformed absorber (shown as red in a) - 60 µm diameter, 525 °C and 131 mbar).

Independently of the annealing temperature, it is clear that $P_{Se,eqm}$ has a crucial impact on the absorber's morphology. In general, the higher the $P_{Se,eqm}$, the higher the number of damaged micro-absorbers, with those with a smaller diameter being the most

sensitive to $P_{Se,eqm}$. Focusing on the micro-absorbers annealed at 525 °C, each diameter seems to have a different pressure threshold $P_{Se,t}$ above which $P_{Se,eqm}$ causes the absorber to be damaged. Furthermore, this pressure threshold shifts to lower values if T_{Anneal} is increased and to higher values if the T_{Anneal} is decreased. As an example, the micro-absorber with 100 µm diameter is damaged when annealed at 550 °C and 120 mbar, whereas it remains intact when annealed at 525 °C with the same $P_{Se,eqm}$. As a side note, a higher $P_{Se,eqm}$ was also observed to cause more fissures and further damage to the SiO_2 layer. To compare with the previous Cu-rich section, where only 60 % of the micro-absorbers were undamaged, the Na-barriered Cu-poor micro-absorbers annealed at the same conditions (450 °C, 150 mg Se, $P_{N,RT} = 350$ mbar, $P_{Se,eqm} = 420$ mbar) did not show any damage. This further emphasizes the importance of the Na barrier, even for Cu-rich micro-absorbers.

From the front surface, the morphology appearance of all the Cu-poor micro-absorbers, damaged or intact, is similar. Thus, to investigate the reason why the diameter is relevant for particular $P_{Se,eqm}$ and T_{Anneal} parameters, it is of interest to explore the interface between the Mo back contact and the CIGSe layer. To access the back side, the micro-absorbers are transferred onto a strip of kapton tape. CLSM optical images are then acquired from micro-absorbers with different diameters, both from the substrate side (see Figures 5.15a-b) and from the micro-absorber back side (in Figures 5.15c-d). Note that with this method, the damaged micro-absorbers, i.e. with smaller diameters, easily transferred to the tape, leaving behind mostly an empty micro-dot. However, for the intact micro-absorbers, only a small portion of the absorber was transferred to the tape and the rest remained attached to the back contact, proving their superior adhesion to the Mo.

Comparing the back interface of the different micro-absorbers, it is evident that those with smaller diameter show an orange crystalline phase that covers most of the back side. In contrast, the micro-absorbers with larger diameters show mostly a grey phase with a granular structure, which resembles the CIGSe phase. Nevertheless, some orange crystals are also visible, however to a much lower extent. This suggests that the holes with smaller diameter induce the formation of micro-absorbers with a double layer structure, whereas the larger holes show the formation of mostly a single phase. Assuming the double layer structure is responsible for the peeling of the micro-absorbers, it seems that the $P_{Se,eqm}$ greatly influences the formation mechanism of the CIGSe phase, as in the cases of lower $P_{Se,eqm}$, all micro-absorbers were intact.

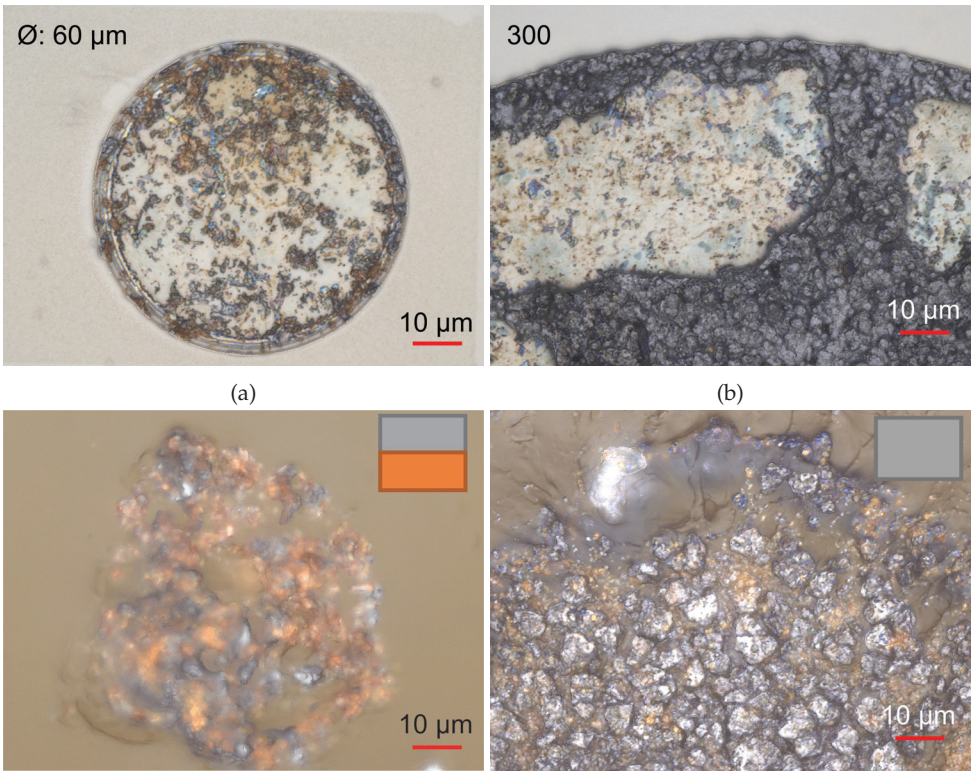

Figure 5.15: CLSM optical image of a a) 60 µm and b) 300 µm diameter micro-dots after removal attempt of the CIGSe absorber. CLSM optical image of the back side of the extracted CIGSe absorber from the c) 60 µm and d) 300 µm micro-dots. The brown background is the kapton tape. A side-view schematic of the double and single layer phase is depicted in the respective image, on the top right corner.

EDX analysis show no sign of Na in this case, which means the Na barrier was effective and these orange crystals are a different phase than that observed in the co-evaporation case, in chapter 4. Furthermore, independently of the diameter of the holes, EDX (at 10 kV) shows a composition ratio (Cu:III:Se) of 1:1:2 at the surface of the micro-absorbers, suggesting a Cu(In,Ga)Se_2 phase. However, concerning the back interface, the analysis could not identify an individual phase. Instead, Raman analysis is able to differentiate phases at the surface and at the back, as shown in Figure 5.16. Figures 5.16a and b are CLSM optical images of micro-absorbers with a large and a small diameter, respectively, to help identifying the investigated regions.

Starting from the front side of the micro-absorbers, remaining inside the holes (spectrum 1), a similar spectrum is obtained for both diameters. The typical modes of CIGSe are observed at 175 cm^{-1} (A_1 mode) at in the range 210-230 cm^{-1} (B_2 and E mixed modes). The A_1 mode's position suggests a low Ga content as also measured with EDX. Additionally, the main peak (A_1 mode) of the the OVC phase, $CuIn_3Se_5$, is measured at 154 cm^{-1} [121]. Focusing on the back interface of the large diameter micro-absorber (spectrum 2), the leftover grey phase shows again the typical modes of the CIGSe phase (A_1 and mixed

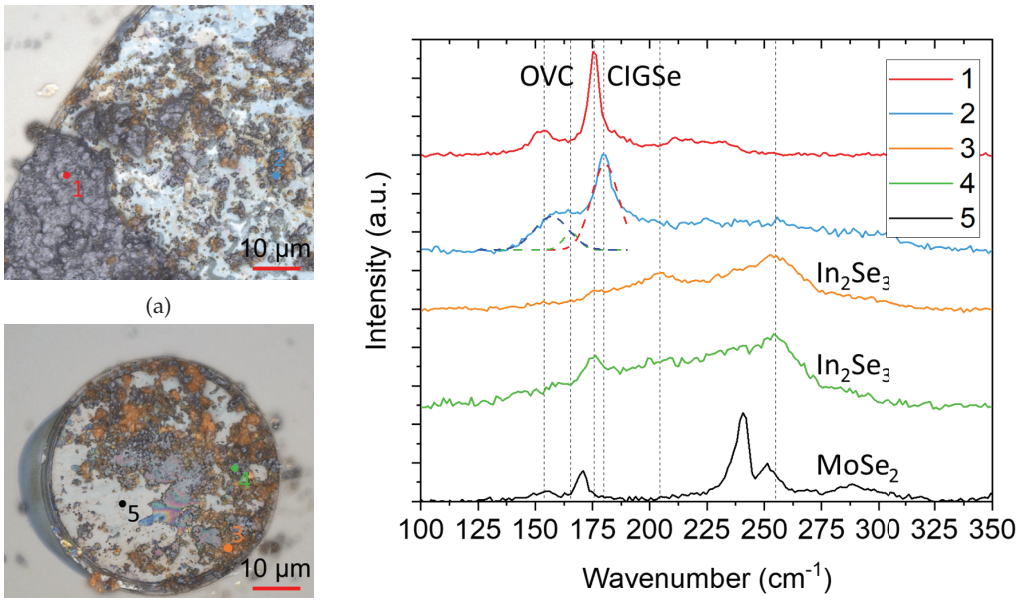

Figure 5.16: CLSM optical image of a a) 400 µm and b) 80 µm diameter micro-dots after removal attempt of the CIGSe absorber. Raman measurement locations are numbered and color-matched to the respective spectra. c) Raman spectra measured from the locations indicated in a) and b). Dashed curves are fittings to the spectrum in location 2, in the 150-190 cm^{-1} range, based on the modes of from the two OVC phases ($CuIn_3Se_5$ - blue peak and $CuGa_3Se_5$ - green peak) and the A_1 mode of CIGSe (red peak).

B_2, E modes), however the wavenumber of the A_1 mode is shifted to 180 cm^{-1}, confirming a Ga-rich CIGSe phase at the back interface. Additionally, a fitting to the 150-190 cm^{-1} range, suggests the presence of two OVC phases at 157 cm^{-1} and 166 cm^{-1}, which match the main modes of $CuIn_3Se_5$ and $CuGa_3Se_5$ phases [121]. Finally, it is possible that some signal from the neighboring orange crystals is measured in the 200-260 cm^{-1} range, as the background level is not reached. To measure these crystals more objectively, two measurements were taken in the hole with smaller diameter, where the density of orange crystals is larger. In both cases (spectra 3 and 4), the most intense peak is located at 255 cm^{-1}, followed by a secondary peak at 204 cm^{-1}. According to literature, this could correspond to a In_2Se_3 phase, where the main peak, at 254 cm^{-1}, is associated with the Se_8 ring vibrations [183, 184]. Given the low CGI (0.72) of the precursor, this phase is in fact expected to be formed. A low intensity Ga-poor CIGSe A_1 mode is also measured at 176 cm^{-1}, given the proximity of the two phases. Lastly, the Raman spectrum of $MoSe_2$ is also shown to insure they do not match with those observed in the In_2Se_3 phase.

To conclude, measurements suggest that the diameter of the micro-absorbers has an influence in the phase formation, where the smaller diameters result in a configuration closer to a double layer of CIGSe and In_2Se_3, whereas the larger diameters form mostly a single layer with a few In_2Se_3 crystals. Since the initial composition was similar, it is hypothesized that the distribution and density of OVC phases is different for distinct diameters.

Influence of Se partial pressure on absorber's ΔE_F

To solve the morphology issue, one could simply anneal with lower $P_{Se,eqm}$, as this reduced the peeling of the micro-absorbers. However, the morphology of the micro-absorbers does not provide direct information about their optoelectronic properties, thus it is relevant to also investigate how the quasi-Fermi level splitting ΔE_F is impacted when the annealing conditions are changed, as it is a figure of merit for the solar cell devices. To separate the effect of the annealing parameters from the effects of the micro-dots diameter, Figure 5.17a shows the ΔE_F measured only from 500 µm micro-absorbers prepared under different annealing parameters, i.e., at different temperatures and different $P_{Se,eqm}$. To address the effects of the micro-dots diameter, Figure 5.17b compares the maximum photoluminescence (PL) counts measured from micro-absorbers with different diameters synthesized under the same conditions.

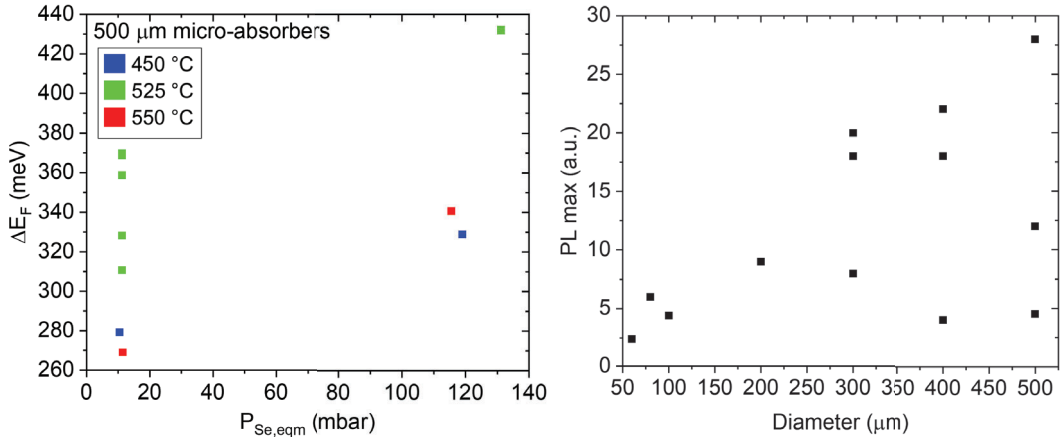

Figure 5.17: a) ΔE_F as a function of the Se partial pressure and temperature during the absorber annealing for micro-dots with a diameter of 500 µm. b) Maximum PL counts as a function of the absorber's diameter. All absorbers compared here were annealed at 525 °C with a $P_{Se,eqm}$ of 130 mbar.

Concerning the impact of the annealing parameters, it stands out firstly that a higher $P_{Se,eqm}$ results in a higher ΔE_F for all annealing temperatures. Conversely, Han et al. had observed that in large area CIGSe the V_{OC}, which is directly connected to ΔE_F, hardly changed (< 5 % change over 1 order of magnitude $P_{Se,eqm}$) with $P_{Se,eqm}$ and was around 400 mV [55]. Here, it is assumed that, like in our process, the deposition of the buffer and window layer only leads to marginal losses in ΔE_F, making it possible to directly compare ΔE_F and V_{OC}. Note that Han et al's process is similar to ours here, except for the annealing temperature which is lower in our case (525 °C compared to 600 °C). Back to Figure 5.17a, increasing the $P_{Se,eqm}$, allowed to improve the ΔE_F up to 430 meV. This highlights that the annealing conditions have a larger impact when using the patterned substrates compared to the typical unpatterned substrates. Regarding the effect of annealing temperature, it is observed that 525 °C had the best result. As mentioned previously, literature has proven that a higher temperature leads to a better performance, which is

also observed here when comparing to 450 °C. However, 550 °C shows a lower performance, which is likely due to the extra stress introduced by the thermal expansion of the SiO_2 matrix and the Na-barrier. Nevertheless, a ΔE_F of 430 meV (or equivalently a ΔE_F loss of 300 meV), without particular process optimization, regarding T_{Anneal} and $P_{\text{Se,eqm}}$, nor post-deposition treatment is encouraging. For comparison, world record CIGSe solar cells have a ΔE_F loss of 106 meV [29].

Moving on to the impact of the micro-absorbers' diameter on their PL signal (proportional to $\exp(\Delta E_F)$), Figure 5.17b suggests a trend where PL signal increases with increasing diameter. However, it also shows an important discrepancy on the PL signal from sister micro-absorber with the same diameter. With the current data, it is not possible to objectively explain the discrepancy, however it could be related to their relative position in the graphite box [141]. Regarding the diameter dependency, it is worth noticing that some of the smaller diameters presented a "damaged" morphology, but still had a significant PL signal. Just like in the discussion about the micro-absorbers' morphology it was observed that different annealing parameters were necessary for each diameter, it is hypothesized that to maximize PL signal in each diameter, a particular set of annealing parameters is required. Thus, from the current dataset, it is not possible to conclude whether or not a particular diameter is better.

A first attempt at performing Na post-deposition treatment, by evaporation in the PVD chamber, was tested with the aim of improving the absorber's ΔE_{F}. This method has generally been adopted for standard sized CIGSe to further improve the absorber's ΔE_{F} [111]. The procedure applied to the standard sized CIGSe absorbers was reproduced with the micro-absorbers. It was observed that, given the low amount of CIGSe material in the micro-dots, the flux of NaF was too large and easily formed large alkali secondary phases, which were detrimental for the morphology of the micro-absorbers. Nevertheless, a slight ($\sim$ 40 meV) improvement in ΔE_{F} was observed, which demonstrates the benefits of the method also in micro-absorbers.

Device characterization

The control of $P_{\text{Se,eqm}}$ was demonstrated to be crucial to obtain a compact morphology and to improve the absorber's ΔE_{F}, both being important parameters to fabricate micro solar cells. In the following, the characterization of absorbers that were converted into micro solar cells is discussed. Given the Cu-poor composition of the absorbers, a KCN (5 wt% for 30 s) treatment [165] is applied to the array, directly followed by the chemical bath deposition of a 50 nm CdS buffer layer. In this case, the KCN treatment is mostly to refresh the absorber's surface from the oxides and Cu-Se phases that may have formed due to air exposition [185]. Stripes of tape were used to form a mask around the individual micro-absorbers. Finally, the transparent conductive oxide layers (i-ZnO/ZnO:Al) are deposited by sputtering, after which the stripes of tape are removed to ensure each cell is electrically isolated from the other.

Figure 5.18a shows the EQE spectrum measured from a 500 µm micro solar cell. The expected parasitic absorption by the CdS buffer layer can be identified in the blue wavelength region, whereas the lower EQE, at longer wavelengths, can be attributed to multiple factors like an incomplete absorption of long-wavelength photons and/or the carrier recombination at the unpassivated back interface. The J_{SC} is calculated by integrating the product of the EQE and the solar spectrum, as detailed in section 2.2.9 of chapter 2, and equates to 31.6 mA/cm^2. Also, the measured bandgap is around 1.0 eV, which agrees with the Cu-poor and low Ga content composition measured from the absorbers [39].

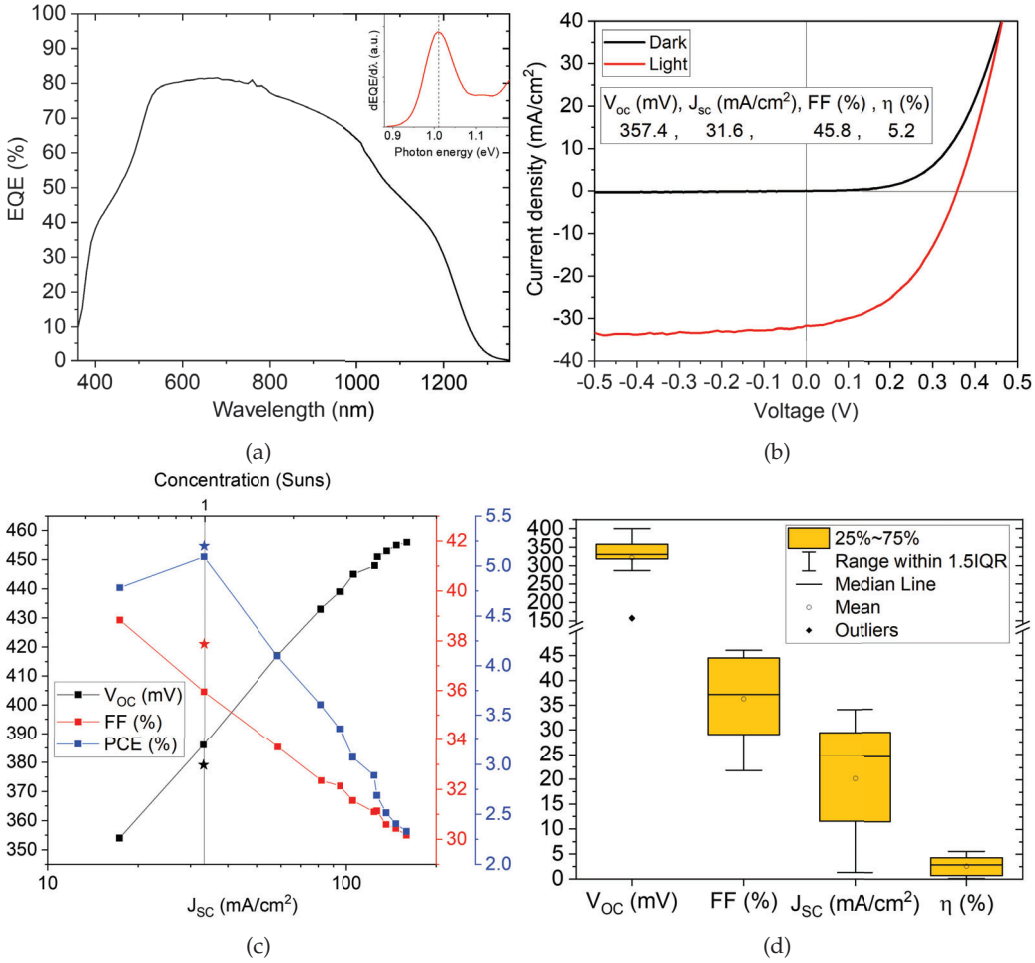

Figure 5.18: a) EQE spectrum measured from a 500 µm micro solar cell, with the respective energy derivative as inset to determine the bandgap. Small bump at 760 nm is an experimental artifact, due to the change of the excitation lamp. b) JV characteristics, in the dark and under illumination, of the same micro solar cell measured in a). Current was corrected based on J_{SC}^{EQE} value measured from EQE. Main JV parameters are shown in a table as inset. c) Concentration series on a sister micro solar cell using a red laser as illumination source. Main JV parameters are reported as a function of the light concentration factor (top axis, shown in log-scale) or equivalently the J_{SC} (bottom axis, shown in log-scale). V_{OC}, FF and PCE were measured for a light concentration up to about 5 Suns. The same micro solar cell was measured with the standard 1 Sun setup and the respective JV parameters are indicated by color-coded star symbols. A vertical black line indicates the 1 Sun illumination. d) Box plot of the main JV parameters, under 1 Sun illumination, covering all 16 measured micro solar cells.

The dark and illuminated JV curves of the same micro solar cell are shown in Figure 5.18b. The champion device showed a V_{OC} of 357 mV, a FF of 45.8 % and a J_{SC} of 31.6 mA/cm^2, leading to a PCE of 5.2 % under 1 Sun. On the one hand, the shunt resistance shows a relatively low value of 100 Ωcm^2, both in the dark and under illumination. On the other hand, the series resistance was estimated to 1-2 Ωcm^2, which is worse than the value measured for the Cu-rich co-evaporated devices (0.1 Ωcm^2), discussed in section 4.2.2 in chapter 4. This difference in series resistance could also explain the lower FF observed here (46 % compared to 60 % for the co-evaporated case).

A light concentration series was measured from a sister micro solar cell using the dedicated micro-setup (red laser as illumination source) and the main JV parameters are plotted in Figure 5.18c as a function of illumination intensity. For comparison purposes, the main JV parameters measured with the standard setup under 1 Sun conditions are also shown. As expected, the V_{OC} increases logarithmically with the excitation intensity, allowing to achieve 456 mV around 5 Suns, which represents an improvement of 70 mV. However, the FF is lower than when measured with the standard setup under 1 Sun conditions. This translates the worse (smaller) shunt resistance measured with the micro-setup (∼23 Ωcm^2 compared to ∼62 Ωcm^2 in the standard setup), the origin of which could not be identified. With higher illumination intensity, even worse values of the shunt resistance were observed, which justifies the observed decrease of the FF. One possible issue could be an inhomogeneous illumination of the micro solar cell. Independently of the setup, it is clear that further efforts are required to improve the shunt resistance, which will allow to further benefit from the PCE gains due to light concentration.

From all the compact CIGSe absorbers in the previous section, 16 micro solar cells with diameters down to 100 µm, were characterized and a box plot of the main JV parameters is plotted in Figure 5.18c. In general, the V_{OC} values are rather close (10-30 mV lower) to the $\Delta E_F/q$ measured from the respective absorbers (see Figure 5.17a). This implies a good band alignment between the absorber, buffer and window layers, which is crucial for optimal device performance. It is worth noting that higher V_{OC} values (400 mV) were measured compared to the champion device (357 mV), however these devices suffered from low FF and J_{SC}, due to a higher series resistance and lower shunt resistance.

To summarize the synthesis of sputtered Cu-poor micro solar cells, it was observed that using a substrate pattern with a higher spacing in-between micro-dots reduced the contamination issues encountered in the previous section. Nevertheless, some level of resist contamination seems to persist. Conversely to the Cu-rich case, an annealing in inert atmosphere was detrimental, given that it led to the formation of larger holes in the absorber's morphology, down to the Mo back contact, and promoted the formation of a secondary phase. In both cases (Cu-rich and Cu-poor), it was highlighted that the precursor's morphology has an important impact in the formation of pure CIGSe. Regarding

the annealing in Se, it was shown that the Se partial pressure and the annealing temperature are key parameters to control the morphology, optoelectronic properties and phase purity of the CIGSe absorber. Furthermore, depending on the diameter of the micro-dot, a different set of parameters were necessary to obtain compact morphologies, which suggests that each diameter requires a distinct set of annealing parameters to optimize the performance of the respective absorber. Finally, multiple Cu-poor micro solar cells were completed and the champion device showed a PCE of 5.2 % under 1 Sun, which is the highest value achieved for bottom-up synthesis of island-shaped micro solar cells. A concentration series was measured and the expected logarithmic increase of the V_{OC} was observed.

To conclude on the sputtering and annealing route, it was demonstrated that the method can produce arrays of CIGSe-based micro solar cells in both Cu-rich and Cu-poor conditions. In the latter case, the implementation of the Na barrier was crucial, as anticipated in chapter 4, however it is hypothesized that it could also be beneficial in the Cu-rich phase, where significant amounts of Na were measured only after annealing in Se. In addition to the Na barrier implementation, further key synthesis parameters for this method were highlighted, which sets guidelines on how to optimize the process in terms of device performance. More precisely, the method has an inherent contamination issue, i.e. resist abrasion into the precursor during the sputtering process, that can be limited by reducing the density of micro-dots in the substrate pattern. In fact, the design of the pattern and the SiO_2 matrix, play important roles in the synthesis process. For instance, the height of the SiO_2 matrix helps shaping the CIGSe absorber, whereas the diameter of the micro-dots has an influence in the formation mechanism. Finally, the Se partial pressure and the annealing temperature have paramount influence in determining the morphology and optoelectronic performance of the CIGSe based micro solar cells.

5.2 Electrodeposited solar cells

The second material efficient method that is explored is a two-step electrodeposition of the metal precursors, followed by the same annealing in a Se-containing atmosphere. The distinction of the electrodeposition steps is that the metal precursors are deposited only in the regions where the metallic Mo layer is exposed, as the SiO_2 layer has the function of masking. This implies that only the required material is deposited locally, resulting in an optimal material consumption. It is worth emphasizing that the substrate, onto which the precursors are deposited, contains no resist layer. Thus, in this case, no resist contamination issues are expected, since the resist is removed before the electrodeposition of the precursor layers, unlike in the sputtering process.

5.2.1 Cu-rich solar cells

Similarly to the sputtered Cu-rich (CGI > 1.0) precursors, no Na blocking layer was used in this case, given the diffusion blocking aspect of Cu-rich precursors observed in chapter 4. The aim here is to also confirm if a different precursor synthesis impacts the Na diffusion.

Precursor characterization

To illustrate the distinct steps in this electrodeposition route, Figure 5.19 presents the optical image, and respective height map, of the same micro-dot at each step of the process. The starting point is the patterned substrate, where the Mo layer is exposed only within the micro-dot structure (in Figures 5.19a and e). The first electrodeposition step is that of Cu, which results in the growth of a Cu layer inside the micro-dots, as exemplified in Figures 5.19b and f. This is followed by the co-electrodeposition of In and Ga, leading to a (In,Ga) layer stacked on the Cu deposit, as visible in Figures 5.19c and g.

An optional step is also shown, in Figures 5.19d and h, that is the annealing of the precursor stack in N_2 inert atmosphere. Focusing on the optical images of the (In,Ga) layer before (Figure 5.19c) and after (Figure 5.19d) annealing, the morphology of the stack does change, as discussed in chapter 3, however the appearance, or color, of the layer remains identical. This again confirms the resist contamination issue, observed in the sputtering synthesis route, is due to the presence of the resist layer during the precursor sputtering step.

The correlative analysis of the electrodeposited precursor layers, discussed in chapter 3, shows that the layers' morphology influences the composition and phase purity of the resulting CIGSe absorber, but also the morphology of the precursor stack itself, which is clearly highlighted here again by the sequence of height maps (Figures 5.19e-g).

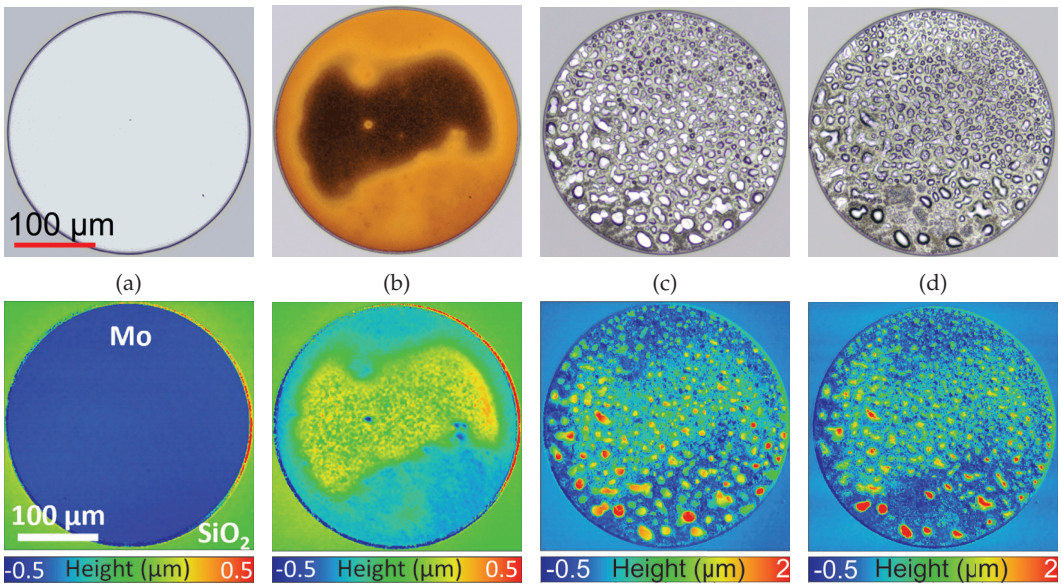

Figure 5.19: CLSM optical images of the same 300 µm diameter micro-dot at each step of the process: a) empty micro-dot. b) electrodeposition of Cu film. c) electrodeposition of In, Ga film. d) inert annealing in N_2. e-h) CLSM height maps of the corresponding optical images (a-d).

Absorber formation

As previously, to convert the precursor stack into the CIGSe absorber, an annealing in Se-containing atmosphere is performed in a tube oven, inside a graphite box. Similar annealing conditions, as for the Cu-rich sputtered precursors, were chosen here. Specifically, the N_2 background pressure was 350 mbar, the mass of Se powder was 150 mg and the annealing duration, at the target temperature, was 10 min. Three different temperatures were considered 450 °C, 500 °C and 550 °C. The range of CGI composition of the absorbers discussed here is 1.1-1.4.

Figure 5.20 shows optical images and height maps illustrating the morphology of a representative absorber synthesized at 550 °C. At this temperature, a few cracks in the SiO_2 are observed, but mostly connected to a micro-dot. Also, at the edge of the sample, the Mo (or $MoSe_2$) layer is peeling locally (not shown). Both observations together suggest that the combination of high temperature and high N_2 background pressure, that is the high resulting Se partial pressure (450 mbar), is causing the growth of an excessively thick $MoSe_2$ layer which leads to the damage observed in the micro-dots and on the SiO_2 layer. This suggests that the thermal expansion is not a problem for this stack (sodalime glass/Mo/SiO_2) and annealing parameters.

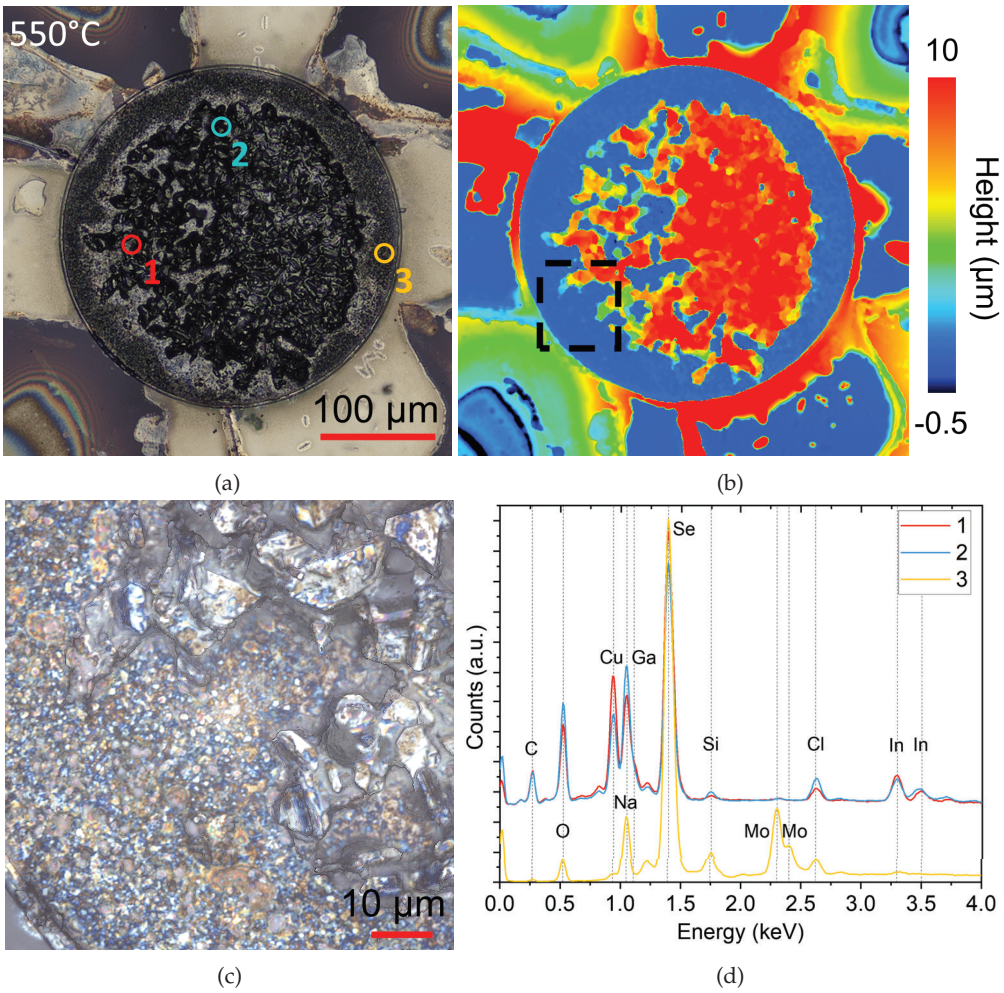

Figure 5.20: a) CLSM optical image of a 300 µm wide micro-dot after an annealing in Se at 550 °C. b) CLSM height map associated with the region shown in a). c) Zoom-in CLSM optical image of the region highlighted by the black dashed box in b). d) EDX spectra acquired from the locations indicated in a). Spectra were measured with 10 kV acceleration voltage.

Focusing on the micro-dot, a damaged $MoSe_2$ layer is clearly visible in dark brown around the micro-dot structure. Inside the 300 µm wide micro-dot, only a portion of the damaged CIGSe absorber remains, leaving the underlying layer also exposed. Figure 5.20c is a zoom-in to the region indicated in the height map, in Figure 5.20b. Here, one can distinguish three different phases by color, which can be guessed from the knowledge acquired with the optical analysis in section 3.3 in chapter 3. In grey, it is the CIGSe phase, in brown/orange the $MoSe_2$. The blue phase was also observed with the Cu-poor sputtered absorber in chapter 4, which allows to guess this phase is Na-related. The EDX spectra analysis, in Figure 5.20d, shows that the composition, in the regions indicated in Figure 5.20a, agree with the suggestions from CLSM analysis. In addition, the presence of the Cl peak allows to further anticipate the formation of NaCl, similarly to the Cu-poor sputtered absorber. Yet again, the Cu-rich precursor was not enough to contain the Na diffusion, as was the case in the co-evaporated absorber.

Reducing the annealing temperature to 500 °C, and thus the Se partial pressure to 420 mbar, considerably reduced the expansion of the $MoSe_2$ layer. Nevertheless, it is still possible to identify an overly thick $MoSe_2$ layer surrounding the micro-dot, in the morphology optical image in Figure 5.21a. Nevertheless, the CIGSe seems intact, as also suggested by the corresponding height map. However, the morphology of the CIGSe layer displays circular lumps, which are considerably higher compared to the remainder of the layer. The optical zoom-in, in Figure 5.21c, does not provide directly a reason for the origin of the lumps, however, in terms of phases, one can identify the light grey CIGSe, a few $Cu_{2-x}Se$ platelets in dark grey and numerous Na-related phases in blue. Here, they are only visible at the surface, as the CIGSe absorber is intact, however they are very likely distributed throughout the absorber's thickness and interfaces, like for the absorber discussed above.

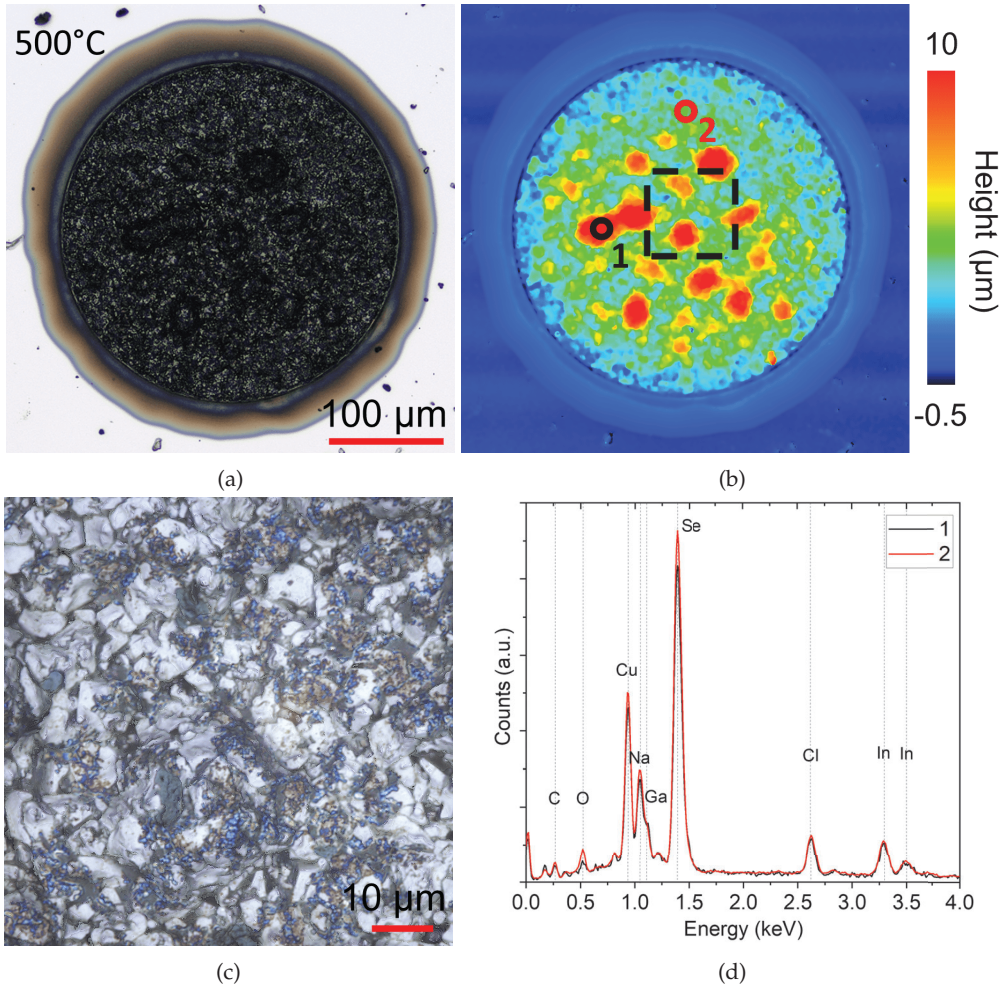

Figure 5.21: a) CLSM optical image of a 300 µm wide micro-dot after an annealing in Se at 500 °C. Brightness adjusted in image a) for visual purposes. b) CLSM height map associated with the region shown in a). c) Zoom-in CLSM optical image of the region highlighted by the black dashed box in b). d) EDX spectra acquired from the locations indicated in b). Spectra were measured with 10 kV acceleration voltage.

Figure 5.21d shows the EDX spectra, taken in the two regions indicated in Figure 5.21b. Both spectra are identical, showing no composition difference. The Cl peak is still present, which indicates that a consequent Na content is present in the absorber, despite the temperature decrease and the Cu-rich composition. It is worth noting that despite using a Na-containing electrolyte for the electrodeposition of the Cu layers, no Na was detected in the precursor stack, which attributes the Na appearance exclusively to its diffusion from the soda lime glass substrate. Although, no particular correlation is observed between the lumps and the Na content, it is worth noting that the average Na/Cu ratio is 1.1, which is excessively high compared to standard CIGSe synthesis (< 0.04) [141]. Thus, it is hypothesized that the excessive Na content is directly or indirectly responsible for the anomalous morphology. Also, as was the case for the highest temperature, the Cu-rich composition does not completely block the Na diffusion, from the substrate, when high Se partial pressures are used. Thus, a Na barrier is also required for the Cu-rich cases.

Further reducing the annealing temperature down to 450 °C (Se partial pressure of 390 mbar), allowed to obtain a promisingly compact absorber morphology, as shown in Figures 5.22a and b. Also, no excessive $MoSe_2$ layer is visible beyond the diameter of the micro-dot. In fact, the optical zoom-in, in Figure 5.22c, shows a light grey CIGSe phase with relatively large grains and dark grey platelets of $Cu_{2-x}Se$, as expected given the Cu-rich precursor's composition. No further phases are visible at the surface and EDX analysis, in Figure 5.22d, confirms that the Na content is considerably reduced in the different regions of the absorber. Note that the Cl signal is also suppressed and this despite using the same Cl-contaminated graphite box. Otherwise, the different regions show distinct relative compositions due to the inhomogeneous Cu layer, as was discussed in chapter 3.

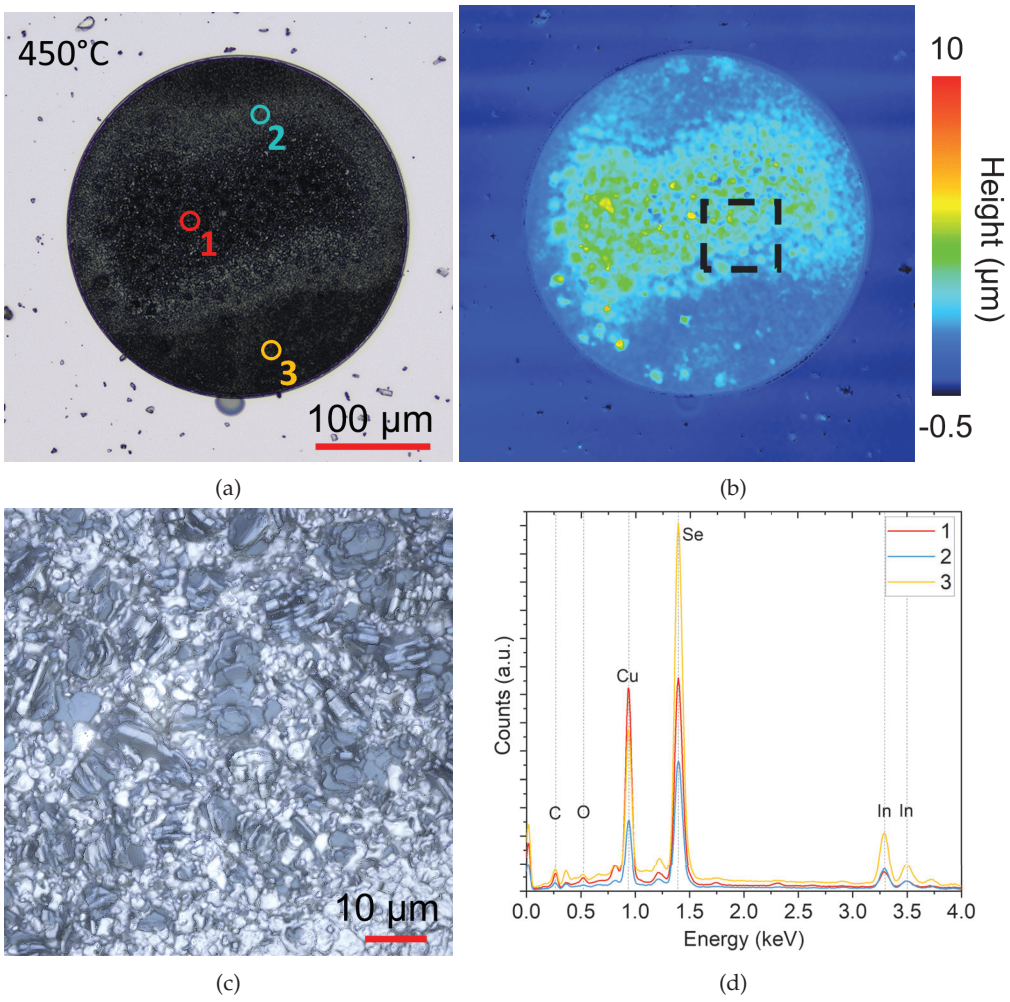

Figure 5.22: a) CLSM optical image of a 300 µm wide micro-dot after an annealing in Se at 450 °C. Brightness adjusted in image a) for visual purposes. b) CLSM height map associated with the region shown in a). c) Zoom-in CLSM optical image of the region highlighted by the black dashed box in b). d) EDX spectra acquired from the locations indicated in a). Spectra were measured with 10 kV acceleration voltage.

Strikingly, despite the same annealing conditions as the sputtered Cu-rich case, no Na is observed here in the absorber, unlike the sputtered case, where a significant amount of Na was present after the annealing in Se. This suggests that the synthesis of the precursor somehow affects the diffusion of Na.

An interesting trend is observed when comparing the morphology of the precursor and that of the absorber. For this, Figure 5.23 regroups the height maps of two absorbers, and respective precursors, synthesized at 450 °C and likewise, two absorbers produced at 500. °C. The top row contains the precursors and bottom row the CIGSe absorbers.

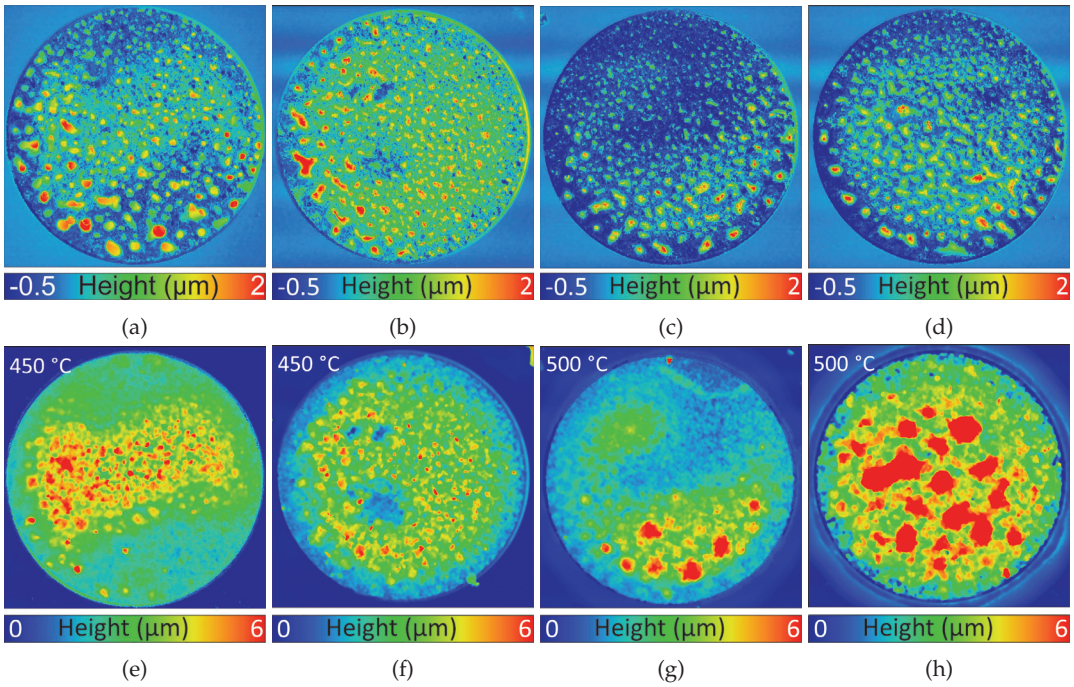

Figure 5.23: CLSM height maps of four (a-d) Cu and (In,Ga) precursor stacks with distinct morphologies and (e-h) respective resulting absorber's morphologies after annealing in Se. The annealing temperatures are indicated at the top left corner of the height map.

As discussed in the precursor section, the particular morphologies of the precursor stacks are mostly induced by the Cu layer. Interestingly, these features remain apparent after the annealing in Se atmosphere, independently of the temperature. This suggests that the diffusion of elements is mostly vertical when forming the CIGSe phase. Furthermore, these results put forward the importance of the precursor's morphology, as it is reflected in the corresponding absorber's morphology. Having achieved compact CIGSe absorbers, in the following, the absorbers were finished into solar cells and characterized.

Device characterization

To assess the optoelectronic quality of the absorbers, synthesized at 450 °C, spectrally-resolved photoluminescence was measured and is plotted in Figure 5.24a in logarithmic scale. The PL signal of the absorber is characterized by the band-to-band transition at around 1.1 eV. Additionally, a broad defect is visible around 0.75 eV, which shows a luminescence of about 1 order of magnitude higher compared to the band-to-band transition. This defect transition seems to be present in low Ga content Cu-rich CIGSe absorbers [186]. This is expected to greatly impact the V_{OC} of the final solar cell.

After completing the absorbers into micro solar cells, JV measurements were performed to measure their efficiency. However, only the solar cells with the absorbers synthesized at 450 °C show a diode behavior, whereas those deposited at 500 °C displayed an ohmic behavior, likely due to the excess of Na observed previously. Figure 5.24b shows the JV characteristics of the best Cu-rich micro solar cell, with the main parameters as

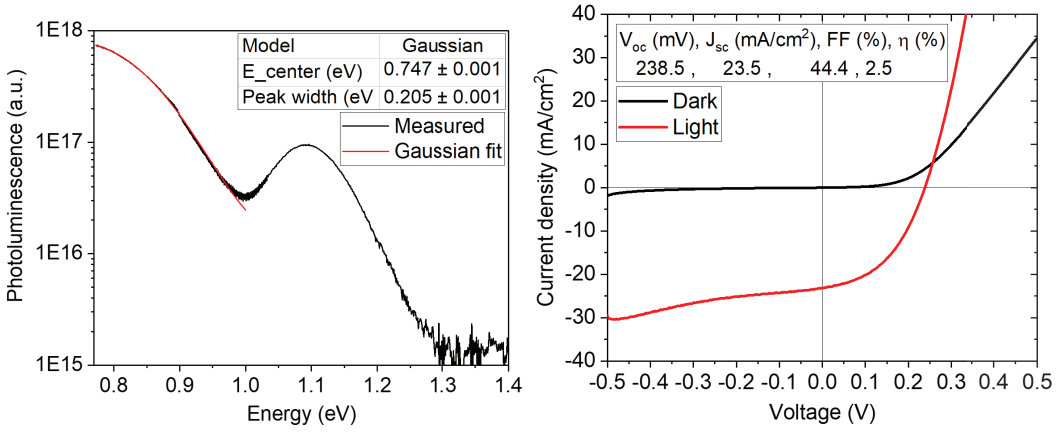

Figure 5.24: a) PL spectrum measured from the Cu-rich CIGSe absorber. Fitting parameters of the broad defect are shown as inset. b) JV characteristics in the dark and under illumination of an electrically isolated micro solar cell. Key parameters are summarized as inset.

inset. As suggested by the PL analysis, V_{OC} of the device is rather limited due to the broad defect observed. The measured J_{SC} also seems to be limited by a shunt path, i.e. a too low shunt resistance, which could not be identified. Thus, the resulting efficiency for the device is 2.5 %.

In summary, Cu-rich micro solar cells were synthesized with the two-step electrodeposition and annealing method. The achieved PCEs are superior to the Cu-rich micro solar cells, made by sputtering and annealing, possibly due to the absence of contaminants during the growth of the precursor layers. A common aspect of the two methods was the presence of Na in the absorber after annealing in Se and this despite that in one case the precursor is a blend of metals and in the second case it is a stack of metal layers. This confirms that the Cu-rich composition is not enough to block the Na diffusion from the soda lime glass, when high Se partial pressures are used in the annealing. Thus, implementing a Na barrier here, like was done for the Cu-poor case, is also beneficial. Furthermore, it was shown that a two-step electrodeposition process requires careful control of the layers' morphology as it dictates the morphology, and phase formation, in the subsequent steps.

5.2.2 Cu-poor solar cells

In the following, Cu-poor CIGSe absorbers are investigated. As for the Cu-poor sputtered case, the precursors were deposited on a patterned substrate with a Na barrier (100 nm SiO_xN_y) below the Mo back contact. The pattern used here was the square pattern with a fix micro-dot diameter (300 µm) to minimize flux inhomogeneities during the electrodeposition of the precursor layers. In terms of synthesis, there is no particular difference between the Cu-rich and Cu-poor precursors, except for the relative thickness of the Cu and In, Ga layers. Except that, due to a technical error during the Cu electrodeposition, also some Ag (from the counter electrode) was deposited.

In sections 4.3 (chapter 4) and 5.1.2 (chapter 5), it was observed that the Se partial pressure (or $P_{Se,eqm}$) influences the morphology of the absorber and its adhesion to the Mo back contact. Given that here the precursor is synthesized with a different method, the question that is addressed in this section is if a distinct precursor synthesis method also impacts the morphology and adhesion of the final CIGSe micro-absorber to the back contact. For this, sister electrodeposited precursors were annealed at distinct $P_{Se,eqm}$ and their morphology is monitored with CLSM. Figures 5.25a, b and 5.25c show CLSM optical images of representative micro-absorbers annealed at 525 °C with a $P_{Se,eqm}$ of 11 mbar, 40 mbar and 131 mbar respectively.

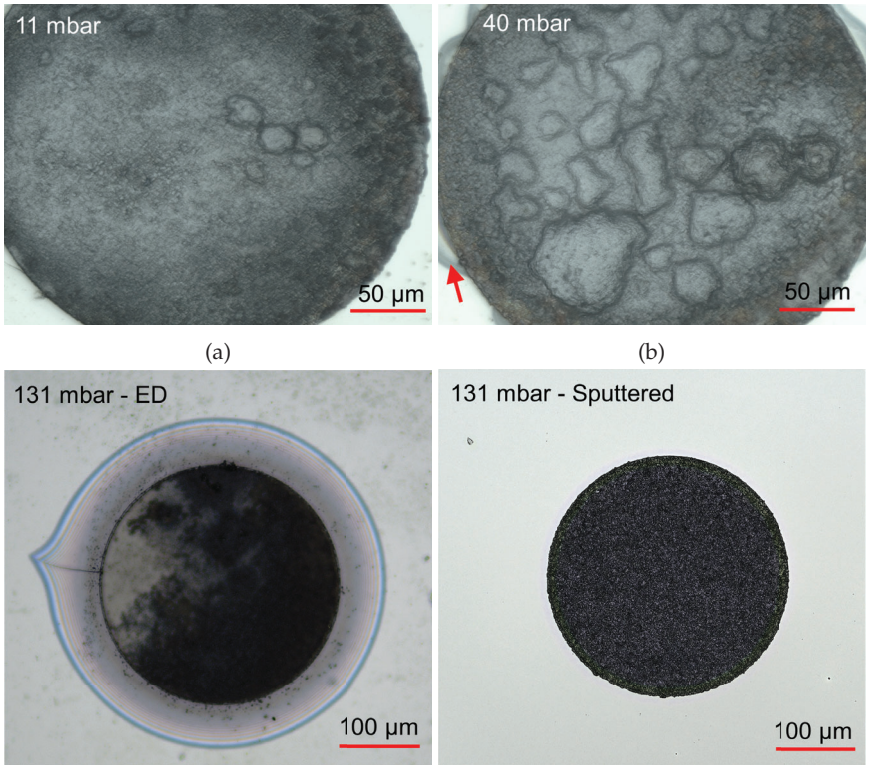

Figure 5.25: CLSM optical image of 300 µm wide CIGSe micro-absorbers after the annealing in Se of the electrodeposited precursors at 525 °C with a Se partial pressure of: a) 11 mbar, b) 40 mbar and c) 131 mbar. Contrast was adjusted in images a) and b) for visual purposes. The red arrow in c) indicates a region where $MoSe_2$ formed (underneath the SiO_2 layer). For comparison purposes, d) is a CLSM optical image of a sputtered micro-absorber annealed under the same conditions as the micro-absorber shown in c).

For the two lower $P_{Se,eqm}$, the absorbers did remain at least partially attached to the Mo back contact, however for the higher $P_{Se,eqm}$ (131 mbar), no absorber material was left inside the micro-dot after the annealing. Furthermore, it can be seen in Figure 5.25c that a $MoSe_2$ layer formed underneath the SiO_2 matrix and even extended about 50 µm beyond the diameter of the micro-dot. Clearly, in this case, too much Se was provided to the precursor, causing the formation of an overly thick $MoSe_2$, compromising the adhesion of the CIGSe itself. Reducing $P_{Se,eqm}$ to 40 mbar ensured that the absorber layer

remained intact and within the micro-dot, nevertheless some $MoSe_2$ can still be identified in some regions along the perimeter of the micro-dot, as highlighted by a red arrow in Figure 5.25b. Regarding the morphology of the absorber itself, multiple protruding lumps are visible, with some reaching heights of 20 µm above the rest of the layer. This suggests that these are hollow lumps, which in turn implies a weak adhesion of the CIGSe to the Mo layer. Both the excess $MoSe_2$ and the lumps are considerably reduced with the lowest $P_{Se,eqm}$ (11 mbar). For comparison purposes, Figure 5.1e shows a CIGSe micro-absorber synthesized from a sputtered precursor at the same conditions as the micro-dot shown in Figure 5.25c (131 mbar). In this case, no $MoSe_2$ is visible. This suggests that for the sputtered case, the Se atoms take longer to diffuse through the precursor/absorber and reach the Mo back contact comparatively to the electrodeposition case, implying a thinner $MoSe_2$ layer and consequently a better CIGSe adhesion.

To also illustrate the impact of $P_{Se,eqm}$ on the morphology of the electrodeposited absorbers, Figure 5.26 shows the average height of the absorbers, compared to the SiO_2 layer, as a function of the $P_{Se,eqm}$, for an annealing temperature of 525 °C. The results for the sputtered absorbers, that were prepared under similar conditions, are also shown. Note that in both cases, a precursor thickness of 0.6-0.8 µm is estimated.

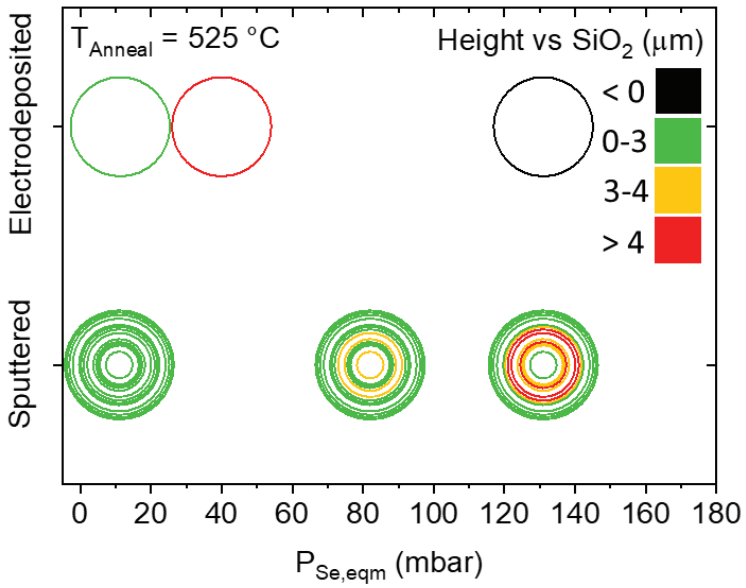

Figure 5.26: Colormap representation of the CIGSe absorber's average height, compared to the surrounding SiO_2 matrix, as a function of the Se partial pressure for electrodeposited and sputtered micro-absorbers. The annealing temperature is 525 °C. The data related to the sputtered samples is the same shown in Figure 5.14. Note that the y-axis here differentiates synthesis method and not annealing temperature. For the electrodeposited samples, the average height of the micro-absorbers is shown as all have the same diameter (300 µm).

In this representation, it is clear the range of $P_{Se,eqm}$, that results in a compact CIGSe absorber, shifts to lower pressure values for the electrodeposited precursor. This implies that the synthesis of the precursor indeed impacts the morphology and adhesion of the CIGSe absorber. Based on these observations, it is speculated that the precursor's double

layer structure, i.e. Cu/(In,Ga) stack, in the electrodeposition case, requires more diffusion of the elements to form the binary $Cu_{2-x}Se$ and In_xSe_y phases, and eventually form the CIGSe phase, which implies that a higher flux of Se atoms (from a higher $P_{Se,eqm}$) increases the possibility of Se atoms to reach the back contact and form $MoSe_2$. By decreasing $P_{Se,eqm}$, less Se atoms are available, effectively slowing down the reaction mechanisms that require Se, allowing for the binary selenides to form without an excess of Se atoms. Conversely, the sputtered precursor is already an alloy, which could facilitate the formation of the binary selenides, and thus the CIGSe phase, at higher $P_{Se,eqm}$.

Device characterization

Given the better adhesion of the CIGSe layers, the absorbers annealed at the lowest $P_{Se,eqm}$ (11 mbar) were finished into micro solar cells. However, since some regions still had an apparent low adhesion, a double layer of CdS buffer layer was deposited to minimize the risk of a shunt path between the window layers and the Mo back contact. The thicker buffer layer is expected to reduce the JV parameters by at most 10 % [187]. For the deposition of the window layers, a similar procedure as for the Cu-poor sputtered case was followed (see section 5.1.2). Prior to the deposition of the window layers, PL measurements were taken from the absorbers made through the electrodeposition route. For comparison, the PL spectrum from a sputtered absorber, with a ΔE_F of 430 meV, is also plotted in Figure 5.27a.

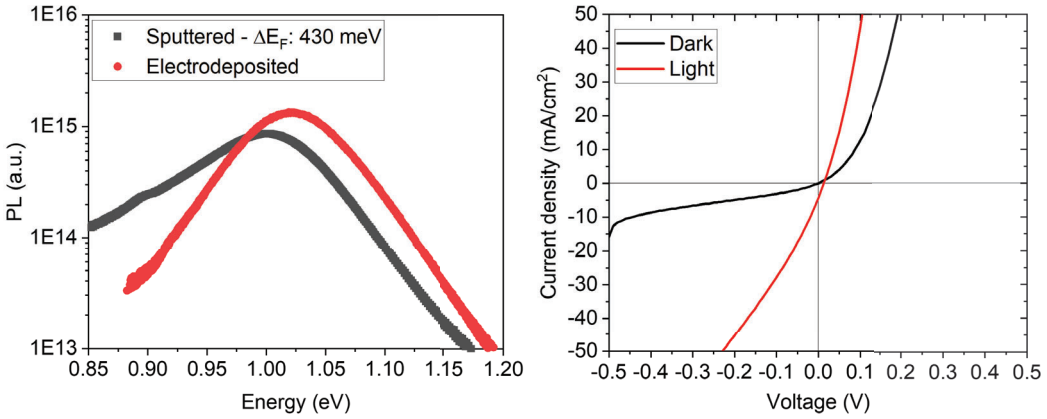

Figure 5.27: a) PL spectra measured, under the same conditions, from an electrodeposited Cu-poor CIGSe absorber and a sputtered Cu-poor CIGSe absorber. b) JV characteristics in the dark and under illumination of a micro solar cell resulting from the electrodeposition synthesis route.

Since the two absorbers were measured under the same conditions, one can compare their PL. In this case, the electrodeposited absorber shows a slightly higher PL signal, which suggests a similar ΔE_F. The shift in the PL peak, of the electrodeposited absorber, may be due to the Ag inclusion [188]. Despite the promising PL signal, both JV curves, in the dark and under light, show issues with the resulting micro solar cell, as is visible in Figure 5.27b. Indeed, the JV in the dark shows a rather low shunt resistance of 40 Ωcm^2.

Under illumination, the observed shunt resistance is further reduced to $5\,\Omega cm^2$, and a very low V_{OC} is observed. It is possible that, given the initially not so good adhesion of the CIGSe to the Mo layer, the deposition of the window layers further damaged the absorber, leading to a very poor conversion of the measured ΔE_F into V_{OC}.

In short, it was observed the synthesis of the precursor layer has an impact on the range of Se partial pressures that result in a compact CIGSe absorber and thus, with better adhesion to the Mo back contact. Specifically, it is suggested that depending on which metallic phases are in the precursor, different fluxes of Se are required to form a similarly compact CIGSe layer.

To conclude the two-step electrodeposition and annealing method, it was demonstrated that also this route requires the implementation of a Na barrier independently of the CGI ratio, reflecting the fact that the Na diffusion is induced by the substrate's geometry. Furthermore, it was observed that the synthesis of the precursor, in particular which phases are formed, impacts how the subsequent annealing in Se should be performed to ensure compact CIGSe absorbers. Finally, although micro solar cells with lower PCE were achieved, it is expected that, with little optimization, this method could yield PCEs similar to those achieved with the sputtering route.

5.3 Summary

In this chapter, two material efficient methods are investigated with the aim of growing CIGSe based micro solar cells on patterned array substrates. For each method, both Cu-rich and Cu-poor CIGSe compositions were synthesized and working devices were obtained, demonstrating the potential application of the two methods.

The implementation of the Na barrier in the array stack was essential, not only for the Cu-poor case, as first anticipated, but also for the Cu-rich CIGSe absorbers. Indeed, the Se partial pressure, during the annealing step, was shown to enhance the diffusion of Na from the soda lime glass, which overcomes the blocking effect of the lack of Cu-vacancies. Furthermore, the morphology, phase purity and optoelectronic properties are also influenced by the Se partial pressure, which puts forward that a fine control of the Se supply is crucial independently of the specific annealing method that is used. This also defines the direction of research on how to optimize the different properties of the CIGSe absorbers. Additionally, the morphology of the metal precursors must also be optimized in both synthesis methods to avoid phase inhomogeneities. As anticipated, Cu-poor CIGSe micro solar cells led to higher PCEs compared to Cu-rich.

The sputtering and annealing method suffers from a contamination issue, during the sputtering of the precursor, which can affect the potential PCEs achieved. Nevertheless, the issue can be partly addressed by adjusting the design of the substrate pattern, more precisely, by increasing the space in-between neighbour micro-dots. Following up on the substrate pattern, the height of the SiO_2 matrix plays an important role in shaping

the CIGSe absorber and the diameter of the micro-dots has an influence in the formation mechanism.

Chapter 6

Energy balance - A pedagogical approach to energy

The previous chapters focused on the scientific work on the investigation of the material efficient synthesis and characterization of CIGSe-based micro solar cells using patterned substrates. As hinted to in the introduction, in addition to pushing the boundaries of science and technology, experts can educate the general public in order to popularize science and give the opportunity to the average citizen to follow the scientific progress and grasp its implications, both at the research level as well as at a societal level. In this way, every citizen can better assess the situation at hand and form their own opinion regarding the latest topics. The current climate crisis is a perfect example of a problem that directly affects the biosphere, and in particular every human being. Therefore, everyone should be able to be informed and discuss it on an equal footing with the pertinent metrics. For this, pedagogic tools can help to overcome the understanding of complex concepts and directly discuss the implications of the actions themselves, which depend on and affect everyone. In this context, experts can fill the gap.

In his book, David MacKay takes an objective approach to assess the anthropogenic environmental impact and presents a methodology on how to attribute meaningful and comparable numbers to the multiple facets that are involved in the problematic of climate change [189]. Based on his approach, the Energy4Life (E4L) team has developed an online pedagogical tool to answer the following question: Can the G.-D. of Luxembourg meet its energetic needs using renewable energy sources and how much land area would it need to deploy? [190]. In a nutshell, by answering a few simple questions on our energy lifestyle, one can find out the approximate land area that would need to be covered with renewable energy sources, to sustain that lifestyle. To provide the audience with more than numbers, the Energy balance game was designed and is a materialization of the E4L online tool. The aim was to develop a pedagogic tool to present the E4L concept to the general public and high school students in a concise and revealing experience. This chapter is a tutoring on how the realisation of the Energy balance, as a pedagogical tool, was developed and may serve as a support for other concepts. The tutoring is showcased for Luxembourg, but can be adapted to any region or country.

In short, the following sections offer a description of the design of the Energy balance game, which is based on a pedagogic approach to address the complex and often intangible concept of energy. A description of the different components is given, as well as, the details of the calculations used to convert the energies into tangible quantities. Additionally, a rules description of the current version of the game is presented along with a discussion of possible expansions or adaptations that could widen the utility of the game into other concepts.

6.1 Components

The different components that make up the energy balance are: (i) a weighing scale, (ii) a question sheet, (iii) an answer sheet, (iv) weighted tokens, representing the possible consumption and production possibilities (v) a map of the region of interest. In the following, an overview of the conception and principle behind each component of the energy balance.

6.1.1 Weighing scale

The weighing scale was chosen to be a wooden two-plate scale based on the *Zenzi-Werken* model [191]. In this configuration, one plate is used as the energy consumption side, whereas the second plate is reserved for the energy production. The mass resolution of the fabricated scale was in the range of 1-2 g, which also defines the lowest mass value to be used. This value mostly depends on the friction of the different parts of the scale. In this case, plywood was used as the base material and individual parts were laser cut. Figure 6.1 is an optical image of the assembled wooden weighing scale.

Figure 6.1: Optical image of the assembled wooden weighing scale.

6.1.2 Question and answer sheets

The next components that are addressed are the question and answer sheet, as these are similar. For ease of visualization and to highlight the answers that are chosen, a separate question and answer sheets are used. Nevertheless, the answer sheet is identical to the question sheet, except that the fields containing the answer tokens are left blank. Given the dimensions of the weighted answer tokens, A3 format sheets are utilized. Figure 6.2 displays the question sheet with and without the weighted answer tokens.

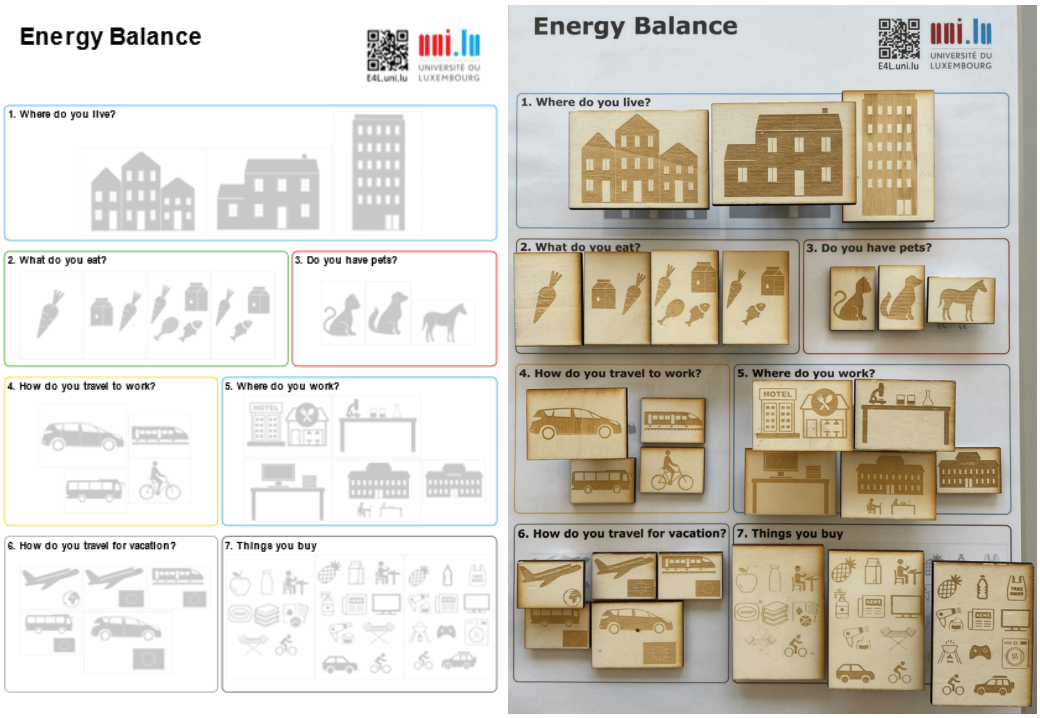

(a) (b)

Figure 6.2: a) Question sheet. b) Optical image of the question sheet with answer tokens prepared.

6.1.3 Production map

The production map is intended to display the percentage area of the region of interest (ROI) that needs to be covered with production units, in order to satisfy the amount of energy consumption. For this, the map consists of the ROI divided in a grid with 100 squares, each having the same dimensions as an individual production unit.

To provide the reader with the most flexibility in terms of dimensions and materials, different constraints for the map areas and tokens' weight and dimensions are suggested. For the production map, two constraints can be considered, either one chooses the dimensions of the ROI in the map sheet (G.-D. of Luxembourg, in this case) or the area of a single production unit (solar cells for instance). Given that A3 sheets are used to print the map, it is more convenient to proceed with the first constraint. For this, one can start from a geographic map, showing the delimitations of the ROI, and rescale it to

the desired real dimensions (to fit an A3 sheet in our case). By measuring the total area of the ROI $A^{ROI}_{A3\,sheet}$ (in cm^2) and dividing it by 100, one can calculate the real area that occupies a single production unit $A_{1\,unit}$. Taking the square root of this value, yields the side length $d_{1\,unit}$ of the equivalent square.

$$d_{1\,unit} = \sqrt{A_{1\,unit}} = \sqrt{\frac{A^{ROI}_{A3\,sheet}}{100}} \tag{6.1}$$

To generate the map itself, one can create a grid of squares, each with an area $A_{1\,unit}$, and overlap it with the map of the ROI. Although this concludes the production map itself, it is required to calculate the equivalent energy $E^{prod.}_{1\,unit}$ that a single production unit can generate, for latter reference. In this case, one can simply calculate an area conversion factor f_{area}, which is the ratio of the real area of the ROI A^{ROI}_{Real} to $A^{ROI}_{A3\,sheet}$.

$$f_{area} = \frac{A^{ROI}_{Real}}{A^{ROI}_{A3\,sheet}} \tag{6.2}$$

The conversion factor allows to calculate the area to which a single production unit corresponds to in real scale. Therewith, one can determine $E^{prod.}_{1\,unit}$ as follows:

$$E^{prod.}_{1\,unit} = A_{1\,unit} \cdot f_{area} \cdot E^{prod.}_{density} \tag{6.3}$$

In our case, $E^{prod.}_{density}$ is the yearly energy density produced by solar cells. As an example, Figure 6.3 shows the finalized map for the G.-D. of Luxembourg.

6.1.4 Weighted tokens

Moving on to the weighted tokens, the aim is to associate each individual token with a possible answer (for consumption and production) and have its mass proportional to the energy that is associated with the answer. Three information channels are thus being used to convey the associated amount of energy: the icon that represents the answer, the dimensions of the token (area and height) and the weight of the token, as shown in Figure 6.4. Note that the tokens are made up of two parts, the wooden plate with the engraving and the aluminum rod for the weight. For simplicity, the description below neglects the weight of the wooden plate itself, since it is much lower than the rod. Also, the choice of using two materials (wooden plate and aluminum rod), instead of one (single weight with the icon engraved on it), was only determined by the availability of resources and services.

The calculations to determine the corresponding mass of each token, relies on defining an energy-mass conversion factor f_{energy}, which depends on the constraint that is chosen. Different approaches can be taken, for instance, define the maximum or minimum weight, impose a specific range of dimensions, the density of material(s) used, etc.

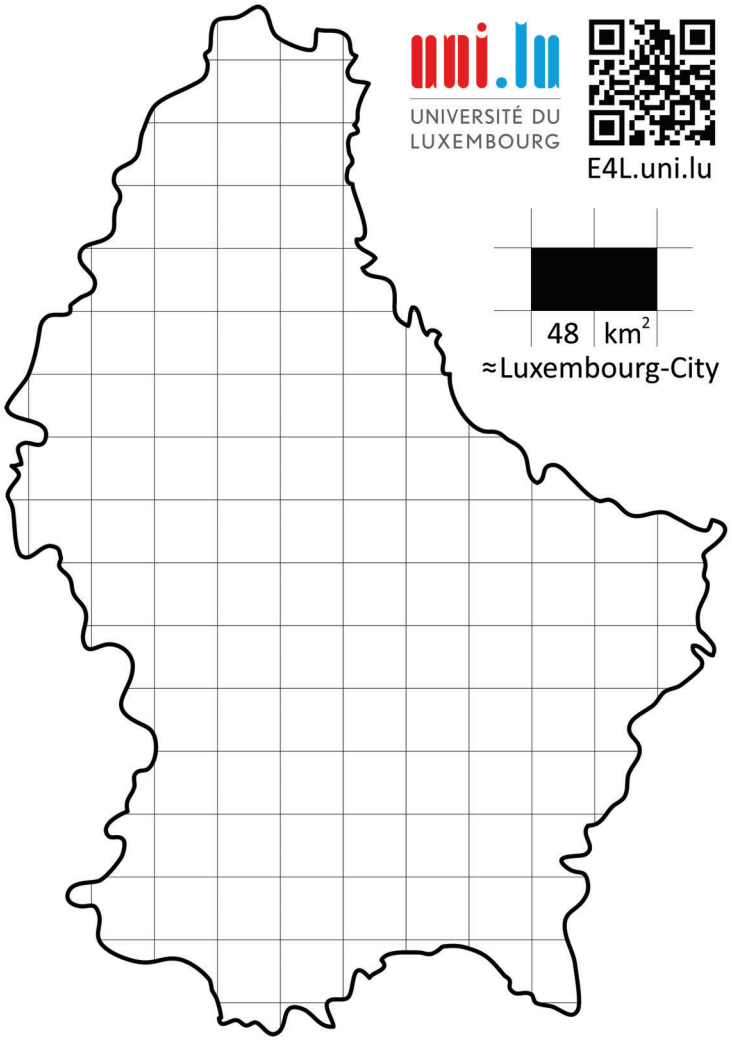

Figure 6.3: Production map for the G.-D. of Luxembourg.

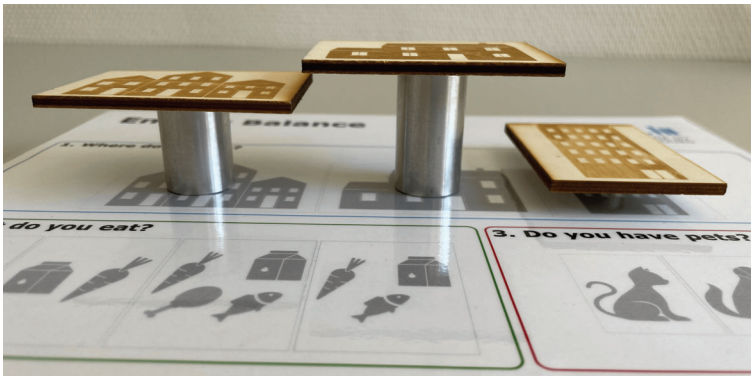

Figure 6.4: Side view of three answer tokens with different areas, heights and weights.

In all cases, the calculations are based on the equations discussed below and only the calculation order changes depending on which constraints are chosen.

To define f_{energy}, one requires to know the energy associated with one unit (of consumption or production) and the mass associated with that unit. An example would be to pick the unit with highest energy requirement and decide on the maximum mass desired for the set of tokens. Alternatively, one can calculate the mass of a unit based on dimensions and material requirements. Taking a production unit as reference, its mass $m^{prod.}_{1\,unit}$ is given by the density of the material $\rho_{material}$, used to fabricate the token's weight, multiplied by its volume $V_{1\,unit}$, as shown in equation 6.4. The weight's volume is given by its cross-section area $A_{1\,unit}$ and height $h_{1\,unit}$.

$$m_{1\,unit} = \rho_{material} \cdot V_{1\,unit} = \rho_{material} \cdot A_{1\,unit} \cdot h_{1\,unit} \tag{6.4}$$

From the previous section, the dimensions of the production map were imposed, which led to the calculated area of one production unit $A_{1\,unit}$. Setting $h_{1\,unit}$ allows to calculate $m_{1\,unit}$, which in turn is used to define f_{energy} (see equation 6.5).

$$f_{energy} = \frac{m_{1\,unit}}{E^{prod.}_{1\,unit}} \tag{6.5}$$

Having determined f_{energy}, the mass of each individual token m_i can be calculated based on the respective yearly energy E_i:

$$m_i = E_i \cdot f_{energy} \tag{6.6}$$

Note that the units of f_{energy} are given by those used for $m_{1\,unit}$ and $E^{prod.}_{1\,unit}$. This means that if a yearly energy is used in equation 6.5, when calculating a mass of a particular token, the input energy E_i must also be a yearly energy. Also, it is worth mentioning that the energies for consumption E_i were scaled to the whole population of the G.-D. of Luxembourg.

Finally, for each token, one can still vary the individual height h_i, area A_i and even the material's density $\rho_{material,\,i}$, if using different materials for the weights. If the individual areas and densities are fixed, then h_i can be calculated as follows:

$$h_i = \frac{m_i}{A_i \cdot \rho_{material,\,i}} \tag{6.7}$$

With this, each token has a calibrated weight, proportional to its energy requirement, and thus can be compared within the set of tokens. This concludes the calculations for the design of the different components.

For completeness, the calculation to determine the required production area ratio $A_{land\%}$, needed to offset the energy consumption is also presented. Note that this is the

answer that the energy balance gives after going through the game. Nevertheless, $A_{land\%}$ can be found with the following equation:

$$A_{land\%} = \frac{\sum_i E_{\mathrm{i}} / E^{prod.}_{density}}{A^{ROI}_{real}} \tag{6.8}$$

Alternatively, one can calculate the number of production units needed $n_{prod.}$:

$$n_{prod.} = \frac{A_{land\,\%} \cdot A^{ROI}_{A3\,sheet}}{A_{1\,unit}} \tag{6.9}$$

This finalizes the description of each of the components of the Energy balance and in the following a brief tutorial on how to run the game is presented.

6.2 How to play the Energy balance game

The game can be divided in three phases. In the first phase, players answer questions by choosing the token(s), that exhibits the answer that best represents their habits, from the Question Sheet and place it on the Answer Sheet. After all questions being covered, the Answer sheet represents energetic footprint of the player.

The second phase consists in placing the answer tokens on the Personal Consumption side of the weighing scale. Then, use the production units (solar modules) on the Renewable Generation side to counterbalance the Personal Consumption.

In the third phase, the player takes the production units that were required to counterbalance his/her consumption, and distributes them on the production map. Since each module fills one square out of the 100 that make up land area of the ROI, one can directly see the equivalent percentage of production land area that would be needed to cover the consumption. In our case, all energies were scaled to the population of the G.-D. of Luxembourg, implying that the area percentage, that is found from the production map, would cover the energetic needs of the whole population, assuming everyone has the same energetic requirement as the player. Thus, to find the equivalent area at an individual level, one has to divide the required area by the population. To have an overview of all the components, Figure 6.5 shows a complete set after a playthrough.

After going through the three phases, the player can change their answers and see what the impact on their energy consumption would be.

6.3 Expanding the game

Multiple directions can be explored to expand or adapt the Energy balance game. In the following, a few suggestions are shortly discussed.

Figure 6.5: Overview of the components of the Energy balance game after a playthrough. The Answer sheet is printed on the back of the Production map.

Climate change being a vast and complex problem, it could be of interest to simply add more possible tokens, both for consumption and production. On the consumption side, distinguishing between electric and combustion cars is of importance given the political discussions on the topic, or as a second example, considering the energetic impact of server-based services, which have energivorous requirements and are consumed without second thoughts. On the production side, one can consider additional renewable sources, like wind and hydroelectric energy, and offer the possibility to choose what combination is most applicable for the situation at hand.

Instead of broadening the choice spectrum, one can subdivide the weights for some of the tokens. This would be particularly pertinent to distinguish the energy consumption of buildings in summer and winter, or to differentiate between car-sharing commuting and a single passenger car commuting. Indeed, in the presented version, the Energy balance game does not consider seasons, but average energies over a year. This avoids the discussion of energy management and energy storage throughout the year. Subdividing the weights allows to change the energy of the tokens (using magnets or attachments) and opens up a winter or summer mode for the tokens. This allows to follow more realistically the consumption and production in a year. Making the production units also modular to summer and winter, opens up the discussion about batteries, which would store the excess of produced energy in summer. These also require land area, in the production map, and would be included in the consumption side during summer and in the production side during winter.

Finally, the parameter chosen for comparison is the energy, however one could also

discuss in terms of CO_2 emissions, given that the majority of the energy is currently generated by burning fossil fuels. In this context, the production side would need to be adapted to represent the impact the renewable production units would have in reducing the CO_2 emissions.

6.4 Summary

To conclude, this chapter addresses the educational gap that exists between entities with diverse background knowledge and suggests a method to design and materialize a pedagogical tool to allow pertinent discussions on the basis of a common denominator, in this case, energy consumption and production for the topic of climate change. A description of the Energy balance game and the details of the respective design calculations are presented, while highlighting the constraints and the possibilities to reproduce the same game with different materials and dimensions. Indeed, the Energy balance game, presented here, allows to easily identify the distribution of energy consumption and meaningfully quantify the abstract concept of energy into PV equivalent land area. It converts a lifestyle into a land use without visible calculations, which hopefully everyone can understand. This provides a common scale to discuss the problem of CO_2 emissions and directly determine and assess the impact of hypothetical measures to be applied.

Chapter 7

Summary and outlook

The objectives of this thesis were (i) to investigate the synthesis of CIGSe on silicon oxide (SiO_2) patterned substrates using material efficient methods, in order to improve the resulting PCE of the respective micro solar cells and (ii) to develop a pedagogical tool to help popularizing scientific topics, in this case energy consumption and provision.

To address the first objective, three distinct steps were followed and are summarized in the following. First, given the high number of individual micro solar cells on each substrate and the multiple steps involved in the synthesis processes, a new methodology, based on CLSM, was developed to characterize the individual micro structures, in order to monitor each step of the synthesis process and perform statistical analysis. More precisely, CLSM was demonstrated to effectively measure the thickness of individual layers, their roughness and assess the evolution of the layers' morphology, for each step in the synthesis process. A detailed analysis both at the individual micro-dot level, as well as, at the array level allowed to identify a thickness gradient during one of the electrodeposition steps. Beyond the usual capacities associated with CLSM, a new methodology to measure relative composition in sequential processes, based on the CLSM morphology maps, was proposed and verified with EDX. Furthermore, combining the composition information with the material's phase diagram, spatial predictions were made of which phases would form at the end of the synthesis process. This demonstrated the impact the initial precursor's morphology has on the final absorber's spatial composition, and consequently on the formed phases. Lastly, examples of how optical microscopy can be used to quickly differentiate phases in a material were discussed. In short, CLSM was shown to be a versatile characterization and diagnosis tool to confirm the good progression of the multi-step synthesis or to rapidly pinpoint possible issues, allowing to intervene at an early stage.

Second, to assess the influence that using a patterned substrate, designed for micro solar cells, has on the synthesis of CIGSe, a reference co-evaporation technique was used to grow CIGSe on patterned substrates and on conventional, unpatterned, substrates. It was found that due to the geometry of the patterned substrate and to the diffusion blocking property of the SiO_2 patterned layer, a locally enhanced diffusion of Na takes place, from the soda lime glass and through the holes in the SiO_2 layer. This interferes with

the growth of the CIGSe absorber, leading to a poor adhesion of the CIGSe layer to the Mo back contact and to the formation of a Na-enriched secondary phase (suggested here to be $Na(In,Ga)_3Se_5$). Both consequences compromise the absorber's final performance, compared to the reference. Three mitigation strategies were tested, in order to reduce the enhanced flux of Na from the patterned substrate, and the implementation of a Na barrier was proven to be the most effective. Nevertheless, with this method, providing some Na externally is essential to ensure CIGSe adhesion. Furthermore, by comparing two annealing routines with widely distinct Se partial pressures, it was demonstrated that the Se partial pressure regulates the Na diffusion from the patterned substrate, and it also influences the morphology and phase formation of the resulting absorber.

Third, with the characterization methodology developed and the knowledge on how to avoid the enhanced Na diffusion from the patterned substrates, two material efficient methods were investigated with the aim of growing CIGSe based micro solar cells. Both are two-step processes (precursor deposition followed by annealing in Se), where the precursor layer is either sputtered or electrodeposited. For each method, both Cu-rich and Cu-poor CIGSe compositions were synthesized. In both cases, the implementation of a Na barrier in the substrate stack is essential. This is the case, given that both synthesis methods require a relatively high Se partial pressure to obtain better absorber properties, and that a higher Se partial pressure enhances the diffusion of Na from the substrate. In fact, the Se partial pressure was shown to influence the morphology, phase purity and optoelectronic properties of the resulting CIGSe absorbers, highlighting the need for a fine control during the annealing in Se. Additionally, the morphology of the metal precursors must also be optimized in both synthesis methods to avoid phase inhomogeneities.

It was observed that the sputtering and annealing method suffers from a contamination issue, occurring during the deposition of the precursor, which was partly addressed by adjusting the design of the substrate pattern. Working micro solar cells were achieved with both material efficient methods, with the champion device having a power conversion efficiency (PCE) of 5.2 % under 1 Sun. Although the gap to top down approaches was indeed reduced, there are multiple directions that can be explored to further develop material efficient methods. A first suggestion is the optimization of the precursor's composition, which for state-of-the-art CIGSe solar cells translates to a CGI in the range 0.8-0.95 [29, 192]. This should already improve the CIGSe phase purity and lead to a higher open-circuit voltage (V_{OC}) independently of the micro-dots diameter. During the annealing in Se, one could additionally introduce alkali salts (like NaCl, RbF, etc) in order to dope the CIGSe absorber directly during its formation, which is expected to improve its V_{OC} without adding an extra synthesis step. Similarly, Na post-deposition treatment was demonstrated, in this work, to improve the absorber's quasi-Fermi level splitting by 40 meV, without particular process optimization. This suggests that micro absorbers can benefit from the potential gains of Na and heavier alkali post-deposition treatments (like Rb) that are reported in literature for planar CIGSe absorber [108, 193]. In the context of resource optimization, it would be interesting to replace the annealing strategy used in

this work with laser annealing. Indeed, most of the heat generated during the annealing in the tube oven is used to heat up the graphite box and the sodalime glass, which makes up most the sample's volume. Since only the absorbers require high temperatures, laser annealing is an adequate annealing technique given its high localized energy input.

Finally, with the aim of bridging the knowledge gap between experts and regular citizens on abstract concepts, a pedagogical tool was presented to allow pertinent discussions on the topic of energy production and consumption. A description of the Energy balance game and the details of the respective design calculations are presented, while highlighting the constraints and the possibilities to reproduce the same game with different materials and dimensions. Indeed, the Energy balance game, presented here, allows to easily identify the distribution of energy consumption and meaningfully quantify the abstract concept of energy into PV equivalent land area.

List of Publications

[1] **R. G. Poeira** et al. "Direct fabrication of arrays of Cu(In,Ga)Se_2 micro solar cells by sputtering for micro-concentrator photovoltaics". In: *Materials & Design* (2023). DOI: 10.1016/j.matdes.2023.111597.

[2] **R. G. Poeira** et al. "Optical Measurement of the Stoichiometry of Thin-Film Compounds Synthetized From Multilayers : Example of Cu(In,Ga)Se_2". In: *Microscopy and Microanalysis* (2023). DOI: 10.1093/micmic/ozad105.

[3] A. Pérez-Rodríguez, **R. G. Poeira** et al. "Current status of bottom-up fabrication approaches for Cu(In,Ga)Se_2 micro-concentrator solar cells". In: *AIP Conference Proceedings*, 2022. DOI: 10.1063/5.0104440.

[4] P. Santos, P. Anacleto, D. Brito, S. Shital, **R. G. Poeira** et al. "Fabrication of semi-transparent Cu(In,Ga)Se_2 solar cells aided by Bromine etching". In: *Thin Solid Films* (2023). DOI: 10.1016/j.tsf.2023.139778.

[5] A. JC. M. Prot, M. Melchiorre, T. Schaaf, **R. G. Poeira** et al. "Improved sequentially processed Cu(In,Ga)$(S,Se)_2$ by Ag alloying". In: *Sol. RRL.* (2024). DOI: 10.1002/solr.202400208.

[6] O. Ramírez, E. M. Lanzoni, **R. G. Poeira** et al. "How much gallium do we need for a p-type Cu(In,Ga)Se_2?". In: *APL Mater*. (June 2022). DOI: 10.1063/5.00916765.

[7] T. Wang, L. Song, S. Gharabeiki, M. Sood, A. JC. M. Prot, **R. G. Poeira** et al. "Shifting the paradigm: a functional hole selective transport layer for chalcopyrite solar cells". In: *Sol. RRL*. (2024). DOI: 10.1002/solr.202400212.

Bibliography

[1] Hannah Ritchie and Pablo Rosado. "Energy Mix". URL: https://ourworldindata.org/energy-mix. *Our World in Data. Accessed on 07-03-2024*.

[2] Gavin A. Schmidt et al. "Attribution of the present-day total greenhouse effect". In: *Journal of Geophysical Research: Atmospheres* 115.D20 (Oct. 2010), pp. 1–6. ISSN: 0148-0227. DOI: 10.1029/2010JD014287 (cit. on p. 15).

[3] V. Ramanathan and Anand Inamdar. "The radiative forcing due to clouds and water vapor". In: *Frontiers of Climate Modeling*. Vol. 9780521791. Cambridge University Press, Aug. 2006, pp. 119–151. ISBN: 9780511535857. DOI: 10.1017/CBO9780511535857.006 (cit. on p. 15).

[4] Michael Ghil and Valerio Lucarini. "The physics of climate variability and climate change". In: *Reviews of Modern Physics* 92.3 (July 2020), p. 035002. ISSN: 0034-6861. DOI: 10.1103/RevModPhys.92.035002 (cit. on p. 15).

[5] Wenyi Zhong and Joanna D. Haigh. "The greenhouse effect and carbon dioxide". In: *Weather* 68.4 (Apr. 2013), pp. 100–105. ISSN: 0043-1656. DOI: 10.1002/wea.2072 (cit. on p. 15).

[6] UNFCCC. *United Nations Framework Convention on Climate Change*. Tech. rep. 1992, pp. 1–33. URL: https://unfccc.int/files/essential_background/background_publications_htmlpdf/application/pdf/conveng.pdf (cit. on p. 15).

[7] Rebecca Lindsey. "Climate Change: Atmospheric Carbon Dioxide". URL: https://www.climate.gov/news-features/understanding-climate/climate-change-atmospheric-carbon-dioxide. *Climate.gov. Accessed on 07-03-2024*.

[8] Rebecca Lindsey and Luann Dahlman. "Climate Change: Global Temperature". URL: https://www.climate.gov/news-features/understanding-climate/climate-change-global-temperature. *Climate.gov. Accessed on 07-03-2024*.

[9] UNFCCC. *Paris Agreement to the United Nations Framework Convention on Climate Change*. Tech. rep. 2015. URL: https://unfccc.int/sites/default/files/resource/parisagreement_publication.pdf (cit. on p. 15).

[10] WMO. "WMO confirms that 2023 smashes global temperature record". URL: https://wmo.int/news/media-centre/wmo-confirms-2023-smashes-global-temperature-record. *Press release. Accessed on 30-04-2024*.

[11] Scott Nicholson and Garvin Heath. *Life Cycle Greenhouse Gas Emissions from Electricity Generation: Update*. Tech. rep. NREL, 2021, pp. 1–4. URL: https://www.nrel.gov/docs/fy21osti/80580.pdf (cit. on p. 16).

[12] Y-m Wei et al. *Climate Change 2022: Mitigation of Climate Change - Energy Systems*. Tech. rep. 2022. Chap. 6, pp. 613–746. URL: https://www.ipcc.ch/report/ar6/wg3/downloads/report/IPCC_AR6_WGIII_Chapter06.pdf (cit. on p. 16).

[13] IEA. "Massive expansion of renewable power opens door to achieving global tripling goal set at COP28". URL: https://www.iea.org/news/massive-expansion-of-renewable-power-opens-door-to-achieving-global-tripling-goal-set-at-cop28. *Press release. Accessed on 01-05-2024*.

[14] IPCC. *Climate Change 2022 - Mitigation of Climate Change - Full Report*. 1. 2022, pp. 1–30. ISBN: 9781107415416 (cit. on p. 16).

[15] Fraunhofer Institute for Solar Energy Systems. "Fraunhofer ISE develops the world's most efficient solar cell with 47.6 percent efficiency". URL: https://www.ise.fraunhofer.de/en/press-media/press-releases/2022/fraunhofer-ise-develops-the-worlds-most-efficient-solar-cell-with-47-comma-6-percent-efficiency.html. *Press release. Accessed on 19-02-2024*.

[16] Hao Lin et al. "Silicon heterojunction solar cells with up to 26.81% efficiency achieved by electrically optimized nanocrystalline-silicon hole contact layers". In: *Nature Energy* 8.8 (May 2023), pp. 789–799. ISSN: 2058-7546. DOI: 10.1038/s41560-023-01255-2 (cit. on p. 17).

[17] Marina Alves et al. "Thin-film micro-concentrator solar cells". In: *Journal of Physics: Energy* 2.1 (Nov. 2019), p. 012001. ISSN: 2515-7655. DOI: 10.1088/2515-7655/ab4289 (cit. on pp. 17, 19, 44).

[18] Giles E. Eperon et al. "Formamidinium lead trihalide: A broadly tunable perovskite for efficient planar heterojunction solar cells". In: *Energy and Environmental Science* 7.3 (2014), pp. 982–988. ISSN: 17545692. DOI: 10.1039/c3ee43822h (cit. on p. 18).

[19] P. T. Landsberg and P. Baruch. "The thermodynamics of the conversion of radiation energy for photovoltaics". In: *Journal of Physics A: Mathematical and General* 22.11 (June 1989), pp. 1911–1926. ISSN: 0305-4470. DOI: 10.1088/0305-4470/22/11/028 (cit. on p. 18).

[20] Marcus Chuang. "Shockley Queisser limit: Theoretical Solar Cell Efficiencies calculator and visualizer". URL: https://github.com/marcus-cmc/Shockley-Queisser-limit. *Github. Accessed on 14-04-2022*.

[21] William Shockley and Hans J. Queisser. "Detailed Balance Limit of Efficiency of p-n Junction Solar Cells". In: *Journal of Applied Physics* 32.3 (Mar. 1961), pp. 510–519. ISSN: 0021-8979. DOI: 10.1063/1.1736034 (cit. on p. 18).

[22] Myriam Paire. "Highly efficient solar cells in low dimensionality based on Cu(In,Ga)Se2 chalcopyrite materials". PhD thesis. Sorbonne Universités, UPMC, 2016. URL: https://hal.science/tel-01393784 (cit. on pp. 17, 18, 44).

[23] J. R. Tuttle et al. "The Performance of Cu(In, Ga)Se2-Based Solar Cells in Conventional and Concentrator Applications". In: *MRS Proceedings* 426.January (Feb. 1996), p. 143. ISSN: 0272-9172. DOI: 10.1557/PROC-426-143 (cit. on p. 18).

[24] Myriam Paire et al. "Physics of Cu(In, Ga)Se2 solar cells in high injection regime". In: *2011 37th IEEE Photovoltaic Specialists Conference*. IEEE, June 2011, pp. 000140–000143. ISBN: 978-1-4244-9965-6. DOI: 10.1109/PVSC.2011.6185863 (cit. on pp. 18, 19, 44).

[25] Sascha Sadewasser. "Geometry and materials considerations for thin film micro-concentrator solar cells". In: *Solar Energy* 158 (Dec. 2017), pp. 186–191. ISSN: 0038092X. DOI: 10.1016/j.solener.2017.09.035 (cit. on p. 18).

[26] Myriam Paire et al. "Thin film microcells for concentrated applications". In: *2013 IEEE 39th Photovoltaic Specialists Conference (PVSC)*. IEEE, June 2013, pp. 2118–2122. ISBN: 978-1-4799-3299-3. DOI: 10.1109/PVSC.2013.6744892 (cit. on p. 19).

[27] Pierre Albert et al. "Miniaturization of InGaP/InGaAs/Ge solar cells for micro-concentrator photovoltaics". In: *Progress in Photovoltaics: Research and Applications* 29.9 (2021), pp. 990–999. ISSN: 1099159X. DOI: 10.1002/pip.3421 (cit. on p. 19).

[28] Myriam Paire et al. "Cu(In, Ga)Se2 microcells: High efficiency and low material consumption". In: *Journal of Renewable and Sustainable Energy* 5.1 (2013), pp. 1–6. ISSN: 19417012. DOI: 10.1063/1.4791778 (cit. on p. 19).

[29] Jan Keller et al. "High-concentration silver alloying and steep back-contact gallium grading enabling copper indium gallium selenide solar cell with 23.6% efficiency". In: *Nature Energy* (Feb. 2024). ISSN: 2058-7546. DOI: 10.1038/s41560-024-01472-3 (cit. on pp. 19, 67, 127, 156).

[30] A. Duchatelet et al. "Self-aligned growth of thin film Cu(In,Ga)Se2 solar cells on various micropatterns". In: *Applied Physics Letters* 109.25 (Dec. 2016), p. 253901. ISSN: 0003-6951. DOI: 10.1063/1.4971975 (cit. on p. 19).

[31] Sascha Sadewasser, Pedro M.P. Salomé, and Humberto Rodriguez-Alvarez. "Materials efficient deposition and heat management of CuInSe2 micro-concentrator

solar cells". In: *Solar Energy Materials and Solar Cells* 159.October 2016 (Jan. 2017), pp. 496–502. ISSN: 09270248. DOI: 10.1016/j.solmat.2016.09.041 (cit. on pp. 19, 24).

[32] F. Ringleb et al. "Regularly arranged indium islands on glass/molybdenum substrates upon femtosecond laser and physical vapor deposition processing". In: *Applied Physics Letters* 108.11 (Mar. 2016), p. 111904. ISSN: 0003-6951. DOI: 10.1063/1.4943794 (cit. on p. 19).

[33] Berit Heidmann et al. "Local growth of CuInSe 2 micro solar cells for concentrator application". In: *Materials Today Energy* 6 (Dec. 2017), pp. 238–247. ISSN: 24686069. DOI: 10.1016/j.mtener.2017.10.010 (cit. on p. 19).

[34] Martina Schmid et al. "Locally grown Cu(In,Ga)Se2 micro islands for concentrator solar cells". In: *Physics, Simulation, and Photonic Engineering of Photovoltaic Devices VII*. Ed. by Alexandre Freundlich, Masakazu Sugiyama, and Laurent Lombez. Vol. 10527. SPIE, Feb. 2018, p. 7. ISBN: 9781510615397. DOI: 10.1117/12.2288253 (cit. on p. 19).

[35] Ana Pérez-Rodríguez et al. "Current status of bottom-up fabrication approaches for Cu(In,Ga)Se2 micro-concentrator solar cells". In: *AIP Conference Proceedings*. Vol. 2550. September. 2022, p. 060005. ISBN: 9780735443921. DOI: 10.1063/5.0104440 (cit. on p. 19).

[36] Daniel Siopa et al. "Micro-sized thin-film solar cells via area-selective electrochemical deposition for concentrator photovoltaics application". In: *Scientific Reports* 10.1 (Dec. 2020), p. 14763. ISSN: 2045-2322. DOI: 10.1038/s41598-020-71717-0 (cit. on pp. 19, 26, 52).

[37] M.I. Alonso et al. "Optical functions of chalcopyrite CuGaxIn1-xSe2 alloys". In: *Applied Physics A: Materials Science & Processing* 74.5 (May 2002), pp. 659–664. ISSN: 0947-8396. DOI: 10.1007/s003390100931 (cit. on p. 20).

[38] F. B. Dejene and V. Alberts. "Structural and optical properties of homogeneous Cu(In,Ga)Se2 thin films prepared by thermal reaction of InSe/Cu/GaSe alloys with elemental Se vapour". In: *Journal of Physics D: Applied Physics* 38.1 (Jan. 2005), pp. 22–25. ISSN: 0022-3727. DOI: 10.1088/0022-3727/38/1/005 (cit. on p. 20).

[39] Jae-Cheol Park et al. "Bandgap engineering of Cu(In_1-xGa_x)Se_2 absorber layers fabricated using CuInSe_2 and CuGaSe_2 targets for one-step sputtering process". In: *Optical Materials Express* 6.11 (Nov. 2016), p. 3541. ISSN: 2159-3930. DOI: 10.1364/OME.6.003541 (cit. on pp. 20, 128).

[40] Jeyakumar Ramanujam and Udai P. Singh. "Copper indium gallium selenide based solar cells – a review". In: *Energy & Environmental Science* 10.6 (2017), pp. 1306–1319. ISSN: 1754-5692. DOI: 10.1039/C7EE00826K (cit. on p. 20).

[41] E. Romero et al. "Phase identification and AES depth profile analysis of Cu(In,Ga)Se2 thin films". In: *Brazilian Journal of Physics* 36.3b (Sept. 2006), pp. 1050–1053. ISSN: 0103-9733. DOI: 10.1590/S0103-97332006000600067 (cit. on p. 20).

[42] Maxim Guc et al. "Evaluation of defect formation in chalcopyrite compounds under Cu-poor conditions by advanced structural and vibrational analyses". In: *Acta Materialia* 223 (Jan. 2022), p. 117507. ISSN: 13596454. DOI: 10.1016/j.actamat.2021.117507 (cit. on pp. 20, 21).

[43] Tilo Gödecke, Thomas Haalboom, and Frank Ernst. "Phase Equilibria of Cu-In-Se I. Stable States and Nonequilibrium States of the In2Se3-Cu2Se Subsystem". In: *International Journal of Materials Research* 91.8 (Aug. 2000), pp. 622–634. ISSN: 2195-8556. DOI: 10.1515/ijmr-2000-910802 (cit. on p. 20).

[44] Susanne Siebentritt et al. "Why do we make Cu(In,Ga)Se2 solar cells non-stoichiometric?" In: *Solar Energy Materials and Solar Cells* 119 (Dec. 2013), pp. 18–25. ISSN: 09270248. DOI: 10.1016/j.solmat.2013.04.014 (cit. on pp. 20, 91, 92, 116).

[45] C.H. Chang et al. "Thermodynamic assessment of the Cu-In-Se system and application to thin film photovoltaics". In: *Conference Record of the Twenty Fifth IEEE Photovoltaic Specialists Conference - 1996*. IEEE, 1996, pp. 849–852. ISBN: 0-7803-3166-4. DOI: 10.1109/PVSC.1996.564261 (cit. on p. 21).

[46] F. Hergert et al. "A crystallographic description of experimentally identified formation reactions of Cu(In,Ga)Se2". In: *Journal of Solid State Chemistry* 179.8 (Aug. 2006), pp. 2394–2415. ISSN: 00224596. DOI: 10.1016/j.jssc.2006.04.033 (cit. on p. 20).

[47] Peter Würfel and Uli Würfel. *Physics of Solar Cells*. 3rd ed. Vol. 6. August. Wiley, Jan. 2005, p. 128. ISBN: 9783527404285. DOI: 10.1002/9783527618545 (cit. on pp. 21, 40, 42, 43).

[48] Antonio Luque and Steven Hegedus, eds. *Handbook of Photovoltaic Science and Engineering*. 2nd editio. Wiley, Dec. 2010. ISBN: 9780470721698. DOI: 10.1002/9780470974704 (cit. on p. 21).

[49] Dominik Matthias Berg. "Kesterite Equilibrium Reaction and the Discrimination of Secondary Phases from Cu2ZnSnS4". PhD thesis. University of Luxembourg, 2012, p. 187. URL: http://hdl.handle.net/10993/15414 (cit. on p. 26).

[50] A. C. Fisher. *Electrode Dynamics*. Illustrate. Oxford University Press, 1996, p. 84. ISBN: 9780198556909 (cit. on p. 26).

[51] Yuliy D. Gamburg and Giovanni Zangari. *Theory and Practice of Metal Electrodeposition*. Vol. 35. 8. New York, NY: Springer New York, 2011, pp. 1–25. ISBN: 978-1-4419-9668-8. DOI: 10.1007/978-1-4419-9669-5 (cit. on p. 26).

[52] David Fuster et al. "System for manufacturing complete Cu(In,Ga)Se2 solar cells in situ under vacuum". In: *Solar Energy* 198.January (Mar. 2020), pp. 490–498. ISSN: 0038092X. DOI: 10.1016/j.solener.2020.01.073 (cit. on pp. 26, 27).

[53] Rainer Behrisch. *Sputtering by Particle Bombardment I*. Ed. by Rainer Behrisch. Vol. 47. Topics in Applied Physics. Berlin, Heidelberg: Springer Berlin Heidelberg, June 1981, p. 284. ISBN: 978-3-540-10521-3. DOI: 10.1007/3-540-10521-2 (cit. on p. 26).

[54] S. Swann. "Magnetron sputtering". In: *Physics in Technology* 19.2 (Mar. 1988), pp. 67–75. ISSN: 0305-4624. DOI: 10.1088/0305-4624/19/2/304 (cit. on p. 26).

[55] Jeong Hyeob Han et al. "Actual partial pressure of Se vapor in a closed selenization system: quantitative estimation and impact on solution-processed chalcogenide thin-film solar cells". In: *Journal of Materials Chemistry A* 4.17 (2016), pp. 6319–6331. ISSN: 2050-7488. DOI: 10.1039/C6TA00145A (cit. on pp. 28, 121, 126).

[56] Taowen Wang. "Comprehending and mitigating backside recombination in Cu(In,Ga)Se2 solar cells". PhD thesis. University of Luxembourg, 2023, p. 213. URL: https://hdl.handle.net/10993/57142 (cit. on pp. 28, 68, 121).

[57] Sebastian Schleussner et al. "Effect of gallium grading in Cu(In,Ga)Se2 solar-cell absorbers produced by multi-stage coevaporation". In: *Solar Energy Materials and Solar Cells* 95.2 (Feb. 2011), pp. 721–726. ISSN: 09270248. DOI: 10.1016/j.solmat.2010.10.011 (cit. on pp. 28, 67).

[58] Mohit Sood et al. "Absorber composition: A critical parameter for the effectiveness of heat treatments in chalcopyrite solar cells". In: *Progress in Photovoltaics: Research and Applications* 28.10 (Oct. 2020), pp. 1063–1076. ISSN: 1062-7995. DOI: 10.1002/pip.3314 (cit. on p. 29).

[59] Amicia D. Elliott. "Confocal Microscopy: Principles and Modern Practices". In: *Current Protocols in Cytometry* 92.1 (Mar. 2020), pp. 139–148. ISSN: 1934-9297. DOI: 10.1002/cpcy.68 (cit. on p. 30).

[60] Weichang Xie. "Transfer characteristics of white light interferometers and confocal microscopes". PhD thesis. University of Kassel, 2017, p. 275. URL: http://files/336/WeichangXie_Dissertation.pdf (cit. on p. 30).

[61] David J. Whitehouse. *Handbook of Surface and Nanometrology*. Vol. 3. 1. CRC Press, Dec. 2010, pp. 10–27. ISBN: 9780429140693. DOI: 10.1201/b10415 (cit. on p. 32).

[62] Peter Eaton and Paul West. "AFM modes". In: *Atomic Force Microscopy*. Oxford University Press, Mar. 2010, pp. 49–81. ISBN: 9780199570454. DOI: 10.1093/acprof:oso/9780199570454.001 (cit. on pp. 33, 49).

[63] Joseph I. Goldstein et al. *Scanning Electron Microscopy and X-Ray Microanalysis*. Ed. by Springer. 4th ed. Vol. 24. New York, NY: Springer New York, Dec. 2018, p. 550. ISBN: 978-1-4939-6674-5. DOI: 10.1007/978-1-4939-6676-9 (cit. on pp. 34–36).

[64] Albert C. Thompson et al. *X-Ray Data Booklet*. 3rd. Berkeley: University of California, Sept. 2009, p. 176. URL: https://xdb.lbl.gov (cit. on pp. 35, 71).

[65] Ewen Smith and Geoffrey Dent. *Modern Raman Spectroscopy – A Practical Approach*. Wiley, Dec. 2004, pp. 101–117. ISBN: 9780471496687. DOI: 10.1002/0470011831 (cit. on p. 37).

[66] Ian R. Lewis and Howell Edwards. *Handbook of Raman Spectroscopy*. CRC Press, Aug. 2001, p. 26. ISBN: 9781420029253. DOI: 10.1201/9781420029253 (cit. on p. 37).

[67] Jacobo Álvarez-García et al. "Raman Spectroscopy on Thin Films for Solar Cells". In: *Advanced Characterization Techniques for Thin Film Solar Cells*. Vol. 2-2. Wiley, Sept. 2016, pp. 469–499. ISBN: 9783527699025. DOI: 10.1002/9783527699025.ch17 (cit. on p. 37).

[68] Sven Rühle. "Tabulated values of the Shockley–Queisser limit for single junction solar cells". In: *Solar Energy* 130 (June 2016), pp. 139–147. ISSN: 0038092X. DOI: 10.1016/j.solener.2016.02.015 (cit. on p. 39).

[69] Susanne Siebentritt et al. "How photoluminescence can predict the efficiency of solar cells". In: *Journal of Physics: Materials* 4.4 (Oct. 2021), p. 042010. ISSN: 2515-7639. DOI: 10.1088/2515-7639/ac266e (cit. on p. 40).

[70] Daniel Abou-Ras, Thomas Kirchartz, and Uwe Rau. *Advanced Characterization Techniques for Thin Film Solar Cells: Second Edition*. Vol. 1-2. 2016, pp. 1–681. ISBN: 9783527699025. DOI: 10.1002/9783527699025 (cit. on pp. 40, 42, 43).

[71] Max Hilaire Wolter. "Optical investigation of voltage losses in high-efficiency Cu(In,Ga)Se2 thin-film solar cells". PhD thesis. University of Luxembourg, 2019, p. 253. URL: http://hdl.handle.net/10993/39611 (cit. on p. 40).

[72] Susanne Siebentritt. "What limits the efficiency of chalcopyrite solar cells?" In: *Solar Energy Materials and Solar Cells* 95.6 (June 2011), pp. 1471–1476. ISSN: 09270248. DOI: 10.1016/j.solmat.2010.12.014 (cit. on pp. 41, 42).

[73] A. S. Najm et al. "An in-depth analysis of nucleation and growth mechanism of CdS thin film synthesized by chemical bath deposition (CBD) technique". In: *Scientific Reports* 12.1 (Sept. 2022), p. 15295. ISSN: 2045-2322. DOI: 10.1038/s41598-022-19340-z (cit. on p. 41).

[74] Steven S. Hegedus and William N. Shafarman. "Thin-film solar cells: device measurements and analysis". In: *Progress in Photovoltaics: Research and Applications* 12.2-3 (Mar. 2004), pp. 155–176. ISSN: 1062-7995. DOI: 10.1002/pip.518 (cit. on pp. 42, 92).

[75] Jean-Francois Guillemoles et al. "Guide for the perplexed to the Shockley–Queisser model for solar cells". In: *Nature Photonics* 13.8 (Aug. 2019), pp. 501–505. ISSN: 1749-4885. DOI: 10.1038/s41566-019-0479-2 (cit. on p. 43).

[76] Myriam Paire et al. "Toward microscale Cu(In,Ga)Se2 solar cells for efficient conversion and optimized material usage: Theoretical evaluation". In: *Journal of Applied Physics* 108.3 (Aug. 2010), p. 034907. ISSN: 0021-8979. DOI: 10.1063/1.3460629 (cit. on p. 44).

[77] Myriam Paire et al. "Microscale solar cells for high concentration on polycrystalline Cu(In,Ga)Se2 thin films". In: *Applied Physics Letters* 98.26 (June 2011), p. 264102. ISSN: 0003-6951. DOI: 10.1063/1.3604789 (cit. on p. 44).

[78] Carlos Algora and Ignacio Rey-Stolle. *Handbook of Concentrator Photovoltaic Technology*. Ed. by Carlos Algora and Ignacio Rey-Stolle. Wiley, Apr. 2016. ISBN: 9781118472965. DOI: 10.1002/9781118755655 (cit. on p. 44).

[79] Seong-Uk Jun et al. "Surface Texturing and Anti-Reflection Coating of Multicrystalline Silicon Solar Cell". In: *Journal of the Korean institute of surface engineering* 40.3 (June 2007), pp. 138–143. ISSN: 1225-8024. DOI: 10.5695/JKISE.2007.40.3.138 (cit. on p. 47).

[80] Anil Kurella and Narendra B. Dahotre. "Review paper: Surface Modification for Bioimplants: The Role of Laser Surface Engineering". In: *Journal of Biomaterials Applications* 20.1 (July 2005), pp. 5–50. ISSN: 0885-3282. DOI: 10.1177/0885328205052974 (cit. on p. 47).

[81] Cheng Yang, Ching Ping Wong, and Matthew M. F. Yuen. "Printed electrically conductive composites: conductive filler designs and surface engineering". In: *Journal of Materials Chemistry C* 1.26 (2013), p. 4052. ISSN: 2050-7526. DOI: 10.1039/c3tc00572k (cit. on p. 47).

[82] Dr Kalliopi K. Aligizaki. "Surface Engineering for Corrosion and Wear Resistance". In: *Anti-Corrosion Methods and Materials* 51.1 (Feb. 2004). ISSN: 0003-5599. DOI: 10.1108/acmm.2004.12851aae.001 (cit. on p. 47).

[83] Mike Conroy and Joe Armstrong. "A comparison of surface metrology techniques". In: *Journal of Physics: Conference Series* 13 (Jan. 2005), pp. 458–465. ISSN: 1742-6588. DOI: 10.1088/1742-6596/13/1/106 (cit. on p. 47).

[84] L Brown and Liam Blunt. "Surface Metrology for the Automotive Industry". In: *Inaugural Automotive Researchers' Conference*. January. University of Huddersfield,

2008. URL: http://eprints.hud.ac.uk/id/eprint/4059/1/08AARC2008.pdf (cit. on p. 48).

[85] Margaret Stedman. "Mapping The Performance Of Surface-Measuring Instruments". In: ed. by Manfred Weck. Vol. d. 2. Jan. 1987, p. 138. DOI: 10.1117/12.941285 (cit. on p. 48).

[86] Hemraj M. Yadav and Jung-Sik Kim. "Fabrication of SiO2/TiO2 double layer thin films with self-cleaning and photocatalytic properties". In: *Journal of Materials Science: Materials in Electronics* 27.10 (Oct. 2016), pp. 10082–10088. ISSN: 0957-4522. DOI: 10.1007/s10854-016-5082-4 (cit. on pp. 49, 51).

[87] Ricardo G Poeira et al. "Optical Measurement of the Stoichiometry of Thin-Film Compounds Synthetized From Multilayers : Example of Cu(In,Ga)Se2". In: *Microscopy and Microanalysis* (2023). DOI: https://doi.org/10.1093/micmic/ozad105 (cit. on p. 51).

[88] Jinlian Bi et al. "Pulse electro-deposition of copper on molybdenum for Cu(In,Ga)Se2 and Cu2ZnSnSe4 solar cell applications". In: *Journal of Power Sources* 326 (2016), pp. 211–219. ISSN: 03787753. DOI: 10.1016/j.jpowsour.2016.07.005 (cit. on p. 52).

[89] Ridha Hamdi et al. "Electrodeposition Study of Silver: Nucleation Process and Theoretical Analysis". In: *Journal of Electronic Materials* 50.10 (2021), pp. 5507–5513. ISSN: 1543186X. DOI: 10.1007/s11664-021-09055-8 (cit. on p. 52).

[90] João C. Malaquias et al. "Tuning the gallium content of metal precursors for Cu(In,Ga)Se2 thin film solar cells by electrodeposition from a deep eutectic solvent". In: *Physical Chemistry Chemical Physics* 16.6 (2014), p. 2561. ISSN: 1463-9076. DOI: 10.1039/c3cp54509a (cit. on pp. 52, 54, 55, 58).

[91] Y. F. Lin et al. "Phase stabilities and interfacial reactions of the Cu–In binary systems". In: *Journal of Materials Science: Materials in Electronics* 31.13 (July 2020), pp. 10161–10169. ISSN: 0957-4522. DOI: 10.1007/s10854-020-03561-x (cit. on pp. 53, 57).

[92] W. M. Haynes. *CRC Handbook of Chemistry and Physics*. Ed. by W. M. Haynes, David R. Lide, and Thomas J. Bruno. 97th ed. Boca Raton: CRC Press, June 2016. ISBN: 9781315380476. DOI: 10.1201/9781315380476 (cit. on p. 56).

[93] H.-J. Fitting et al. "Electron beam excitation in thin layered samples". In: *Journal of Electron Spectroscopy and Related Phenomena* 159.1-3 (June 2007), pp. 46–52. ISSN: 03682048. DOI: 10.1016/j.elspec.2007.03.014 (cit. on p. 56).

[94] Hans Joachim Fitting et al. "EDX depths analysis of MIS-structures". In: *Mikrochimica Acta* 125.1-4 (Mar. 1997), pp. 235–238. ISSN: 0026-3672. DOI: 10.1007/BF01246189 (cit. on p. 56).

[95] Daniel Abou-Ras et al. "Inhomogeneities in Cu(In,Ga)Se2 Thin Films for Solar Cells: Band-Gap Versus Potential Fluctuations". In: *Solar RRL* 2.1 (Jan. 2018), p. 1700199. ISSN: 2367198X. DOI: 10.1002/solr.201700199 (cit. on p. 58).

[96] Peter O. Grabitz et al. "Spatial inhomogeneities in Cu(In,Ga)Se2 solar cells analyzed by an electron beam induced voltage technique". In: *Journal of Applied Physics* 100.12 (Dec. 2006), p. 124501. ISSN: 0021-8979. DOI: 10.1063/1.2402345 (cit. on p. 58).

[97] Thomas Schmid, Norbert Schafer, and Daniel Abou-Ras. "Raman microspectroscopy provides access to compositional and microstructural details of polycrystalline materials". In: *Spectroscopy Europe* 28.5 (2016), pp. 16–20. ISSN: 0966-0941 (cit. on pp. 59, 91).

[98] Wolfram Witte, Robert Kniese, and Michael Powalla. "Raman investigations of Cu(In,Ga)Se2 thin films with various copper contents". In: *Thin Solid Films* 517.2 (Nov. 2008), pp. 867–869. ISSN: 00406090. DOI: 10.1016/j.tsf.2008.07.011 (cit. on pp. 59, 63).

[99] Wolfram Witte et al. "Influence of the Ga Content on the Mo/Cu(In,Ga)Se2 Interface Formation". In: *2006 IEEE 4th World Conference on Photovoltaic Energy Conference*. Vol. 1. IEEE, May 2006, pp. 553–556. ISBN: 1-4244-0016-3. DOI: 10.1109/WCPEC.2006.279515 (cit. on pp. 59, 63).

[100] Pedro Santos et al. "Fabrication of semi-transparent Cu(In,Ga)Se2 solar cells aided by Bromine etching". In: *Thin Solid Films* 770.June 2022 (Apr. 2023), p. 139778. ISSN: 00406090. DOI: 10.1016/j.tsf.2023.139778 (cit. on p. 61).

[101] S. Roy et al. "Characterization of Cu(In,Ga)Se2 films by Raman scattering". In: *Materials Chemistry and Physics* 73.1 (Jan. 2002), pp. 24–30. ISSN: 02540584. DOI: 10.1016/S0254-0584(01)00345-5 (cit. on pp. 63, 73).

[102] Jun-feng Han et al. "Investigation of chalcopyrite film growth at various temperatures: analyses from top to the bottom of the thin films". In: *Journal of Materials Science: Materials in Electronics* 25.5 (May 2014), pp. 2237–2243. ISSN: 0957-4522. DOI: 10.1007/s10854-014-1864-8 (cit. on p. 63).

[103] Dahyun Nam, Jae-ung Lee, and Hyeonsik Cheong. "Excitation energy dependent Raman spectrum of MoSe2". In: *Scientific Reports* 5.1 (Nov. 2015), p. 17113. ISSN: 2045-2322. DOI: 10.1038/srep17113 (cit. on p. 63).

[104] A. H. Goldan et al. "Molecular structure of vapor-deposited amorphous selenium". In: *Journal of Applied Physics* 120.13 (Oct. 2016). ISSN: 0021-8979. DOI: 10.1063/1.4962315 (cit. on p. 63).

[105] T. P. Moffat et al. "Electrodeposition of Cu on Ru Barrier Layers for Damascene Processing". In: *Journal of The Electrochemical Society* 153.1 (2006), p. C37. ISSN: 00134651. DOI: 10.1149/1.2131826 (cit. on p. 64).

[106] E. Camacho-Espinosa, A. I. Oliva-Avilés, and A. I. Oliva. "Effect of the Substrate Cleaning Process on Pinhole Formation in Sputtered CdTe Films". In: *Journal of Materials Engineering and Performance* 26.8 (Aug. 2017), pp. 4020–4028. ISSN: 1059-9495. DOI: 10.1007/s11665-017-2842-0 (cit. on p. 64).

[107] Philip Jackson et al. "Properties of Cu(In,Ga)Se2 solar cells with new record efficiencies up to 21.7%". In: *physica status solidi (RRL) - Rapid Research Letters* 9.1 (Jan. 2015), pp. 28–31. ISSN: 18626254. DOI: 10.1002/pssr.201409520 (cit. on p. 67).

[108] Philip Jackson et al. "Effects of heavy alkali elements in Cu(In,Ga)Se2 solar cells with efficiencies up to 22.6%". In: *physica status solidi (RRL) – Rapid Research Letters* 10.8 (Aug. 2016), pp. 583–586. ISSN: 1862-6254. DOI: 10.1002/pssr.201600199 (cit. on pp. 67, 156).

[109] Bart Vermang et al. "Development of rear surface passivated Cu(In,Ga)Se2 thin film solar cells with nano-sized local rear point contacts". In: *Solar Energy Materials and Solar Cells* 117 (Oct. 2013), pp. 505–511. ISSN: 09270248. DOI: 10.1016/j.solmat.2013.07.025 (cit. on p. 67).

[110] Wei Peng et al. "Reducing nonradiative recombination in perovskite solar cells with a porous insulator contact". In: *Science* 379.6633 (Feb. 2023), pp. 683–690. ISSN: 0036-8075. DOI: 10.1126/science.ade3126 (cit. on p. 67).

[111] D. Rudmann et al. "Efficiency enhancement of Cu(In,Ga)Se2 solar cells due to post-deposition Na incorporation". In: *Applied Physics Letters* 84.7 (Feb. 2004), pp. 1129–1131. ISSN: 0003-6951. DOI: 10.1063/1.1646758 (cit. on pp. 68, 89, 127).

[112] Yazi Wang, Shasha Lv, and Zhengcao Li. "Review on incorporation of alkali elements and their effects in Cu(In,Ga)Se2 solar cells". In: *Journal of Materials Science & Technology* 96 (Jan. 2022), pp. 179–189. ISSN: 10050302. DOI: 10.1016/j.jmst.2020.07.050 (cit. on p. 68).

[113] Lei Tian and Rüdiger Dieckmann. "Bulk diffusion measurements to study the effectiveness of barrier layers: II. Exchange of sodium between liquid crystal display glass substrates with different barrier layers". In: *Journal of Applied Physics* 90.8 (Oct. 2001), pp. 3810–3815. ISSN: 0021-8979. DOI: 10.1063/1.1402151 (cit. on p. 68).

[114] N. Akcay et al. "Characterization of Cu2ZnSnS4 thin films prepared with and without thin Al2O3 barrier layer". In: *Solar Energy* 234.January (Mar. 2022), pp. 137–151. ISSN: 0038092X. DOI: 10.1016/j.solener.2022.01.074 (cit. on p. 68).

[115] William N. Shafarman, Susanne Siebentritt, and Lars Stolt. "Cu(InGa)Se2 Solar Cells". In: *Handbook of Photovoltaic Science and Engineering*. Vol. 346. 2010. Chichester, UK: John Wiley & Sons, Ltd, Mar. 2011, pp. 546–599. ISBN: 9780470721698. DOI: 10.1002/9780470974704.ch13 (cit. on p. 68).

[116] Pyuck-Pa Choi et al. "Comparative atom probe study of Cu(In,Ga)Se2 thin-film solar cells deposited on soda-lime glass and mild steel substrates". In: *Journal of Applied Physics* 110.12 (Dec. 2011). ISSN: 0021-8979. DOI: 10.1063/1.3665723 (cit. on p. 71).

[117] Jinwoo Lee et al. "Effect of Three-Stage Growth Modification on a CIGS Microstructure". In: *IEEE Journal of Photovoltaics* 6.6 (Nov. 2016), pp. 1645–1649. ISSN: 2156-3381. DOI: 10.1109/JPHOTOV.2016.2598264 (cit. on p. 71).

[118] V. Nadenau et al. "Sodium induced secondary phase segregations in CuGaSe2 thin films". In: *Journal of Crystal Growth* 233.1-2 (Nov. 2001), pp. 13–21. ISSN: 00220248. DOI: 10.1016/S0022-0248(01)01554-8 (cit. on p. 71).

[119] M R Balboul et al. "Sodium Induced Phase Segreations in CuGaSe2 and CuInSe2 Thin Films". In: *17th EC Photovoltaic Solar Energy Conferenc, Munich Germany, Oct* (2001), pp. 22–26 (cit. on p. 71).

[120] A. Vladar and M. Postek. "Electron Beam-Induced Sample Contamination in the SEM". In: *Microscopy and Microanalysis* 11.S02 (Aug. 2005), pp. 764–765. ISSN: 1431-9276. DOI: 10.1017/S1431927605507785 (cit. on p. 73).

[121] C. Rincón et al. "Raman spectra of the ordered vacancy compounds CuIn3Se5 and CuGa3Se5". In: *Applied Physics Letters* 73.4 (July 1998), pp. 441–443. ISSN: 0003-6951. DOI: 10.1063/1.121893 (cit. on pp. 73, 124, 125).

[122] Junfeng Han et al. "Raman and XPS studies of CIGS/Mo interfaces under various annealing temperatures". In: *Materials Letters* 136 (Dec. 2014), pp. 278–281. ISSN: 0167577X. DOI: 10.1016/j.matlet.2014.08.087 (cit. on p. 73).

[123] I. P. Kaminow, E. Buehler, and J. H. Wernick. "Vibrational Modes in ZnSiP2". In: *Physical Review B* 2.4 (Aug. 1970), pp. 960–966. ISSN: 0556-2805. DOI: 10.1103/PhysRevB.2.960 (cit. on p. 73).

[124] U. Rau et al. "Oxygenation and air-annealing effects on the electronic properties of Cu(In,Ga)Se2 films and devices". In: *Journal of Applied Physics* 86.1 (July 1999), pp. 497–505. ISSN: 0021-8979. DOI: 10.1063/1.370758 (cit. on p. 74).

[125] D. Braunger et al. "Influence of sodium on the growth of polycrystalline Cu(In,Ga)Se 2 thin films". In: *Thin Solid Films* 361-362 (Feb. 2000), pp. 161–166. ISSN: 00406090. DOI: 10.1016/S0040-6090(99)00777-4 (cit. on p. 75).

[126] Roland Scheer and Hans-Werner Schock. *Chalcogenide Photovoltaics*. Weinheim, Germany: Wiley-VCH Verlag GmbH & Co. KGaA, Feb. 2011. ISBN: 9783527633708. DOI: 10.1002/9783527633708 (cit. on pp. 75, 81, 83).

[127] B. H. Torrie. "Raman and Infrared Spectra of Na2SeO3, NaHSeO3, H2SeO3, and NaH3(SeO3)2". In: *Canadian Journal of Physics* 51.6 (Mar. 1973), pp. 610–615. ISSN: 0008-4204. DOI: 10.1139/p73-080 (cit. on p. 75).

[128] John Wiley Sons Inc. SpectraBase. "SpectraBase Compound ID: BC1pE7zBD5G SpectraBase Spectrum ID: CLdfl1Pbqau". URL: https://spectrabase.com/spectrum/CLdfl1Pbqau. *Last accessed: 2023-10-28*.

[129] John Wiley Sons Inc. SpectraBase. "SpectraBase Compound ID:LruCIP76Zzy SpectraBase Spectrum ID:9Fp1xiU5Xim". URL: https://spectrabase.com/spectrum/9Fp1xiU5Xim. *Last accessed: 2023-09-26*.

[130] Hamda A. Al-Thani et al. "The effect of Mo back contact on Na out-diffusion and device performance of Mo/Cu(In,Ga)Se2/CdS/ZnO solar cells". In: *Conference Record of the IEEE Photovoltaic Specialists Conference* April (2002), pp. 720–723. ISSN: 01608371. DOI: 10.1109/pvsc.2002.1190666 (cit. on p. 76).

[131] Robert V. Forest. "Diffusion of sodium in copper indium gallium diselenide based materials". PhD thesis. University of Delaware, 2015, p. 171. URL: http://udspace.udel.edu/handle/19716/17423 (cit. on pp. 76, 78, 79, 82, 83, 89).

[132] Dimitrios Hariskos and Michael Powalla. "Thermodynamic limitations for alkali metals in Cu(In,Ga)Se 2". In: *Journal of Materials Research* 32.20 (Oct. 2017), pp. 3789–3800. ISSN: 0884-2914. DOI: 10.1557/jmr.2017.394 (cit. on p. 79).

[133] Howard C. Berg. *Random Walks in Biology*. Princeton University Press, Dec. 1984. ISBN: 9781400820023. DOI: 10.1515/9781400820023 (cit. on p. 79).

[134] Anke Laemmle et al. "Investigation of the diffusion behavior of sodium in Cu(In,Ga)Se2 layers". In: *Journal of Applied Physics* 115.15 (2014). ISSN: 10897550. DOI: 10.1063/1.4871457 (cit. on p. 79).

[135] Xiaoli Sun and Zhiguo Wang. "Sodium adsorption and diffusion on monolayer black phosphorus with intrinsic defects". In: *Applied Surface Science* 427 (Jan. 2018), pp. 189–197. ISSN: 01694332. DOI: 10.1016/j.apsusc.2017.08.199 (cit. on p. 80).

[136] E Seebauer. "Estimating surface diffusion coefficients". In: *Progress in Surface Science* 49.3 (July 1995), pp. 265–330. ISSN: 00796816. DOI: 10.1016/0079-6816(95)00039-2 (cit. on p. 80).

[137] F. Hergert et al. "Formation reactions of chalcopyrite compounds and the role of sodium doping". In: *Thin Solid Films* 515.15 (May 2007), pp. 5843–5847. ISSN: 00406090. DOI: 10.1016/j.tsf.2006.12.037 (cit. on p. 81).

[138] Marika Bodegard, Karin Granath, and Lars Stolt. "Growth of Cu(In,Ga)Se2 thin films by coevaporation using alkaline precursors". In: *Thin Solid Films* 361-362 (Feb. 2000), pp. 9–16. ISSN: 00406090. DOI: 10.1016/S0040-6090(99)00828-7 (cit. on p. 81).

[139] Marika Bodegard. "The influence of sodium on the grain structure of CuInSe_2 films for photovoltaic applications". In: *Proc. 12th European Photovoltaic Solar Energy Conference, 1994* (1994), pp. 1743–1746. URL: https://cir.nii.ac.jp/crid/1572261549854625024 (cit. on p. 81).

[140] V. Probst et al. "The impact of controlled sodium incorporation on rapid thermal processed Cu(InGa)Se2-thin films and devices". In: *Proceedings of 1994 IEEE 1st World Conference on Photovoltaic Energy Conversion - WCPEC (A Joint Conference of PVSC, PVSEC and PSEC)*. Vol. 1. IEEE, 1994, pp. 144–147. ISBN: 0-7803-1460-3. DOI: 10.1109/WCPEC.1994.519828 (cit. on p. 81).

[141] Diego Colombara et al. "Deliberate and Accidental Gas-Phase Alkali Doping of Chalcogenide Semiconductors: Cu(In,Ga)Se2". In: *Scientific Reports* 7.1 (Apr. 2017), p. 43266. ISSN: 2045-2322. DOI: 10.1038/srep43266 (cit. on pp. 81, 89, 94, 111, 116, 127, 135).

[142] D. Rudmann et al. "Effects of NaF coevaporation on structural properties of Cu(In,Ga)Se2 thin films". In: *Thin Solid Films* 431-432 (May 2003), pp. 37–40. ISSN: 00406090. DOI: 10.1016/S0040-6090(03)00246-3 (cit. on p. 81).

[143] Stephan Brunken et al. "Co-evaporated CuInSe2: Influence of growth temperature and Na on solar cell performance". In: *2014 IEEE 40th Photovoltaic Specialist Conference (PVSC)*. IEEE, June 2014, pp. 3629–3632. ISBN: 978-1-4799-4398-2. DOI: 10.1109/PVSC.2014.6924893 (cit. on p. 81).

[144] B. Bissig et al. "Effects of NaF evaporation during low temperature Cu(In,Ga)Se2 growth". In: *Thin Solid Films* 582 (May 2015), pp. 56–59. ISSN: 00406090. DOI: 10.1016/j.tsf.2014.11.026 (cit. on p. 81).

[145] S. Puttnins et al. "Effect of sodium on material and device quality in low temperature deposited Cu(In,Ga)Se2". In: *Solar Energy Materials and Solar Cells* 119 (Dec. 2013), pp. 281–286. ISSN: 09270248. DOI: 10.1016/j.solmat.2013.08.029 (cit. on p. 83).

[146] A. Rockett et al. "Na in selenized Cu(In,Ga)Se2 on Na-containing and Na-free glasses: distribution, grain structure, and device performances". In: *Thin Solid Films* 372.1-2 (Sept. 2000), pp. 212–217. ISSN: 00406090. DOI: 10.1016/S0040-6090(00)01028-2 (cit. on p. 83).

[147] J.E. Granata et al. "Quantitative incorporation of sodium in CuInSe2 and Cu(In,Ga)Se2 photovoltaic devices". In: *Conference Record of the Twenty Sixth IEEE*

Photovoltaic Specialists Conference - 1997. IEEE, 1997, pp. 387–390. ISBN: 0-7803-3767-0. DOI: 10.1109/PVSC.1997.654109 (cit. on p. 83).

[148] "Diffusion in metals". In: *Smithells Metals Reference Book*. Ed. by E A Brandes and G B Brook. Seventh Ed. Oxford: Elsevier, 1992, pp. 13–1. ISBN: 978-0-08-051730-8. DOI: 10.1016/B978-0-08-051730-8.50018-2 (cit. on p. 84).

[149] Ramis Hertwig et al. "ALD-ZnMgO and absorber surface modifications to substitute CdS buffer layers in co-evaporated CIGSe solar cells". In: *EPJ Photovoltaics* 11.2020 (Jan. 2020). Ed. by Romain Carron et al., p. 12. ISSN: 2105-0716. DOI: 10.1051/epjpv/2020010 (cit. on p. 84).

[150] John K. Katahara and Hugh W. Hillhouse. "Quasi-fermi level splitting and sub-bandgap absorptivity from semiconductor photoluminescence". In: *Journal of Applied Physics* 116.17 (2014). ISSN: 10897550. DOI: 10.1063/1.4898346 (cit. on p. 87).

[151] Chan Bin Mo et al. "Impact of Buffer Layer Process and Na on Shunt Paths of Monolithic Series-connected CIGSSe Thin Film Solar Cells". In: *Scientific Reports* 9.1 (Mar. 2019), p. 3666. ISSN: 2045-2322. DOI: 10.1038/s41598-019-38945-5 (cit. on p. 88).

[152] Chuen-Lin Tien and Tsai-Wei Lin. "Thermal expansion coefficient and thermomechanical properties of SiNx thin films prepared by plasma-enhanced chemical vapor deposition". In: *Applied Optics* 51.30 (Oct. 2012), p. 7229. ISSN: 1559-128X. DOI: 10.1364/AO.51.007229 (cit. on p. 94).

[153] Friedrich Kessler and Dominik Rudmann. "Technological aspects of flexible CIGS solar cells and modules". In: *Solar Energy* 77.6 (Dec. 2004), pp. 685–695. ISSN: 0038092X. DOI: 10.1016/j.solener.2004.04.010 (cit. on p. 94).

[154] I. R. McKerracher et al. "Thermal expansion coefficients and composition of sputter-deposited silicon oxynitride thin films". In: *Journal of Physics D: Applied Physics* 43.33 (Aug. 2010), p. 335104. ISSN: 0022-3727. DOI: 10.1088/0022-3727/43/33/335104 (cit. on p. 94).

[155] A. Hultqvist et al. "Performance of Cu(In,Ga)Se2 solar cells using nominally alkali free glass substrates with varying coefficient of thermal expansion". In: *Journal of Applied Physics* 114.9 (Sept. 2013), p. 094501. ISSN: 0021-8979. DOI: 10.1063/1.4819802 (cit. on p. 94).

[156] F. Couzinié-Devy, N. Barreau, and J. Kessler. "Re-investigation of preferential orientation of Cu(In,Ga)Se2 thin films grown by the three-stage process". In: *Progress in Photovoltaics: Research and Applications* 19.5 (Aug. 2011), pp. 527–536. ISSN: 1062-7995. DOI: 10.1002/pip.1079 (cit. on p. 94).

[157] Diego Colombara, Billy J. Stanbery, and Giovanna Sozzi. "Revani diffusion model in Cu(In,Ga)Se 2". In: *Journal of Materials Chemistry A* 11.48 (2023), pp. 26426–26434. ISSN: 2050-7488. DOI: 10.1039/D3TA03690A (cit. on p. 94).

[158] Veronika Haug. "Cu(In,Ga)Se2 thin-film solar cells based on a simple sputtered alloy precursor and a low-cost selenization step". In: *Journal of Photonics for Energy* 1.1 (Jan. 2011), p. 018002. ISSN: 1947-7988. DOI: 10.1117/1.3659500 (cit. on p. 95).

[159] Junhyun Park and Woo Kyoung Kim. "Effect of sputtering conditions of co-sputtered Cu–In–Ga precursors on Cu(InGa)Se2 photovoltaic absorber formation". In: *Thin Solid Films* 572 (Dec. 2014), pp. 61–67. ISSN: 00406090. DOI: 10.1016/j.tsf.2014.08.017 (cit. on p. 95).

[160] Ricardo G. Poeira et al. "Direct fabrication of arrays of Cu(In,Ga)Se2 micro solar cells by sputtering for micro-concentrator photovoltaics". In: *Materials & Design* 225 (Jan. 2023), p. 111597. ISSN: 02641275. DOI: 10.1016/j.matdes.2023.111597 (cit. on pp. 104, 106).

[161] S. M. Rossnagel et al. "Collimated magnetron sputter deposition". In: *Journal of Vacuum Science & Technology A: Vacuum, Surfaces, and Films* 9.2 (Mar. 1991), pp. 261–265. ISSN: 0734-2101. DOI: 10.1116/1.577531 (cit. on p. 105).

[162] Zahra Bahari et al. "The equilibrium phase diagram of the copper–indium system: a new investigation". In: *Thermochimica Acta* 401.2 (May 2003), pp. 131–138. ISSN: 00406031. DOI: 10.1016/S0040-6031(02)00500-2 (cit. on p. 108).

[163] C Suryanarayana and Soon-Jik Hong. "Mechanism of low-temperature θ-CuGa2 phase formation in Cu-Ga alloys by mechanical alloying". In: *Journal of Applied Physics* 96.11 (2004), pp. 6120–6126. DOI: 10.1063/1.1808243 (cit. on p. 108).

[164] Roland Mainz et al. "Time-resolved investigation of Cu(In,Ga)Se2 growth and Ga gradient formation during fast selenisation of metallic precursors". In: *Progress in Photovoltaics: Research and Applications* 23.9 (Sept. 2015), pp. 1131–1143. ISSN: 10627995. DOI: 10.1002/pip.2531 (cit. on p. 114).

[165] Yasuhiro Hashimoto et al. "Surface Characterization of Chemically Treated Cu(In,Ga)Se2 Thin Films". In: *Japanese Journal of Applied Physics* 35.Part 1, No. 9A (Sept. 1996), pp. 4760–4764. ISSN: 0021-4922. DOI: 10.1143/JJAP.35.4760 (cit. on pp. 114, 127).

[166] Wolfram Witte et al. "Gallium gradients in Cu(In,Ga)Se2 thin-film solar cells". In: *Progress in Photovoltaics: Research and Applications* 23.6 (June 2015), pp. 717–733. ISSN: 10627995. DOI: 10.1002/pip.2485 (cit. on p. 114).

[167] Jae-Cheol Park et al. "10% efficiency Cu(In,Ga)Se2 solar cell with strongly (220)/(204) oriented Cu-poor absorber layers sputtered using single quaternary

target". In: *Journal of Alloys and Compounds* 812 (Jan. 2020), p. 152065. ISSN: 09258388. DOI: 10.1016/j.jallcom.2019.152065 (cit. on p. 116).

[168] Sanping Wu et al. "Over 12% efficient low-bandgap CuIn(S, Se)2 solar cells with the absorber processed from aqueous metal complexes solution in air". In: *Nano Energy* 62 (Aug. 2019), pp. 818–822. ISSN: 22112855. DOI: 10.1016/j.nanoen.2019.06.010 (cit. on p. 116).

[169] Lung-Hsin Tu, Chung-Hao Cai, and Chih-Huang Lai. "Tuning Ga Grading in Selenized Cu(In,Ga)Se 2 Solar Cells by Formation of Ordered Vacancy Compound". In: *Solar RRL* 5.3 (Mar. 2021), p. 2000626. ISSN: 2367-198X. DOI: 10.1002/solr.202000626 (cit. on p. 117).

[170] Florian Oliva et al. "Optical methodology for process monitoring of chalcopyrite photovoltaic technologies: Application to low cost Cu(In,Ga)(S,Se)2 electrodeposition based processes". In: *Solar Energy Materials and Solar Cells* 158 (Dec. 2016), pp. 168–183. ISSN: 09270248. DOI: 10.1016/j.solmat.2015.12.036 (cit. on p. 119).

[171] Chuan-Ming Xu et al. "Composition dependence of the Raman A1 mode and additional mode in tetragonal Cu–In–Se thin films". In: *Semiconductor Science and Technology* 19.10 (Oct. 2004), pp. 1201–1206. ISSN: 0268-1242. DOI: 10.1088/0268-1242/19/10/006 (cit. on p. 119).

[172] C. Insignares-Cuello et al. "Raman scattering analysis of electrodeposited Cu(In,Ga)Se2 solar cells: Impact of ordered vacancy compounds on cell efficiency". In: *Applied Physics Letters* 105.2 (July 2014), p. 021905. ISSN: 0003-6951. DOI: 10.1063/1.4890970 (cit. on p. 119).

[173] M Marudachalam et al. "Phases , morphology , and diffusion in Cu(Inx,Ga1-x)Se2 thin films". In: *Journal of Applied Physics* 2896.May 2014 (2009). DOI: 10.1063/1.366122 (cit. on p. 120).

[174] Byungwoo Kim and Byoung Koun Min. "Strategies toward highly efficient CIGSe thin-film solar cells fabricated by sequential process". In: *Sustainable Energy and Fuels* 2.8 (2018), pp. 1671–1685. ISSN: 23984902. DOI: 10.1039/c8se00158h (cit. on p. 120).

[175] Thomas P. Weiss et al. "Bulk and surface recombination properties in thin film semiconductors with different surface treatments from time-resolved photoluminescence measurements". In: *Scientific Reports* 9.1 (Mar. 2019), p. 5385. ISSN: 2045-2322. DOI: 10.1038/s41598-019-41716-x (cit. on p. 120).

[176] Jean-François Guillemoles et al. "One step electrodeposition of CuInSe2: Improved structural, electronic, and photovoltaic properties by annealing under high selenium pressure". In: *Journal of Applied Physics* 79.9 (May 1996), pp. 7293–7302. ISSN: 0021-8979. DOI: 10.1063/1.361446 (cit. on p. 121).

[177] T. Wada et al. "Fabrication of Cu(In,Ga)Se2 thin films by a combination of mechanochemical and screen-printing/sintering processes". In: *physica status solidi (a)* 203.11 (Sept. 2006), pp. 2593–2597. ISSN: 1862-6300. DOI: 10.1002/pssa.200669652 (cit. on p. 121).

[178] Sejin Ahn et al. "Effects of selenization conditions on densification of Cu(In,Ga)Se2 (CIGS) thin films prepared by spray deposition of CIGS nanoparticles". In: *Journal of Applied Physics* 105.11 (June 2009). ISSN: 0021-8979. DOI: 10.1063/1.3141755 (cit. on p. 121).

[179] Alexander R. Uhl et al. "Liquid-selenium-enhanced grain growth of nanoparticle precursor layers for CuInSe2 solar cell absorbers". In: *Progress in Photovoltaics: Research and Applications* 23.9 (Sept. 2015), pp. 1110–1119. ISSN: 1062-7995. DOI: 10.1002/pip.2529 (cit. on p. 121).

[180] Grayson M. Ford et al. "CuIn(S,Se)2 thin film solar cells from nanocrystal inks: Effect of nanocrystal precursors". In: *Thin Solid Films* 520.1 (Oct. 2011), pp. 523–528. ISSN: 00406090. DOI: 10.1016/j.tsf.2011.08.007 (cit. on p. 121).

[181] Jonathan J. Scragg. "Studies of Cu2ZnSnS4 films prepared by sulfurisation of electrodeposited precursors". PhD thesis. University of Bath, 2010. URL: https://researchportal.bath.ac.uk/files/187949402/UnivBath_PhD_2010_J_Scragg.pdf (cit. on p. 121).

[182] Bing Li et al. "Smooth Cu electrodeposition for Cu(In, Ga)Se2 thin-film solar cells: Dendritic clusters elimination by Ag buffer layer". In: *Energy Reports* 8 (Nov. 2022), pp. 1847–1852. ISSN: 23524847. DOI: 10.1016/j.egyr.2021.12.079 (cit. on p. 121).

[183] J. Weszka et al. "Raman scattering in In2Se3 and InSe2 amorphous films". In: *Journal of Non-Crystalline Solids* 265.1-2 (Mar. 2000), pp. 98–104. ISSN: 00223093. DOI: 10.1016/S0022-3093(99)00710-3 (cit. on p. 125).

[184] Yun-ju Chu and Ching-hwa Ho. "Amorphous effect on the advancing of structural-phase transition in γ-In2Se3 polycrystalline layers". In: *2015 International Symposium on Next-Generation Electronics (ISNE)*. IEEE, May 2015, pp. 1–3. ISBN: 978-1-4799-4208-4. DOI: 10.1109/ISNE.2015.7131960 (cit. on p. 125).

[185] Diego Colombara et al. "Chemical instability at chalcogenide surfaces impacts chalcopyrite devices well beyond the surface". In: *Nature Communications* 11.1 (July 2020), p. 3634. ISSN: 2041-1723. DOI: 10.1038/s41467-020-17434-8 (cit. on p. 127).

[186] Conrad Spindler. "Optical detection of deep defects in Cu(In,Ga)Se2". PhD thesis. University of Luxembourg, 2018. URL: https://hdl.handle.net/10993/37016 (cit. on p. 137).

[187] A. Khadir. "Simulation of Effects of Defects and Layers Thickness on the Performance of CIGS Solar Cells". In: *Acta Physica Polonica A* 137.6 (June 2020), pp. 1128–1134. ISSN: 1898-794X. DOI: 10.12693/APhysPolA.137.1128 (cit. on p. 141).

[188] Jan Keller et al. "Wide-gap (Ag,Cu)(In,Ga)Se 2 solar cells with different buffer materials—A path to a better heterojunction". In: *Progress in Photovoltaics: Research and Applications* 28.4 (Apr. 2020), pp. 237–250. ISSN: 1062-7995. DOI: 10.1002/pip.3232 (cit. on p. 141).

[189] David Mackay. *Sustainable energy - without the hot air*. Cambridge: UIT Cambridge Ltd., 2009, p. 383. ISBN: 978-0-9544529-3-3 (cit. on p. 145).

[190] E4L Team. "Energy4Life". URL: https://e4l.uni.lu/. *Accessed on 05-03-2024*.

[191] ZenziWerken. "Kids Toy Scale cnc/laser". URL: https://www.thingiverse.com/thing:1643194. *Accessed on 10-09-2022*.

[192] Jan Keller et al. "Effect of Cu Content on Post-Sulfurization of Cu(In,Ga)Se 2 Films and Corresponding Solar Cell Performance". In: *physica status solidi (a)* 216.20 (Oct. 2019), p. 1900472. ISSN: 1862-6300. DOI: 10.1002/pssa.201900472 (cit. on p. 156).

[193] Yu-han Chang et al. "Impact of RbF and NaF Postdeposition Treatments on Charge Carrier Transport and Recombination in Ga-Graded Cu(In,Ga)Se 2 Solar Cells". In: *Advanced Functional Materials* 31.40 (Oct. 2021). ISSN: 1616-301X. DOI: 10.1002/adfm.202103663 (cit. on p. 156).